

Abstract

Title of Document: A CHEMICAL CLIMATOLOGY OF LOWER TROPOSPHERIC TRACE GASES AND AEROSOLS OVER THE MID-ATLANTIC REGION

Jennifer Carrie Hains, Doctor of Philosophy, 2007

Directed By: Professor Russell R. Dickerson, Department of Atmospheric and Oceanic Science

Ozone and aerosols affect air quality, visibility and human health. The University of Maryland research aircraft conducted flights over the Mid-Atlantic region between 1995 and 2005 to characterize pollution events. I developed a chemical climatology of trace gases and aerosols that can be used to validate and improve models. O₃ and SO₂ measured aboard the aircraft were compared with O₃ and SO₂ generated with the Community Multiscale Air Quality (CMAQ). In general, CMAQ under-estimates O₃ above 500 m and over-estimates O₃ below 500 m (possible reasons for this include chemistry not being properly represented in the model). A sensitivity test of the rate of photolysis of NO₂ was performed and improving the photochemistry did improve the modeled O₃. CMAQ over-predicts the SO₂ column content by about 50%, possibly because the model gives SO₂ too long a lifetime. To test this theory I developed a method for calculating the SO₂ lifetime using *in-situ* measurements. The mean SO₂ lifetime was 19 ± 7 hours for measurements made in the daytime in the summer in the Mid-Atlantic region with in-

cloud processes responsible for ~80% of the removal. I made comparisons of three aerosol sampling systems and found the uncertainty of PM_{2.5}, sulfate, and ammonium measured with the Speciation Trends Network is larger than what has been reported and is at least 20%. I have developed clustering methodologies to group back trajectories associated with aircraft profiles as well as group trace gas and aerosol profiles by size and shape. The first clustering method produced eight distinct meteorological regimes associated with pollution and haze events. I quantified the amount of O₃ transported for each meteorological regime. Using the second method, I found a strong correlation between O₃ profiles and point source NO_x emissions. The comparisons of model and measured profiles, comparisons of surface measurements, and clustering methods are used to explain sources, sinks and distributions of trace gases and aerosols in the mid-Atlantic thus improving the understanding of the lower atmospheric composition in this area.

A CHEMICAL CLIMATOLOGY OF LOWER TROPOSPHERIC TRACE GASES
AND AEROSOLS OVER THE MID-ATLANTIC REGION

By

Jennifer Carrie Hains

Dissertation submitted to the Faculty of the Graduate School of the
University of Maryland, College Park, in partial fulfillment
of the requirements for the degree of
Doctor of Philosophy
2007

Advisory Committee:

Professor Russell R. Dickerson, Chair

Professor Neil Blough

Professor Douglas English

Professor John M. Ondov

Professor Robert Hudson

© Copyright by
Jennifer Carrie Hains
2007

Dedication

To Julie, Peter, Brendan, Miss Elisabeth and Cindy Rollo. Thank you for all of your love and support.

Acknowledgements

Funding for this work was provided in part by the Maryland Department of the Environment and Constellation Energy Group, Baltimore Gas and Electric Company and Potomac Electric Power Company through the Electric Power Research Institute and Maryland Industrial Partnership. Work related to GOME was supported by the University of Bremen. Special thanks to Russell Dickerson for infinite patience and inspiring creativity. Also many thanks to Brett Taubman, Jeff Stehr, Lung-Wen Chen, Charles Piety and Lackson Marufu for great ideas and support. Many thanks to Dale Allen the IDL master. Also many thanks to Bruce Doddridge, Mian Chin, Andreas Richter, Annette Ladstätter-Weißmayer, John Burrows, Anne Thompson, Peter Mueller, Robert Hudson, Tad Aburn, Diane Franks, Matthew Seybold, David Krask, Can Li, Pedro Bueno, Zahra Chaudry, Bryan Bloomer, and Rob Levy.

Table of Contents

Abstract.....	1
Dedication.....	ii
Acknowledgements.....	iii
Table of Contents.....	iv
List of Tables.....	vi
List of Figures.....	vii
Chapter 1: Introduction.....	1
1.1 Background.....	1
1.2 Chemical Transport Models.....	3
1.3 Meteorology Associated with Elevated O ₃	5
1.4 O ₃ Chemistry.....	6
1.5 SO ₂ Chemistry.....	7
1.6 Determination of Meteorological Influences on Pollution Episodes: Clustering Back Trajectories.....	9
1.7 Determining the influence of Point Source on Pollution Episodes: Clustering species profiles.....	12
1.8 Surface Measurements.....	14
1.9 Overview.....	17
Chapter 2: Sampling Platform and Instrumentation.....	20
2.1 Introduction.....	20
2.2 Aircraft.....	20
2.3 SO ₂	22
2.4 CO.....	26
2.5 O ₃	27
2.6 Aerosol Absorption.....	28
2.7 Scattering.....	30
Chapter 3: Determination of Meteorological Influences on Pollution Episodes: Clustering Back Trajectories.....	33
3.1 Introduction.....	33
3.2. Observations.....	34
3.2.1 Measurements.....	34
3.2.2 Trajectory Calculations.....	39
3.2.3. Cluster Analysis.....	40
3.3. Results and Discussion.....	44
3.3.1 Cluster Solution.....	44
3.3.2 Pollution Profiles.....	50
3.3.3 O ₃ Transport.....	57
3.4. Conclusions.....	59
Chapter 4: Cluster Analysis of Pollutant Profiles.....	62
4.1 Introduction.....	62
4.1.1 Background.....	62
4.1.2 Cluster Analysis.....	62
4.2 Results.....	64

4.2.1 O ₃	64
4.2.2 SO ₂	71
4.2.3 Particle Scattering	74
4.2.4 Angstrom Exponent	79
4.2.5 CO	82
4.2.6 Particle Absorption.....	85
4.3 Discussion	88
4.4 Conclusions	92
Chapter 5: Comparisons of University of Maryland Aircraft and Trace Gas Profiles with Models CMAQ and GOCART	94
5.1 Introduction	94
5.1.1 Background.....	94
5.1.2 Description of Models.....	95
5.2 Comparisons Between Models and Measurements	97
5.2.1 O ₃ Comparisons	97
5.2.2 The Effects of Aerosols on the Photolysis Rate of NO ₂ and the Production of O ₃	105
5.2.3 SO ₂ Comparisons	131
5.2.4 Lifetime Calculation.....	148
5.2.5 Verification of Lifetime Equation and Results.....	149
5.3 Conclusions	167
Chapter 6: A Side by Side Comparison of Filter-based PM _{2.5} Measurements at a Suburban Site: A Closure Study.....	169
6.1 Introduction	169
6.1.1 Background.....	169
6.1.2 Experiment.....	170
6.2 Results and Discussion.....	177
6.2.1 Uncertainty Analysis	177
6.2.2 Gravimetric Mass Comparisons.....	184
6.2.3 Chemical Compositions.....	189
6.2.4 Mass Closure.....	193
6.3 Conclusions	198
Chapter 7: Conclusions.....	201
7.1 Summary	201
7.2 Recommendations for Future Work.....	205
Appendix A	207
Appendix B	215

List of Tables

Chapter 2.

Table 1. Years when trace gases and aerosols were sampled.....	22
--	----

Chapter 3.

Table 1. Cluster median profile ranks and % O ₃ transported.....	48
Table 2. Cluster median profile values for $\omega_{0.550}$ and AOD.....	49
Table 3. Statistical difference among cluster values.....	50

Chapter 4.

Table 1. Altitude bins used in Equation 1.....	64
Table 2. SO ₂ /CO ratios for O ₃ Clusters.....	90

Chapter 5.

Table 1. CMAQ and aircraft O ₃ column contents.....	99
Table 2. Statistics for aerosol optical depth.....	107
Table 3. Median O ₃ column contents for the test episode.....	119
Table 4. The average aircraft and CMAQ SO ₂ column content.....	133
Table 5. The average aircraft and GOCART SO ₂ column content.....	135
Table 6. Location of box edges (from Figure 32).....	154
Table 7. Statistics of SO ₂ lifetimes generated with 8 hr model.....	157
Table 8. Statistics of SO ₂ lifetimes generated with 16 hr model.....	158
Table 9. Statistics of SO ₂ lifetimes generated with 24 hr model.....	159
Table 10. Statistics of SO ₂ lifetimes generated with 32 hr model.....	160
Table 11. Statistics for SO ₂ lifetime from measurements.....	164

Chapter 6.

Table 1. Analytical methods for PM _{2.5} species.....	171
Table 2. Comparison of 2- σ uncertainties for PM _{2.5} species.....	179
Table 3. Average PM _{2.5} concentrations and uncertainties.....	181-183
Table 4. Percentage of significant differences between STN _{RS} and DRI _F	185
Table 5. Regression statistics for STN _S vs. TEOM and the DRI _F vs TEOM.....	189
Table 6. Average reconstructed mass for STN _{RS} and DRI _F	195

Chapter 7.

Table 1. Percentage of transported O ₃	202
---	-----

Appendix A.

A.4. Comparisons of trace gas column averages between aircraft and surface.....	212
---	-----

List of Figures

Chapter 1

Figure 1. Counties out of compliance with O ₃ standards.....	1
Figure 2. Counties out of compliance with PM _{2.5} standards.....	2

Chapter 2

Figure 1. Locations of aircraft flights.....	21
Figure 2. Flow diagram for SO ₂ monitor.....	24
Figure 3. Flow schematic for the CO detector.....	26
Figure 4. Flow schematic for O ₃ analyzer.....	28
Figure 5. Flow diagram for PSAP.....	30
Figure 6. Flow schematic for nephelometer.....	31

Chapter 3.

Figures 1. Median values for O ₃ , SO ₂ , CO, and aerosols.....	35-37
Figure 2. Percent change in the TRMSD.....	44
Figure 3. Spaghetti plots of the back trajectories.....	45
Figure 4. Trajectory density maps.....	46
Figure 5. The median morning profiles for Clusters.....	55
Figure 6. The median afternoon profiles for Clusters.....	56
Figure 7. Pie chart showing the transport in the region.....	58

Chapter 4.

Figure 1. Median O ₃ profiles for each cluster.....	65
Figure 2. Back trajectory density plots for O ₃ Clusters.....	67
Figure 3. Circles drawn around an example back trajectory.....	69
Figure 4. Statistics for NO _x emissions for O ₃ clusters.....	70
Figure 5. Median O ₃ column content and NO _x emissions.....	71
Figure 6. Median SO ₂ profiles for each cluster.....	72
Figure 7. Back trajectory density plots for SO ₂ Clusters.....	73
Figure 8. Statistics for SO ₂ emissions for SO ₂ clusters.....	74
Figure 9. Median scattering profiles for each cluster.....	76
Figure 10. Back trajectory density plots for scattering clusters.....	77
Figure 11. Statistics for SO ₂ emissions for scattering clusters.....	78
Figure 12. Median Angstrom exponent profiles for each cluster.....	80
Figure 13. Back trajectory density plots for Angstrom exponent clusters.....	81
Figure 14. Statistics for SO ₂ emissions for Angstrom exponent clusters.....	82
Figure 15. Median CO profiles for each cluster.....	83
Figure 16. Back trajectory density plots for CO Clusters.....	84
Figure 17. Median absorption profiles for each cluster.....	86
Figure 18. Back trajectory density plots for absorption Clusters.....	87
Figure 19. Matching species profiles for O ₃ clusters.....	89
Figure 20. Matching species profiles for scattering clusters.....	91
Figure 21. Matching species profiles for absorption clusters.....	92

Chapter 5

Figure 1. Median CMAQ and aircraft O ₃ profiles.....	98
Figure 2. The ratio of CMAQ/Aircraft O ₃	99
Figure 3. CMAQ and aircraft O ₃ profiles for smallest differences.....	102
Figure 4. CMAQ and aircraft O ₃ profiles for median differences.....	103
Figure 5. CMAQ and aircraft O ₃ profiles for largest differences.....	104
Figure 6. The median Angstrom exponent for test episode.....	106
Figure 7. The median single scattering albedo for test episode.....	109
Figure 8. The median asymmetry parameter.....	110
Figure 9. Standard and revised j-NO ₂ values used in CMAQ.....	111
Figure 10. O ₃ profiles from the aircraft, standard and revised CMAQ runs.....	114-118
Figure 11. Median CMAQ O ₃ differences (standard – revised).....	119
Figure 12. Differences between revised and standard CMAQ O ₃	121-122
Figure 13. O ₃ differences (revised-standard) for a single swath.....	124
Figure 14. Swath used in curtain plot (Figure 13).....	125
Figure 15. Median CMAQ ozone reductions.....	127-128
Figure 16. Changes in O ₃ reductions.....	129-130
Figure 17. Median CMAQ and aircraft profiles of SO ₂	132
Figure 18. The ratio of median CMAQ/aircraft SO ₂	133
Figure 19. Median GOCART and aircraft profiles of SO ₂	134
Figure 20. The ratio of median GOCART/aircraft SO ₂	135
Figure 21. CMAQ and aircraft SO ₂ profiles for smallest differences.....	137
Figure 22. CMAQ and aircraft SO ₂ profiles for median differences.....	138
Figure 23. CMAQ and aircraft SO ₂ profiles for largest differences.....	139
Figure 24. GOCART and aircraft SO ₂ profiles for smallest differences.....	141
Figure 25. GOCART and aircraft SO ₂ profiles for median differences.....	142
Figure 26. GOCART and aircraft SO ₂ profiles for largest differences.....	143
Figure 27. US state population and area sources of SO ₂	145
Figure 28. The SO ₂ flux from national emissions and GOCART.....	146
Figure 29. CMAQ average H ₂ O ₂	148
Figure 30. SO ₂ generated using a Gaussian plume model.....	152
Figure 31. The locations of the sampling points used in the model.....	153
Figure 32. Boxes used to determine SO ₂ flux.....	154
Figure 33. Histogram of SO ₂ lifetimes from model.....	156
Figure 34. Back trajectories associated with the SO ₂ profiles.....	162
Figure 35. Histogram of SO ₂ lifetimes.....	164
Figure 36. Lifetime of SO ₂ with respect to OH oxidation.....	167

Chapter 6.

Figure 1. Sampler configuration for STN _R , STN _S and DRI _F	173
Figure 2. Time series of PM _{2.5} concentrations.....	186
Figure 3. Comparisons of PM _{2.5} among TEOM, DRI _F and STN _S	188
Figure 4. Frequency of gravimetric – reconstructed PM _{2.5} differences.....	199
Figure 5. Contributions of individual species to PM _{2.5} mass.....	197

Appendix A.

A.1. Comparison of aircraft and surface measurements of O ₃	209
A.2. Comparison of aircraft and surface measurements of SO ₂	210
A.3. Comparison of aircraft and surface measurements of CO.....	211
A.5. Comparison of aircraft and surface measurements of CO (outliers removed).....	214

Appendix B

B.1. SO ₂ absorption cross section.....	217
B.2. Map of GOME SO ₂	218
B.3. GOME and aircraft SO ₂	220
B.4. Light is scattering through absorbing and aerosol layers.....	222
B.5. Aircraft and GOME (revised AMF) SO ₂	223
B.6. Diagram of the steps used to calculate the revised O ₃ correction.....	225
B.7. Aircraft and GOME (revised AMF and O ₃ correction) SO ₂	226

Chapter 1: Introduction

1.1 Background

Numerous locations in the Mid-Atlantic US do not comply with National Ambient Air Quality Standards (NAAQS) for O₃ (80 ppb eight hour standard, formerly 120 ppb one hour standard) and PM_{2.5} (15 µg/m³ annual average standard and 35 µg/m³ daily average standard). Figures 1 and 2 show counties in the Mid-Atlantic that violate the NAAQS eight hour O₃ standard and the annual PM_{2.5} air quality standards.

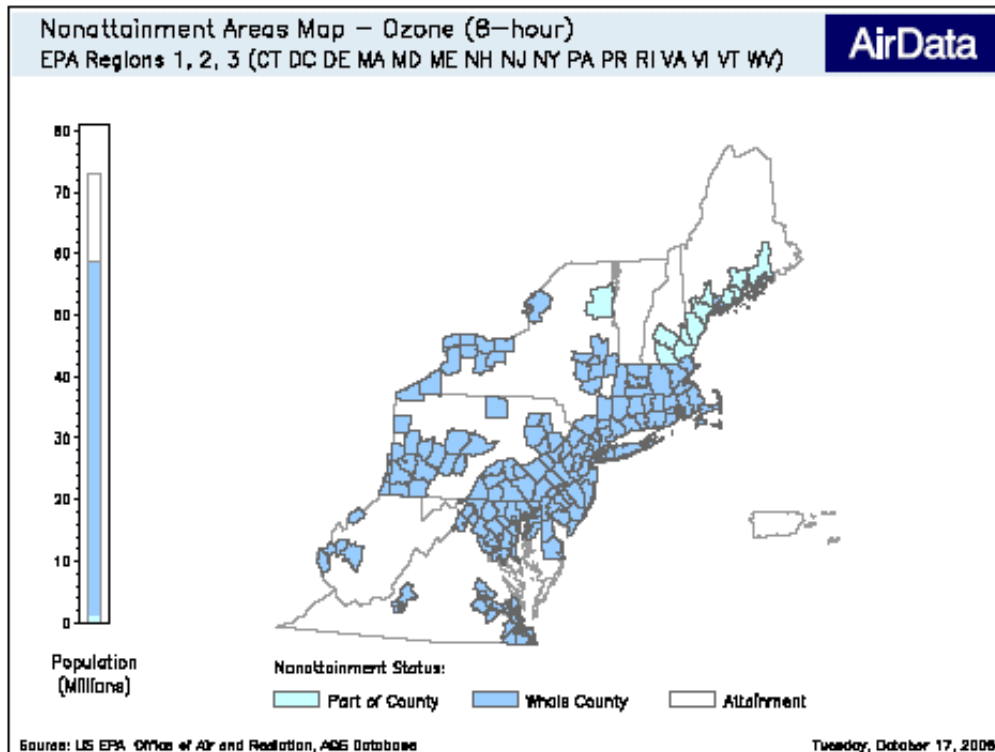


Figure 1. Counties in the Mid-Atlantic Region out of compliance with NAAQS 8-hr O₃ standards.

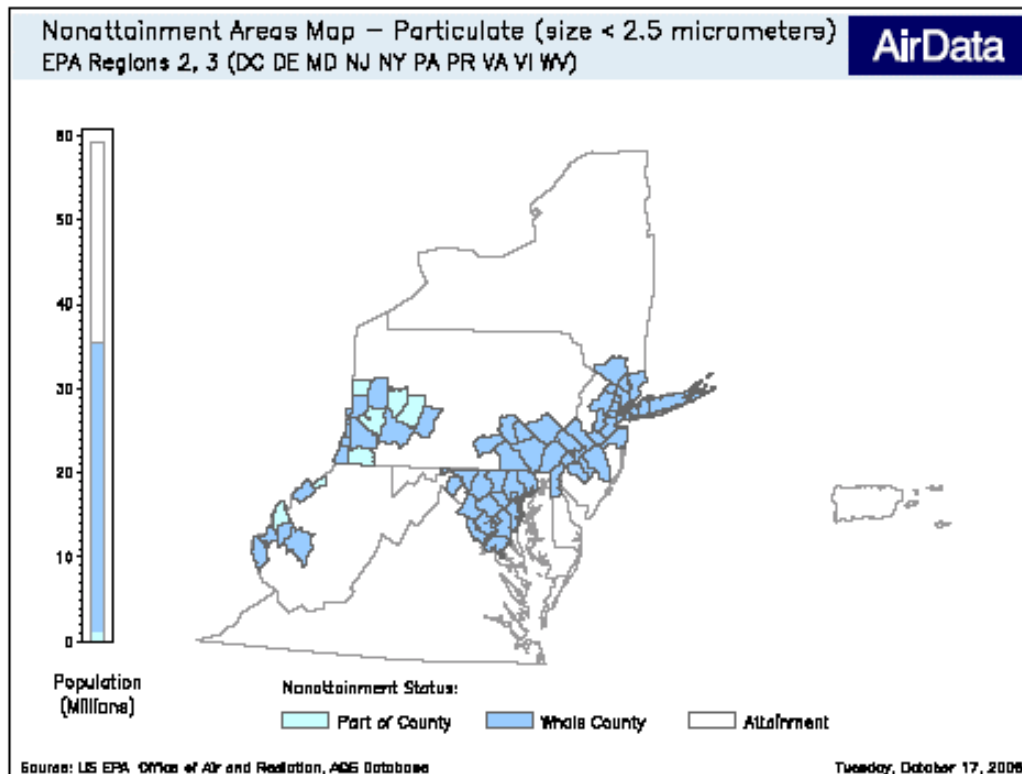


Figure 2. Counties in the Mid-Atlantic Region out of compliance with NAAQS annual PM_{2.5} standards.

Asthma hospitalizations (Buchdahl et al., 2000; White et al., 1994; Wong et al., 2001), reduced lung function in children (Frischer et al., 1999; Gauderman et al., 2002) and acute myocardial infarction (Ruidavets et al., 2005) have been associated with exposure to large O₃ concentrations. Fine particulate matter (PM_{2.5} with an aerodynamic diameter $\leq 2.5 \mu\text{m}$) alters the radiative balance of the Earth, decreases visibility and acts as cloud condensation nuclei (CCN). Increases in the CCN concentration can impact the global climate (IPCC, 2001). These increases in CCN lead to smaller cloud droplets which make clouds brighter and more reflective. Recent studies (Laden et al., 2000; Schwartz and Neas, 2000; Peters et al, 2001a)

have shown that elevated levels of PM_{2.5} are associated with cardiovascular and respiratory problems and even increased mortality rates. SO₂ is a major precursor of fine particulate matter in the Mid-Atlantic region of the United States and accounts for 30-60% of PM_{2.5} mass (Chen et al., 2002; Malm et al., 2004; Rees et al., 2004; Schwab et al., 2004; Frank et al., 2006; Ondov et al., 2006).

1.2 Chemical Transport Models

Models are used to predict pollution events and can be used in regulatory measures (such as when to issue warnings to the public to not drive, pump gas, paint, run electrical appliances, etc.) in order to reduce the pollution impact on the area. To achieve good predictions, accurate initial conditions are needed. A chemical climatology of the vertical and horizontal distribution of trace gases and aerosols can be used to improve model initial conditions and determine how well models generate these three-dimensional distributions.

The Community Multiscale Air Quality (CMAQ) system was developed by the EPA to improve predictions of pollution events associated with O₃, PM_{2.5} and reactive nitrogen species. The CMAQ modeling system incorporates outputs from meteorological modeling systems and emissions databases into a chemical transport model. Hogrefe et al. (2004) describe comparisons between O₃ surface measurements and CMAQ model results for 5 years of data (1993-1997) in the Eastern US. They found that CMAQ tends to overestimate small values of one and eight –hour maximum O₃, and underestimate large values of 1-hr maximum O₃. They also found that CMAQ captures the higher eight-hr maximum O₃. Tesche et al. (2006) compared daily CMAQ sulfate with surface measurements made using six

different networks in the United States in 2002. They found that the monthly averages of daily CMAQ simulations overestimated sulfate in the summer and fall and underestimate sulfate in the winter and spring with a fractional bias $\leq 30\%$. I found the opposite, in summary, CMAQ overestimates SO₂ (and likely underestimates sulfate) when compared with aircraft profiles (presented in Chapter 5). Levy (2007) found that CMAQ underestimates PM_{2.5} in Maryland. Because sulfate accounts for 30-60% of PM_{2.5} (Chen et al., 2002; Malm et al., 2004; Rees et al., 2004; Schwab et al., 2004; Frank et al., 2006; Ondov et al., 2006) it is likely that CMAQ underestimates sulfate. Mueller et al. (2006) also found that CMAQ underestimates sulfate. Mueller et al. (2006) found that CMAQ consistently underestimates cloud cover for model simulations in summertime episodes of 1992, 1993 and 1995 in the Eastern US. They also compared surface SO₂ and sulfate measurements to CMAQ model results and they found that CMAQ typically overestimated SO₂ and underestimated sulfate. They concluded that this is likely because CMAQ does not properly account for in-cloud oxidation of SO₂.

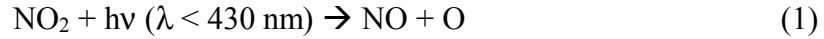
The Georgia Tech/ Goddard Global Ozone Chemistry Aerosol Radiation and Transport (GOCART) model was developed to simulate the atmospheric sulfur cycle (Chin et al., 2000a). Chin et al., (2000b) compared daily surface measurements of SO₂ in the US and Europe with GOCART simulations for 1989 and 1990. They found that GOCART was able to capture daily variations in SO₂ and sulfate, but the model overestimates SO₂ in the summer (by more than a factor of two) and underestimates measured maximum sulfate for the US.

1.3 Meteorology Associated with Elevated O₃

Understanding the relationship between meteorology and pollution events can improve forecasting of these events. In the Mid-Atlantic region voluntary measures such as car-pooling, public transportation, refueling after dark, and limiting electrical usage are encouraged on days when pollution events are predicted. These measures can help reduce pollution levels and their effectiveness is determined in part by how well pollution levels can be predicted. Elevated levels of O₃ are generally associated with high pressure systems and weak winds (Vukoich, 1994). Vukovich et al. (1999) and Ryan et al. (1998) found that larger O₃ levels are generally associated with areas with high pressure systems just above the surface as well as high pressure systems to the west or northwest. These high pressure systems are generally associated with little cloud cover, weak winds, subsidence and low-level inversions that allow for local O₃ accumulation. These conditions are also conducive for transport of O₃ and O₃ pre-cursors from the industrialized Mid-West. Vukovich et al. (1999) found that the most O₃ exceedences occur in July. These O₃ exceedences can be reduced if energy saving programs are implemented during this time period. The development of a chemical climatology and determination of meteorological conditions associated with pollution events can aid in the improvement of model predictions and forecasting these events as well as improve the understanding of transport over source regions.

1.4 O₃ Chemistry

O₃ is formed from oxides of nitrogen (NO_x) and volatile organic compounds (VOC). O₃ is produced by the following reaction of NO₂ and light



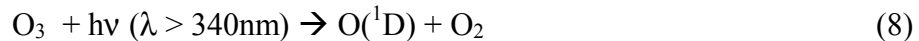
However, the NO formed in Reaction 1, readily reacts with O₃ to form NO₂ as shown below:



This results in a steady state between O₃ and NO₂. O₃ production is driven by reactions with the hydroxyl radical (OH) and organic compounds that provide a sink for NO, shown in equations 4-7 below:



Here R represents a portion of the organic compound C_nH_m, where n and m are integers. The major sources of OH include photodissociation of O₃.



In polluted areas, sources can include photodissociation of nitrous acid (HONO) and hydrogen peroxide (H₂O₂). The reaction between the hydroperoxyl radical (HO₂) and NO can also form OH. Sources of NO_x (NO and NO₂) in the United States include transportation (56% for 2002, EPA, 2003) and fuel combustion (37% for 2002, EPA,

2003). Though the sources of NO_x are generally at or near the surface the peak in O₃ production does not occur at the surface because the amount of light needed for NO₂ photodissociation increases with altitude (Kelley et al., 1995, Taubman et al., 2004a).

1.5 SO₂ Chemistry

Annual emissions of SO₂ for 2000 in the US were 1.65 x 10⁷ kg (EPA, 2003). Fuel combustion accounted for 86%, industrial processes accounted for 9% and transportation sources accounted for 5%. SO₂ is the pre-cursor for most sulfate; Rees et al.(2004) found that sulfate accounts for 38% of PM_{2.5} annually in Pittsburgh, PA, Frank et al. (2006) found that sulfate accounts for 44-53% of PM_{2.5} annually in Bronx, NY, Schwab et al. (2004) found that sulfate accounts an average of 30% of PM_{2.5} in the summer, at six sites in NY; Ondov et al. (2006) found sulfate accounts for 32-40% of PM_{2.5} mass in Baltimore, MD, and Malm et al. (2004) found it accounts for 50-60% of PM_{2.5}, and Chen et al.(2002) found it accounts for 35% of PM_{2.5}. SO₂ is a short lived species that is oxidized quickly with the OH radical to form sulfate; other loss processes include dry and wet deposition. The reaction with OH proceeds as follows:



When sufficient water vapor is available, SO₃ is converted to H₂SO₄



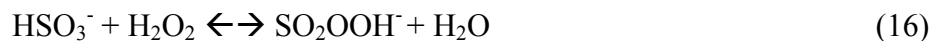
Typical atmospheric concentrations of OH give rise to an atmospheric lifetime for SO₂ of about a week. Seinfeld and Pandis (1998) suggest that by accounting for a typical dry deposition velocity of 1 cm s⁻¹ and a boundary layer of 1km, the lifetime

of SO₂ is about one day. I have found that the lifetime of SO₂ is 19 ± 7 hours (presented in Chapter 5) for the Mid-Atlantic for summertime and daytime conditions. The oxidation of SO₂ with OH (determined from CMAQ) accounts for about 11% of SO₂ removal. This lifetime was determined from profiles made when fair weather cumulus clouds were common. The reaction between SO₂ and aqueous H₂O₂ (found in fair weather cumulus clouds) also account for a significant amount of SO₂ oxidation. Using the calculated SO₂ lifetime (presented in Chapter 5) and assuming OH and H₂O₂ contribute significantly to the SO₂ loss, it appears that the Seinfeld and Pandis (1998) theoretical estimate of SO₂ dry deposition velocity is too fast for the Mid-Atlantic in the summer during daylight hours.

Global model calculations have shown the SO₂ lifetime to vary from, 0.6 – 2.6 days (Pham *et al.*, 1995; Chin *et al.*, 1996; Rested *et al.*, 1998; Koch *et al.*, 1999; Roelofs *et al.*, 1998; Berglen *et al.*, 2004). SO₂ in the gas phase can also dissolve in water to form the following species depending on the pH:



Here the bisulfite (HSO₃⁻) form is most often produced at a pH of 2-6, common for atmospheric droplets. SO₂ can also be oxidized by H₂O₂ in clouds and fogs at a pH less than 4.5 (Finlayson-Pitts and Pitts, 2000).



Edgerton et al. (2006) measured hourly SO₂, sulfate and other trace gases and aerosols at surface stations in the Southeast US in early spring 2002 (as part of the Southeastern Aerosol Research and Characterization Study, SEARCH). Using back trajectories and pollutant ratios they calculated SO₂ to sulfate conversion rates in SO₂ plumes (generally from coal-fired power plants, in the first 10 hours of transit time from the source) corresponding to an e-folding lifetime of 500- 40 hours.

1.6 Determination of Meteorological Influences on Pollution Episodes:

Clustering Back Trajectories

In order to effectively reduce pollution, major sources and meteorological conditions associated with pollution events need to be accurately determined. Clustering, a statistical technique to group data in space has been used to assess the impacts of emissions and meteorology on pollutant concentrations at receptor sites. This technique has been employed to group back trajectories into different meteorological regimes (Moody and Galloway, 1988; Dorling *et al.*, 1992a; Dorling *et al.*, 1992b; Lee *et al.*, 1994; Moy *et al.*, 1994; Dorling and Davies, 1995; Moody *et al.*, 1995; Harris and Oltmans, 1997; Brankov *et al.*, 1998; Moody *et al.*, 1998; Cape *et al.*, 2000; Eneroth *et al.*, 2003; Berto *et al.*, 2004; Jorba *et al.*, 2004; Russell *et al.*, 2004). The clustered back trajectories can then be used to determine source regions and synoptic regimes that support the regional transport of different atmospheric constituents. The studies listed above differ mainly in methods used to calculate the trajectories and the different techniques used to cluster the trajectories.

A major limitation of the published studies cited above arises from the fact that all of the receptor sites were surface-based. This restricts the amount of

information available on regional transport and the influences of lower atmospheric dynamics on the pollution measured at the surface. Eneroth et al. (2003) and Jorba *et al.* (2004) clustered trajectories at multiple altitudes to better describe the general circulation patterns in the troposphere, but the measurements were still fixed at the surface. Taubman et al. (2006) improved upon the previous studies by using similar statistical techniques to analyze several years of data collected from aircraft.

Aircraft provide a horizontally and vertically mobile sampling platform. The horizontal mobility allows for deployment to specific areas of interest, while the vertical mobility provides insight into boundary layer dynamics, and allows for measurements representative of a larger area. The ability to deploy to specific locations enables the investigation of multi-day haze and O₃ episodes, the influences of regionally transported pollution on urban and rural areas as well as the impacts large metropolitan areas have on Mid-Atlantic air quality. The vertical profile information presents a more complete picture of the composition and dynamics of the lower atmosphere, and this allows for the investigation of factors influencing the transport and chemical transformations of air pollutants and their precursors. Specifically, the nocturnal emissions from elevated sources and transport of pollution in the residual layer can be calculated from vertical profiles taken before the stable, nocturnal boundary layer has eroded and the pollution mixed down to the surface. The identification of transported pollution allows for a more accurate assessment of the effects of mixed layer development on surface pollution as well as local emissions and photochemical production.

The Regional Atmospheric Measurement Modeling and Prediction Program (RAMMPP) (<http://www.atmos.umd.edu/~RAMMPP/>) was formed to address problems with air pollution over the Mid-Atlantic US. To perform long term air quality studies and analyze tran-boundary pollution transport RAMMPP uses – measurements (ground-based and airborne), chemical transport modeling (Models-3/CMAQ), meso-scale modeling (MM5), and air quality forecasting. The airborne measurements have been conducted by the University of Maryland since 1992 with an instrumented light aircraft outfitted for atmospheric research. The aim of the aircraft analyses thus far has been to answer specific questions regarding lower atmospheric CO (Dickerson *et al.*, 1995; Doddridge *et al.*, 1998), pollutant transport and boundary layer dynamics during individual, Mid-Atlantic haze and O₃ episodes (Ryan *et al.*, 1998; Taubman *et al.*, 2004a), and the air quality and radiative impacts of smoke in the Mid-Atlantic from Canadian forest fires (Taubman *et al.*, 2004b). Additionally, a fortuitous experiment demonstrated the regional air quality benefits of the 2003 North American blackout (Marufu *et al.*, 2004). In Chapter 3 a chemical climatology of trace gases and aerosols (some of which was published in Taubman *et al.*, 2006) that answers some of the overarching questions not yet addressed by these case studies will be presented.

Typical clustering analyses clustered back trajectories ending at a single location. However, there were limited individual locations over which enough flights were performed to provide statistical meaning using this typical analysis. Furthermore, narrowly focusing on a few locations would fail to take advantage of the regional coverage offered by the dataset. For these reasons I have developed a novel

approach to clustering the data using multiple spatially heterogeneous receptor locations (presented in Taubman et al., 2006). Ozone events have long been identified as regional in nature with variability expected on scales of hundreds of km (Logan, 1985), so the use of multiple receptor locations is justified. I modified the standard distance calculation to account for spatial variability in the cluster algorithm. A detailed description of the methods is presented in Chapter 3. The statistical analysis of vertical profiles that I have developed is inherently different from analyses of single measurements at surface-based receptor sites. Using these techniques we were able to quantify the impacts of source regions and transport patterns on Mid-Atlantic air quality.

The measurements from this study overlap in time with those from the Mid-Atlantic EPA Supersites in Baltimore, New York, and Pittsburgh. Because of the regional nature of the study, the results presented in Chapter 3 will complement the investigations from those sites, aiding in measurement comparisons, model validation, and understanding the processes that control regional pollutant transport to and between the individual sites. The analyses should also be useful for air quality forecasting and modeling of pollution episodes as well as pollution control strategies.

1.7 Determining the influence of Point Source on Pollution Episodes:

Clustering species profiles

Methods that clarify the influence of meteorology and emissions on the vertical distribution of trace gases and aerosols can improve modeling and prediction of pollution events. I developed a method for clustering vertical profiles of trace gases and aerosols to group distinct profile shapes that may be associated with

different meteorological patterns or various transport regimes. This complements the previous section that clustered back trajectories and then formed associated trace gas and aerosol profiles. Many previous studies (Dorling *et al.*, 1992a; Dorling *et al.*, 1992b; Lee *et al.*, 1994; Moy *et al.*, 1994; Dorling and Davies, 1995; Moody *et al.*, 1995; Harris and Oltmans, 1997; Brankov *et al.*, 1998; Moody *et al.*, 1998; Cape *et al.*, 2000; Eneroth *et al.*, 2003; Berto *et al.*, 2004; Jorba *et al.*, 2004; Russell *et al.*, 2004, Taubman *et al.*, 2006) were devoted to clustering back trajectories to describe meteorological patterns associated with different trace gas and aerosol values. Moy *et al.* (1994), Brankov *et al.* (1998), and Taubman *et al.* (2006) were able to use back trajectory clusters to describe meteorological patterns associated with smog events. The converse of this method, clustering by O₃ profiles to identify different transport patterns, has been applied to ozonesonde and aircraft data (Diab *et al.*, 2003; Diab *et al.*, 2004, Colette *et al.*, 2005 a; Colette *et al.*, 2005 b).

Models used to predict O₃ and PM_{2.5} levels have limited ability to describe lower tropospheric transport within the planetary boundary layer (Seigneur, 2001; Mebust *et al.*, 2003; Zhang *et al.*, 2004; Hodzic, *et al.*, 2005). There is inadequate information on the planetary boundary layer distribution of trace gases and aerosols to improve the models. The University of Maryland has conducted summertime aircraft measurement campaigns since 1993 to gain a better understanding of the chemistry and dynamics of the lower troposphere including (Dickerson *et al.*, 1995; Doddridge *et al.*, 1998; Ryan *et al.*, 1998; Taubman *et al.*, 2004a; 2004b; 2006). Species measured aboard the University of Maryland research aircraft include O₃, SO₂, CO, particle light absorption at 565 nm, and total particle scattering at 450, 550, and 700

nm. I have clustered vertical profiles of the species by shape and absolute value to improve understanding of meteorological and emissions influences on trace gases and aerosols in the lower troposphere.

Taubman *et al.* (2006) grouped 48 hr back trajectories associated with 550 of the University of Maryland profiles into eight distinct meteorological regimes and used these clusters of back trajectories to describe differences among morning and afternoon profiles of O₃, SO₂, CO, particle scattering, Ångström exponent (α) calculated from the 450/700 nm ratio of particle scattering, and particle absorption. In Chapter 4, I will introduce a method for clustering these same profiles by their shape and magnitude (mixing ratio and scattering and absorption coefficients). This allows for separation of profiles based on small-scale structure and these differences may be ascribable to other factors such as emissions. The characterization of the planetary boundary layer and the lower free tropospheric composition of trace gases and aerosols can be used to evaluate and improve chemical transport modeling of these species, and aid in the forecasting of pollution events. It can also improve understanding of the relationship between the meteorology and chemistry of the lower troposphere.

1.8 Surface Measurements

The EPA has developed a Speciation Trends Network (STN) which has measured aerosols at the surface for 54 sites in the US since 1999. Precise measurements are critical for PM_{2.5} source apportionment tasks based on chemical mass balance and/or multivariate receptor models (Hopke, 1984; Watson *et al.*, 1984; Kim and Hopke, 2005; Kim *et al.*, 2005; Ogulei *et al.*, 2005).

NAAQS calls for the use of a Federal Reference Method, FRM, (Code of Federal Regulations (CFR), 1997) for the measurement of filter-based gravimetric $PM_{2.5}$ mass to determine compliance. However, other sampling and analytical protocols have been used extensively in air quality monitoring projects, such as the Speciation Trends Network –STN (US EPA, 1999), the Interagency Monitoring and Protective Visual Environment network –IMPROVE (Malm et al., 1994; Ames et al., 2001; Malm et al., 2002; 2004; 2005) and the California Regional $PM_{10}/PM_{2.5}$ air quality study (Chow et al., 2006). Equivalence of $PM_{2.5}$ mass determined with different protocols is currently under evaluation (Peters et al., 2001b; Watson and Chow, 2002; Solomon et al., 2003; Chow et al., 2005a). A FRM for $PM_{2.5}$ speciation has not yet been established by the United States Environmental Protection Agency.

I collected $PM_{2.5}$ samples during the 2002 intensive sampling periods at Fort Meade, Maryland (FME). I have used the samples to evaluate the STN speciation samplers and filter analyses under typical and elevated $PM_{2.5}$ events. FME, a suburban site located in the Baltimore-Washington urban corridor, approximately 3 km east of the Baltimore-Washington Parkway (I-295) and 10 km east of Interstate 95, was the anchor site for the Maryland Aerosol Characterization (MARCH-Atlantic) study (Chen et al., 2002) and part of the nationwide Speciation Trends Network (STN). It also served as one of the satellite sites for the Baltimore Supersite experiment during 2001 – 2003 (Lake et al., 2003; Harrison et al., 2004; Lee et al., 2005a; Ogulei et al., 2005; Park et al., 2005a; Park et al., 2005b; Ondov et al., 2006). Previous studies indicate that FME observations often reflect regional haze episodes and local accumulation under stagnant conditions. The annual mean $PM_{2.5}$

concentration at FME is around $13 \mu\text{g}/\text{m}^3$, and is influenced by local and regional sulfate, wood smoke, industry, mobile sources and secondary nitrate (Chen et al., 2001; 2002; 2003).

During January and July 2002, $\text{PM}_{2.5}$ speciation monitors from two different protocols (Speciation Trends Network-STN and Desert Research Institute-DRI) were installed at FME to concurrently measure atmospheric aerosol on a 24-h basis. Two Sequential Filter Samplers (SFS, Desert Research Institute, Reno, NV) from DRI were deployed in both January and July, while a Reference Ambient Air Sampler (RAAS $\text{PM}_{2.5}$, Thermo Scientific, Waltham, MA) and a Met One Speciation Air Sampling System (SASS, Met One Instruments Inc., Grants Pass, OR) represented the STN operation in January and July, respectively. The change of STN sampling systems (from January to July) was made with the understanding that both samplers had been equally approved by EPA for the STN application (US EPA, 1999). However their performances are not the same with respect to the DRI sampler. The SFS samples were analyzed by DRI and the RAAS and SASS samples were analyzed at the Research Triangle Institute (RTI, Research Triangle Park, NC) using methods described in Chow et al. (1996) and US EPA (1999). I will refer to the SFS samplers as DRI_F and the RAAS and SASS samplers as STN_R and STN_S (STN_{RS} denotes both instruments) hereafter. Components quantified by both DRI and RTI include gravimetric $\text{PM}_{2.5}$ mass, 35 trace elements, elemental carbon (EC), organic carbon (OC), total carbon (TC), and water soluble ions such as sulfate, nitrate and ammonium. DRI and RTI often used different techniques and instruments for the

analyses. Continuous measurements of PM_{2.5} mass were made in July with a Tapered Element Oscillating Microbalance (TEOM 1400a, Thermo Scientific, Waltham, MA).

Field performance of the STN_R and performance of the STN_{RS} size-selective inlet was assessed during the early stage of STN_{RS} development (Peters et al., 2001b, 2001c), but up-to-date evaluations of the STN_{RS} speciation data under real-world operation are rather limited. I will compare the STN_{RS} data from FME with collocated DRI measurements and investigate the PM_{2.5} chemical composition and mass closure within the context of uncertainty analysis. Approaches and conclusions presented in Chapter 6 can be tested in other studies facilitating a weight of evidence approach (e.g., Burton et al., 2002; Weed, 2005) to improve the design of ambient PM_{2.5} networks. The objective and results of this study are coordinated with others in the region including Lee et al., (2005a, 2005b), Flanagan et al., (2006) and the EPA-sponsored Eastern Supersites program (Solomon et al., 2003; Rees et al., 2004; Ondov et al., 2006).

1.9 Overview

The chemical climatology was developed with 10 years of summertime measurements of trace gases and aerosols made aboard the UMD research aircraft. Chapter 2 will provide specifics on instrumentation used aboard the aircraft. Most flights were made in the Mid-Atlantic region and Chapter 2 will present locations and times when flights were made.

An introduction to the chemical climatology with statistics of trace gas and aerosol measurements will be presented in Chapter 3. Diurnal variations in measurements will also be discussed. I performed a cluster analysis of back

trajectories associated with the aircraft flights in order to describe different meteorological regimes associated with the profiles. Results from this cluster analysis will be presented in Chapter 3, and some results from this Chapter were published in Taubman et al. (2006). The typical flight pattern consisted of flying upwind of pollution centers in the morning and downwind of the centers in the afternoon. This allowed for quantification of transported lower tropospheric O₃. A description of how transported O₃ was calculated and which meteorological regimes were associated with the most transport is presented in Chapter 3.

I developed of a methodology to cluster profiles of trace gases and aerosols to separate extreme events and to better understand meteorological and point source influences on aircraft profiles. This clustering methodology is presented in Chapter 4 along with the relationship between trace gas and aerosol profiles with point source emissions of SO₂ and NO_x.

To better understand how well models predict trace gases in the Mid-Atlantic I have compared O₃, SO₂, and CO with a regional model (CMAQ) presented in Chapter 5. I have also compared aircraft measured SO₂ with a global model (GOCART). The SO₂ column content generated from CMAQ and GOCART was 50% larger than that measured aboard the University of Maryland aircraft. As described in Chapter 4 the SO₂ profiles were not well correlated with SO₂ emissions encountered along a 48 hour back trajectory. These findings support the hypothesis that the lifetime of SO₂ in the Mid-Atlantic region in the summer is less than 48 hours. I developed a method for calculating the SO₂ lifetime using the UMD research

aircraft profiles and the EPA's SO₂ emissions database. This lifetime calculation is presented in Chapter 5.

In 2002 I collected surface filter samples of aerosols with two different American sampling systems. Comparisons of surface PM_{2.5} measurements made and the uncertainties associated with the sampling systems will be presented in Chapter 6. A summary of the research and recommendations for future work will be presented in Chapter 7.

Chapter 2: Sampling Platform and Instrumentation

2.1 Introduction

The chemical climatology was developed with 10 years of aircraft measurements of trace gases and aerosols. These measurements were made aboard the UMD research aircraft, mostly in the Mid-Atlantic region during regional haze and O₃ episodes. This Chapter will give specifics on where flights were made and how they were made. It will also provide details on the instruments used to collect trace gases O₃, SO₂ and CO as well as aerosol scattering and absorption.

2.2 Aircraft

A twin engine Piper Aztec was used to collect vertical profiles of trace gases and aerosols. Instruments were housed inside the aircraft and the sampling inlets were attached to the upper fuselage. On the upper fuselage there was an aft facing inlet that was attached to the trace gas instruments. There was also a forward facing isokinetic inlet that sampled aerosols. There were line losses of particles due to impaction on the side walls of the forward facing inlet and for this reason only submicron particles (< 1 μ m) were sampled. Flights were made mostly in the Mid-Atlantic region from 1995-2005. Spirals from 3 m above the surface to about 3000 m were made at small airports shown in Figure 1.

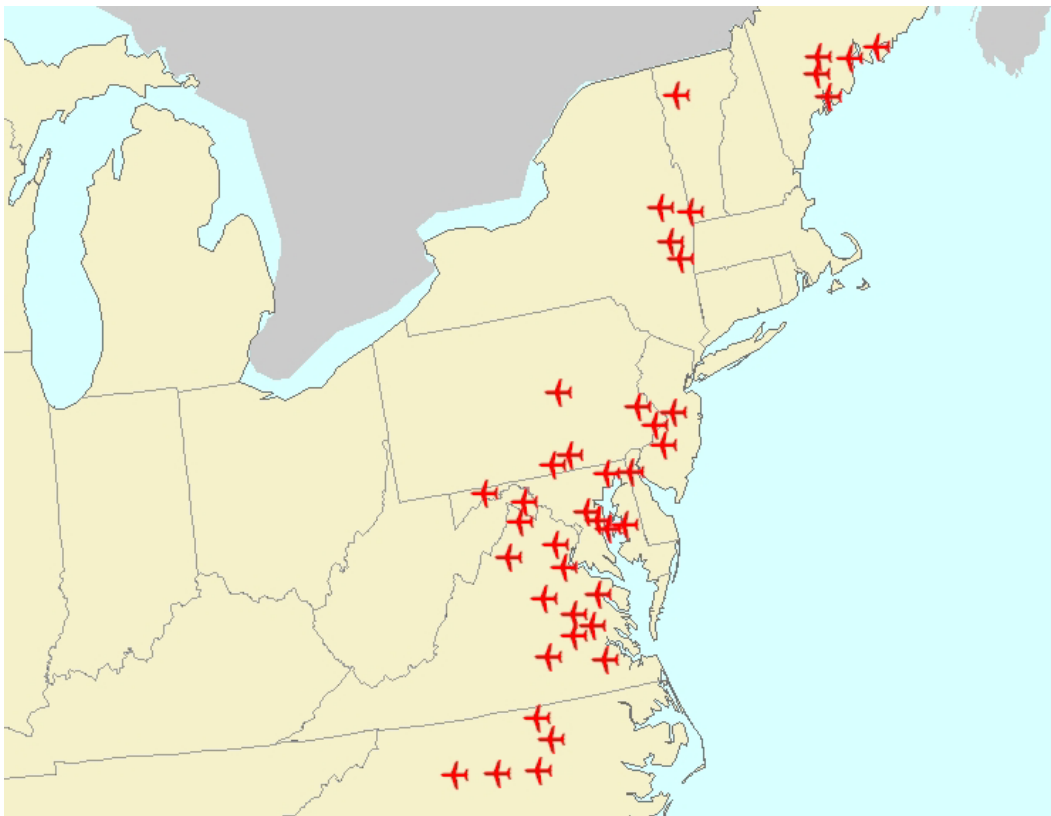


Figure 1. Locations of University of Maryland research aircraft flights made in the Eastern US between 1995 and 2005.

Spirals were completed within 30 minutes at a vertical climb rate of 100 m min^{-1} . Flight patterns were generally chosen to capture transport of pollutants to areas downwind of urban areas, and so flights conducted in the morning (before 12 noon EST) were upwind of urban areas in the Mid-Atlantic, while flights conducted in the afternoon (after 12 noon EST) were downwind of urban areas. The full instrument suite was not used every year and Table 1 shows the years in which new instruments were added to the suite. I collected samples aboard the aircraft for 12 of the flights (30 profiles) in 2005.

	O ₃	CO	SO ₂	PSAP	Nephelometer
1996	X				
1997	X				
1999	X	X			
2000	X	X	X	X	
2001	X	X	X	X	X
2002	X	X	X	X	X
2003	X	X	X	X	X
2004	X	X	X	X	X
2005	X	X	X	X	X

Table 1. Years when O₃, CO, SO₂, absorption with the PSAS and scattering with the nephelometer were sampled.

2.3 SO₂

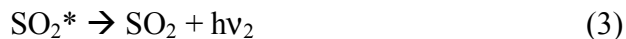
Thermo Scientific SO₂ analyzer (43C, Franklin, MA) measures SO₂ fluorescence from a pulsating UV light. SO₂ absorbs radiation in three wavelength regions, 1) 390-340 nm, 2) 320-250nm and 3) 230-190 nm. SO₂ absorbs weakly in region 1 and is quenched rapidly. SO₂ is also quenched rapidly by O₂ and N₂ in region 2. SO₂ is quenched least in region 3. In this region SO₂ absorbs a quantum of energy ($h\nu_1$) and forms an electronically excited molecule



The light intensity absorbed by SO₂, I_a , is a function of the incident light, I_o , the absorption coefficient, a , the path length, x , and the SO₂ concentration (SO_2) and described by beer's law:

$$I_a = I_o * \{1 - \exp[-a*x*(SO_2)]\} \quad (2)$$

The electronically excited SO₂ molecule can release the excess energy in three ways: fluorescence, quenching and dissociation. Fluorescence of SO₂ can be written as:



Here the quantum of energy released, $h\nu_2$, is at a lower frequency than the quantum of energy absorbed, $h\nu_1$. Reaction 3 proceeds with a rate constant k_f . Quenching of the excited SO_2 can be written as



Here M is a molecule of air that absorbs the excess energy. The rate constant for Reaction 4 is k_q . Dissociation of SO_2 can be written as:



Dissociation occurs with a rate constant of k_d . The fluorescent intensity measured by the detector, F , can be written as

$$F = [G \cdot k_f \cdot I_0 \cdot \{1 - \exp[-a \cdot x \cdot (\text{SO}_2)]\}] / (k_f + k_d + k_q \cdot [\text{M}]) \quad (6)$$

Here G accounts for the geometry of the fluorescent chamber design. Assuming the SO_2 concentration and path length are small, this equation reduces to:

$$F = [G \cdot k_f \cdot I_0 \cdot a \cdot x \cdot (\text{SO}_2)] / (k_f + k_d + k_q \cdot [\text{M}]) \quad (7)$$

The reaction rates (k_f , k_d and k_q) are relatively constant over a wide range of temperatures and pressures. The incident light I_0 can be engineered to remain constant, and G and x are also constants so the fluorescent intensity is directly proportional to the SO_2 concentration. This direct proportionality between fluorescent intensity and SO_2 concentration is the basis of the SO_2 instrument.

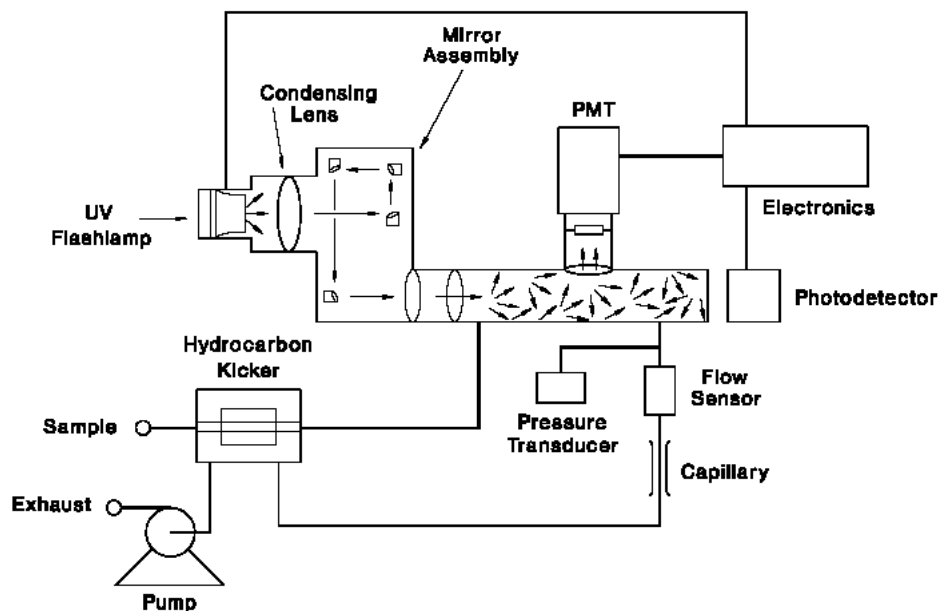


Figure 2. Schematic of flow diagram for SO₂ pulsed fluorescence monitor (Thermo Scientific, 2004a).

Figure 2 shows a schematic of gas flow through the SO₂ monitor. The monitor draws air in through a sample port at a rate of 0.5 L/min. Air then moves through a Nafion hydrocarbon kicker. The hydrocarbon kicker is used because there are significant interferences from polynuclear aromatic hydrocarbons (PAH); the most common of these being naphthalene. The hydrocarbon kicker is a semi permeable membrane, allowing only hydrocarbons through. A differential pressure is established by passing the sample air through a capillary tube. SO₂ enters a fluorescence chamber and is excited to a higher energy state. The excited SO₂ emits in 3 wavelength ranges with the 190-230 nm range being the most easily measured. The instrument runs on a switch able zero or measure mode. During the zero modes sampled air is run through a K₂CO₃ filter to remove SO₂. The zero modes are averaged and subtracted from the measure mode to decrease background noise (Thermo Scientific, 2004a).

In order to reduce the effects of non-methane hydrocarbons (NMHC) an extra PFA Teflon canister packed with activated charcoal was added to the kicker. The addition of the canister helps to reduce the partial pressure of the NMHCs in the sampling device and increases their diffusion out of the semi-permeable membrane (Luke, 1997). These modifications make interferences from most hydrocarbons negligible, though there are still interferences from NO_x that can only be removed through zeroing.

A UV lamp source is used to generate light in the 230-190 nm region. The light passes through a condensing lens (to focus the beam) and a series of reflective bandpass filters to stabilize and intensify the beam. The beam is passed through a relay lens and a circular baffle to remove stray light. The beam then enters the reaction volume, which contains the ambient air. The detector is perpendicular to the incident beam of light. Before the fluorescent light reaches the photo multiplier tube, the beam passes through a condensing lens and then a bandpass filter to ensure only light from SO_2 fluorescence enters the detector.

Luke (1997) approximated the detection limit to be around 0.3 ppb during the 1994 National Science Foundation-sponsored Gas-Phase Sulfur Intercomparison Experiment. I calculated the detection limit in 2005 for the SO_2 monitor used aboard the Maryland Research aircraft. I measured zero mode SO_2 1-minute averages for 30 minutes. I assume that the detection limit is two times the standard deviation of the zeros and this was 0.25 ppb. Luke (1997) approximated the uncertainty of the instrument to be 16% (at the 95% confidence level) when sampling mixing ratios were greater than 0.5 ppb.

2.4 CO

A modified (Dickerson and Delany, 1988) Thermo Scientific CO infrared filter correlation analyzer (43C, Franklin, MA) was used to measure CO. An IR source of 4.6 μm wavelength radiation is used because CO absorbs in this region.

Figure 3 shows the schematic of the instrument.

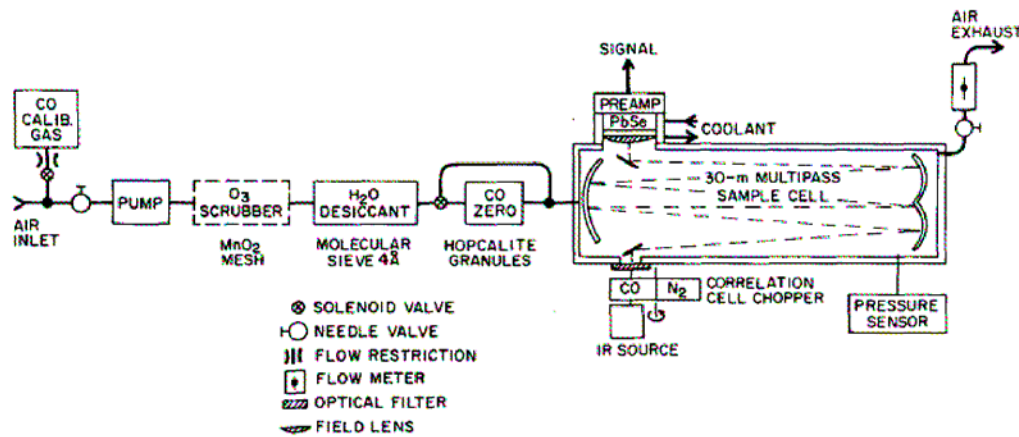


Figure 3. Flow schematic for the CO detector (Dickerson and Delany, 1988). Modifications include a collecting lens, cooling chamber, dessicant, chemical zero, and operation at positive pressure.

The air sample is drawn into the instrument and enters the sample chamber. The source is chopped and then travels through a gas filter wheel. Half of the filter wheel contains high concentrations of CO and the other half contains N₂. N₂ does not absorb in this IR region and so light that passes through this half of the wheel becomes the measure beam. The high concentration of CO in the other half of the wheel absorbs all the IR radiation and this produces a reference beam. Both beams pass through the sample cell, with a 30 m effective path length. The CO concentration being measured is derived from the relative intensity of the measure

and reference beam (Thermo Scientific, 2004b). The instrument is capable of a 2-5% precision determined from a 1-min mean of 10 s data.

2.5 O₃

Ozone is measured with a Thermo Scientific UV photometric analyzer (49, Franklin, MA). This analyzer operates on the Beer-Lambert law by measuring the attenuation of light due to O₃ absorption at 254 nm. The source is a low pressure mercury vapor lamp, which has 95% output at 254 nm. The detector is a solar blind vacuum photodiode sensitive to UV light only. Figure 4 gives a schematic of the instrument. The sample enters the instrument and is split into two gas streams. One of the streams is scrubbed of O₃, which allows it to be the reference beam, I_0 . The reference beam then passes onto the sample solenoid valve. The other gas stream flows directly to the sample solenoid and is the measure beam, I . The solenoid switches the instrument between zero and measure modes (sampling from the I and I_0 beam). The ratio of I/I_0 is directly proportional to the concentration of O₃.

$$I/I_0 = \exp^{-KlC} \quad (8)$$

Where $K = 308 \text{ cm}^{-1} \text{ atm}^{-1}$ at 0°C and 1 atm, l is the length of the cell (38 cm), and C is the O₃ partial pressure in atm. In order to register a change of 1ppb concentration, the instrument must be able to detect a change in I/I_0 of 2 parts in 10^5 . It takes about 10 seconds to measure I and I_0 , and the source must be stable to 2 parts in 10^5 .

Because this stability is difficult to reach, a second detector is used to monitor and correct the changes in light intensity. The instrument employs 2 photometers with a single light source and two absorption cells and detector systems. These photometers operate synchronously but out of phase so that when one is in measure mode, the

other is in zero mode. A flush time of about 7 seconds is used to remove the ambient air from the sample cell, and then the measurement is made during the next 3 seconds. By taking the average of the 2 photometer readings, the fluctuations of the lamp intensity are cancelled out. The instrument is capable of 1 ppb precision for 10 s data.

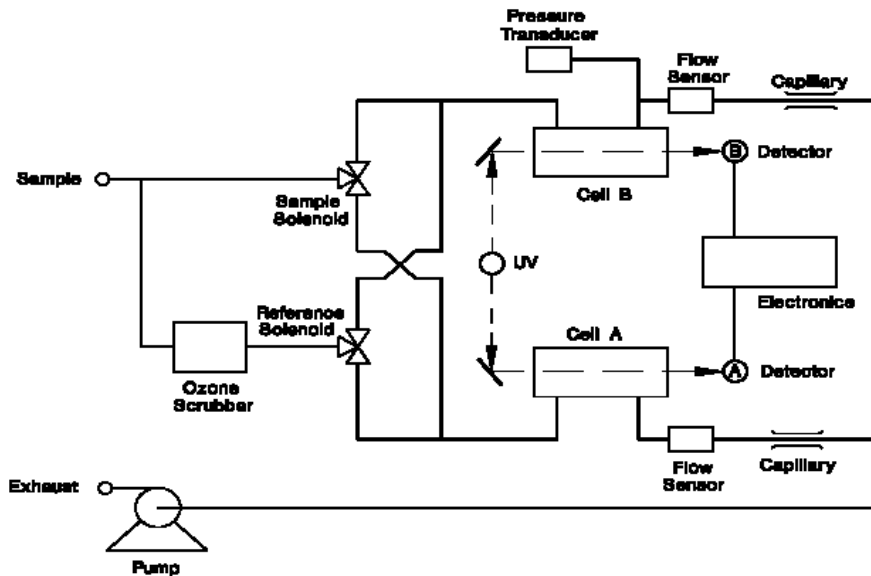


Figure 4. Flow schematic for U.V. photometric O₃ analyzer (Thermo Scientific, 2004c).

2.6 Aerosol Absorption

A Particle Soot Absorption Photometer (PSAP; Radiance Research, Seattle, WA) was used to measure near real-time aerosol absorption on a filter. An LED light source shines 567 nm light through an opal glass and onto a Pallafax filter. The PSAP measures the absorption coefficient, σ_{ap} ($Mm^{-1} = 10^6 m^{-1}$), with an integrating technique. The absorption coefficient is determined from the volume of air sampled during an averaging time using Beers law:

$$\sigma_{ap} = A/V * \ln (I_o/I) \quad (9)$$

Where A is the area of the filter exposed to the light beam, V is the average volume of air sampled by the instrument, I_o is the average filter transmittance for averaging time j and I is the average filter transmittance for averaging time $j + 1$. The σ_{ap} is then corrected for filter nonlinearities including filter loading and filter characteristics.

This correction can be written as:

$$\sigma_{ap} = \sigma_{ap} f(Tr) \quad (10)$$

Where $f(Tr)$ is a transfer function based on filter loading (or transmittance, which is recorded by the instrument), for Pallafex filters. Figure 5 shows a diagram of the air flow. Ambient air flows through the first filter (measurement filter), where all particles are removed. The particle-free air then flows through the reference filter. The transmission of light through the filter is measured with a photodiode. A second filter, adjacent to the first is used to ensure that changes in the change in intensity results from buildup of particles on the filter and not fluctuations in the LED source.

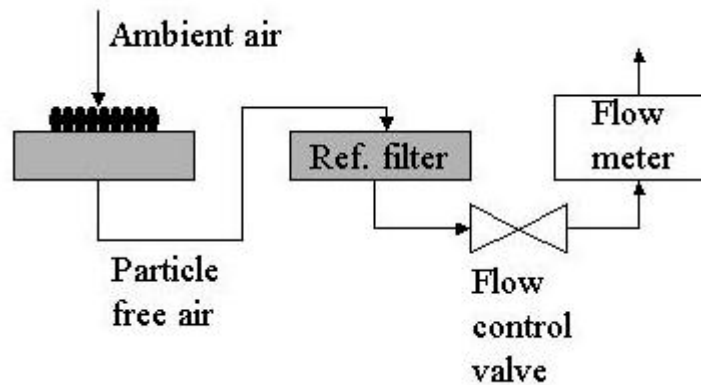


Figure 5. Flow diagram for PSAP
 (http://www.cmdl.noaa.gov/aero/instrumentation/psap_desc.html).

The detection limit is $0.9 \times 10^{-6} \text{ m}^{-1}$ (95% confidence level) when 1-min measurement averages are used (Bond et al., 1999). Bond et al. (1999) has recommended corrections for differences in flow rates, spot size, and exaggerations of absorption due to scattering, and these have been applied to PSAP measurements.

2.7 Scattering

The TSI integrating nephelometer (Model 3563, TSI, St. Paul, MN) was used to measure light scattering of atmospheric particles at 450, 550, and 700 nm. Figure 6 show a diagram of the instrument.

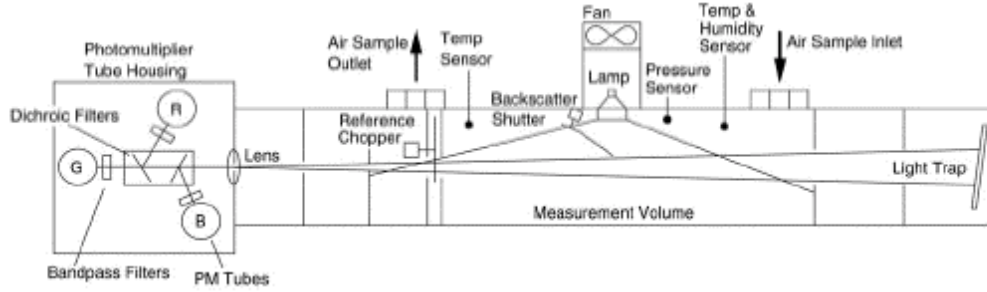


Figure 6. Flow schematic for the integrating nephelometer.

The light source travels through a diffuser plate, ensuring a lambertian source. A photomultiplier tube detector is positioned parallel to the incoming light and measures scattering over 7° to 170° . The light source flux that reaches the detector is defined by the following:

$$B = I_o / y \int_{\phi_1}^{\phi_2} \beta(\phi) \sin(\phi) d\phi \quad 11$$

where I_o is the intensity of the incident light, y is the distance between the source and the detector, ϕ is angle between the light reaching the source and the incident light, and $\beta(\phi)$ is the angular scattering function (TSI, 1997). Integrating the scattering function from $\phi_1=0$ to $\phi_2 = \pi$ gives:

$$B = (I_o / y) * (\sigma_{scat} / 2\pi) \quad (12)$$

Where σ_{scat} is the scattering coefficient (TSI, 1997).

A chopper is used to generate an AC signal. The light passes through three different filters to correct for interferences. The first filter lets through all light for the full signal measurement. The second filter is used to remove the dark signal from the photomultiplier. The third filter measures the light source to monitor the lamp stability (TSI, 1997). Corrections were made for truncation errors (where forward

scattered light at angles less than 7° is blocked) and nonlambertian errors as suggested by Anderson and Ogren (1998).

The inlet airstream was dried to an RH $< 20\%$. To account for hygroscopic particle growth an estimated growth factor, F(RH), was calculated. F(RH) is the ratio of scattering from ambient particles to scattering from dried particles

$$F(\text{RH}) = \sigma_{\text{sp}}(\lambda, \text{RH}) / \sigma_{\text{sp}}(\text{ref}) = \{(1-\text{RH}_{\text{amb}})/(1-\text{RH}_{\text{ref}})\}^{-\gamma} \quad (13)$$

Here $\sigma_{\text{sp}}(\lambda, \text{RH})$ represents light scattering from the ambient particles, $\sigma_{\text{sp}}(\text{ref})$ represents light scattering from the dried particles, RH_{amb} is the ambient RH, RH_{ref} is the RH inside the nephelometer, and γ is derived from parallel nephelometers. A γ value of 0.35 was used, similar to that in Remer et al. (1997), because the region of their study is similar to those presented here. The detection limits for scattering are 0.44×10^{-6} , 0.17×10^{-6} and 0.26×10^{-6} m for scattering at 450, 550, and 700 nm. The instrument is calibrated with CO_2 for Raleigh scattering

Chapter 3: Determination of Meteorological Influences on Pollution Episodes: Clustering Back Trajectories.

3.1 Introduction.

This chapter will address the two questions: 1) Is there a statistical link between characteristic regional transport patterns in the Mid-Atlantic US during summertime haze and O₃ episodes and specific pollution loadings? 2) Can the local O₃ contributions be differentiated from regionally imported O₃; if so, are the regional contributions quantifiable? Much of the work in this chapter was published in Taubman et al. (2006). In this chapter I will present statistics of trace gasses and aerosols from all flights made in June-August for 1995-2005. I collected measurements aboard the aircraft for 12 of the flights (36 profiles) in 2005. I calculated statistics for morning (before 12 noon EST) and afternoon (after 12 noon EST) profiles. Most morning flights were made upwind of pollution centers and most afternoon flights were made downwind of pollution centers. I clustered back trajectories for flights from 1997-2003 to determine meteorological regimes associated with the flights. The method for clustering back trajectories will be described and the resulting meteorological regimes determined by the clusters will be analyzed. I calculated statistics for profiles of trace gases and aerosols associated with the meteorological regimes and will discuss the results. I also calculated transported O₃ using *in-situ* measurements. The method and the amount of transport associated with each of the meteorological regimes will be discussed.

3.2. Observations

3.2.1 Measurements

All flights analyzed for this study were conducted in the summertime (June, July, and August) and were specifically designed to characterize episodic pollution events. The observations reported herein represent polluted periods, not background values. Statistics for all flights made between 1995 and 2005 are presented first. The flight locations for statistics of all flights are presented in Figure 1 in Chapter 2.

From 1995 through 2005, there were 658 summertime flights, which included 305 morning spirals (before noon EST, average time 09:30 EST) and 353 afternoon spirals (after noon EST, average time 13:30 EST). The median profiles for the morning and afternoon O₃, CO, SO₂, scattering at 550 nm and absorption at 550 nm are shown in Figure 1. The single scattering albedo represents the relative contribution of scattering from particles and was calculated using:

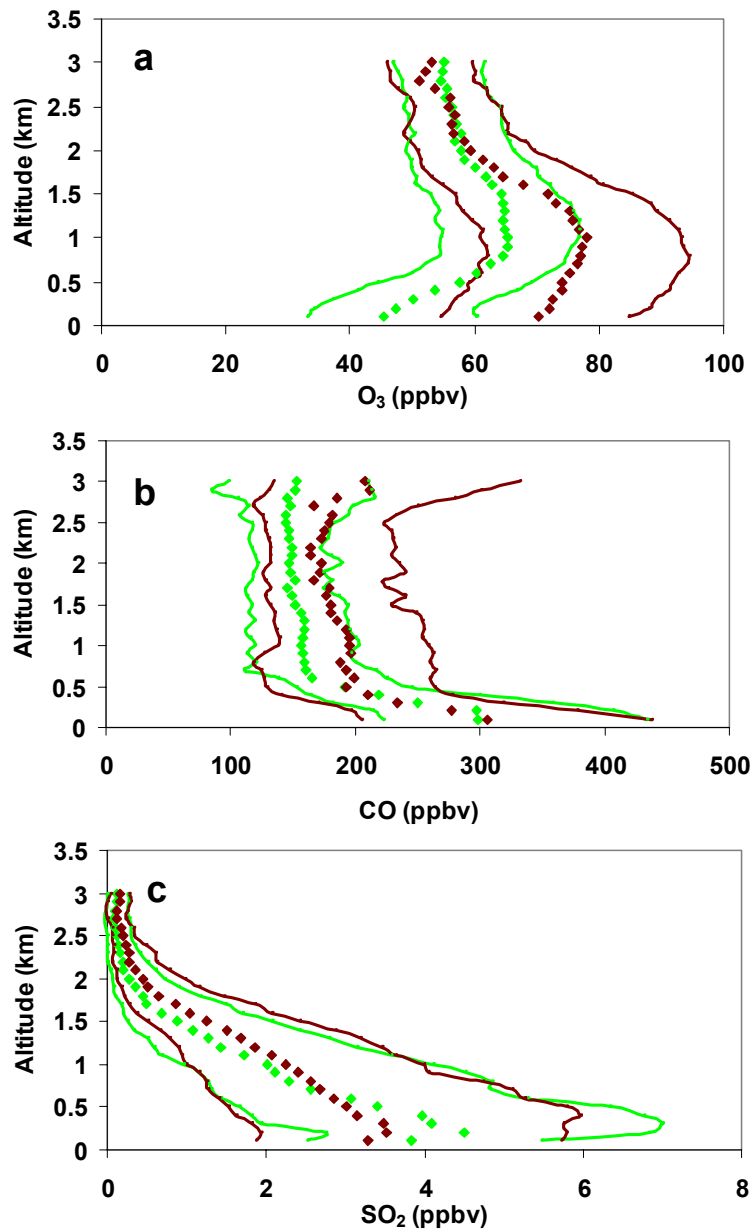
$$\text{single scattering albedo} = \sigma_{550} / (\sigma_{550} + \text{abs}_{550}) \quad (1)$$

Where σ_{550} is the scattering coefficient at 550 nm and abs_{550} is absorption coefficient at 550 nm. The Ångström exponent (α) represents the relative size of particles and was calculated using:

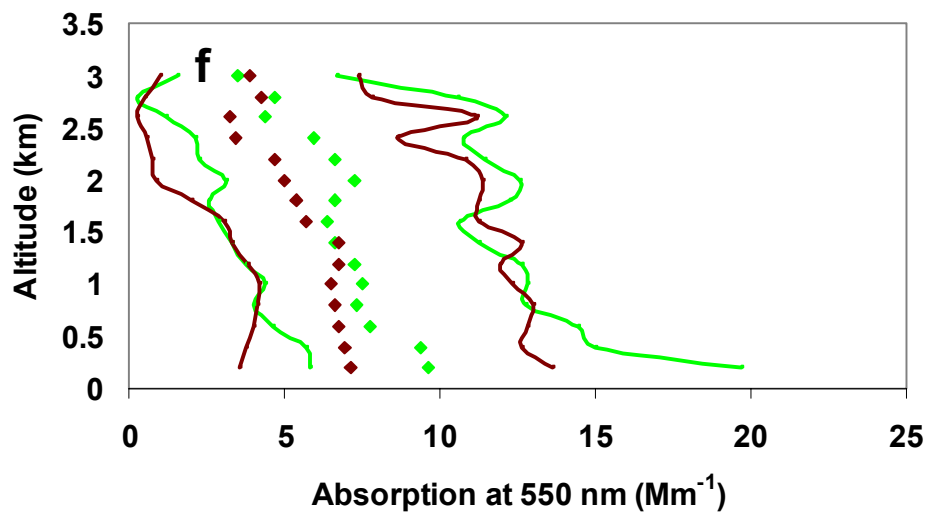
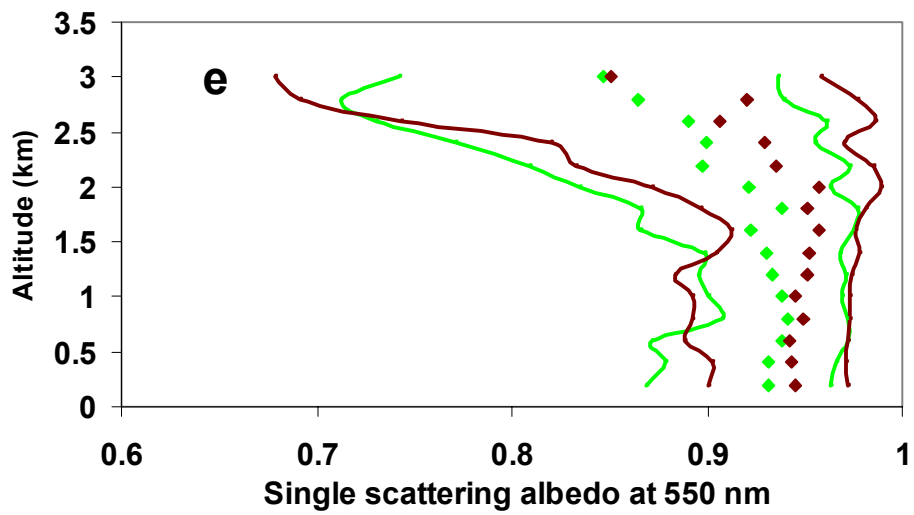
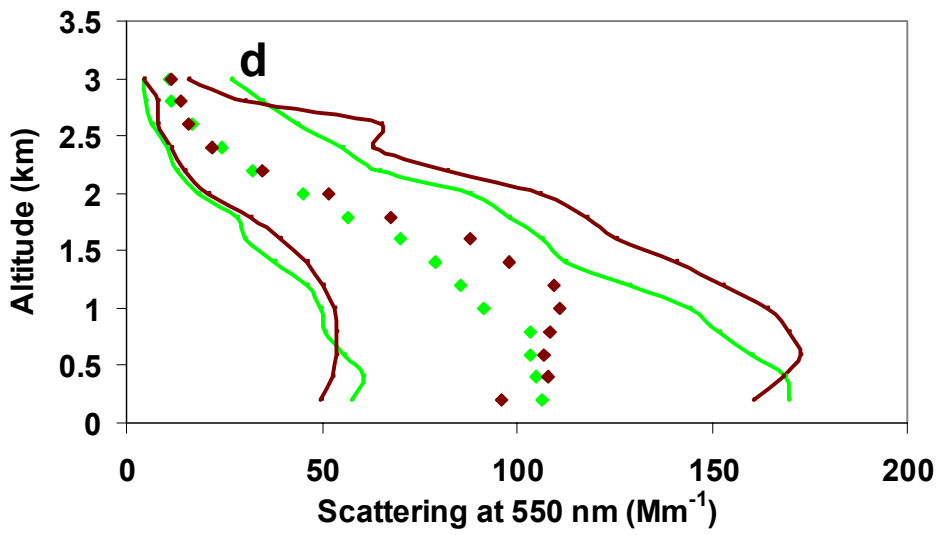
$$A = [\log(\sigma_{450}) - \log(\sigma_{700})] / [\log(450) - \log(700)] \quad (2)$$

Here σ_{450} and σ_{700} are the scattering coefficients at 450 and 700 nm respectively.

Statistics for the single scattering albedo and α are also presented in Figure 1. The profiles shown were generated by calculating the median value at each altitude layer from all of the measured profiles.



Figures 1a-c. Median values calculated every 100 m from all morning (green diamonds, before 12:00 EST) and afternoon (red diamonds, after 12:00 EST) profiles for a) O₃ (305 morning profiles, 353 afternoon profiles), b) CO (134 morning profiles, 178 afternoon profiles), and c) SO₂ (234 morning profiles, 254 afternoon profiles). The solid lines represent the 25th and 75th percentiles.



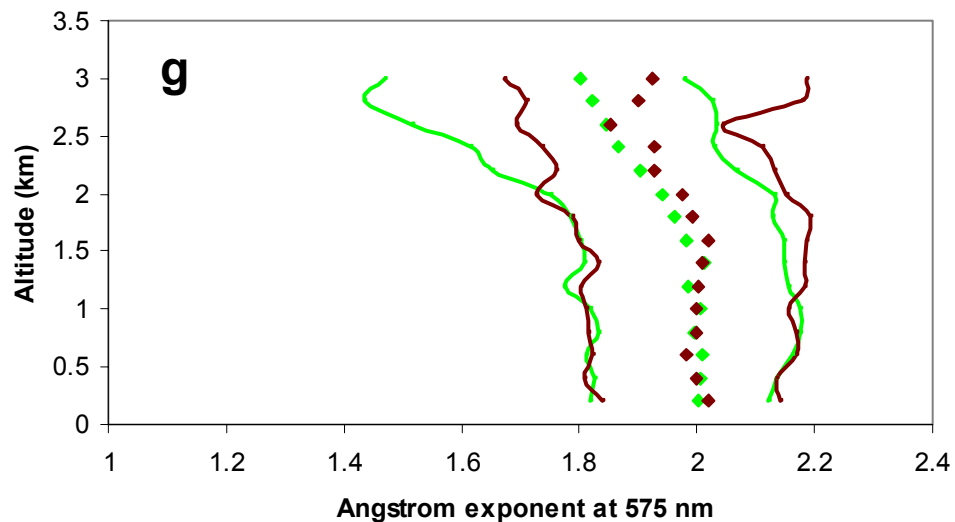


Figure 1d-g. Median values calculated every 100 m from all morning (green, before 12:00 EST) and afternoon (red, after 12:00 EST) profiles for d) scattering at 550 nm (189 morning profiles, 185 afternoon profiles), e) single scattering albedo at 550 nm (132 morning profiles, 153 afternoon profiles), f) absorption at 550 nm (175 morning profiles, 214 afternoon profiles), and g) Ångström exponent (189 morning profiles, 185 afternoon profiles). The solid lines indicate the 25th and 75th percentiles.

The morning O₃ profile (Figure 1a) shows relatively small values (~45-55 ppbv) within the nocturnal boundary layer (roughly the lowest 500 m), with considerably more O₃ in the residual layer above. This results from surface deposition and titration with freshly emitted NO within the nocturnal boundary layer combined with night-time regional transport from upwind sources within the residual layer. Solar heating induces a more thoroughly mixed afternoon O₃ profile with photochemical production adding to that which was transported overnight. Above approximately 2 km, the morning and afternoon values are nearly identical (~55 ppbv), indicating a summertime continental background value.

The morning and afternoon CO profiles (Figure 1b) are nearly identical below ~1 km, with large values near the surface that fall off with altitude. The shape of the

vertical profiles is similar to those presented by Dickerson *et al.* (1995) for spring, although the absolute values presented herein are slightly greater than in the previous study. Above 1 km, the afternoon values are slightly larger than the morning, indicating convective outflow from the boundary layer, the preamble to long range transport.

The SO₂ profiles (Figure 1c) show little difference between the morning and afternoon. The afternoon profile shows somewhat smaller values near the surface, likely the result of oxidation to sulfate. There is also evidence of vertical mixing in the afternoon; however, both profiles show greater values near the surface that decrease sharply with altitude. Sulfur dioxide is a fairly short-lived species, typically less than a day in summertime (Seinfeld and Pandis, 1998), with sources generally elevated slightly above the surface.

The afternoon scattering profiles (Figure 1d) are somewhat larger than the morning profiles between 200 and 2000 m and this may be explained by SO₂ oxidation to sulfate, the primary scattering component in fine particles over the eastern U.S. There is a maximum in the afternoon single scattering albedo near the top of the boundary layer where RH is also at a maximum. Both profiles decrease considerably above 2 km. The single scattering albedo profiles are similar to the scattering profiles and the single scattering albedo in the afternoon boundary layer average is greater than that in the morning profile (0.94 ± 0.01 vs. 0.93 ± 0.01) (Figure 1e). This increase of single scattering albedo in the afternoon is presumably the result of SO₂ oxidation and RH changes due to the planetary boundary layer growth. The absorption was relatively invariant with altitude (Figure 1f), so the

decline in single scattering albedo with altitude is driven by a decrease in scattering values. These observations are consistent with those of Novakov *et al.* (1997), who reported an increase in the relative amounts of carbonaceous to sulfate species with altitude over the Eastern U.S. coastline. No diurnal pattern in Ångström exponent was observed (Figure 1g); however a slight decrease with altitude is apparent in both the morning and afternoon profiles. The presence of larger particles aloft may be due to particle growth through preferential aging in the lower free troposphere as articulated in Taubman *et al.* (2004a).

3.2.2 Trajectory Calculations

Back trajectories are a standard tool for determining the source regions and transport patterns of air parcels observed at receptor sites. While they may not represent the exact transport path of an air parcel, back trajectories are good representations of the general 3-dimensional wind flow and are useful in identifying particular synoptic situations. The accuracy and errors associated with the different estimations of air parcel trajectories have been quantified (Stohl *et al.*, 1995; Stunder, 1996; Stohl, 1998). Individual trajectories may be subject to errors; however, clustering multiple trajectories together minimizes errors and uncertainties.

I calculated 48 hour, 3-dimensional kinematic back-trajectories ending at the time and location of each aircraft spiral (made from 1997 – 2003 with the UMD research aircraft) using the NOAA Air Resources Laboratory (ARL) HYbrid Single-Particle Lagrangian Integrated Trajectory (HY-SPLIT) model (Version 4) (R. R. Draxler and G. D. Rolph, 2003, <http://www.arl.noaa.gov/ready/hysplit4.html>) and 80 km Eta Data Assimilation System (EDAS) 3-hourly archive data. Kinematic back

trajectories were used because, due to improvements to the accuracy of the vertical wind component, they have been shown to be more accurate than other methods (e.g., isentropic and isobaric) (Stohl *et al.*, 1995; Stohl, 1998; Jorba *et al.*, 2004). Two-day back trajectories were long enough to capture regional transport patterns and short enough to keep trajectory errors, which accumulate with simulation time, to acceptable levels. The air parcel latitudes, longitudes, and pressures were recorded at 1 h intervals. Trajectories were calculated ending at 1, 2, and 3 km (above ground level). Back trajectories associated with 550 flights made from 1997-2003 were used in the clustering analysis.

3.2.3. Cluster Analysis

I performed a separate cluster analysis for back trajectories ending at 1, 2, and 3 km. These ending altitudes describe the vertical range over which the aircraft vertical survey spirals were performed. By clustering the trajectories at each of the three altitudes, any variations in the atmospheric circulation patterns in the lower atmosphere and the impacts on regional transport could be identified. The results of the cluster analysis for the three altitudes were similar. The 2 km trajectory cluster results were used for the remainder of the analysis because this altitude is near the middle of the aircraft spirals and most representative of the entire spiral.

The trajectories trace a 3-dimensional path through time to the receptor site. To determine the similarity among individual trajectories, the total variability between each trajectory pair must be quantified. The variability may be calculated as a scalar distance between trajectories. At each time step, the position of the air parcel is defined by its latitude, longitude, and pressure. These data were converted to

Cartesian coordinates by treating the Earth as a sphere and calculating their position in 3-dimensional space. The x, y and z distances in km are given as:

$$x = (r_e + alt_i) * \cos(\pi/180 * lon_i) * \sin(\pi/2 - \pi/180 * lat_i) \quad (3)$$

$$y = (r_e + alt_i) * \sin(\pi/180 * lon_i) * \sin(\pi/2 - \pi/180 * lat_i) \quad (4)$$

$$z = (r_e + alt_i) * \cos(\pi/2 - \pi/180 * lat_i) \quad (5)$$

Where r_e is the radius of the earth (approximated at 6378 km), alt_i , lat_i , and lon_i are the altitude, latitude and longitude at a specific hour i , in the back trajectory.

Vertical variability along the trajectory paths may have a large impact on transport and hence, pollution levels, but the spatial distances described by the variability in the vertical wind component are typically less than the horizontal spatial distances covered by the air parcels. Thus, without normalizing the data, the vertical variability may not have an equal impact on the cluster analysis when examining the similarity among trajectories. To account for this inconsistency I calculated the mean value and standard deviation for each coordinate at every time step (x_{avg} , y_{avg} , z_{avg} and x_{stdev} , y_{stdev} , z_{stdev}). I then subtracted the mean value from the individual coordinates and normalized them with the standard deviation.

$$x^* = (x - x_{avg}) / x_{stdev} \quad (6)$$

Normalized differences (like x^*) were also calculated for y and z. In this way, the coordinates were all converted to a standardized distance from the mean value of that particular coordinate and equal weighting was given to all three coordinates in the cluster analysis.

The Euclidean distance, D , between each trajectory pair was calculated according to the equation:

$$D_{ij} = \sqrt{\sum_{k=1}^n (x^*_{ik} - x^*_{jk})^2 + (y^*_{ik} - y^*_{jk})^2 + (z^*_{ik} - z^*_{jk})^2} \quad (7)$$

In the above equation, D is the 3-dimensional distance between the two trajectories under comparison, represented here by the subscripts i and j . The variables x^* , y^* , and z^* represent the normalized distances from the means of the Cartesian coordinates. The number of time steps used in the analysis is given by k (48 for hourly time steps over 2 days). However, the first six time steps back from the receptor site were given zero weighting to account for the spatial heterogeneity of the aircraft spiral locations. To further discount the spatial variability of the receptor locations and place the emphasis on the source regions, the trajectory time steps were weighted linearly back in time, increasing the weighting for each hour after the initial six zero-weighted time steps.

After the distances between individual trajectories were calculated I clustered the trajectories using an agglomerative, hierarchical clustering algorithm in Matlab. The algorithm used an average linkage function, where the average distances between all pairs of objects in clusters i and j are calculated, to determine the distances between the trajectories making up the clusters. Average linkage minimizes the within-cluster variance while maximizing between-cluster variance and has been identified as an effective method for categorizing different synoptic situations (Kalkstein *et al.*, 1987). Newly formed clusters were linked to other trajectories to create successively larger clusters until all of the trajectories were connected by a hierarchical dendrogram. The algorithm has no inherent mechanism for identifying an appropriate terminus for this iterative process. Barring manual intervention, all

objects are eventually grouped into one cluster. So, the final number of clusters was specified arbitrarily from 1 to 15 clusters.

To determine the appropriate number of clusters I first calculated an “average” trajectory, or trajectory center, for each cluster. The root mean square deviation (RMSD) of each trajectory within a cluster from the cluster center was quantified. The RMSDs were then summed to give the total root mean square deviation (TRMSD). The percent change in the TRMSD was plotted against the total number of clusters (e.g., Cape *et al.*, 2000; Brankov *et al.*, 1998) (Figure 2). Large changes were interpreted as the merging of significantly different trajectories into the same cluster. Accordingly, the appropriate number of clusters would be found just prior to the large percent change in TRMSD. While this technique lends objectivity to the analysis, a subjective interpretation of the optimal number of clusters based on the meteorology and pollutant profiles as well as what value constitutes a large enough percent change in TRMSD is still required. When eight clusters were merged into fewer clusters the change in TRMSD remained consistently high (~10%) and grew larger upon further agglomeration. After reviewing the meteorology and pollutant profiles associated with each cluster, eight was determined to be the appropriate number of clusters

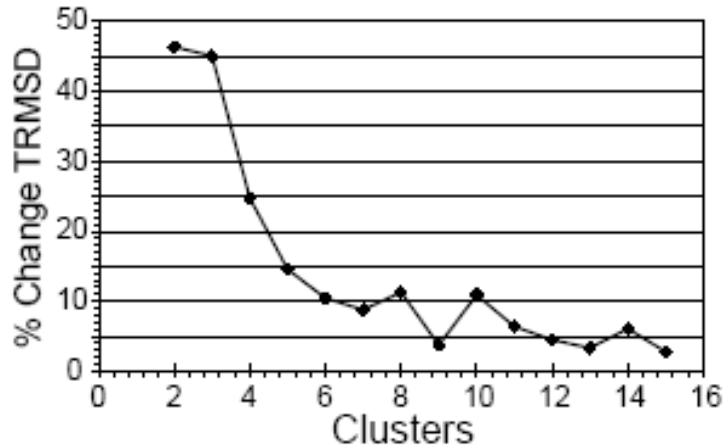


Figure 2. Percent change in the total root mean square deviation (TRMSD) calculated by summing the root mean square deviation of each cluster versus the number of total clusters.

3.3. Results and Discussion

3.3.1 Cluster Solution

The eight cluster solution is shown in Figure 3 with trajectory “spaghetti” plots of each cluster. The relative density of air parcel locations in each cluster, however, is better described by trajectory density plots, given in Figure 4. A linear interpolation method was used to generate values between the original trajectory latitude and longitude points and smooth the density plots. The locations of the largest (top 0.3%) annual NO_x and SO₂ emitters in the eastern U.S. (EPA AirData Facility Emissions Report – Criteria Air Pollutants 1999, <http://www.epa.gov/air/data/>) are overlaid on the trajectory density maps. The trajectory densities represent the relative amount of time the air parcels from every trajectory in a cluster spent over the areas defined by the spaghetti plots before reaching the receptor location. This is a technique based on the “residence time

analysis” (Ashbaugh, 1983) and it will be shown below that it is an effective means of determining downwind pollutant loadings.

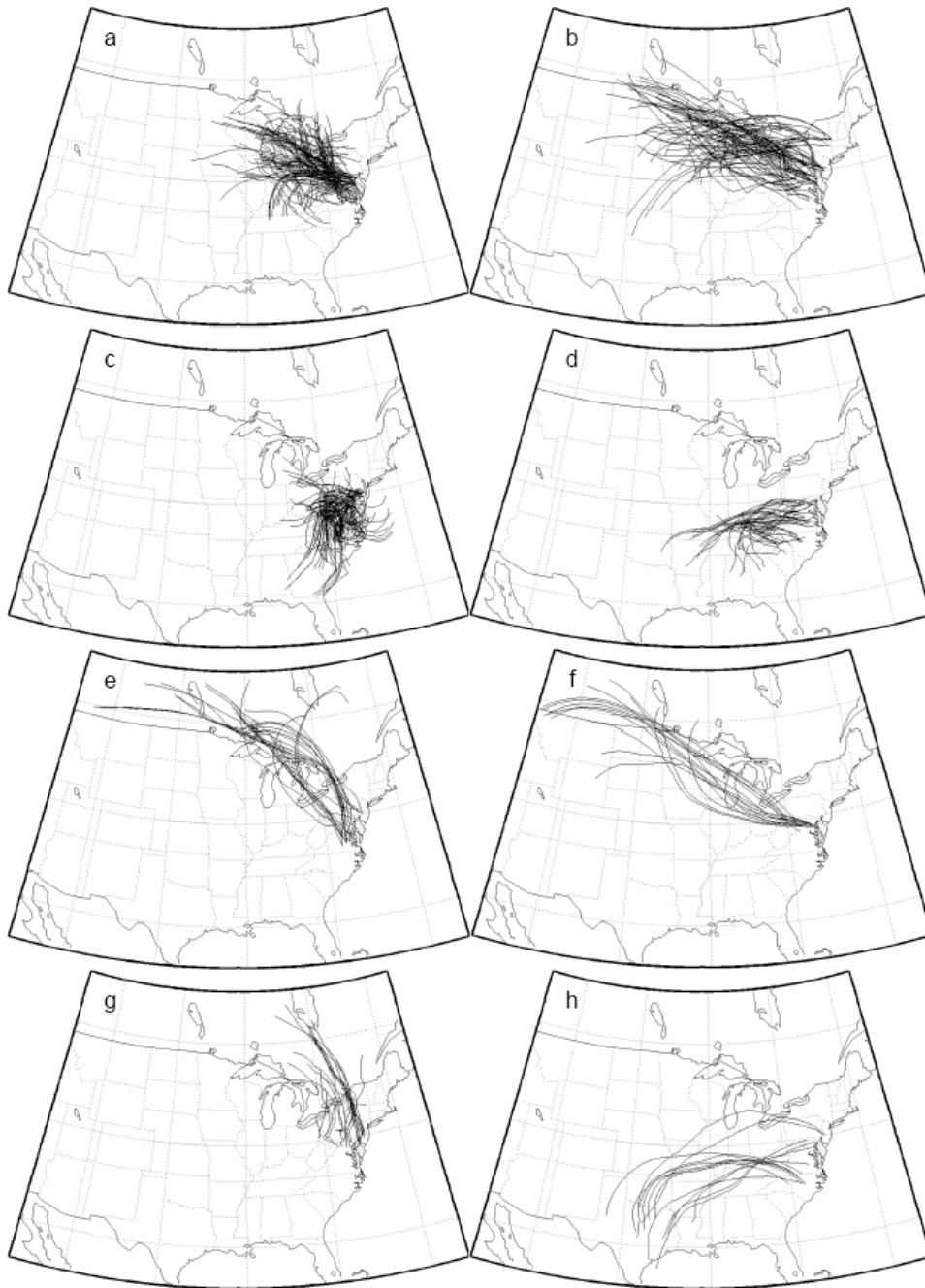


Figure 3. Spaghetti plots of the 48 hr HY-SPLIT back trajectories ending at 2km altitude that make up a) Cluster 1, b) Cluster 2, c) Cluster 3, d) Cluster 4, e) Cluster 5, f) Cluster 6, g) Cluster 7, and h) Cluster 8.

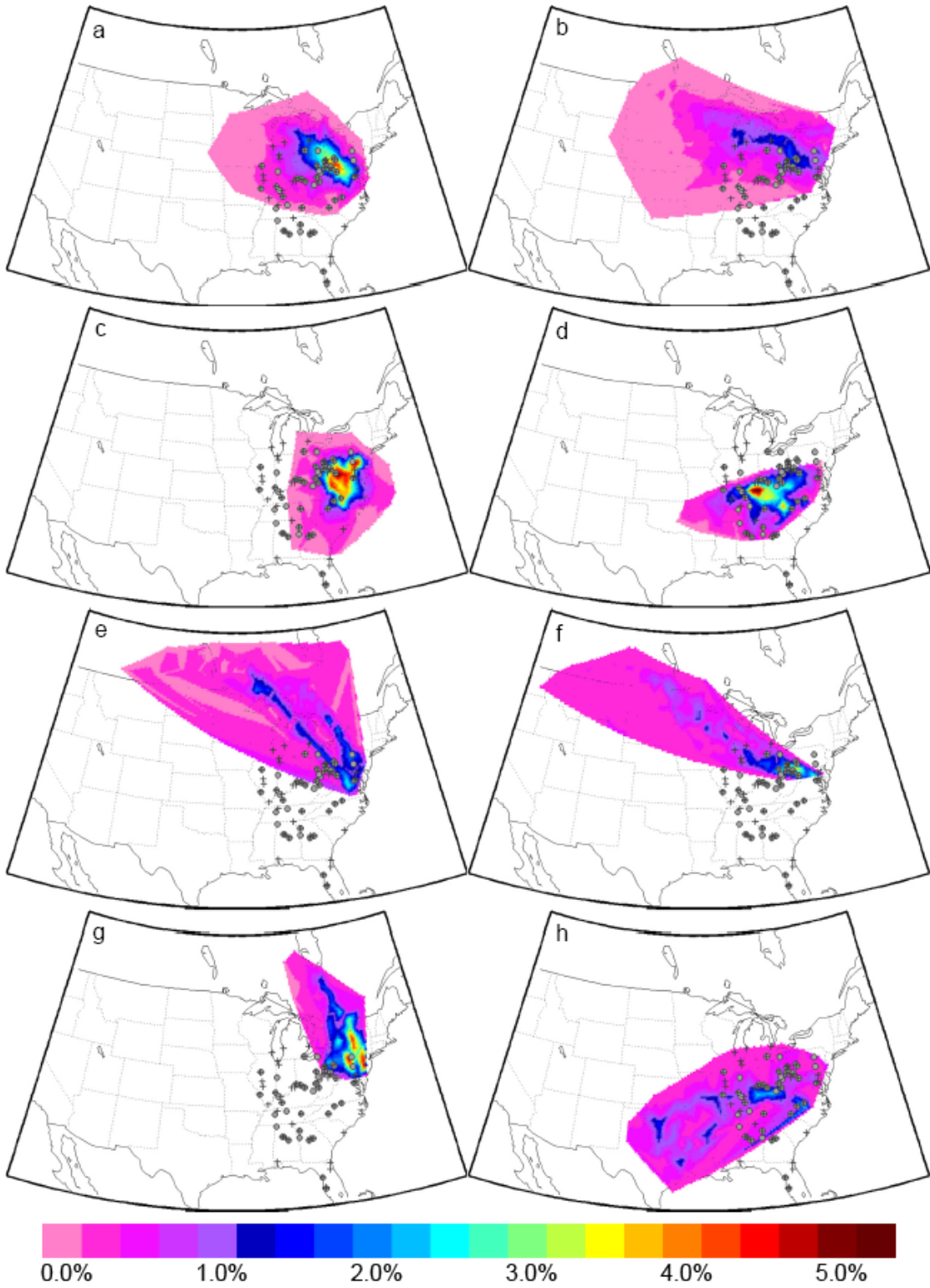


Figure 4. Trajectory density maps for a) Cluster 1, b) Cluster 2, c) Cluster 3, d) Cluster 4, e) Cluster 5, f) Cluster 6, g) Cluster 7, and h) Cluster 8. The plots were generated using a linear interpolation method between the trajectory end points. They indicate the relative density (%) of air parcels over the total area described by the spaghetti plots. Also pictured are the locations of the top 0.3% emitters annually of NO_x (diamonds) and SO₂ (crosses) in the eastern U.S.

To determine the statistical difference between the constituents associated with each cluster I first subdivided the clusters into morning and afternoon profiles according to the aforementioned criteria. For all trace gas profiles but morning O₃, I calculated the boundary layer (defined here as the layer between 100 m and 2000 m) column content (in matm-cm). For morning O₃, the residual layer (defined here as the layer between 500 m and 2000 m) column content (also in matm-cm) was quantified to capture the impacts of regionally transported pollution on the receptor locations. For the aerosol profiles I calculated the extinction weighted single scattering albedo column average, aerosol optical depth at 550 nm between the surface and 3 km (AOD), and scattering weighted α . The cluster median values were then determined. The cluster median ranks are given in Table 1 and the cluster median values for the extinction weighted single scattering albedo and AOD are given in Table 2.

Table 1. Cluster median profile ranks, % O₃ transported, and cluster median column content SO₂/CO ratios for the morning (upper number) and afternoon (lower number). Values in parentheses under the cluster number are the total profiles that went into that cluster (left) and the percent of the total profiles (right). The grey area indicates insufficient data to calculate statistical values for Cluster 8.

clusters	Median O ₃ rank	% O ₃ transported	Median CO rank	Median SO ₂ rank	SO ₂ /CO	Median $\omega_{0.550}$ rank	Median AOD rank	Median α rank
1 (107,26.3)	1 2	67 ± 4 ^a	4 7	4 2	0.014 0.017	2 1	1 1	6 7
2 (77,19.0)	4 5	67 ± 6	8 8	5 4	0.015 0.016	1 2	2 2	7 6
3 (108,26.6)	3 1	54 ± 8	3 3	7 3	0.009 0.011	3 4	3 4	4 4
4 (39,9.6)	6 8	82 ± 8	7 2	8 6	0.010 0.006	4 3	5 3	2 5
5 (24,5.9)	5 3	62 ± 16	5 6	3 7	0.015 0.008	5 5	6 7	1 1
6 (15,3.7)	2 4	73 ± 17	2 4	1 1	0.026 0.016	6 7	4 5	3 3
7 (23,5.7)	8 7	56 ± 16	6 5	6 8	0.013 0.008	7 6	7 6	5 2
8 (13,3.2)	7 6	55 ± 11	1 1	2 5	0.008 0.006			

^a error estimated by adding in quadrature $1\sigma/\sqrt{n}$ from the residual layer and afternoon boundary layer mean values.

Table 2. Cluster median profile values for the morning and afternoon aerosol extinction weighted $\omega_{0.550}$ and AOD.

clusters ^a	am $\omega_{0.550}$	pm $\omega_{0.550}$	am AOD	pm AOD
1	0.91 ± 0.05^b	0.95 ± 0.04	0.37 ± 0.19	0.35 ± 0.30
2	0.91 ± 0.06	0.94 ± 0.05	0.31 ± 0.23	0.31 ± 0.25
3	0.90 ± 0.06	0.93 ± 0.04	0.30 ± 0.28	0.26 ± 0.12
4	0.88 ± 0.06	0.94 ± 0.03	0.22 ± 0.06	0.29 ± 0.07
5	0.87 ± 0.08	0.91 ± 0.05	0.17 ± 0.10	0.15 ± 0.10
6	0.82 ± 0.09	0.85^c	0.25 ± 0.08	0.25^c
7	0.81 ± 0.17	0.85 ± 0.12	0.15 ± 0.12	0.20 ± 0.12

^a there were not enough data to calculate statistical values for Cluster 8

^b the error represents 1σ of the cluster mean value

^c no error is given because there was only one profile that went into the Cluster 6 pm $\omega_{0.550}$ and AOD values

Using the individual profile values, I calculated the statistical difference between the cluster medians using a multiple comparison procedure with statistical values generated from the Kruskal-Wallis test. This test is similar to the standard one-way analysis of variance, but is a non-parametric version. The one-way analysis of variance requires data to be normally distributed whereas in the Kruskal-Wallis test the data must only be continuously distributed. The test ranks the values and performs an analysis of variance on the ranks rather than the values themselves. For this study, the cutoff for the probability value (p-value) was set to 0.05. When the p-value was less than this limit, the null hypothesis was rejected and the cluster medians were declared statistically different with greater than 95% confidence. The results are summarized in Table 3.

Table 3. Statistical difference among cluster morning and afternoon profile median values. The > (<) signifies that the median value for the cluster is statistically greater (less) than, with 95% confidence, the median values of the cluster numbers listed after the symbol. Grey areas indicate no statistical difference.

Clusters								
	1	2	3	4	5	6	7	8
am O₃	>7,8		>8			>8	<1	<1,3,6
pm O₃	>4	<3	>2,4,7	<1,3			<3	
am CO		<8		<8				>2,4
pm CO								
am SO₂			<6	<6		>3,4		
pm SO₂								
am $\omega_{0.550}$								
pm $\omega_{0.550}$								
am AOD	>4,5			<1	<1			
pm AOD	>5	>5			<1,2			
am α	<5	<5			>1,2,7		<5	
pm α	<5,7				>1		>1	

3.3.2 Pollution Profiles

Figures 5 and 6 show the morning and afternoon median vertical profiles, respectively, for each constituent. Cluster 1, associated with large amounts of O₃, a

large SO_2/CO ratio, large, highly scattering particles, and a large AOD (see Figures 5, 6, and Tables 1, 2), shows moderate northwesterly flow. These values are indicative of aged point source pollution. The greatest trajectory density lies over the northern Ohio River Valley where there are several large NO_x and SO_2 sources (see Figure 4). Fresh NO_x and SO_2 emissions from these sources have had ample opportunity under a moderate flow regime to produce O_3 and secondary aerosols en route to the Mid-Atlantic.

Cluster 2 shows similar wind direction to Cluster 1, but with higher wind speeds (see Figure 3). The greatest trajectory density also lies mainly over the northern Ohio River Valley and extends into the Great Lakes region. The particles are also large and highly scattering, but the AOD is lower. The CO is even less than in Cluster 1, the SO_2/CO ratio is large, and the O_3 values, particularly in the afternoon, are small (see Figures 5, 6, and Tables 1, 2). These values are all consistent with northwesterly flow similar to Cluster 1 that brings northern Ohio River Valley point source pollution, but with higher wind speeds, so that there is less time for local, photochemical O_3 production or mixing with urban, mobile source pollution. Figure 4 shows that, in fact, the greatest trajectory density intersects many large NO_x and SO_2 sources.

Cluster 3 is typified by stagnant conditions with light, southerly flow (see Figure 3). The greatest air parcel density is found over the central Mid-Atlantic region. Ozone values, particularly in the afternoon, are large, as are CO values, whereas SO_2 values, especially in the morning, are small. Hence, the SO_2/CO ratio is small. The particle property values are moderate (see Figures 5, 6, and Tables 1, 2).

These values, together with the stagnant conditions associated with Cluster 3, indicate local, urban, mobile source-dominated pollution. Figure 4 shows that there are few large NO_x and SO₂ sources in the area of greatest trajectory density. Presumably, because there is less hygroscopic sulfate available for particle growth, the particles are smaller and less scattering than in the first two clusters.

The transport pattern identified by Cluster 4 is characterized by moderate southwesterly flow and the greatest trajectory density lies over the southern Ohio River Valley (see Figures 3, 4). For the most part, this cluster is associated with little pollution loading and the SO₂/CO ratio is small (see Figures 5, 6, and Tables 1, 2), suggesting that there are fewer point sources located farther south along the Ohio River. Figure 4 shows no large NO_x or SO₂ sources in the area of greatest trajectory density, although many do encircle this area. Also, the afternoon O₃ values are particularly small, and not much larger than the morning values (see Figures 5, 6, and Table 1), indicating there was little photochemical production during the air parcels transport.

Cluster 5 shows fairly fast north-northwesterly flow over the northern Great Lakes region into the Mid-Atlantic region (see Figure 3). Generally, this flow pattern seems to transport little pollution into the region. However, the O₃ values are large below ~1200 m in the morning and ~1500 m in the afternoon and only fall off to lower values aloft (see Figures 5, 6). The areas of greatest trajectory density do intersect large NO_x and SO₂ sources (see Figure 4), a fact corroborated by a high SO₂/CO ratio in the morning (Table 1), but the wind speeds, particularly aloft, are too great to allow for pollution to accumulate in the Mid-Atlantic region. The fast wind

speeds are also not conducive to particle growth, so the smallest particles are found in this cluster.

The wind direction of the trajectories in Cluster 6 is northwesterly as in Clusters 1 and 2, with still faster wind speeds than in Cluster 2 (see Figure 3). The greatest trajectory density again lies over the northern Ohio River Valley and several large NO_x and SO₂ sources (see Figure 4). The pollution loadings of this cluster are also consistent with these sources, but because of the higher wind speeds, the pollution appears to be relatively fresher. The O₃ values are moderately large, with smaller values in the afternoon, the CO values are moderate, and the SO₂ values are very large, so that the SO₂/CO ratio is also very large (see Figures 5, 6, and Table 1). The SO₂ apparently did not have much opportunity for oxidation before entering the Mid-Atlantic region. The particles were smaller and less scattering and the AOD was smaller than in Clusters 1 and 2 (see Figures 5, 6, and Tables 1, 2).

Overall, Cluster 7 is associated with the least pollution of any of the clusters (see Figures 5, 6, and Tables 1, 2). The flow is out of the north, bringing relatively cool, dry, continental air to the Mid-Atlantic region. There are no major urban centers, nor are there many NO_x or SO₂ sources in the area of greatest trajectory density (see Figure 4).

Cluster 8 comprises very few trajectories. The flow is fast and from the southwest, originating near Texas (see Figure 3). There were not enough particle data to generate any statistical values. The O₃ values are small, the SO₂ values are moderate, and the CO is very large (see Figures 5, 6, and Table 1). The areas of greatest trajectory density do not intersect many large NO_x or SO₂ sources (see Figure

4). Despite the fast wind speeds, the air parcels appear to be picking up a local, mobile source, indicated by the large CO values, small SO₂/CO ratio, and trajectory densities. Figure 7 summarizes the transport from the areas of greatest trajectory density into the Mid-Atlantic region as a percent of the total number of profiles examined in this study.

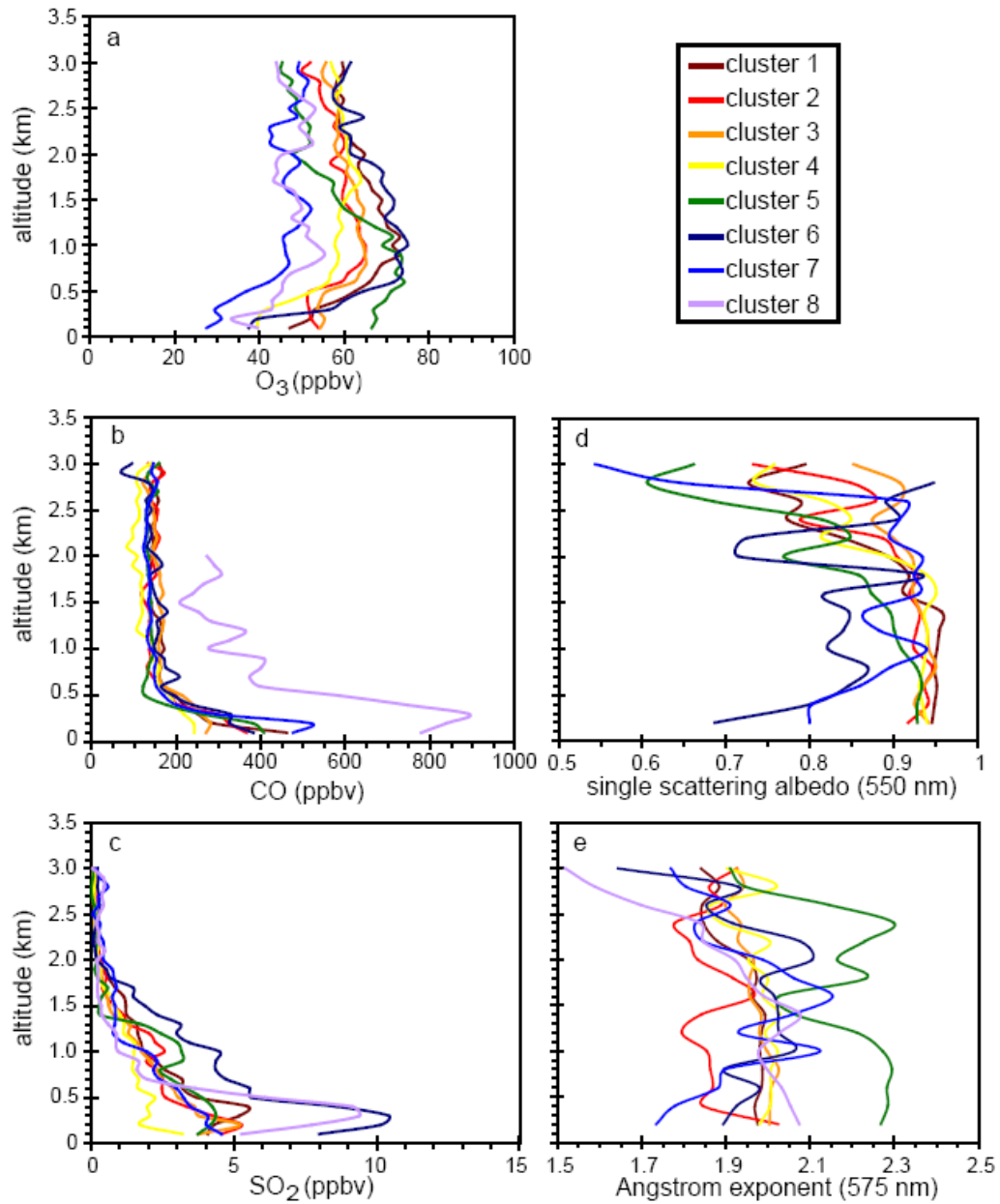


Figure 5. The median morning profiles for Clusters 1 (brown), 2 (red), 3 (orange), 4 (yellow), 5 (green), 6 (dark blue), 7 (blue), and 8 (violet) of a) O₃, b) CO, c) SO₂, d) single scattering albedo (550 nm), and e) Ångström exponent (575 nm).

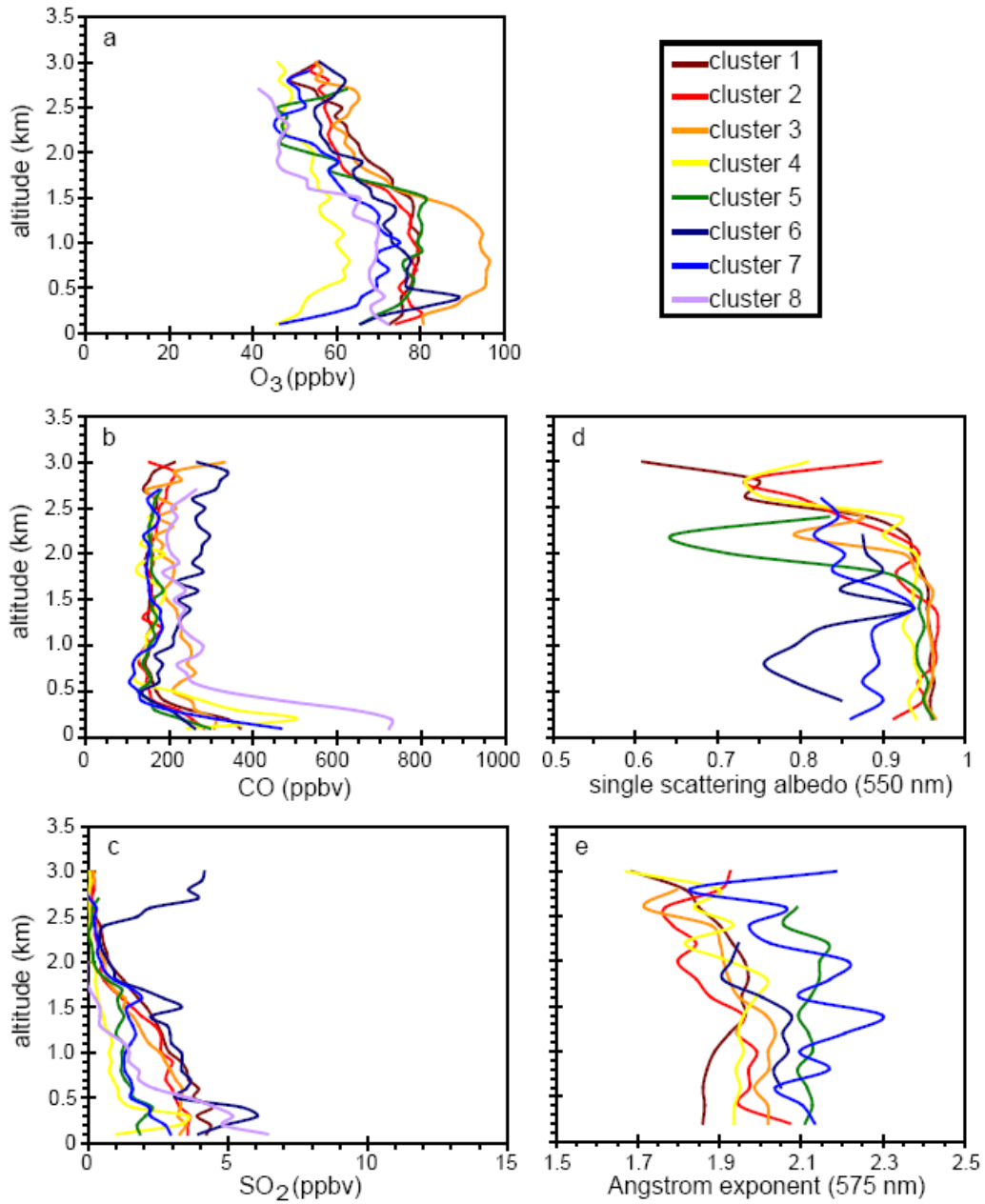


Figure 6. The median afternoon profiles for Clusters 1 (brown), 2 (red), 3 (orange), 4 (yellow), 5 (green), 6 (dark blue), 7 (blue), and 8 (violet) of a) O₃, b) CO, c) SO₂, d) single scattering albedo (550 nm), and e) Ångström exponent (575 nm).

3.3.3 O₃ Transport

Thus far, the first of the two original questions posed has been addressed. Namely, a statistical link between characteristic regional transport patterns into the Mid-Atlantic during summertime haze and O₃ episodes and specific pollution loadings has been established. In this section I will quantify the contribution of regionally transported O₃ to afternoon boundary layer O₃ over the Mid-Atlantic.

The percent of the afternoon O₃ boundary layer column content for each cluster that can be accounted for by regional transport was estimated with the following equation:

$$\% O_3 \text{ transported} = \left(\frac{RL}{MBL} \right) \times \left(\frac{MBL}{ABL} \right) \times 100, \quad (2)$$

where *RL* is the residual layer column content, *MBL* is the morning boundary layer column content, and *ABL* is the afternoon boundary layer column content. The equation simplifies to the ratio of *RL/ABL* after the *MBLs* cancel out. The accuracy of this method depends upon the Lagrangian nature of the morning and afternoon profiles from each cluster. Because flight plans were designed in a Lagrangian manner, where morning flights were upwind of afternoon flights, the estimate should be accurate. The results are shown in Table 1 and Figure 7. The amount of afternoon O₃ that can be accounted for by regional transport ranges from a low of 55% to a high of 82%. One of the smallest contributions from transport (58%) corresponds to Cluster 3. This cluster shows the most stagnant conditions so that transport would not be expected to contribute as much to the afternoon totals (the weak winds allow for transport of only a few hundreds of km in a 24 hr period). The largest contributions from regional transport are seen in Clusters 1(70%), 2(69%), 4(82%) and 6(73%).

The trajectory density plots (see Figure 4) show that their greatest air parcel densities are over the Ohio River Valley. Those of Cluster 4 lie over the southern Ohio River Valley whereas those of the other three Clusters all lie over the northern portion of the Ohio River. While the pollution loadings associated with Cluster 4 are relatively small, those in Clusters 1, 2, and 6, particularly with respect to O₃, SO₂, and particle pollution, are large. In general, the greatest regional O₃ transport was from the Ohio River Valley, while some of the least transport occurred during clean, northerly flow (Cluster 7) and when stagnant conditions persisted and photochemical production was highest (Cluster 3). Our analysis neglected O₃ produced locally from precursors transported from upwind and may thus be an under-estimate of the role of transport.

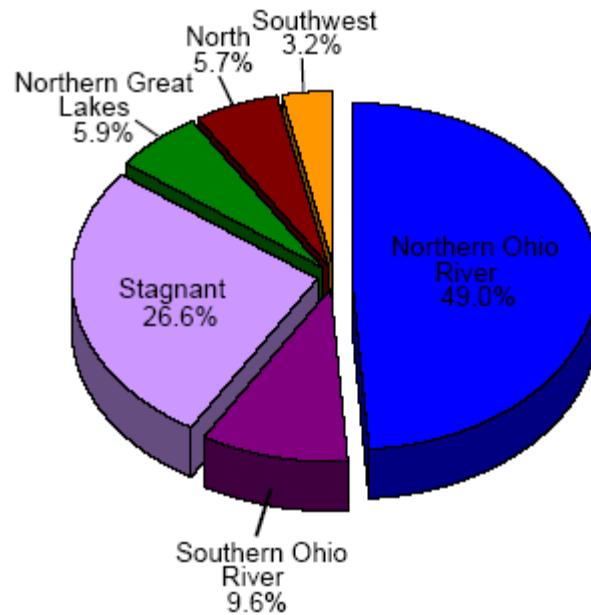


Figure 7. Pie chart showing the transport from the particular areas, as defined by the trajectory densities in each cluster, into the Mid-Atlantic region as a percent of the total number of profiles examined in the study. The Northern Ohio River slice comprises Clusters 1, 2, and 6.

3.4. Conclusions

Several years of episodic, summertime aircraft vertical profile trace gas and aerosol data collected as part of the Regional Atmospheric Measurement, Modeling, and Prediction Program (RAMMPP) were analyzed in this study. The data were divided into morning and afternoon profiles to identify diurnal patterns. Little diurnal variation was observed in the CO, SO₂, or Ångström exponent but O₃ values were greater in the afternoon than the morning. O₃ above the planetary boundary layer in the lower free troposphere, amenable to long range transport, was consistently ~55 ppbv. The single scattering albedo was larger in the afternoon than the morning, likely the result of VOC and SO₂ oxidation to secondary organic aerosols and sulfate, respectively. A decrease in the single scattering albedo above 2000 m was due to invariant absorption values with altitude combined with scattering values that declined with altitude. This phenomenon could have a large-scale radiative impact, although the aerosol extinction in the lower free troposphere may be too low to have any significant effects. Even so, this occurrence merits further investigation.

Characteristic transport patterns and source regions during summertime haze and O₃ episodes were analyzed with an agglomerative hierarchical cluster analysis of back trajectory data. Eight clusters were identified, which were then divided into morning and afternoon profiles. The median profile values were calculated and statistical differences were determined using a nonparametric procedure. When the greatest trajectory density lay over the northern Ohio River Valley and large NO_x and SO₂ sources, the result was large O₃ values, a large SO₂/CO ratio, large, scattering particles, and high AOD over the Mid-Atlantic U.S. In contrast, relatively clean

conditions over the Mid-Atlantic occurred when the greatest trajectory density lay over the southern Ohio River Valley and nearly missed many large NO_x and SO_2 sources. The greatest afternoon O_3 occurred during periods of near stagnation (when the average wind speed was 4.4 m s^{-1} at 2km) that were most conducive to photochemical production. The least pollution occurred when flow from the north-northwest was too fast for pollution to accumulate and when flow was from the north, where there are few urban or industrial sources.

O_3 transport over several hundred kilometers into the Mid-Atlantic U.S. was estimated by calculating the ratio of the residual layer O_3 in the upwind morning profiles to the downwind afternoon boundary layer values. The greatest O_3 transport (69-82%) occurred when the maximum trajectory density lay over the southern and northern Ohio River Valley (~59% of the total profiles). The least O_3 transport (55-58%) was associated with fast southwesterly flow (~3% of the total profiles), clean northerly flow (~6% of the total profiles), and stagnant, polluted conditions (~27% of the total profiles). Altogether, about 64% of the O_3 during an episode is already present as the air enters the Baltimore/Washington area from the West.

In summary, this investigation demonstrated the ability to identify important statistical differences among pollution profiles that resulted from seemingly minor variations of the typical summertime, polluted meteorological regime. When trajectory density plots were overlaid on maps with the largest annual NO_x and SO_2 emitters, specific source regions were identified. The results indicate that the areas of maximum trajectory density together with wind speed are effective predictors of regional pollutant loadings. Additionally, due to the Lagrangian nature of the dataset,

the regionally transported contribution to the total afternoon boundary layer column
O₃ content in each cluster could be quantified.

Chapter 4: Cluster Analysis of Pollutant Profiles.

4.1 Introduction

4.1.1 Background

Understanding the influences of meteorology and emissions on the vertical distribution of trace gases and aerosols can improve modeling and prediction of pollution events. Some work presented in this chapter is from Hains et al. (2007a). I have developed a method to cluster vertical profiles of trace gases and aerosols. I then examined meteorological conditions as indicated by back trajectories associated with each cluster. Results from this cluster analysis are used to explain meteorological and emission influences on the vertical distribution of trace gases and aerosols. I have clustered over 150 profiles of O₃, CO, SO₂, absorption, scattering, and Ångström exponent (α) collected between 1997-2003 in June, July and August. I developed a method for integrating point source emission sources (from the EPA's AirData database) encountered by a 48-hr back trajectory. I have employed this method to explain the relationship between point source emissions and the different clustered profiles.

4.1.2 Cluster Analysis

Statistical cluster analysis involves determining the differences between the objects being analyzed, and clustering those objects with the smallest differences. The trace gases presented in Chapter 3 showed distinctive profiles; for example, most of the SO₂ was found below 500 m throughout the day, while O₃ was most concentrated

above 500 m in the morning and was more uniform from the surface to 2000 m in the afternoon (the largest values in the profile were found near the 1100 m level).

For this work, the raw data were averaged into altitude layers of 100 m (gases) or 200 m (aerosols) and then the layers were grouped into bins shown in Table 1. The slope and correlation of the points in each pair of profiles under comparison were considered as well as the total difference in values between the two profiles within each altitude bin. The following equation was used to calculate the differences among the aircraft profiles:

$$D_{ij} = \sum_{k=1}^{k=4} \left\{ \left(\sum_{a=1}^{a=n_k} \text{abs}(c_{ia} - c_{ja}) \right)^2 * \left(1 + [1 - r] + [1 - \exp(-(s - 1)^2)] \right) \right\} \quad (1)$$

Here, k is the index for the four different altitude bins for the profiles and a is an index for the n_k layers within the k^{th} bin (Table 1). The species value is represented by c for the i^{th} and j^{th} profile. In each altitude bin, k , there are at least four layers of trace gas or aerosol data. A regression was made to obtain the slope, s , and the correlation coefficient, r , for each pair of profiles using the mixing ratio (or aerosol coefficient) within the k bins. The first part of Equation 1 determines the square of the sum of the differences between values at each altitude bin, k . The second part of the equation multiplies the difference by one plus differences associated with the correlation and slope. When the correlation is small or negative the profiles are very different and the $1 - r$ portion increases, which increases the total difference D_{ij} . As the correlation coefficient approaches unity the $1 - r$ portion approaches zero, and this decreases the total difference D_{ij} . The exponent of the slope portion is used to account for the slope between the pairs of profiles. A slope near unity suggests that the profiles are similar and thus should add little to the total difference. The exponent

of the slope was used to guarantee that slopes much different from unity will make the exponential term small and thus increase the total difference. Once the difference between each pair of profiles has been calculated, the profiles with the smallest differences are clustered. These clusters are constructed from hierarchical cluster trees generated with an average linkage algorithm in Matlab (described in Chapter 3 section 3.2.3).

k bin	Altitude bins for trace gases	Number of layers in bin (m_k)	Altitude bins for aerosols	Number of layers in bin (m_k)
1	151-650 m	5	100-900 m	4
2	651-1150 m	5	901-1700 m	4
3	1151-1650 m	5	1701-2500 m	4
4	1651-2450 m	8		

Table 1. Altitude bins for trace gases and aerosols used in Equation 1.

4.2 Results

4.2.1 O₃

Figure 1 shows the median profiles for each of the six O₃ clusters calculated in the above manner. The clustering technique identified a small group of outliers, Cluster 6, with large values of O₃ above 2000 m altitude. These profiles were made on 8 and 9 July 2002 when smoke from Canadian forest fires impacted the Mid-Atlantic region (Colarco *et al.*, 2004; Taubman *et al.*, 2004a). The transported O₃ can be seen in the peak (up to 150 ppb) above 2000 m. This shows that the statistical technique employed can separate anomalous episodes. The quartiles for the six clusters rarely overlap, which further exemplifies how the method was able to separate distinct events.

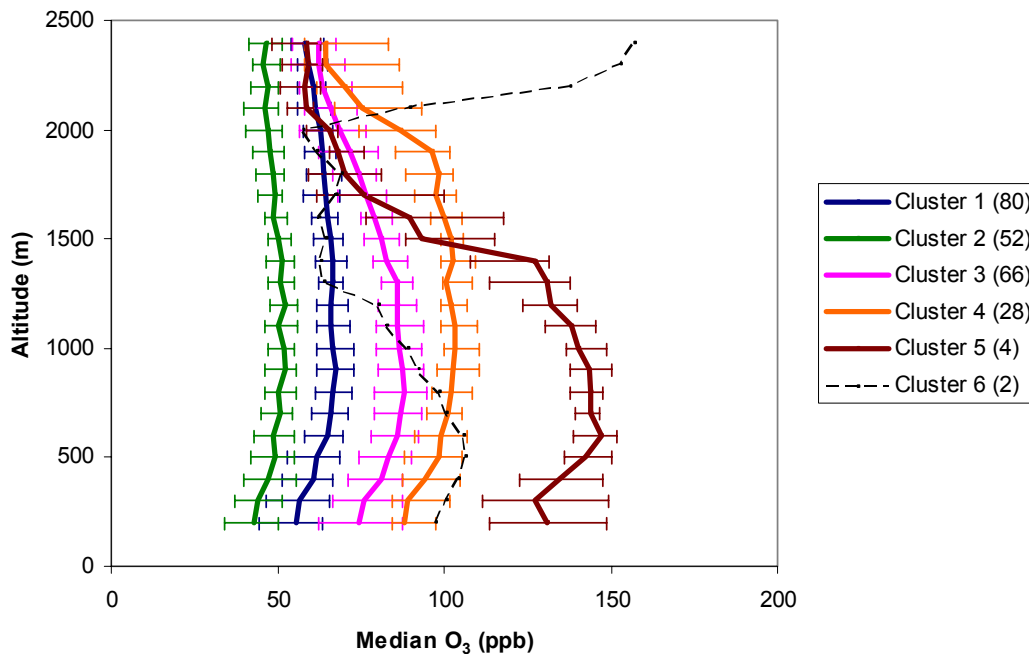


Figure 1. Median O₃ profiles for each cluster. Error bars represent the 25th and 75th percentiles. The number of profiles in each cluster is shown in parentheses in the key. Clusters 1 and 2 show the smallest O₃ values, while Clusters 3, 4 and 5 show the largest. Cluster 6 profiles were made when the Canadian forest fires impacted the region and the peak above 2000 m shows their influence.

I calculated two-day HYSPLIT back trajectories for each spiral, ending at an altitude of 1, 2 and 3 km, at the latitude and longitude of the spiral and at the time the spiral was made. Back trajectories were similar at all altitudes and so I chose those ending at 1 km because these are most likely to be closer to point source emissions. Profiles from Clusters 3, 4 and 5 had large O₃ values and the back trajectory density plots (Figure 2) show passage over the Northern Ohio River Valley, where there is a higher concentration of NO_x sources. Taubman et al. (2006) found a similar relationship between back trajectories concentrated over the Northern Ohio River Valley and large mixing ratios of O₃ and suggested that the large concentration of

power plants in this region contributes to the O₃ in the Mid-Atlantic region. The back trajectory density plots for Clusters 3-5 also show larger densities around the I-95 corridor, which is suggestive of stagnation events that lead to higher O₃ values.

Cluster 2 has back trajectories that pass over the Atlantic Ocean, which may explain the smaller O₃ values associated with this cluster. Cluster 1 has the second smallest O₃ values (Cluster 1 column content is 19% less than that of Cluster 3), even though the back trajectories associated with Cluster 1 are similar to those of Cluster 3. To address this discrepancy, the integrated NO_x point source emissions along the back trajectories were examined.

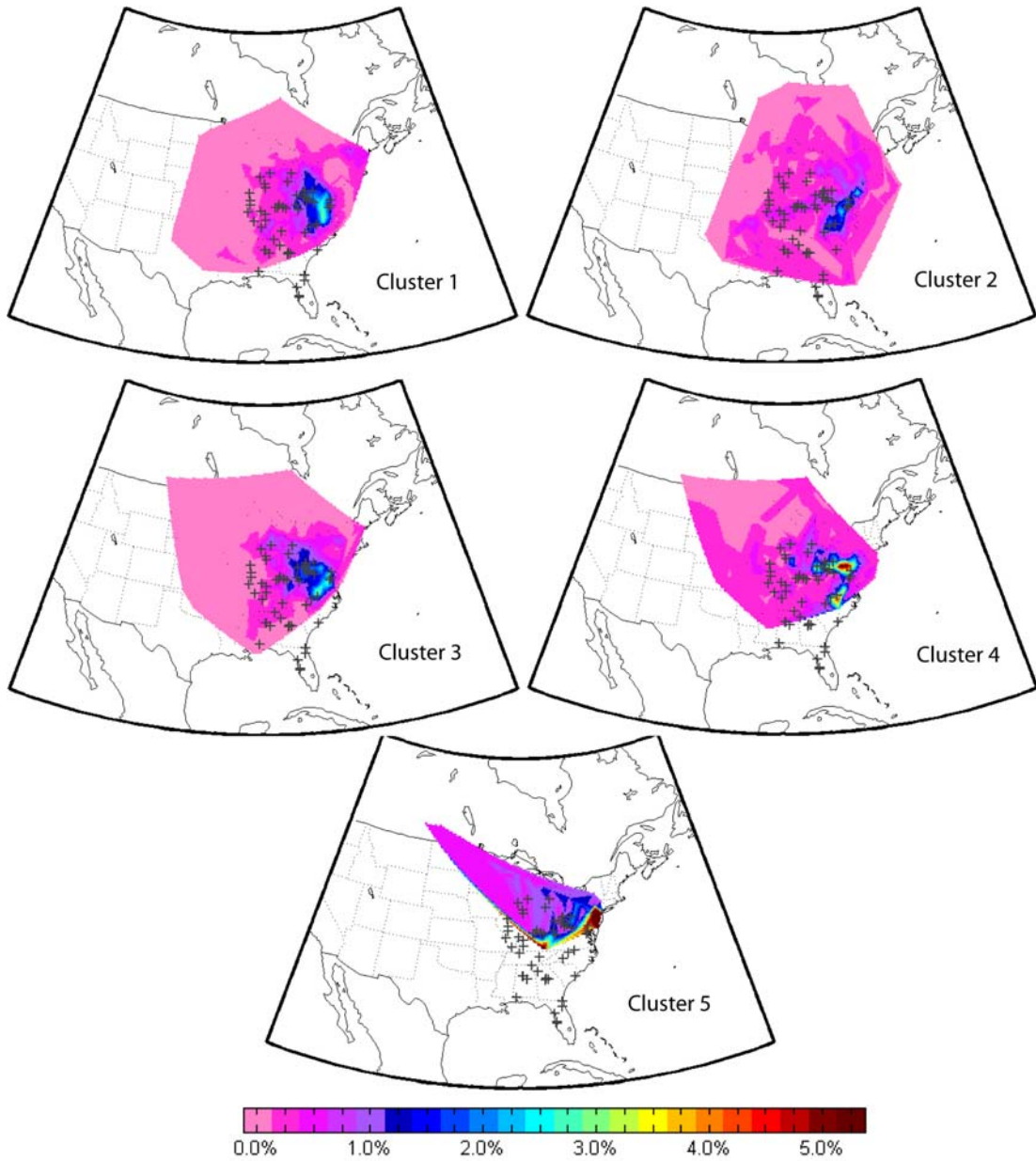


Figure 2. Back trajectory density plots for O₃ Clusters 1-5. The top 0.3% NO_x sources are shown with a + symbol. Clusters 3, 4 and 5 associated with larger O₃ values show larger densities near point sources as well as along the I-95 corridor, suggestive of stagnation. Cluster 5 also has an unusual flow pattern from the northeast. Clusters 1-2, with smaller O₃ values are associated with more variable winds.

I integrated the NO_x emissions along each back trajectory to explain the influence of upwind emissions on upwind ozone mixing ratios. Emissions from the daily EPA Clean Air Market unit level emissions database (<http://cfpub.epa.gov/gdm/index.cfm?fuseaction=emissions.wizard>) were used in this study. I drew a circle, centered at each back trajectory position for each hour of the two day back trajectory (Figure 3). The radius of the circle was 80 km to account for uncertainties associated with the back trajectory position and the influence of eddy diffusion and mixing processes. The emissions within each circle were summed. The sum of the emissions for each circle was divided by the area of the circle. I used emissions from the day on which the back trajectory crossed a circle for the date of each back trajectory position. The summed emissions will be referred to as integrated emissions. Statistics (median, 5th, 25th, 75th and 95th percentiles) for the integrated NO_x emissions for each O₃ cluster are shown in Figure 4.

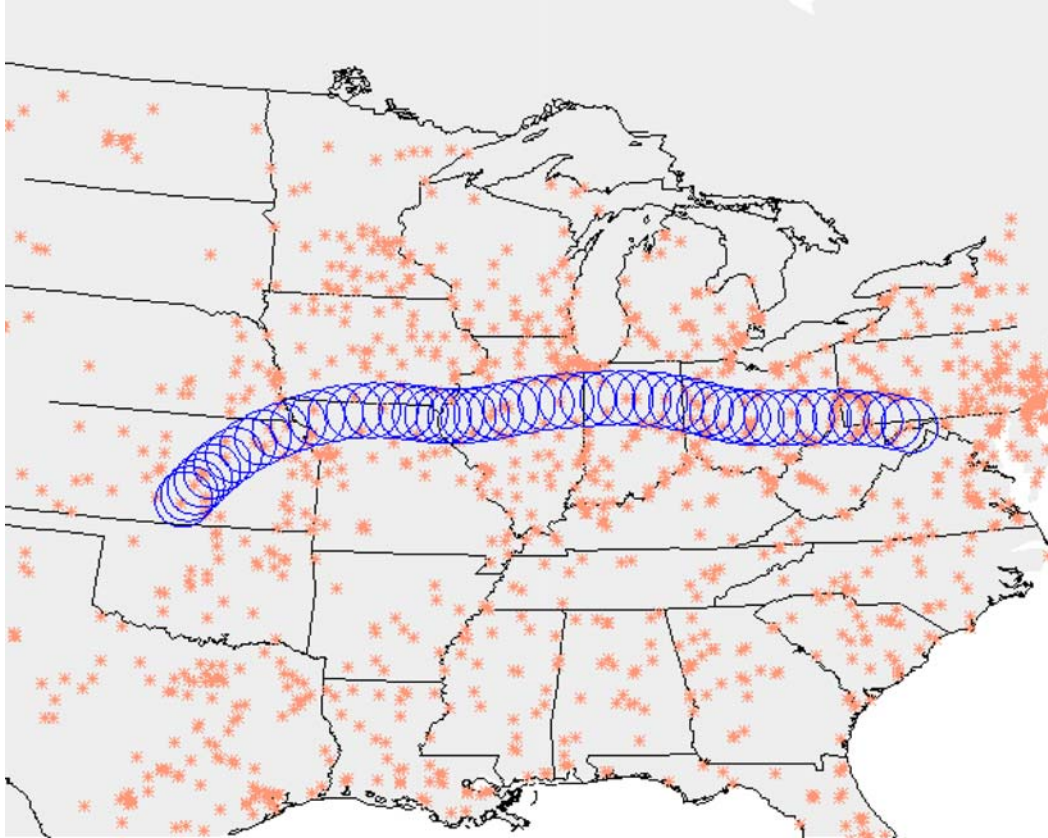


Figure 3. Circles drawn around an example back trajectory. The emissions contained in each circle were summed and divided by the area of the circle. Then emissions from each circle were summed. The pink * represent point source locations.

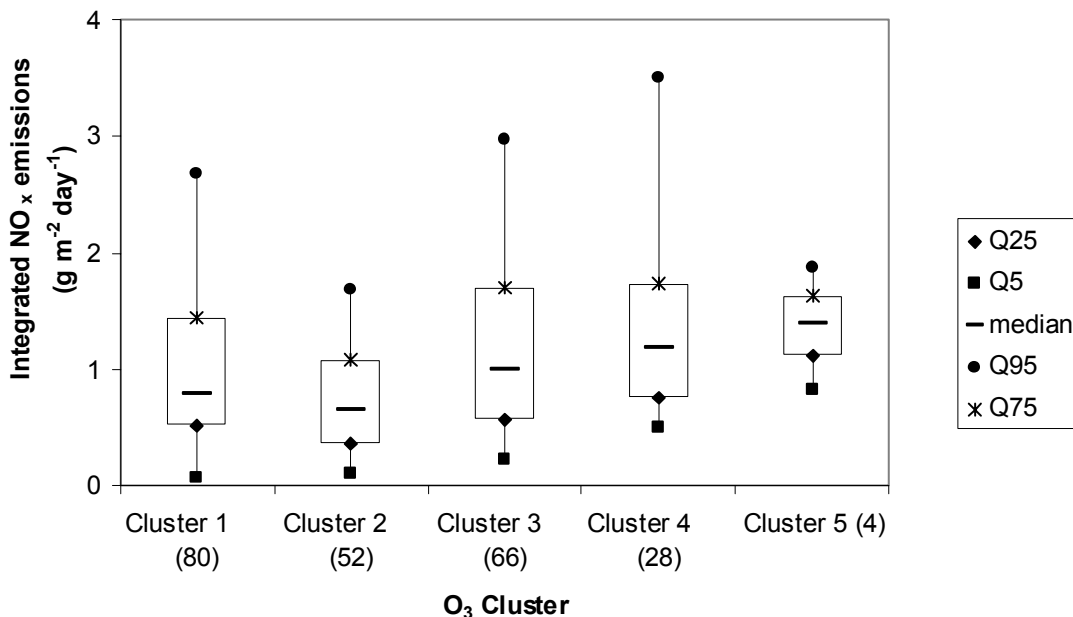


Figure 4. Statistics for NO_x emissions encountered by back trajectories for each O₃ cluster. The NO_x emissions are sums of all emissions (g day⁻¹) encountered by a back trajectory divided by the area of the circle drawn around the back trajectory point (m²). Clusters 1 and 2, with the smallest O₃ values are also associated with the smallest NO_x emissions. Clusters 3, 4 and 5, with the largest O₃ values are associated with the largest NO_x emissions.

Clusters 3, 4 and 5 have the largest O₃ column contents and the largest NO_x emissions, while Clusters 1 and 2 have the smallest O₃ column contents and the smallest NO_x emissions. Even though back trajectory density maps for Clusters 1 and 3 are similar, Cluster 1 is associated with 21% less integrated NO_x emissions, explaining the 18% smaller O₃ values. The median O₃ column content and integrated NO_x emissions for Clusters 1 through 5 show a positive relationship (Figure 5), suggesting that NO_x emissions from point sources play an important role in downwind O₃ production.

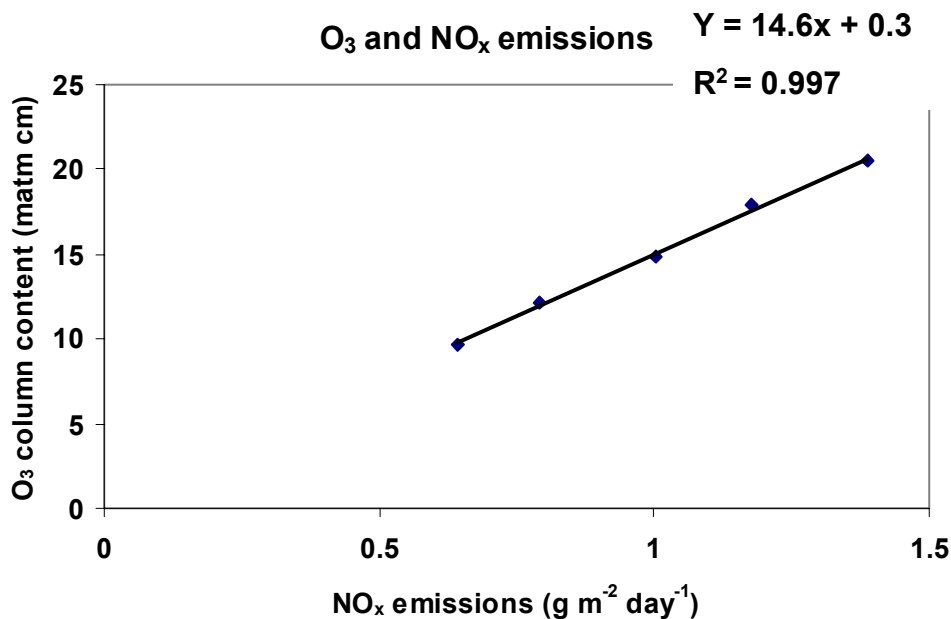


Figure 5. Median O₃ column content and median integrated NO_x emissions (from point sources) for O₃ Clusters 1 through 5. The O₃ is positively correlated with integrated NO_x emissions.

Profiles were also analyzed by time of day, where morning profiles are defined as those made before 12 noon EST and afternoon as profiles made after 12 noon EST. Sixty-one and sixty-eight percent of the profiles in Clusters 3 and 4 were measured in the afternoon, whereas only 38% and 46% of the profiles in Clusters 1 and 2 were measured in the afternoon. Greater O₃ values in Clusters 3 and 4 may be partly explained by the increased number of afternoon profiles which were generally made downwind of urban centers, and had more time for O₃ production.

4.2.2 SO₂

I also clustered the SO₂ profiles and generated three distinct SO₂ profile clusters (Figure 6). Of the 192 profiles analyzed, 170 (89%) fell into the relatively clean Cluster 3. The other clusters reflect large values of SO₂ at altitudes from near

the surface (Cluster 2) to 1000 m (Cluster 1). Back trajectories associated with Cluster 3 show a broader area of origin than the more heavily polluted Clusters 1 and 2 (Figure 7). The median SO₂ profile from Cluster 2 shows large values near the surface that decrease above 500 m. Profiles in Cluster 1 show large values near the surface that do not drop off as rapidly as those in Cluster 1, indicating better mixing in the lower troposphere.

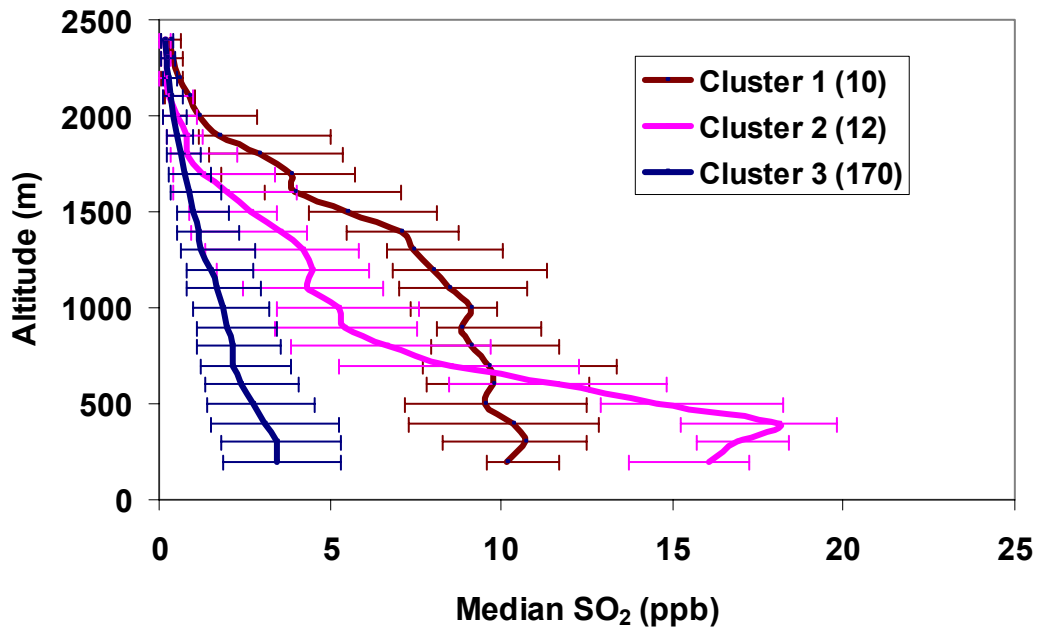


Figure 6. Median SO₂ profiles for each cluster. Error bars represent the 25th and 75th percentiles. The number of profiles in each cluster is shown in parentheses in the key. Cluster 3 is the background Mid-Atlantic summertime SO₂ profile, representing the majority of SO₂ profiles measured. Clusters 1 and 2 represent profiles impacted by chance plume encounters.

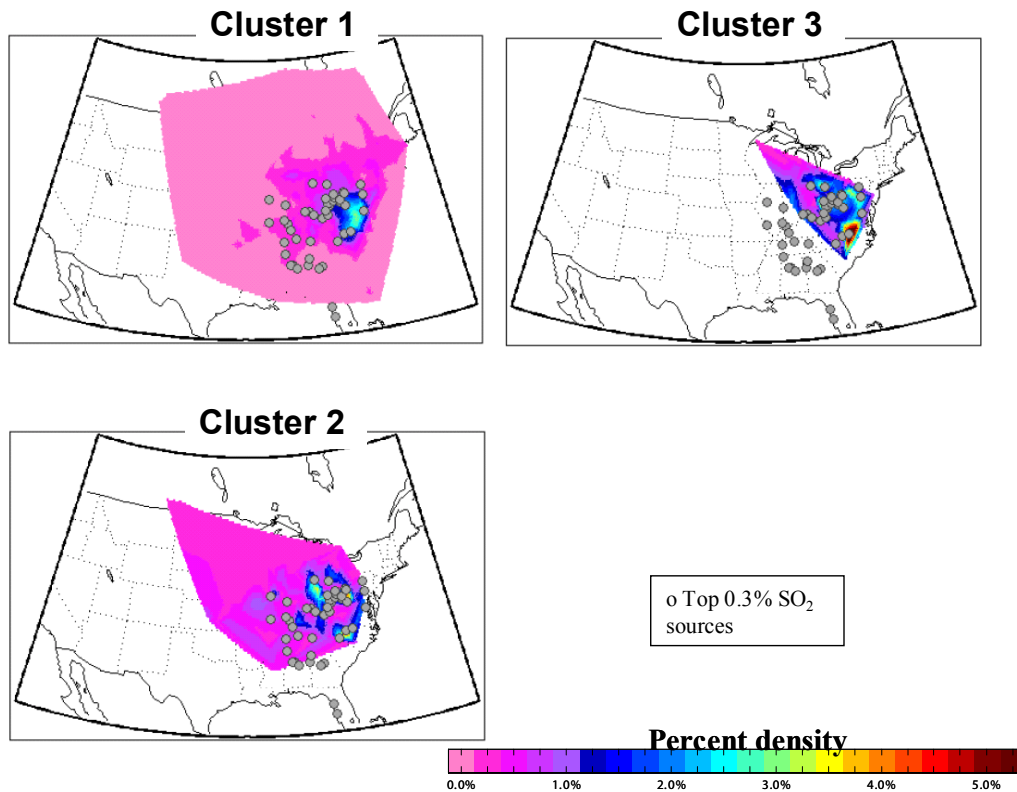


Figure 7. Back trajectory density plots for SO₂ Clusters 1-3. The top 0.3% SO₂ sources are shown with a circle. Back trajectories associated with Clusters 2 and 3 show more density over SO₂ sources while the back trajectories associated with Cluster 1 show more variable origins.

The integrated SO₂ emissions along each back trajectory and statistics for each SO₂ cluster were calculated (Figure 8). The SO₂ emissions do not show as much range as the NO_x emissions. The lack of relationship between emissions and the SO₂ profiles, and the small number of meaningful SO₂ clusters generated, suggests profiles with larger values are likely the result of chance encounters with fresh plumes, and that the lifetime of SO₂ in the summer is shorter than 48 hours. The lifetime of SO₂ is addressed in Chapter 5.

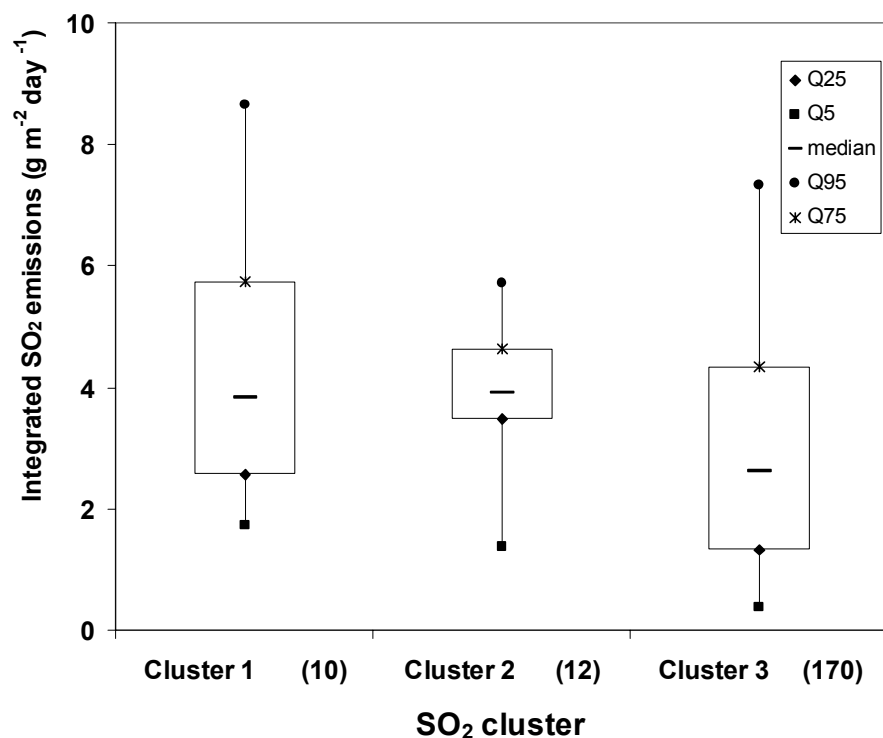


Figure 8. Statistics for SO₂ emissions encountered by back trajectories for each SO₂ cluster. The SO₂ emissions are sums of all emissions (g day⁻¹) encountered by a back trajectory divided by the area of the circle drawn around the back trajectory point (m²). The SO₂ emissions show little relationship with the profiles.

4.2.3 Particle Scattering

Figure 9 shows the median scattering coefficients (in units of m⁻¹) for all flights conducted between 2001 and 2003 (June through August). The clustering methodology produced four scattering clusters, but two are sparsely populated (Clusters 3 and 4) and associated with the Canadian forest fire episode (Figure 9). The median scattering profile for Cluster 1 is similar to the median profile of all flights. Cluster 1, with 125 profiles, has smaller values than Cluster 2, with 48 profiles (Figure 9). Back trajectories associated with profiles from Cluster 2 show winds from the Northern Ohio River Valley, while Cluster 1 has back trajectories

with more variable winds and greater mean wind speeds (Figure 10). Slower wind speeds or stagnant conditions allow time for the conversion of SO₂ to sulfate. Figure 11 shows statistics of integrated SO₂ emissions for each cluster. The median SO₂ emissions for Cluster 2 are almost a factor of two greater than those for Cluster 1. This suggests that the aerosol loading reflects the SO₂ emitted into the air parcel over the previous 48 hours.

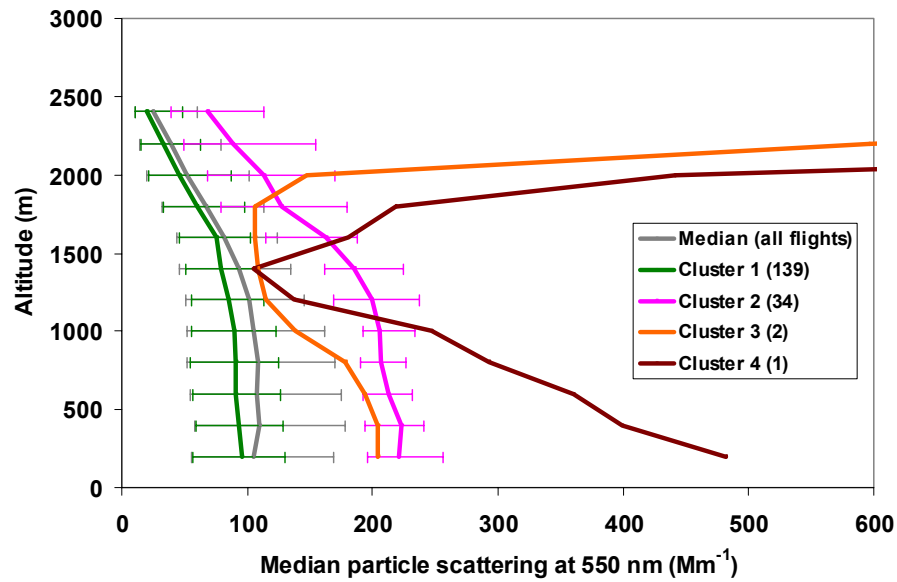
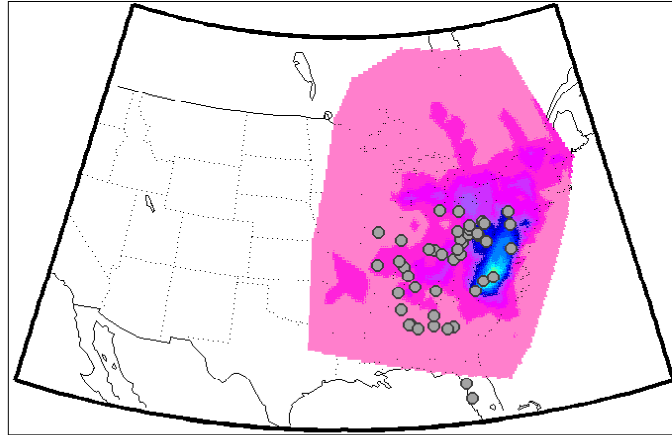
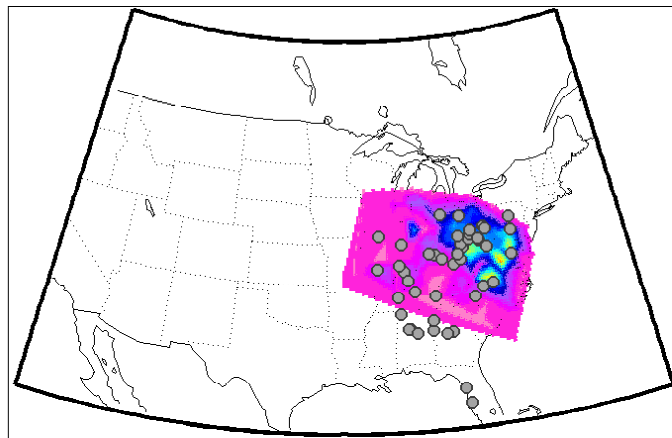


Figure 9. Median scattering profiles for each cluster. Error bars represent the 25th and 75th percentiles. The number of profiles in each cluster is shown in parentheses in the key. Cluster 2 has profiles with twice the scattering value as Cluster 1. Profiles from Clusters 3 and 4 were measured when the Canadian forest fires impacted the region.

Cluster 1



Cluster 2



o Top 0.3% SO₂
sources

Percent density



Figure 10. Back trajectory density plots for scattering Clusters 1 and 2. The top 0.3% SO₂ sources are shown with a circle. Back trajectories associated with Clusters 2 show more density over SO₂ sources while the back trajectories associated with Cluster 1 show more variable origins.

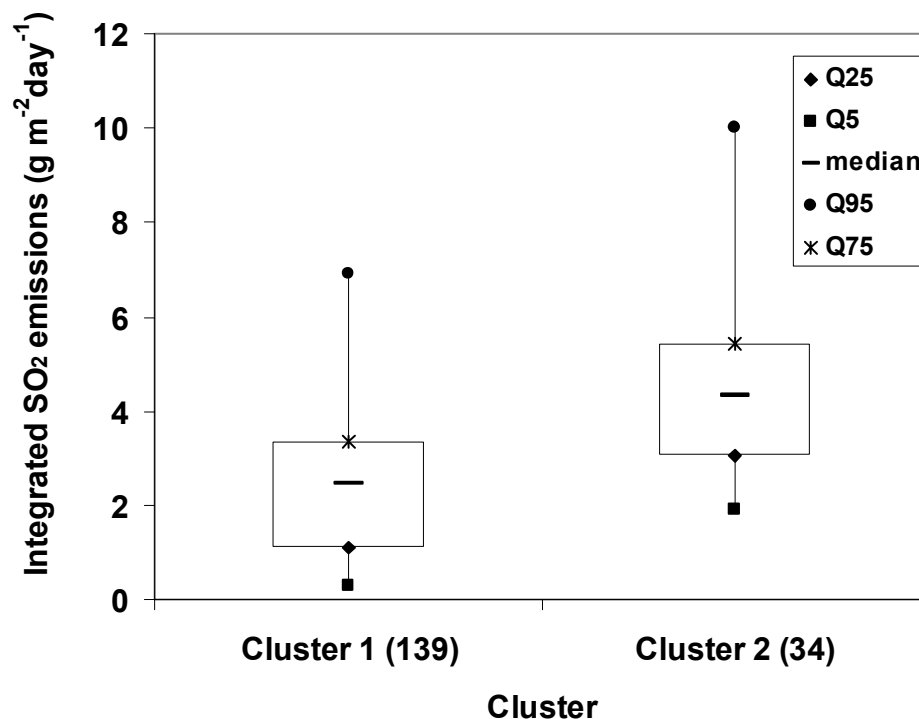


Figure 11. Statistics for SO₂ emissions encountered by back trajectories for each scattering cluster. The SO₂ emissions are sums of all emissions (g day⁻¹) encountered by a back trajectory divided by the area of the circle drawn around the back trajectory point (m²). Cluster 2 is associated with almost double the emissions of Cluster 1, explaining why cluster 2 profiles have double the scattering values as Cluster 1 (Figure 9).

The conversion from SO₂ to sulfate in the summer is so rapid that there is little discernable relationship between SO₂ emissions from the Ohio River Valley and SO₂ values in the Mid-Atlantic. There is a positive relationship between SO₂ emissions in the Northern Ohio River Valley and particle scattering in the Mid-Atlantic, indicating an important source of sulfate aerosols is from Northern Ohio River Valley coal fired power plants (e.g., Taubman et al. 2006). The stronger relationships between emissions and SO₂ and aerosol profiles suggest that the lifetime of sulfate is longer than 48 hours.

4.2.4 Angstrom Exponent

The clustering methodology produced four distinct α clusters (Figure 12). The median profile for Cluster 1 has relatively small α values and thus represents larger particles. The back trajectories associated with Clusters 1 and 2 are concentrated over point sources in the Northern Ohio River Valley (Figure 13). Cluster 1 back trajectories however, are slower allowing more time for particle growth. Profiles from Cluster 1 are associated with larger integrated SO₂ emissions than the other clusters (Figure 14). Profiles in Cluster 4 have the largest α values and the least integrated SO₂ emissions. The α values are calculated from scattering measurements, explaining why they show a relationship similar to that between SO₂ emissions and scattering. Profiles in Cluster 3 decrease sharply above 2000 m and represent large particles. Four of the profiles in Cluster 3 were measured during the Canadian forest fires and one profile was measured on the 4th of July, when large particles would also be expected.

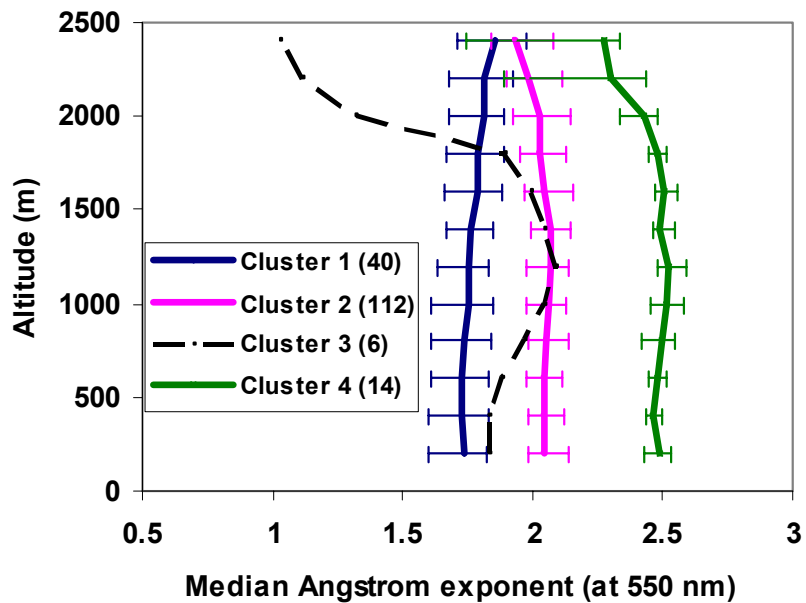


Figure 12. Median Angstrom exponent profiles for each cluster. Error bars represent the 25th and 75th percentiles. The number of profiles in each cluster is shown in parentheses in the key. Clusters 1 and 3 have the smallest angstrom exponents (largest particles), while Clusters 2 and 4 have the largest angstrom exponents (smallest particles). Profiles in Cluster 3 were measured when Canadian forest fires impacted the region, bringing in large particles aloft (above 2000 m).

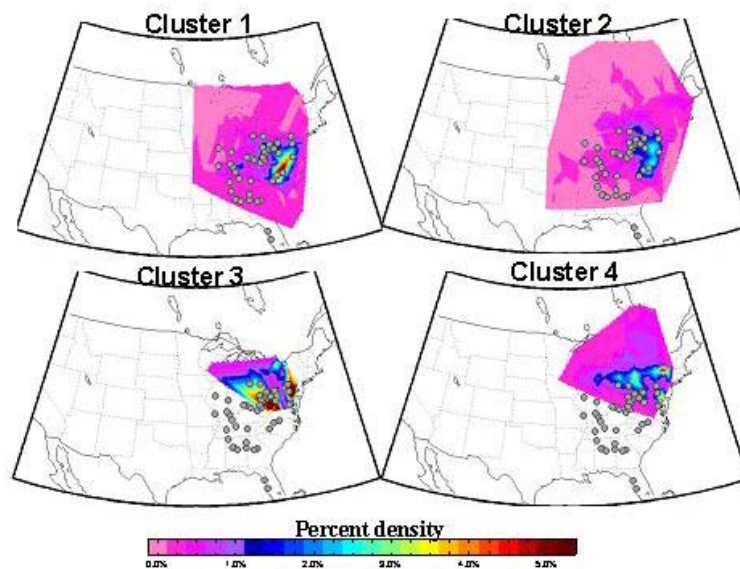


Figure 13. Back trajectory density plots for Angstrom exponent Clusters 1-4. The top 0.3% SO₂ sources are shown with a circle. Back trajectories associated with Clusters 1 and 2 show density over SO₂ sources, however back trajectories associated with Cluster 1 has the weakest winds allowing for more particle growth.

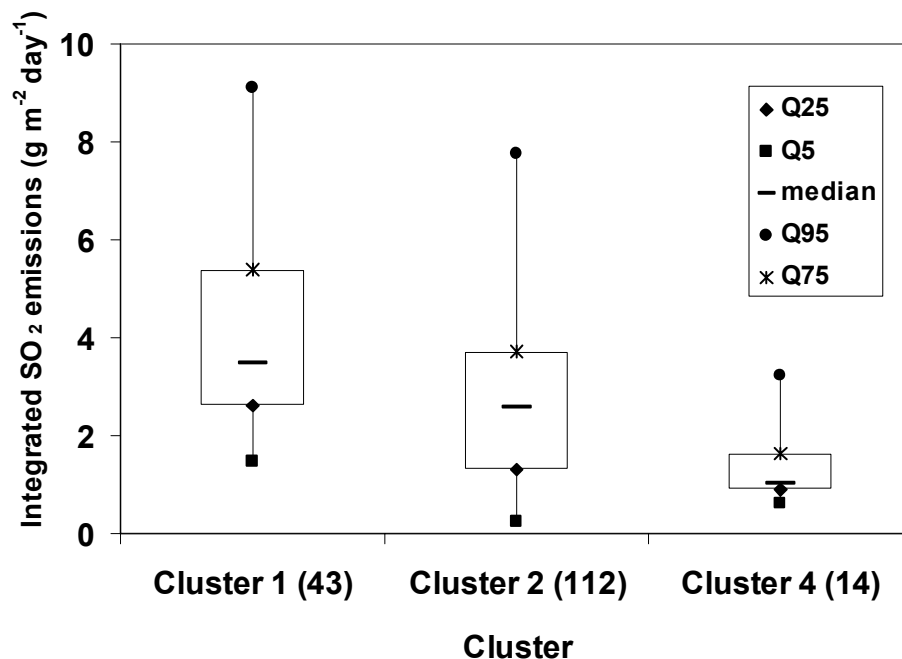


Figure 14. Statistics for SO₂ emissions encountered by back trajectories for each Angstrom exponent cluster. The SO₂ emissions are sums of all emissions (g day⁻¹) encountered by a back trajectory divided by the area of the circle drawn around the back trajectory point (m²). Cluster 1 is associated with the largest SO₂ emissions, while Clusters 2 and 4 emissions are much smaller. This explains the larger particles seen in Cluster 1 profiles (Figure 12).

4.2.5 CO

The clustering methodology produced three CO clusters (Figure 15). Cluster 3 had only one profile which was measured during the Canadian forest fire episode of 2002 and shows the signature peak in CO values above 2000 m (Taubman *et al.*, 2004a). Cluster 1, with 87% of the profiles, represents the background CO measured in the summer months in the Mid-Atlantic region. Cluster 2 values are about twice as large as Cluster 1 values. The back trajectories for Cluster 2 are short and concentrated around the I-95 corridor (a source for CO); while the back trajectories for Cluster 1 are more diffuse (Figure 16). This may explain the difference in CO

values between Clusters 1 and 2. Many of the profiles in Cluster 2 were made near Philadelphia and Baltimore, where the urban environments likely added to CO values. Most of the other flight locations for Cluster 2 were downwind of the I-95 corridor between Virginia and Pennsylvania. Cluster 2 not only has larger peaks near the surface but also larger values aloft. This suggests that the Eastern US is a major source for regional CO.

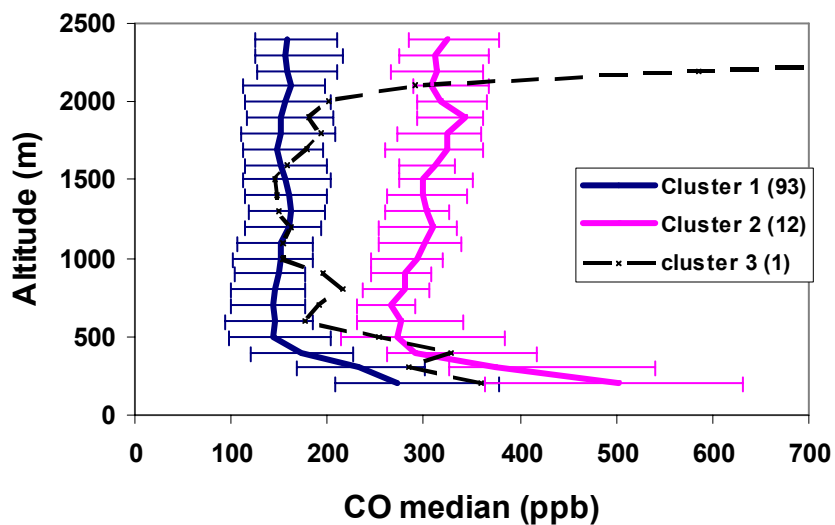
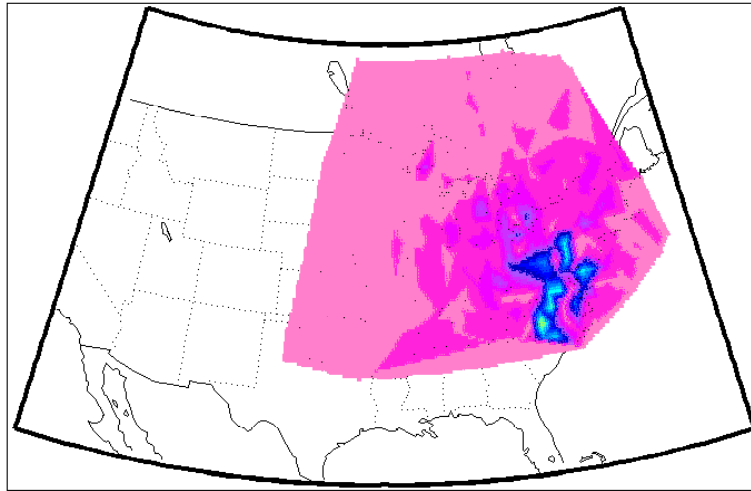


Figure 15. Median CO profiles for each cluster. Error bars represent the 25th and 75th percentiles. The number of profiles in each cluster is shown in parentheses in the key. Cluster 3 profiles have double the CO values in Cluster 1. Profiles in Cluster 4 were made when Canadian forest fires impacted the region.

Cluster 1



Cluster 2

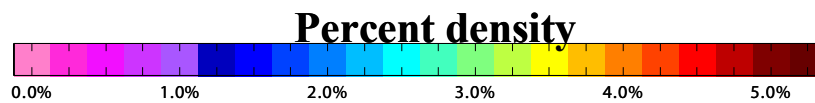
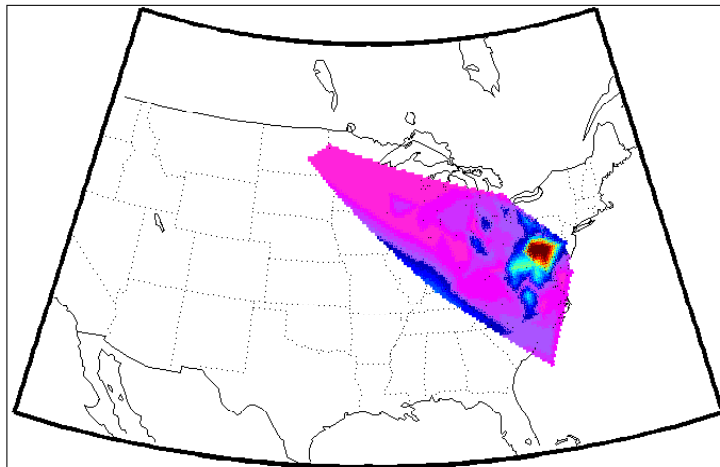


Figure 16. Back trajectory density plots for CO Cluster1 (clean profile) and Cluster 2 (polluted profile). Back trajectories for Cluster 2 are short and concentrated around the I-95 corridor (a source for CO); while the back trajectories for Cluster 1 are more diffuse.

4.2.6 Particle Absorption

The clustering methodology produced three absorption clusters and the associated median profiles are shown in Figure 17 along with the median of all flights made between 2000 and 2003 (June through August). The median profile for Cluster 2 represents 77% of the profiles and is similar to the median of all flights made. The median profile for Cluster 1 has on average twice the absorption values of Cluster 2, and is greater than the 75th percentile of the median of all profiles. The back trajectory densities for Clusters 1 and 2 both show northwesterly winds, however, Cluster 1 winds are slightly faster (Figure 18). These faster back trajectories associated with Cluster 1 may bring in air from the industrialized Midwest to mix with local, mobile emissions. Cluster 3 contains only profiles measured during the Canadian forest fires and shows the characteristic peak above 2000 m (Taubman *et al.*, 2004a).

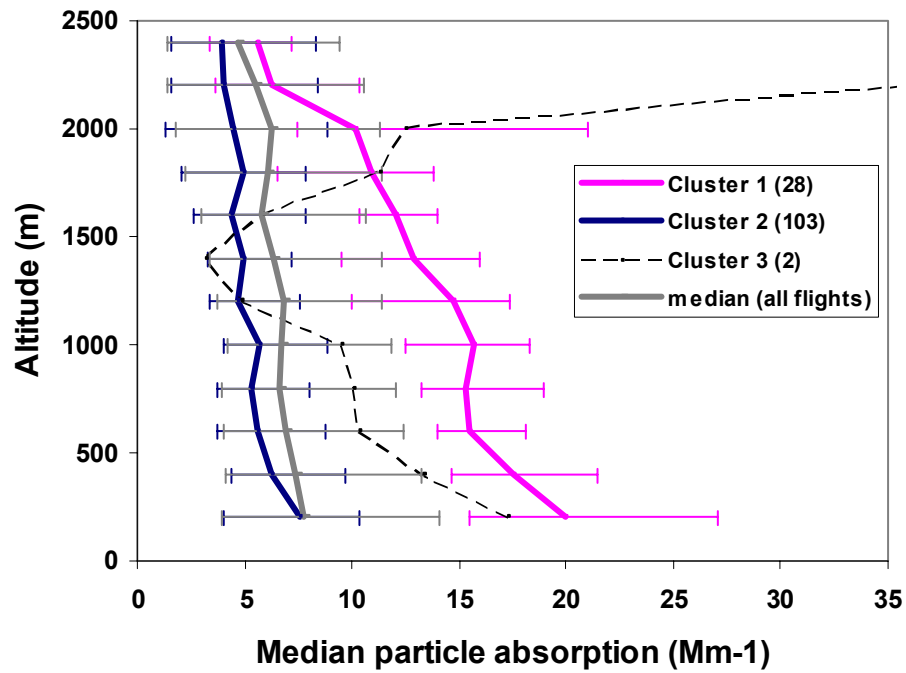
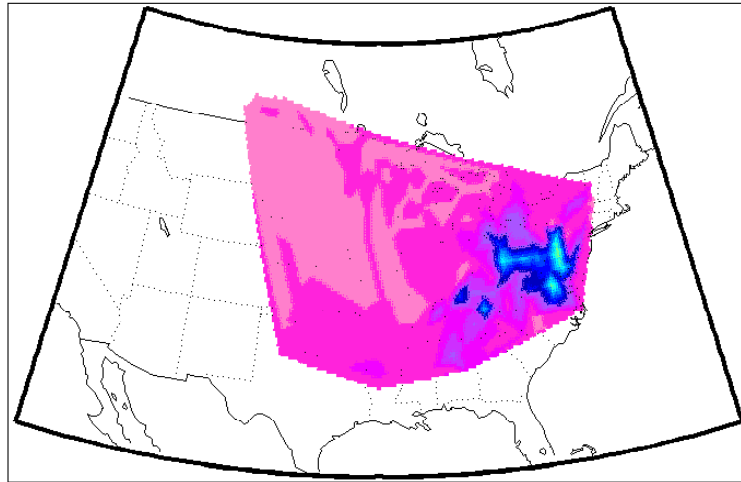


Figure 17. Median absorption profiles for each cluster. Error bars represent the 25th and 75th percentiles. The number of profiles in each cluster is shown in parentheses in the key. Absorption values in Cluster 1 are double those in cluster 2 below 1200 m. Profiles in Cluster 3 were made when Canadian forest fires impacted the region.

Cluster 1



Cluster 2

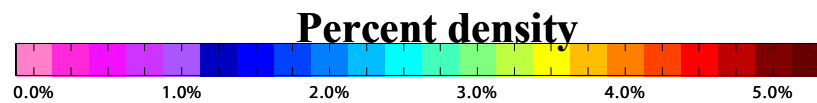
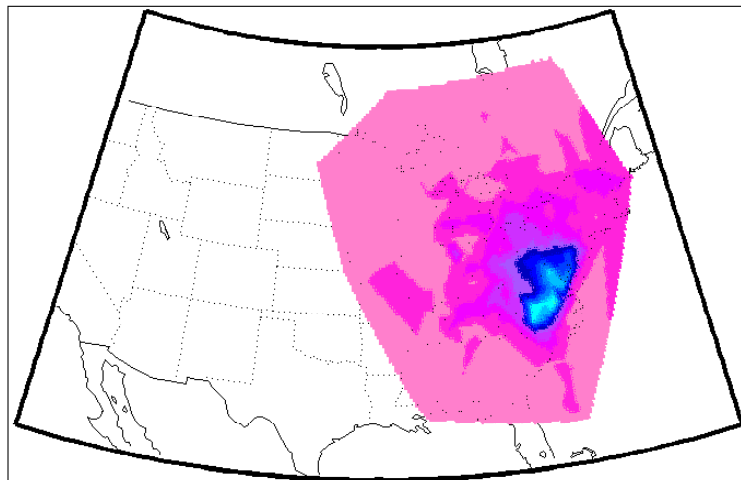


Figure 18. Back trajectory density plots for absorption Clusters 1 and 2. The back trajectory densities for clusters both show northwesterly winds, however, Cluster 1 winds are slightly faster. These faster back trajectories associated with Cluster 1 may bring in air from the industrialized Midwest to mix with local, mobile emissions.

4.3 Discussion

In order to better understand the chemistry associated with each O₃ cluster, the median profiles for SO₂, particle scattering and CO measured simultaneously with the O₃ profiles from each of the clusters (herein referred to as matching species profiles) were examined (Figure 19). The clusters with the least O₃ (Clusters 1 and 2) are associated with the least SO₂ and scattering particles, while the clusters with more O₃ (Clusters 3 and 4) are associated with the most SO₂ and scattering particles (measurements of scattering and SO₂ were not made for Cluster 5). The SO₂/CO ratio (Table 2) was also used to determine whether mobile or point source pollution was most influential on the O₃ values. The larger SO₂/CO ratio for Clusters 3 and 4, with large O₃ values, suggests that these clusters were impacted most by point source emissions. CO profiles were similar for Clusters 1-4, but very large CO was measured in Cluster 5 (only one CO profile was measured for this small cluster), suggesting that localized pollution from mobile sources may affect these profiles.

Matching species profiles for O₃ clusters

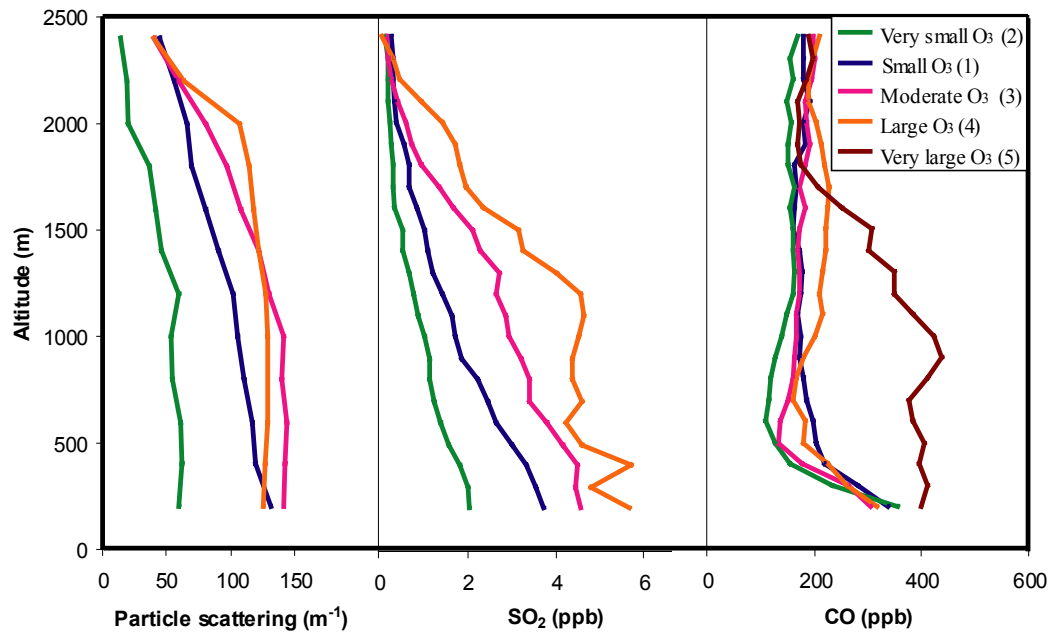


Figure 19. Matching species profiles for O₃ clusters. The O₃ cluster number is in parentheses in the key. Profiles with the smallest O₃ values are associated with the smallest scattering and SO₂ values, while profiles with larger O₃ values are associated with more SO₂ and scattering. The profile with the largest O₃ is associated with the most CO, suggesting that this cluster was influenced by mobile sources.

Table 2. SO₂/CO ratios for O₃ Clusters 1-4. Clusters 3 and 4, with large O₃ values also have large SO₂/CO ratios, suggesting that they are most heavily influenced by point source emissions.

Cluster	SO₂/CO ratio	n
1	0.010528	38
2	0.005548	18
3	0.014472	25
4	0.019471	10

Median matching profiles of SO₂, O₃ and α were examined for the scattering clusters (Figure 20). Cluster 2, with the most scattering particles, was also associated with the most O₃ and SO₂, as well as the largest particles (small α values). This suggests that days with more aerosol pollution are often associated with conditions conducive to O₃ production and is consistent with the idea the NO_x from elevated sources is more effective at producing O₃ than NO_x from mobile sources.

Matching species profiles for particle scattering clusters

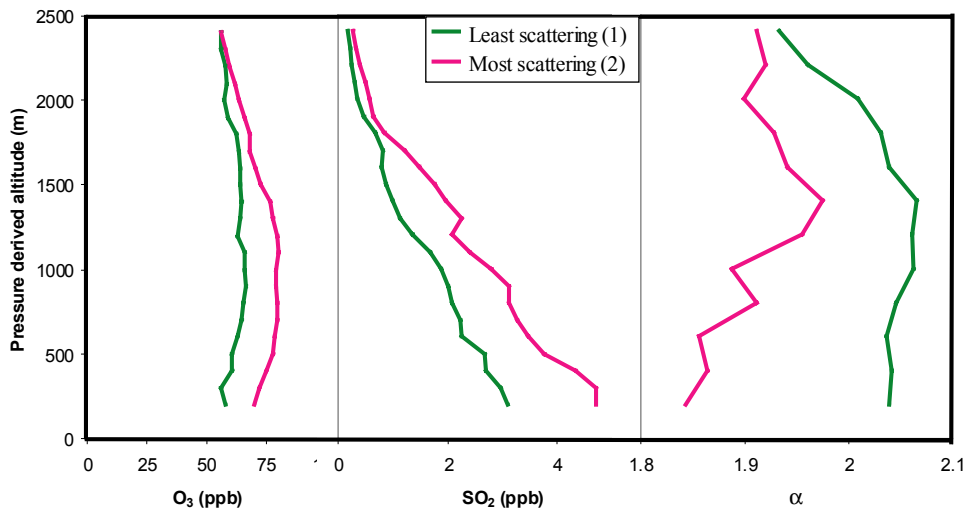


Figure 20. Matching species profiles for particle scattering clusters. Profiles with the most particle scattering are associated with the most O₃ and SO₂ as well as the largest particles (smallest α values).

Median matching species of CO were examined for the absorption clusters (Figure 21). Cluster 1 profiles, that are twice as absorbing as Cluster 2 profiles, have matching species profiles of CO that are on average 30% larger. This relationship between absorption and CO suggests that increased levels of absorbing species are likely the result of mobile emissions.

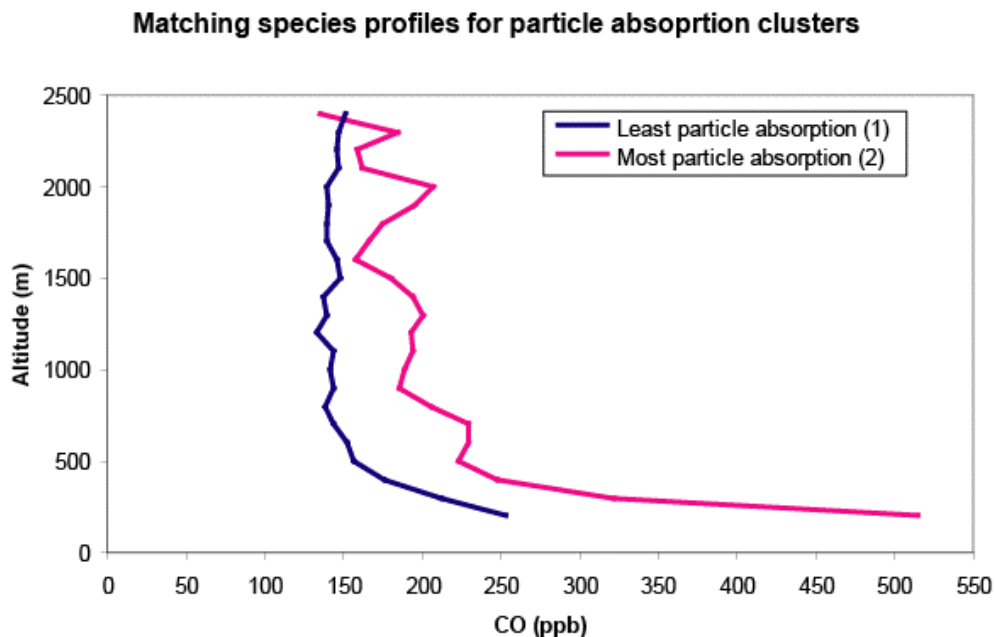


Figure 21. Matching species profiles for particle absorption clusters. The profile with the most particle absorption is associated with the most CO.

4.4 Conclusions

Clustering profiles of species allows for separation of distinct pollution events from a large collection of profiles, enabling a better understanding of how meteorology and chemistry affect the shape and size of the profiles. Profiles with the largest O₃ values were associated with larger integrated NO_x emissions from point sources. The clustering methodology also separated profiles affected by Canadian forest fires. SO₂ profiles were less influenced by regional emissions than local emissions. The amount of SO₂ emitted into an air parcel over the previous 48 hours did not correlate well with observed SO₂ values. The product of SO₂ oxidation, as evidenced by particle light scattering, does correlate with SO₂ emissions integrated

over the previous 48 hours. This suggests the sulfate lifetime is longer than 48 hours. Particle size, calculated using scattering values, shows a similar relationship to emissions as scattering. Profiles with the largest CO values were made downwind of urban regions, and so these profiles appear to be characteristic of local/mobile sources. Profiles with highly absorbing particles are likely representative of urban scale pollution and are strongly influenced by mobile sources because they are associated with increased CO concentrations.

Chapter 5: Comparisons of University of Maryland Aircraft and Trace Gas Profiles with Models CMAQ and GOCART

5.1 Introduction

5.1.1 Background

I compared O₃ measured aboard the University of Maryland Research aircraft in the summer of 2002 with the EPA Models-3 Community Multiscale Air Quality (CMAQ) modeling system. I examined differences among individual profiles as well as the statistical spread of all profiles. The standard CMAQ algorithm does not account for aerosols in the photochemistry of NO₂. A revised version of CMAQ was run to account for aerosol effects (typically found in the Mid-Atlantic US) on NO₂ photochemistry. I compared O₃ from the standard and revised model run and results are presented below. Emissions of NO_x are expected to be reduced by 2018 because of improved technology in motor vehicles and EPA imposed restrictions on power plant emissions. I have investigated how these reductions would be impacted by including aerosol effects in the photochemistry of NO₂ in CMAQ.

I compared SO₂ from the aircraft to CMAQ and the Georgia Tech/Goddard Global Ozone Chemistry Aerosol Radiation and Transport (GOCART) model output; both models over-predict the SO₂. This suggests the models assume a lifetime that is too long. A method for calculating the lifetime of SO₂ from *in-situ* measurements is described below as well as results from the calculation.

5.1.2 Description of Models

CMAQ uses the PSU/NCAR Mesoscale Model (MM5) for meteorological modeling. The MM5 uses a non-hydrostatic model with sigma coordinates that follow the terrain (<http://www.mmm.ucar.edu/mm5/>). CMAQ uses the Sparse Matrix Operator Kernel Emissions (SMOKE) to represent natural and anthropogenic emissions. There are four processors that account for chemistry in the model; these include the Meteorology-Chemistry Interface Processor (MCIP), the Photolysis rate processor (JPROC), the Initial Conditions Processor (ICON) and the Boundary Conditions Processor (BCON). Transport of emissions is modeled with the CMAQ Chemical Transport Model (CCTM). CMAQ has 172×172 grid cells and the size of each grid cell is $12 \text{ km} \times 12 \text{ km}$. There are 16 vertical layers in the lower tropospheric boundary layer from the surface to 3400 m. The temporal resolution is 1 hour.

The GOCART model uses assimilated meteorology from the Goddard Earth Observing System Data Assimilation System (GEOS-DAS; Schubert *et al.*, 1993). This is an online model which allows for daily results to be compared with measurements. GOCART has a spatial resolution of 2° latitude by 2.5° longitude. The GEOS DAS meteorological data uses 30 vertical layers from the surface to 80 km and 7 layers between the surface and 1.8 km. GOCART has a temporal resolution of 6 hours and calculates three dimensional SO_2 , dimethylsulfide, sulfate and methanesulfonic acid. Anthropogenic emissions used in GOCART emissions are from the Emission Database for Global Atmospheric Research (EDGAR) and include DMS from the ocean, SO_2 and sulfate from anthropogenic sources, SO_2 from biomass

burning, aircraft, and volcanoes. The anthropogenic emissions include industrial processes (81%), residential and commercial fuel consumption (12%), and transportation (road, rail, shipping, 7%), with an annual rate of 72.8 Tg S yr⁻¹. Anthropogenic emission rates over the United States are assumed constant for the year for the US (Chin et al., 2000a).

Chemical reactions for SO₂ in the GOCART model include oxidation by OH in air and H₂O₂ in cloud to form sulfate. It is assumed that H₂O₂ is regenerated to prescribed values every 3 hours. Dry deposition is represented as a function of aerodynamic resistance, sublayer resistance, and surface resistance. Dry deposition velocities of SO₂ over land are usually 0.2-0.4 cm s⁻¹. In-cloud and below-cloud precipitation are also accounted for (Chin et al., 2000a).

I compared CMAQ trace gases from the lowest 16 layers (around 10, 24, 68, 116, 185, 282, 398, 544, 727, 949, 1212, 1523, 1886, 2312, 2820, 3393 m above ground level) of the model to aircraft measurements made in 2002. The CMAQ layers were converted to meters above sea level, by adding the surface elevation of each grid point. The model output was extracted at the location and time closest to the aircraft measurements. SO₂ was interpolated in altitude and time to match aircraft measurements. The same extraction process was performed for CMAQ O₃.

The resolution of GOCART SO₂ is 2° latitude by 2.5° longitude, with the first seven altitude layers around 118, 223, 377, 590, 880, 1265, 1768 m above ground level for the Mid-Atlantic US for June-August. GOCART has a 6 hour temporal resolution at 6, 12, 18, and 24 UT. Aircraft SO₂ profiles measured within the latitude longitude box and within the 6 hour time period were compared with GOCART SO₂.

Generally, only one aircraft profile was compared with GOCART model output (70% of the time) although in some cases, up to five aircraft profiles were averaged.

5.2 Comparisons Between Models and Measurements

5.2.1 O₃ Comparisons

Figure 1 shows the median aircraft measured and CMAQ O₃ profiles with the 25th and 75th percentiles for 136 profiles made in 2002. CMAQ is 10% (~6 ppb) smaller than aircraft O₃ between 600 and 2600 m. The ratio of the CMAQ/Aircraft O₃ mixing ratio is shown in Figure 2 and this shows that CMAQ under-predicts O₃ above 600 m and over-predicts O₃ below 600m. The CMAQ O₃ column content is 3% smaller than the aircraft column content (Table 1).

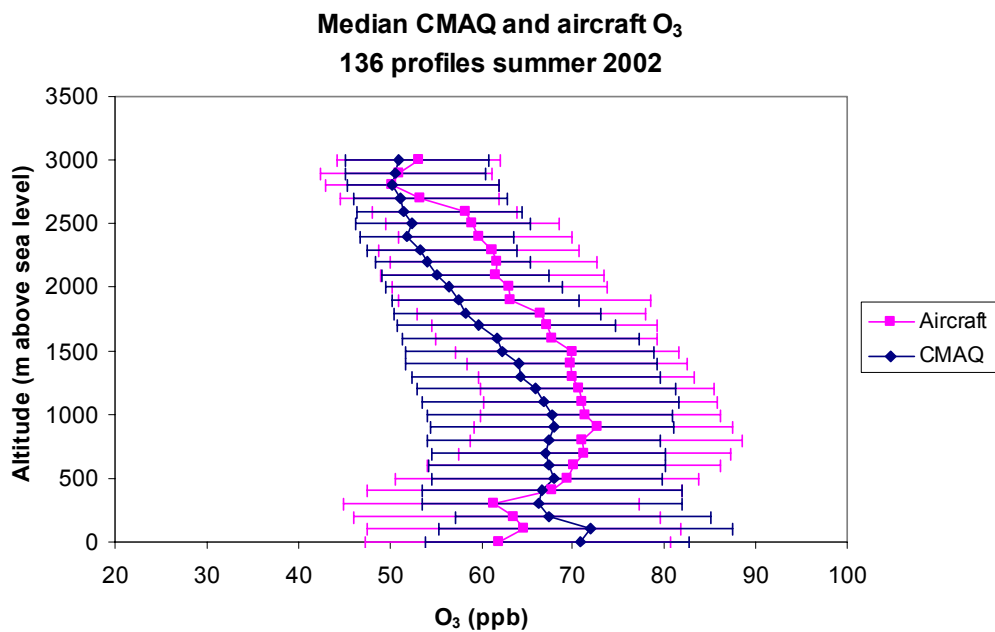


Figure 1. Median CMAQ and aircraft O₃ profiles from 2002 (June –August). The median was obtained from 136 profiles. The error bars represent the 25th and 75th percentiles. Though the error bars overlap, CMAQ under-predicts O₃ by 10% between 600 and 2600m.

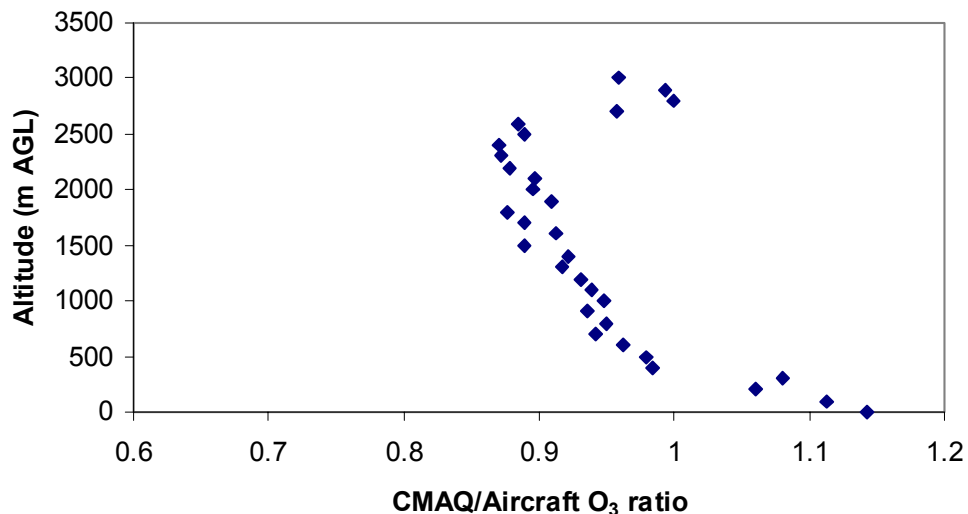


Figure 2. The ratio of CMAQ/Aircraft O₃ as a function of altitude. Below 600 m CMAQ over-predicts O₃, above 600 m CMAQ under-predicts O₃.

Column content (g m ⁻²)	Aircraft	CMAQ
average	0.29	0.28

Table 1. CMAQ and aircraft O₃ column contents calculated from near the surface (~3 m above ground level) to the top of the aircraft spiral (~ 2500 m). The CMAQ column content is 3% smaller than the aircraft column content.

I also compared individual profiles to better understand the relationship between aircraft and CMAQ profiles. I have developed a method to look at these profiles in an objective manner by sorting the differences (between profiles) into three categories, the smallest, median and largest differences. This method is described below.

The differences between aircraft and model profiles were calculated accounting for shape (location of minima and maxima in the profiles) as well as size (absolute differences in mixing ratio). All aircraft spirals and matching CMAQ modeled outputs were initially averaged into 100 m altitude levels. This allowed for consistent comparisons between each pair of modeled and measured O₃ profiles. The difference between modeled and measured O₃ at each altitude bin accounted for the size. The profiles were examined at four altitude bins (250 – 650 m, 651-1150 m, 1151-1650 m, and 1651-2150 m). In each altitude bin there were at least five altitude layers examined. A linear regression was made between the O₃ mixing ratios of the two profiles being compared at these altitude layers. The slope and correlation coefficient were used to account for the shapes of the profiles being compared. The difference equation from Chapter 4 (Equation 2) was used.

The differences were sorted and profiles associated with three of the 5th percentile (smallest) differences, three of the median differences and three of the 95th percentile (largest) differences were examined. Figure 3 shows the three modeled and measured profiles with the 5th percentile smallest differences. I examined profiles in the grid cell closest to where the airplane flew (the center cell) as well as the profiles in the 8 grid cells surrounding this center cell. Figure 3 shows the CMAQ profiles associated with the center cell in dark blue as well as the smallest and largest profiles from the surrounding grid cells. There are some jumps in the CMAQ profiles as shown for the Louisa, VA profile at 1200 m. The aircraft profiles have a diameter of about 1 km, and sometimes they crossed two different CMAQ grid cells. CMAQ O₃ for the closest grid cell was used for the difference calculation and sometimes

more than one grid cell was used in a profile. Figure 4 shows three of the modeled and measured profiles with median differences. The differences between profiles were calculated between 250 and 2150 m and the portions of the profile not included in this calculation are shown in grey. On July 8, 2002 Canadian forest fires impacted the region, and the aircraft profile over Easton, MD shows the signature peak of O₃ above 2200 m. Below the forest fire peak the aircraft profile compared reasonably well with CMAQ O₃. This example presents a limitation of the difference method. Figure 5 shows three of the modeled and measured profiles with the 95th percentile largest differences. The comparison of CMAQ and aircraft O₃ over Winchester, VA shows that the model does not always under-predict O₃ aloft. The differences between profiles seem to be independent of altitude and the shape of the profiles. Also shown in Figures 3-5 are the 24 hour back trajectories ending at the location of the aircraft spiral (at 1000, 2000, and 3000 m) for each of the CMAQ-aircraft comparisons. The differences between profiles also seem to be independent of wind speed and direction (from back trajectories).

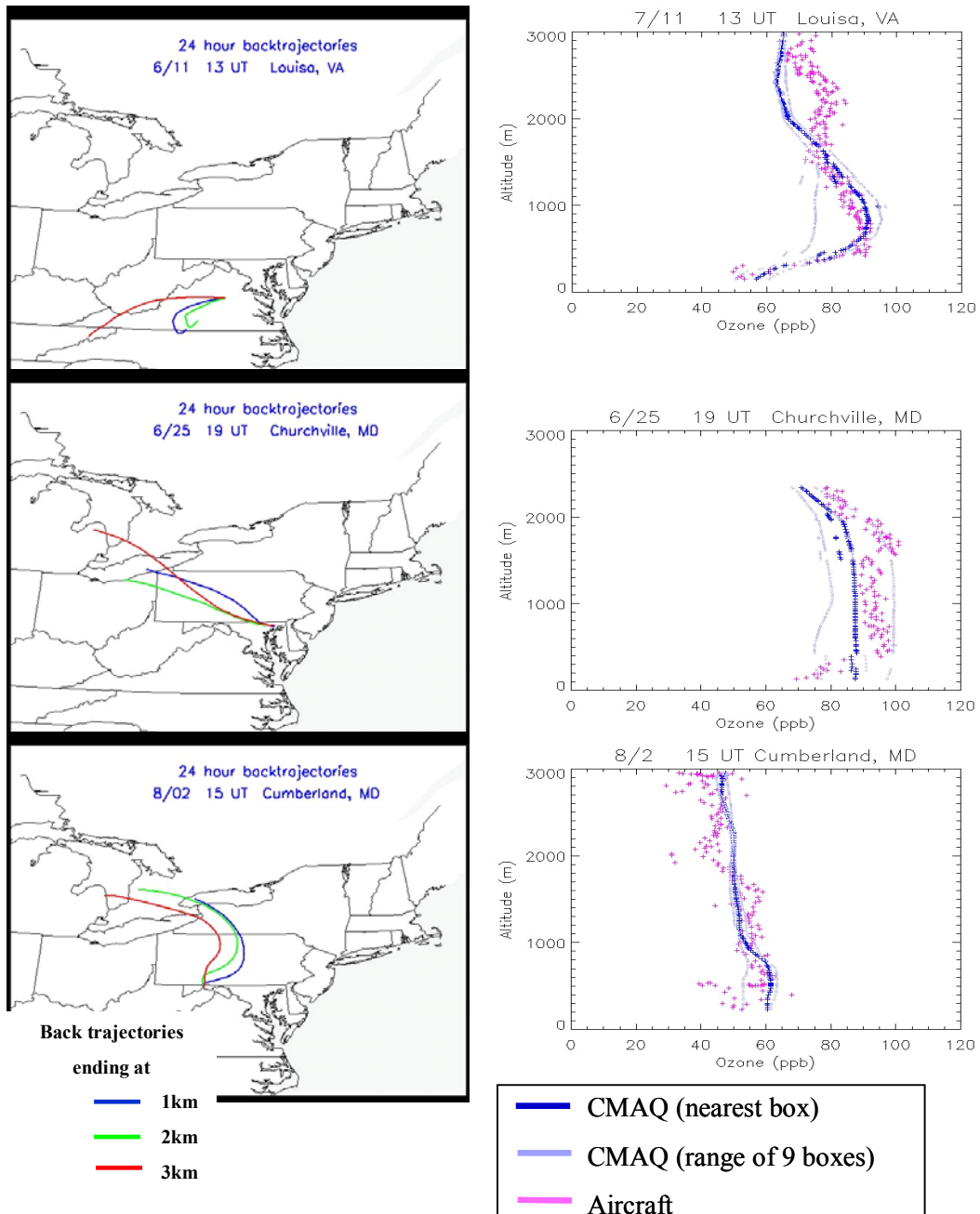


Figure 3. CMAQ and aircraft O₃ profiles associated with the 5th percentile smallest differences (the best agreement). The dark blue profiles represent CMAQ O₃ from the closest (center) grid cell. The light blue profiles represent the smallest and largest O₃ from the surrounding 8 grid cells. There are some jumps in the Louisa, VA CMAQ profile. The aircraft profiles have a diameter of about 1 km, and sometimes they crossed two different CMAQ grid cells. CMAQ O₃ for the closest grid cell was used in the difference calculation and sometimes more than one grid cell was used in a profile. Back trajectories at three altitudes are also shown.

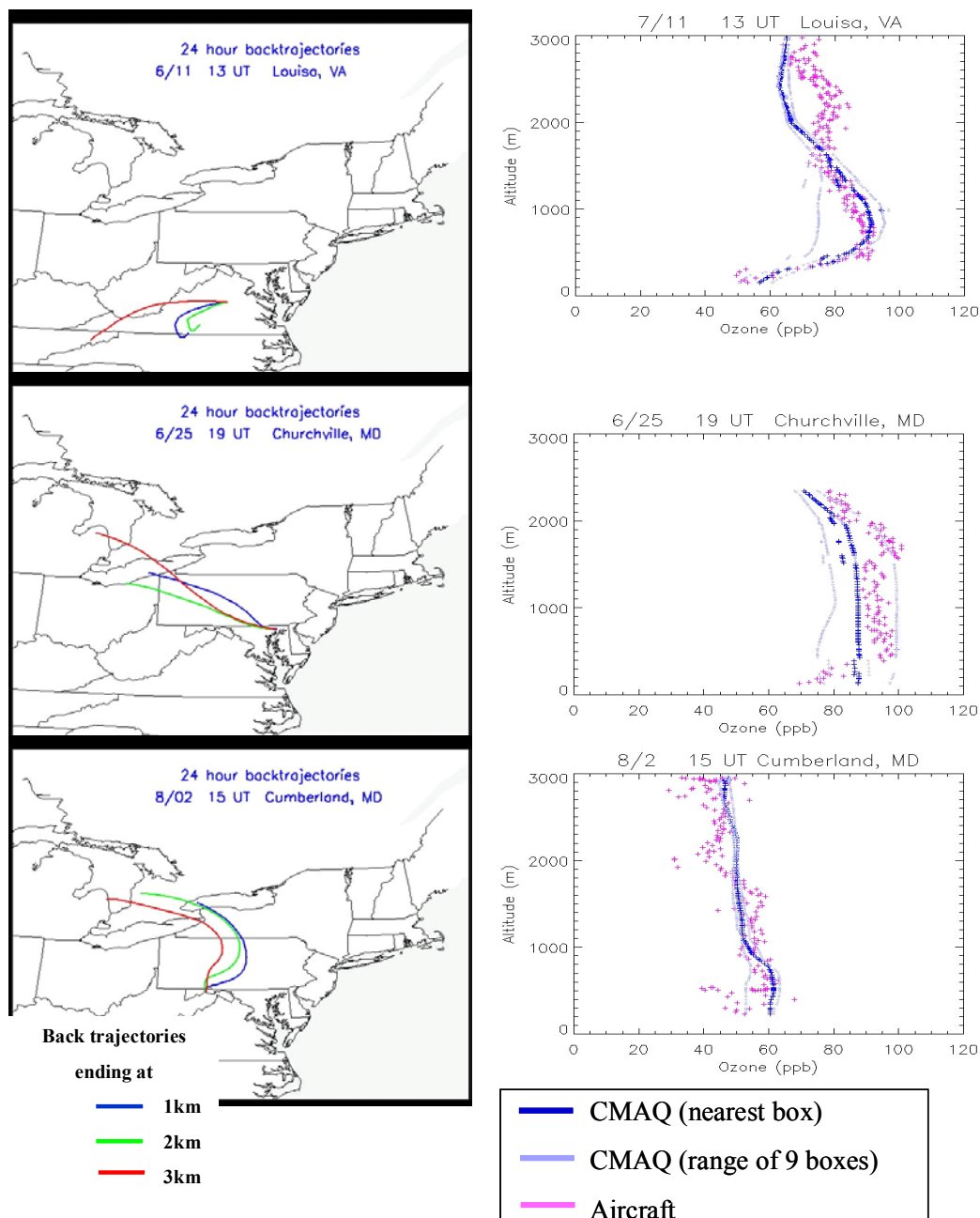


Figure 4. CMAQ and aircraft O₃ profiles associated with the median differences. The dark blue profiles represent CMAQ O₃ from the closest (center) grid cell. The light blue profiles represent the smallest and largest O₃ from the surrounding 8 grid cells. Canadian forest fires impacted the region on July 8, and this is seen in the aircraft O₃ profile over Easton. The differences were calculated between 250 and 2150 m and so the influence of the fires was not accounted for in the equation. This shows a limitation of the method.

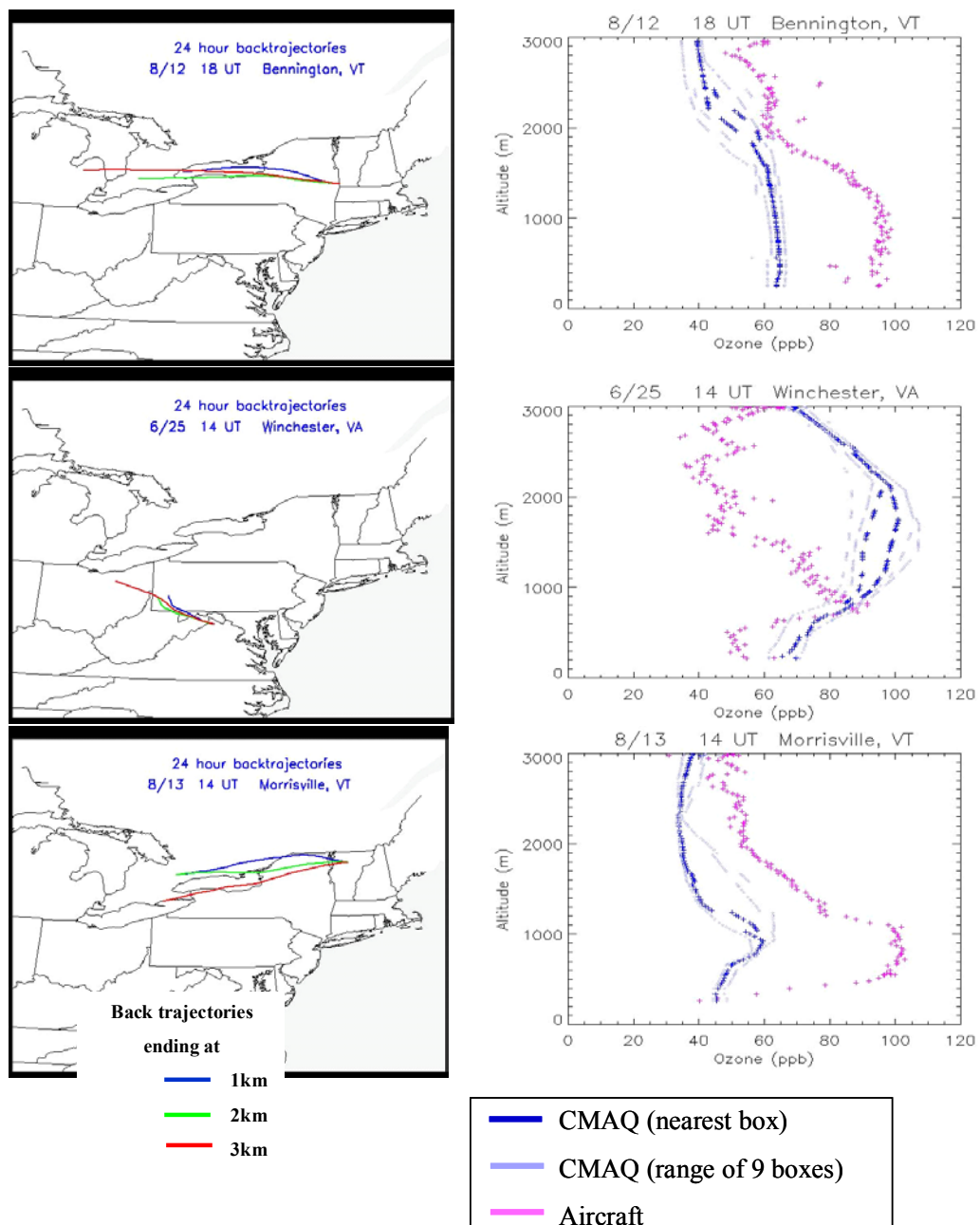


Figure 5. CMAQ and aircraft O₃ profiles associated with the 95th percentile largest differences (the worst agreement). The dark blue profiles represent CMAQ O₃ from the closest (center) grid cell. The light blue profiles represent the smallest and largest O₃ from the surrounding 8 grid cells. The comparison at Winchester shows that CMAQ sometimes over-predicts O₃ aloft.

5.2.2 The Effects of Aerosols on the Photolysis Rate of NO₂ and the Production of O₃

In general CMAQ under-predicts O₃ aloft. Reasons for this under-prediction include problems with emissions inventories as well as problems with meteorology, cloud cover, and CMAQ's ability to describe transport. The NO₂ photolysis rates that CMAQ uses also impact how much O₃ is produced by the model. The reaction rate coefficient for the photolysis of NO₂ (hereafter referred to as j-NO₂ value) used by the standard version of CMAQ assumes no aerosol loading. Dickerson et al. (1997) show that an increase of aerosols from an optical depth of 0 to 2 increases the j-NO₂ values by 30% above the boundary layer (1000 m). Park (2001) performed a sensitivity test of CMAQ using j-NO₂ values associated with CMAQ aerosols. He used the aerosol properties generated by CMAQ to develop a program to modify the j-NO₂ values accordingly, and then compared the O₃ generated with the modified CMAQ run to surface measurements. He found that the effects on O₃ production were variable, and there were still numerous disagreements between modeled and measured O₃.

Aerosols generated with CMAQ are often under-predicted (Mebust et al., 2003; Mueller et al., 2006; Tesche et al., 2006) and this may partly explain the mixed results Park (2001) found. I performed a sensitivity study using j-NO₂ values associated with typical aerosols measured in the Mid-Atlantic from July 15-18, 2002 using the Park (2001) program that allows for adjustment of the Angstrom slope and intercept defined in the Angstrom equation:

$$\tau = \beta \lambda^{-\alpha} \quad (1)$$

Here, τ is the aerosol optical depth, α is the Angstrom slope (Angstrom exponent) that represents the size of aerosols, λ is the wavelength in μm , and β is the intercept related to the amount of aerosols present in the atmosphere. The Angstrom coefficient intercept can be assigned a value of 0, 0.1, 0.2, 0.3, 0.4, or 0.5. The Angstrom coefficient slope can be assigned a value between 0.5, 1.0, 1.5, 2.0, or 2.5. Figure 6 shows the median of Angstrom exponent measurements made during July 15-18, 2002 for 20 aircraft profiles. Of the values allowed in the Park (2001) model, the median Angstrom exponent (Angstrom slope) is closest to 2.0. The Park (2001) model also allows for the adjustment of single scattering albedo, asymmetry parameter and aerosol layer depth.

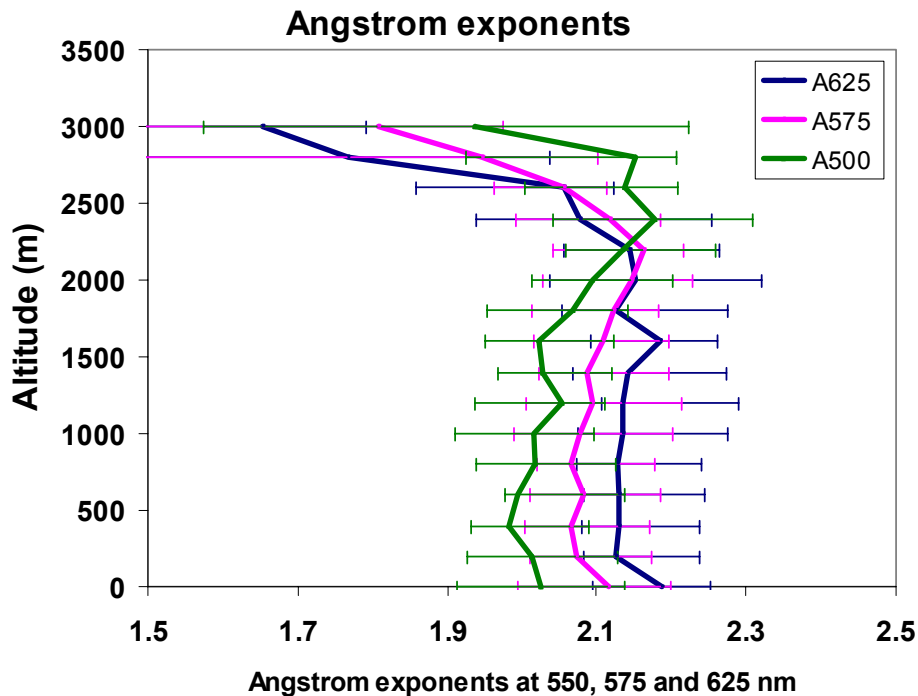


Figure 6. The median Angstrom exponent calculated with the ratio of scattering at 450 and 550 nm (A500), 450 and 700 nm (A575), and 550 and 700 nm (A625) for flights made between July 15-18, 2002. The error bars represent the 25th and 75th percentile. The Angstrom exponent measured aboard the aircraft is closest to the 2.0 input for the Park (2001) model.

	Aerosol optical depth	
	550 nm	380 nm
average	0.31	0.68
median	0.28	0.63
minimum	0.12	0.26
maximum	0.66	1.41

Table 2. Statistics for aerosol optical depth calculated at 550 nm and 380 nm for 17 flights made between July 15-18, 2002.

Table 2 shows that the average optical depth at 550 nm is 0.31. Because the photolysis of NO₂ occurs at wavelengths of 380 nm and not at wavelengths of 550 nm (where the aircraft made measurements), I interpolated the aerosol properties to the 380 nm wavelength. The absorption coefficient (*abs*, with units of m⁻¹) can be approximated at different wavelengths, λ , using the relationship (from Bodhaine, 1995):

$$abs = c_a/\lambda \quad (2)$$

Here c_a is a constant. From Equation 2, abs_{380} can be solved using:

$$abs_{380} = abs_{550} \times 550/380 \quad (3)$$

I also converted the scattering coefficient (with units of m⁻¹) at 550 nm to the scattering coefficient at 380 nm, $scat_{380}$, using the relationship (from Bodhaine, 1995):

$$Scat_{550} = c_s/550^{A_{550}} \quad (4)$$

$$Scat_{380} = c_s/380^{A_{380}} \quad (5)$$

Here c_s is a constant. From Equation 5, $scat_{380}$ can be solved using:

$$Scat_{380} = Scat_{550} * 550^{A_{550}}/380^{A_{380}} \quad (6)$$

Here A_{550} represents the Angstrom exponent calculated from the ratio of scattering measurements at two different wavelengths (as shown in Equation 2 in Chapter 3) where the average wavelength is 550 nm. A_{380} is just the Angstrom exponent calculated from the ratio of scattering at two different wavelengths where the average wavelength is 380 nm. Figure 6 shows the Angstrom exponent calculated from the ratio of scattering at 450 and 550 nm (A_{500}), 450 and 700 nm (A_{575}), and 550 and 700 nm (A_{600}). There is little variability among the Angstrom exponents calculated from different wavelength ratios and so I assumed that A_{550} and A_{380} (from Equation 6) are equal. I then calculated aerosol optical depth at 380 nm (Table 2). Using the optical depth at 380 nm or 550 nm in Equation 1, results in an Angstrom intercept closest to 0.1. The Park (2001) model allows values of single scattering albedo of 0.92, 0.96 and 1.0. Figure 7 shows the median profile for single scattering albedo at 550 nm measured during July 15-18, 2002 and composed of 17 profiles. For the values allowed in the Park (2001) model the median single scattering albedo is closest to 0.96.

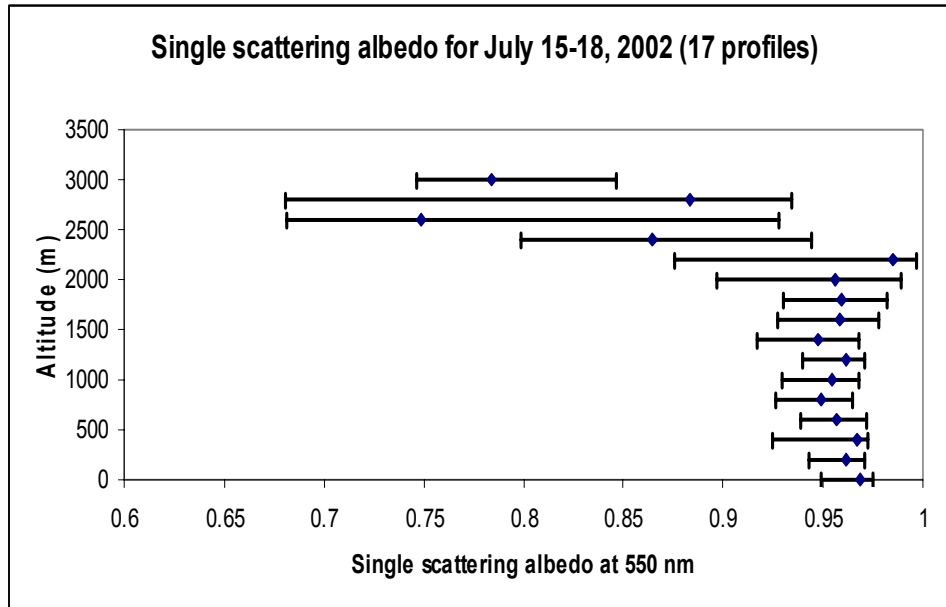


Figure 7. The median single scattering albedo at 550 nm for flights made between July 15-18. The error bars represent the 25th and 75th percentile. The single scattering albedo measured aboard the aircraft is closest to the 0.96 input for the Park (2001) model

The model allows values of asymmetry parameter to be 0.6, 0.7, or 0.8. The asymmetry parameter is calculated from the backscatter to total scattering ratio using the equation

$$g = -2x + 1 \quad (7)$$

Where g is the asymmetry parameter and x is the backscatter to total scattering ratio. The aircraft did not make measurements of backscatter to total scattering in 2002, but measurements were made in 2003-2005. Figure 8 shows the asymmetry parameter for 139 flights measured in 2003-2005. For the values allowed in the Park (2001) model the median profile of asymmetry parameter is closest to 0.8. The Park (2001) model allows for aerosol layer depths to be 0.5, 1.5, or 2.5 km. Figures 1d and 1f in Chapter 3 show the median scattering and absorption profiles for all flights made in the Mid-Atlantic region. The depth of the aerosol layer for these profiles is closest to

1.5. These aerosol values were used in the Park (2001) model and the resultant j-NO₂ values are shown in Figure 9. Above 1000 m the j-NO₂ values calculated with aerosols were 25% larger than those with no aerosols.

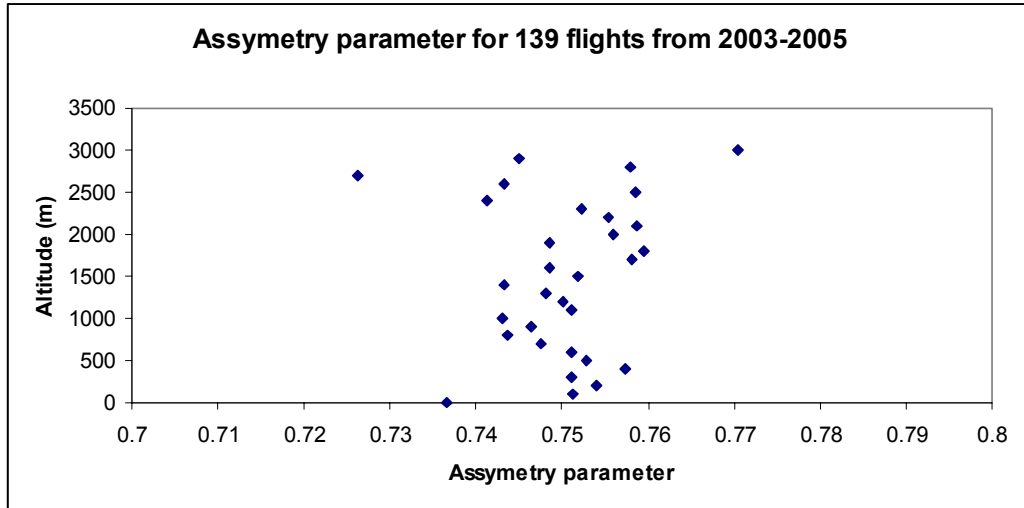


Figure 8. The median asymmetry parameter at 550 nm for 139 flights made between 2003 and 2005. The error bars represent the 25th and 75th percentile. The asymmetry parameter measured aboard the aircraft is closest to the 0.8 input for the revised CMAQ run.

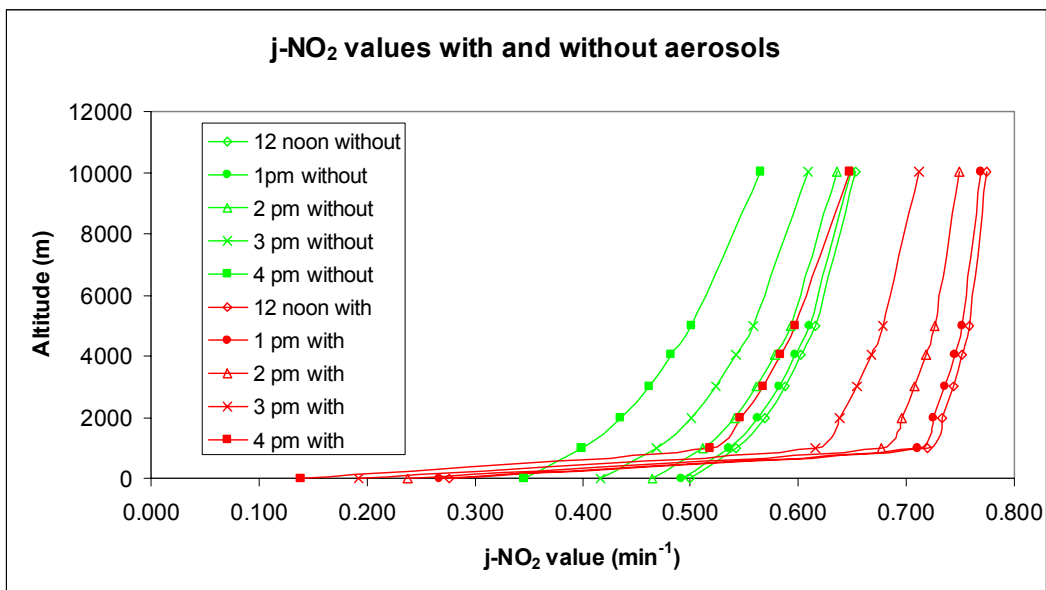


Figure 9. Standard and revised $j\text{-NO}_2$ values used in CMAQ (at 0, 1, 2, 3, 4.05, 5 and 10 km). The standard $j\text{-NO}_2$ values assume there are no aerosols (without) and the revised $j\text{-NO}_2$ values (with) were calculated using aerosol properties presented in Figures 6,7 and 8 and Table 2. The different symbols represent the $j\text{-NO}_2$ values at different times of the day.

I ran CMAQ from July 15-18, 2002 with the standard $j\text{-NO}_2$ values (assuming no aerosol) and revised $j\text{-NO}_2$ values (assuming aerosol typical for the episode). The same aerosol values were used throughout the domain. The aircraft flies downwind of urban and suburban areas with large optical depths, and also rural areas with small optical depths. Using the average optical depth from all of the flights should be a reasonable approximation of the Mid-Atlantic average optical depth. Levy (2007) found a correlation coefficient (r^2) of 0.26 between MODIS satellite retrievals and aircraft calculated aerosol optical depth. Two emissions scenarios were used; one with 2002 emissions and one with 2018 emissions that are substantially lower than those from 2002. This resulted in four model runs for comparison:

- 2002 emissions with standard j-NO₂ values (2002, standard)
- 2002 emissions with revised j-NO₂ values (2002, revised)
- 2018 emissions with standard j-NO₂ values (2018, standard)
- 2018 emissions with revised j-NO₂ values (2018, revised).

CMAQ O₃ values were generated during a previous run by the New York State Department of Environmental Quality (NYDEQ) using the standard j-NO₂ values. The NYDEQ runs used TOMS data to determine the stratospheric O₃ influence on radiative forcing and on boundary layer O₃ production. I did not have access to the TOMS data, so I performed the four runs using CMAQ default overhead O₃ (generated from Nicolet et al., 1982). The O₃ I generated from the CMAQ run using 2002 emissions and j-values with no aerosols correlated well with the NYDEQ runs using the same emissions and j-values (but different overhead O₃). However, the O₃ generated from my CMAQ run was up to 5 ppb smaller than that generated from the NYDEQ run. In order to make meaningful comparisons between aircraft O₃ and O₃ generated with the revised CMAQ run (2002, revised), I adjusted the CMAQ O₃ using the following:

$$O_3 \text{ (2002, revised)} = O_3 \text{ (NYDEQ)} * \frac{O_3 \text{ (2002, revised without TOMS O}_3\text{)}}{O_3 \text{ (2002, standard with TOMS O}_3\text{)}} \quad (8)$$

Figures 10a-e show O₃ generated by CMAQ using the standard j-NO₂ values, O₃ generated using the revised j-NO₂ values (adjusted using Equation 8) and O₃ from the aircraft. The revised CMAQ run generated more O₃ (~1 ppb) above 500 m than the standard run. The revised CMAQ run generated less O₃ (1-4 ppb) below 500 m than the standard run. The revised run did not eliminate measurement/model differences, but brought the CMAQ output closer to observations. Figures 10a-e are

limited in space because they only represent a few grid cells. Figure 11 shows the median differences in O₃ between revised and standard runs (revised CMAQ–standard CMAQ) for the 16 profiles. Table 3 compares the average O₃ column contents among the aircraft, standard CMAQ runs, and revised CMAQ runs for the July 15-18, 2002 episode. CMAQ O₃ column content from the standard and the revised runs were ~7% smaller than the aircraft O₃. The O₃ column content from the revised run was 0.3% larger than the O₃ column content from the standard run.

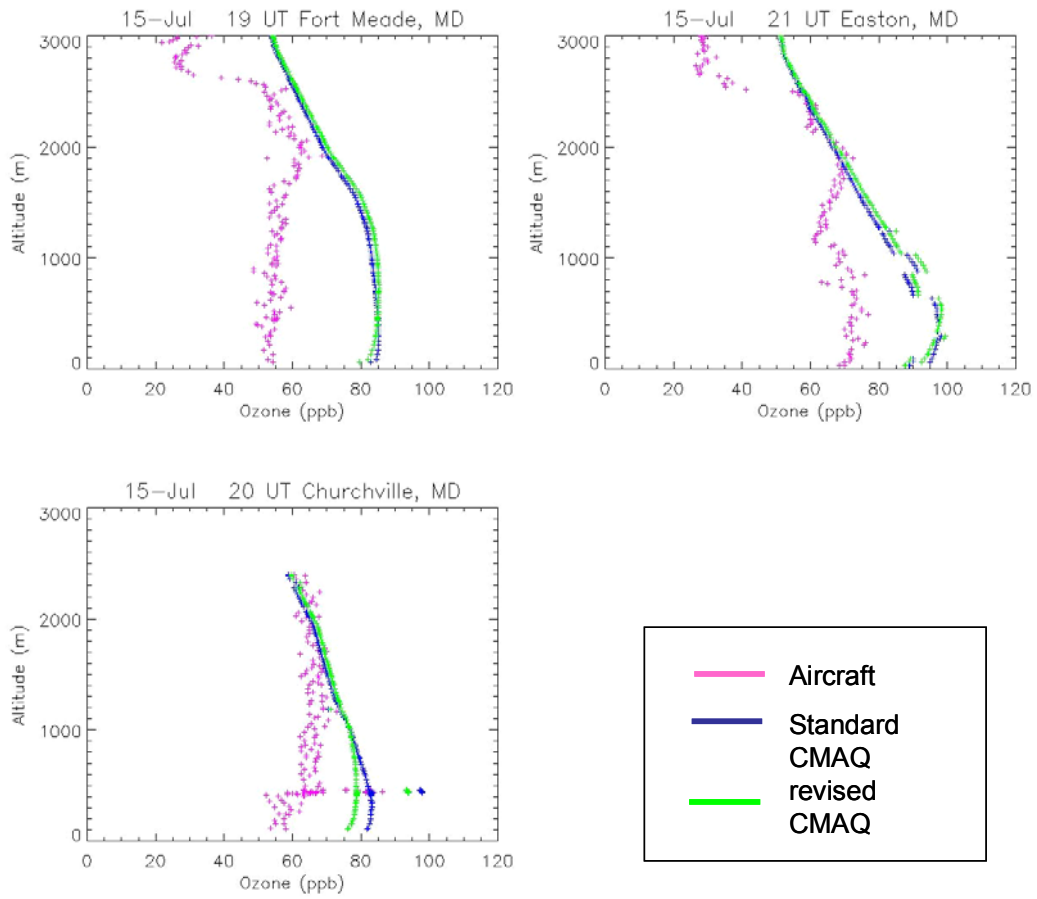


Figure 10a. O₃ profiles from the aircraft (pink), standard CMAQ runs (shown in blue), and revised CMAQ runs (shown in green) for July 15, 2002. Above 500 m the revised CMAQ profiles are about 1 ppb larger than the standard CMAQ profiles shown in blue. Below 500 m the revised CMAQ O₃ is smaller than the standard CMAQ O₃.

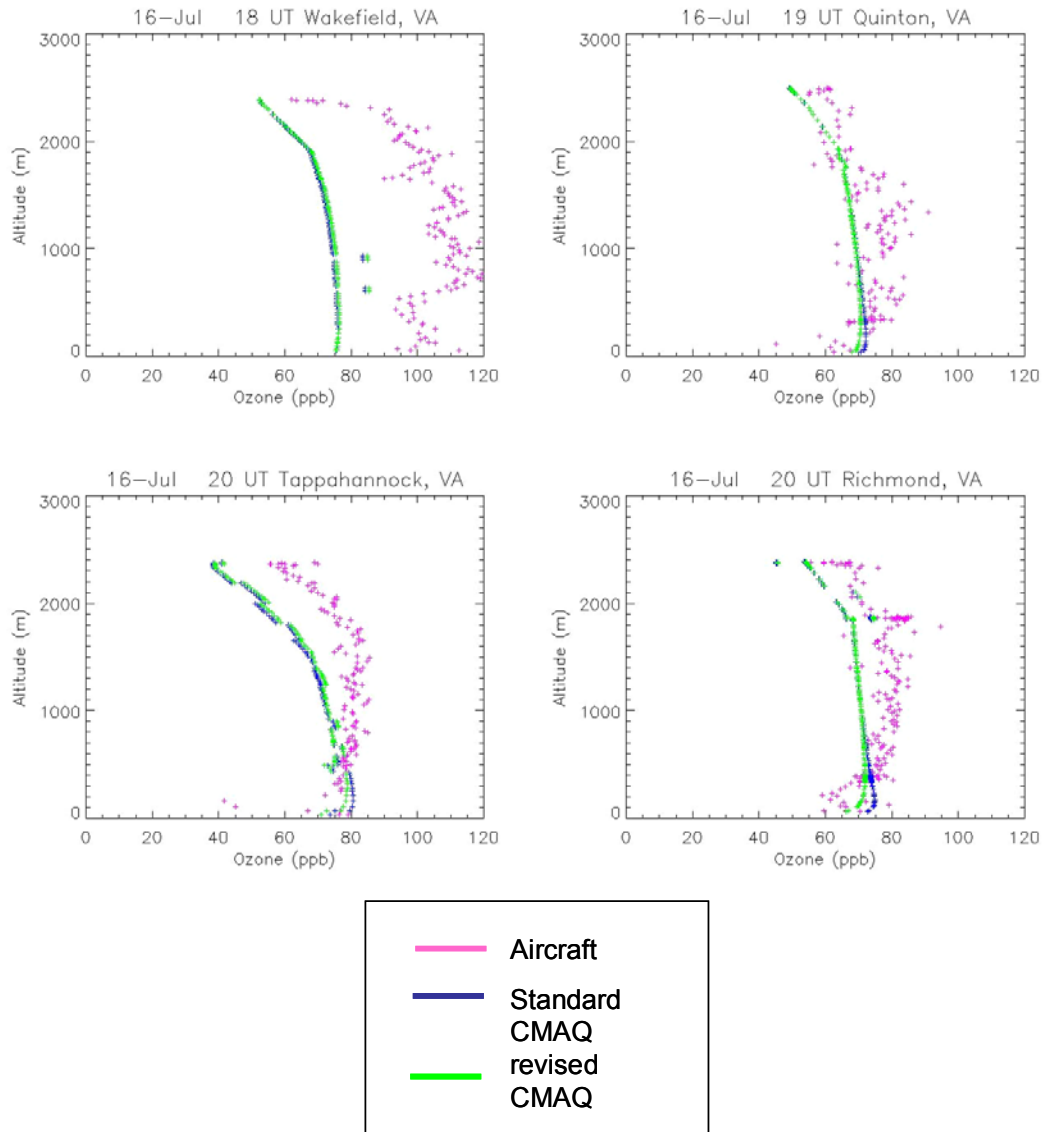


Figure 10b. O₃ profiles from the aircraft (pink), standard CMAQ runs (shown in blue), and revised CMAQ runs (shown in green) for the morning of July 16, 2002. Above 500 m the revised CMAQ profiles are about 1 ppb larger than the standard CMAQ profiles shown in blue. Below 500 m the revised CMAQ O₃ is smaller than the standard CMAQ O₃.

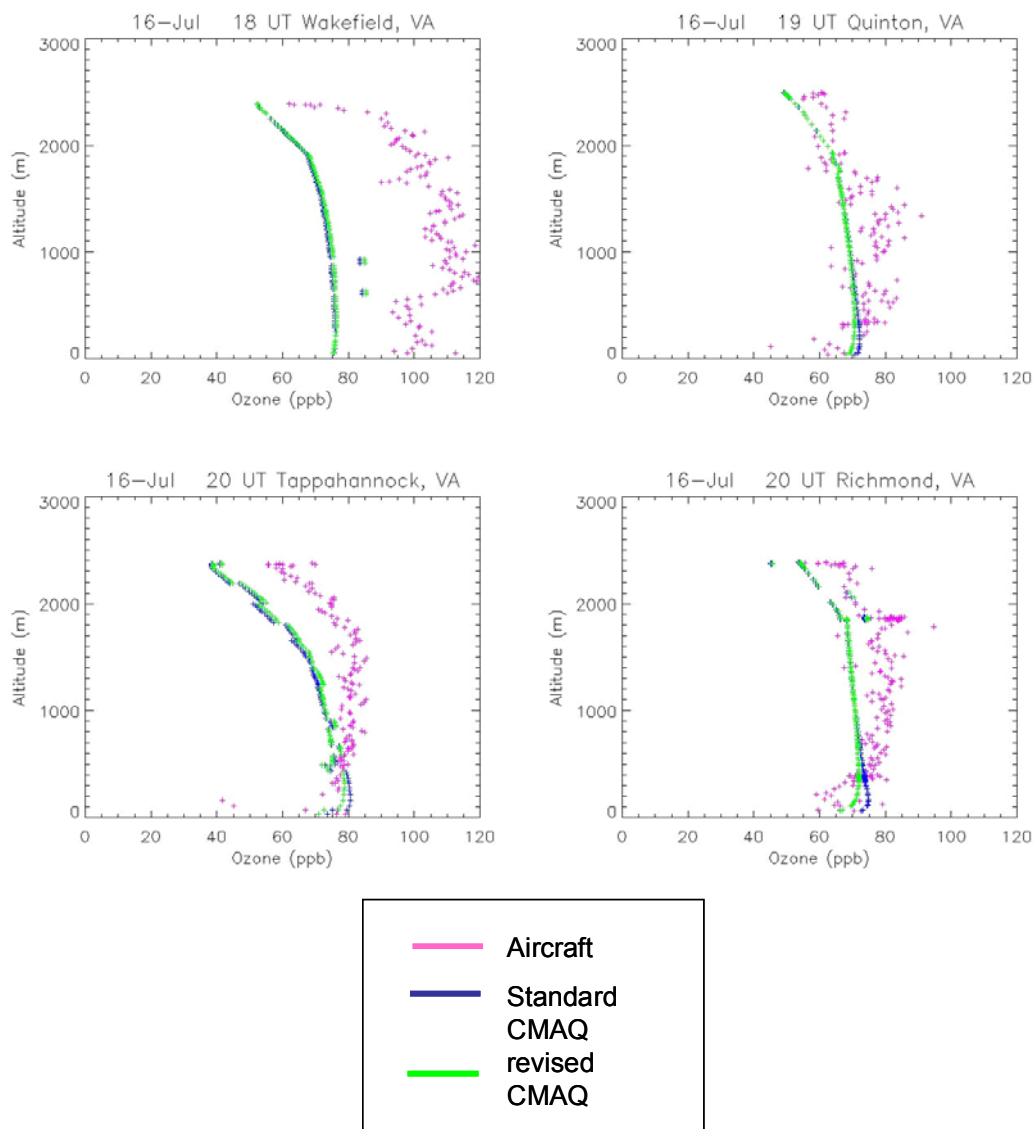


Figure 10c. O₃ profiles from the aircraft (pink), standard CMAQ runs (shown in blue), and revised CMAQ runs (shown in green) for the afternoon of July 16, 2002. Above 500 m the revised CMAQ profiles are about 1 ppb larger than the standard CMAQ profiles shown in blue. Below 500 m the revised CMAQ O₃ is smaller than the standard CMAQ O₃.

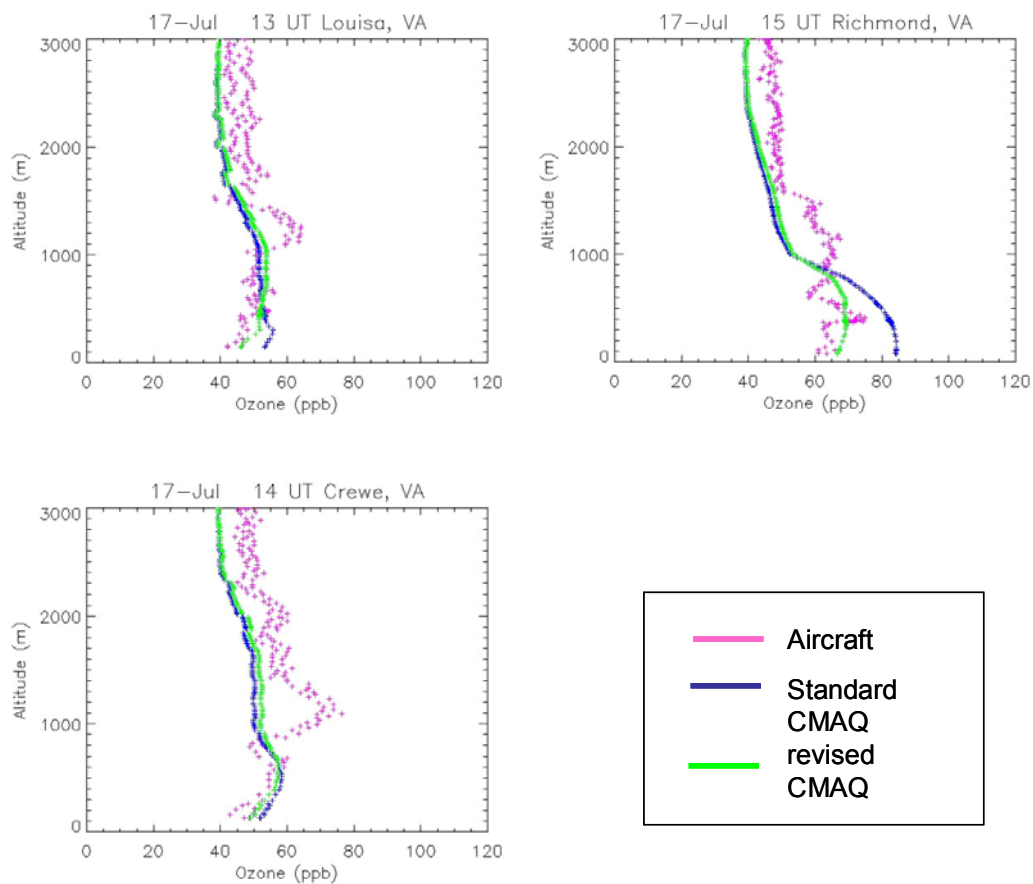


Figure 10d. O₃ profiles from the aircraft (pink), standard CMAQ runs (shown in blue), and revised CMAQ runs (shown in green) for July 17, 2002. Above 500 m the revised CMAQ profiles are about 1 ppb larger than the standard CMAQ profiles shown in blue. Below 500 m the revised CMAQ O₃ is smaller than the standard CMAQ O₃.

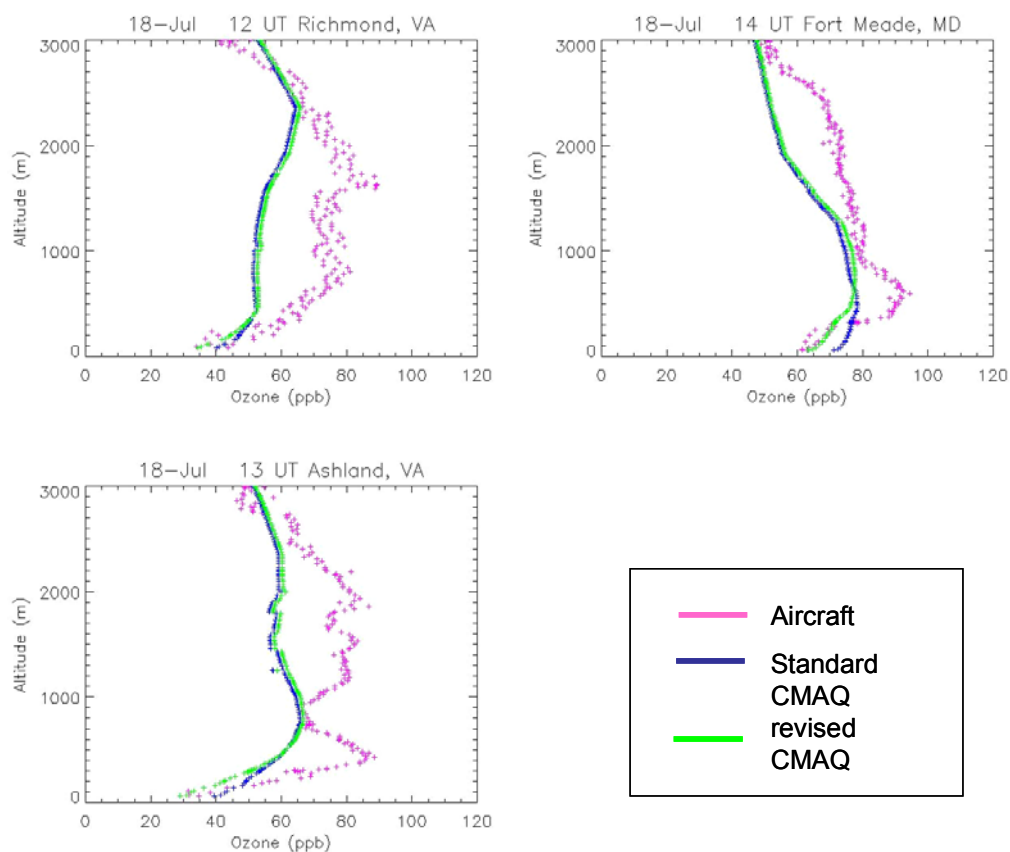


Figure 10e. O₃ profiles from the aircraft (pink), standard CMAQ runs (shown in blue), and revised CMAQ runs (shown in green) for July 18, 2002. Above 500 m the revised CMAQ profiles are about 1 ppb larger than the standard CMAQ profiles shown in blue. Below 500 m the revised CMAQ O₃ is smaller than the standard CMAQ O₃.

	Average O ₃ column content (g m ⁻²)
Aircraft	0.3093
CMAQ 2002 (standard run)	0.2885
CMAQ 2002 (revised run)	0.2888
CMAQ 2018 (standard run)	0.2561
CMAQ 2018 (revised run)	0.2555

Table 3. Median O₃ column contents for the July 15-18, 2002 episode (for locations sampled by the aircraft) from the aircraft, standard CMAQ 2002 run, revised CMAQ 2002 run, standard CMAQ 2018 run, and revised CMAQ 2018 run.

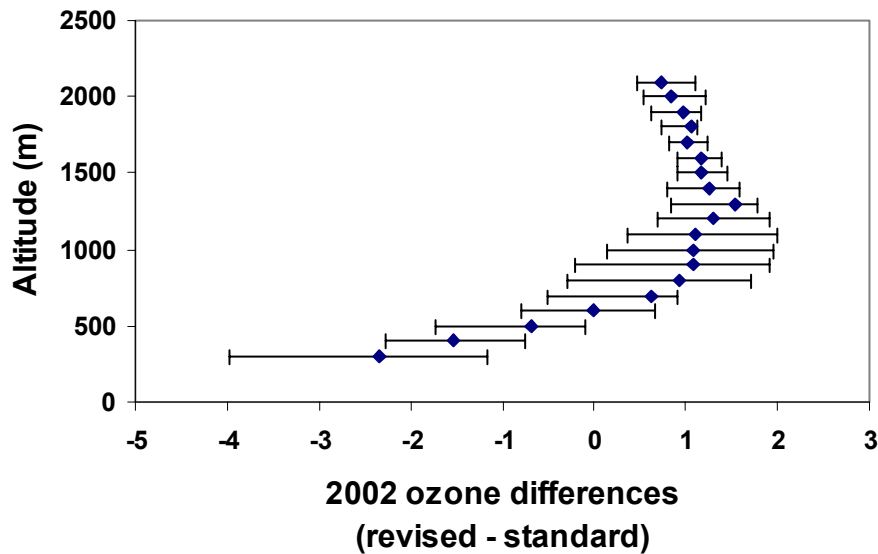


Figure 11. Median CMAQ O₃ differences (standard – revised) for 16 profiles generated between July 15-18, 2002. Error bars represent the 25th and 75th percentiles. Near the surface the revised CMAQ run generates less O₃ than the standard CMAQ run. Above 500 m the revised CMAQ run generates more O₃ than the standard run.

Figure 12 shows the difference between revised CMAQ and standard CMAQ runs for three different levels (1, 8, and 16 that are approximately at the surface, 500, and 2000m) for the Eastern US at 14 UT and 18 UT. The largest O₃ production generally occurs within these times. Here negative values, when the revised CMAQ run generates less O₃ than the standard CMAQ run, are shown with cooler colors. These differences, of up to 10 ppb, are seen mainly at the surface. Positive values, when the revised CMAQ run generates more O₃ than the standard run, are shown with warm colors. These differences, of up to 1 ppb, generally occur above 500 m.

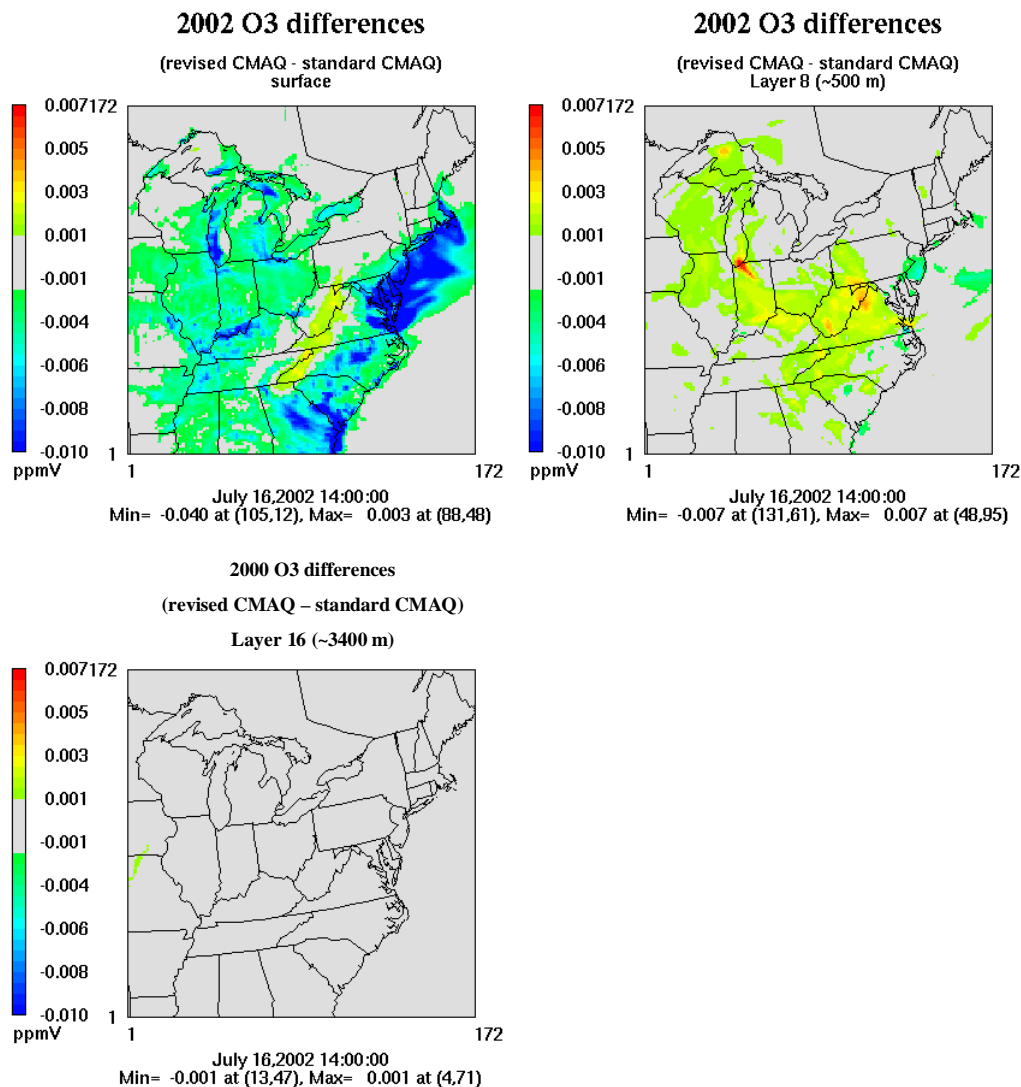


Figure 12a. Differences between revised and standard CMAQ O₃ (revised-standard) for a July 2002 smog and haze episode. These plots are for 14 UT (10 EST). The differences are negative at the surface meaning that the revised CMAQ run generates less O₃ than the standard run. Above 500 m the differences are positive and the revised CMAQ run produces more O₃ than the standard CMAQ.

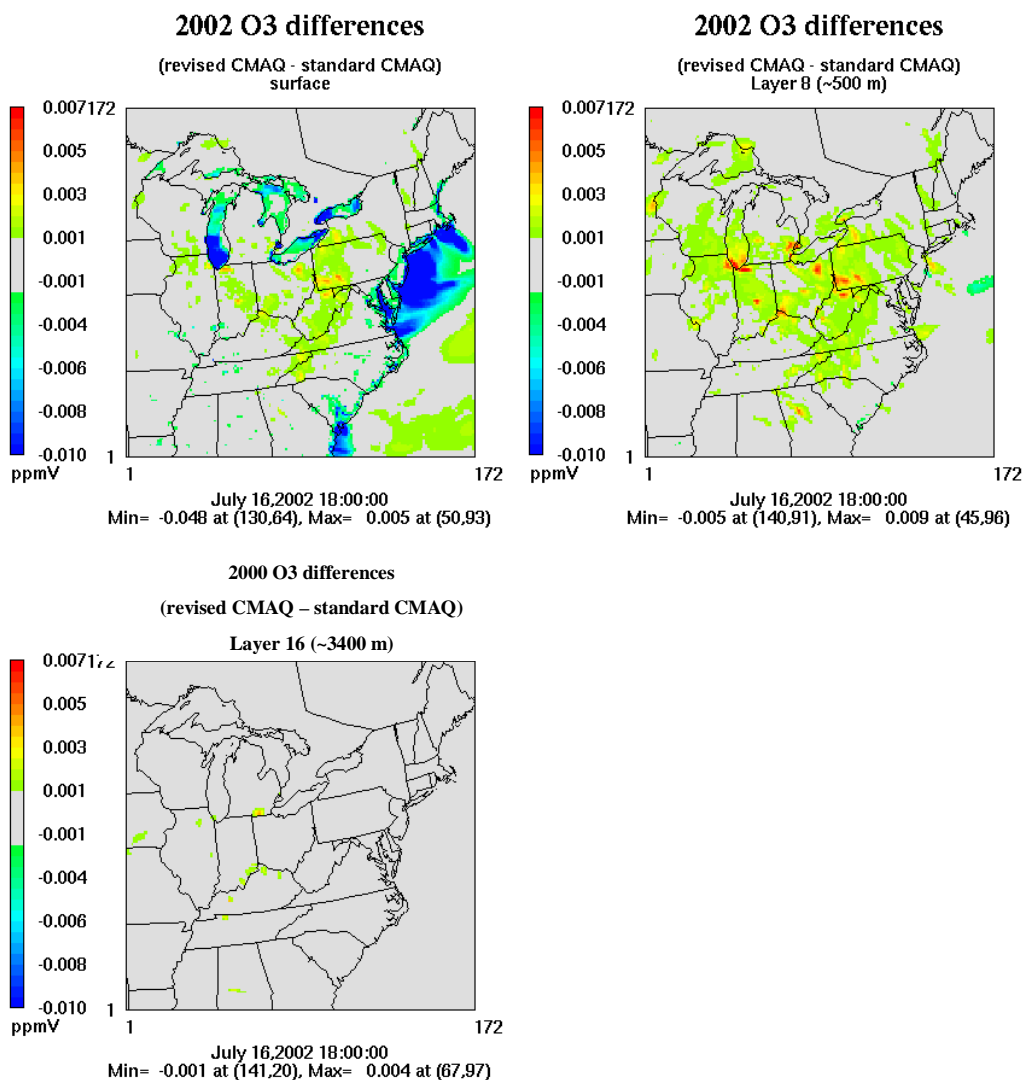


Figure 12b. Differences between revised and standard CMAQ O₃ (revised-standard) for a July 2002 smog and haze episode. These plots are for 18 UT (14 EST). The differences are negative at the surface meaning that the revised CMAQ run generates less O₃ than the standard run. Above 500 m the differences are positive and the revised CMAQ run produces more O₃ than the standard CMAQ.

A curtain plot (Figure 13) was used to examine the diurnal variation in the first 16 layers of CMAQ showing the differences in O₃ generated from:

$$\text{Revised CMAQ} - \text{standard CMAQ} \quad (9)$$

The x-axis represents a swath made one grid cell wide (East and West) extending from the southernmost grid cell to the northernmost grid cell in the Eastern US shown in Figure 14. The y-axis represents the first 16 layers of CMAQ. Six time periods of 3, 7, 11, 15, 19 and 23 UT are shown for July 17, 2002. In the early morning (from 3 to 11 UT) there are positive differences (where the revised CMAQ generated O₃ is larger than the standard CMAQ O₃) above 500 m that are mixed down to the surface. At 15 and 23 UT, right after rush hour, there are negative differences (where the revised CMAQ O₃ is smaller than the standard CMAQ O₃) near the surface.

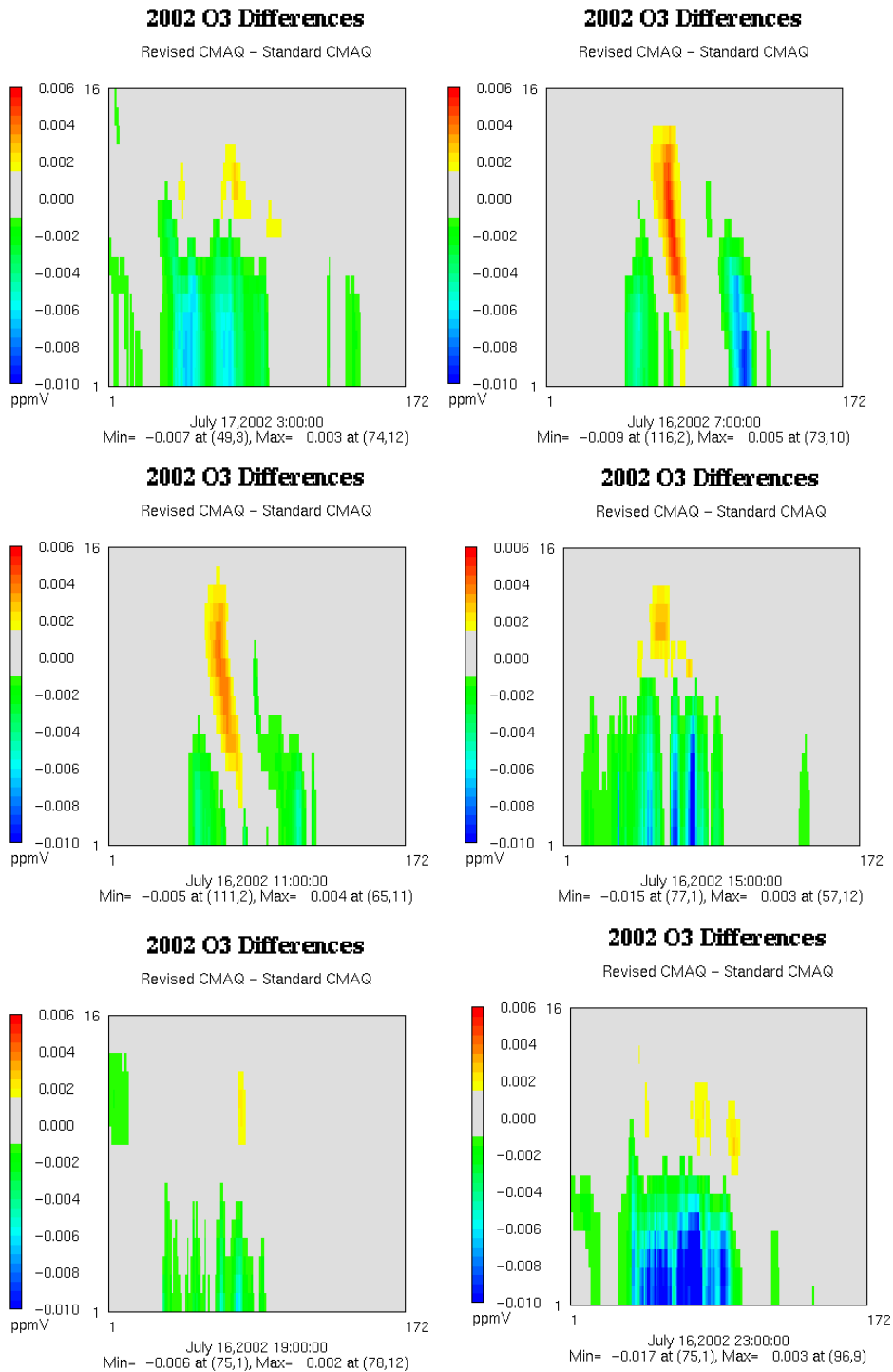


Figure 13. O₃ differences (revised-standard) for a single swath in the CMAQ grid. The y-axis represents the first 16 altitude layers used in CMAQ. The x-axis represents a swath of the grid cells examined (Figure 14), where 1 is the Southernmost grid cell and 172 is the Northernmost grid cell. Here negative differences mean that O₃ generated with the revised CMAQ is smaller than the standard CMAQ O₃ and these are seen closer to the surface.

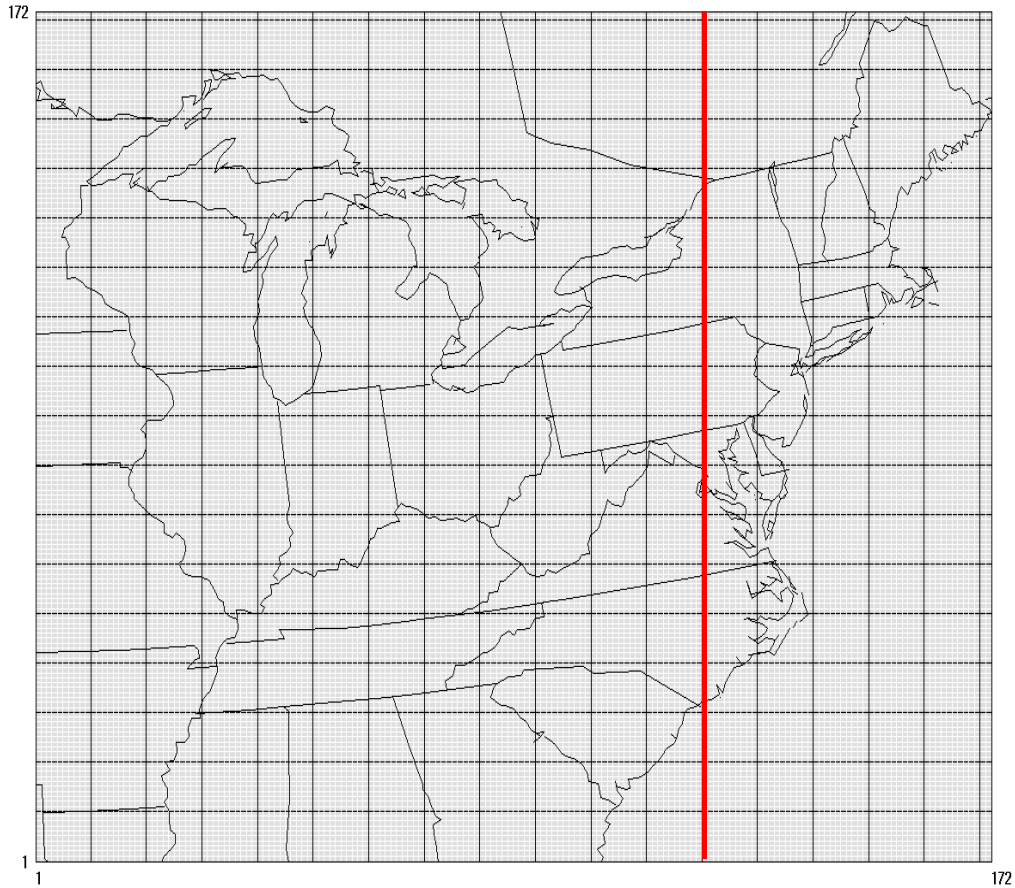


Figure 14. The curtain plot in Figure 13 was made from a vertical swath, shown in red. This swath represents the x-axis in Figure 13.

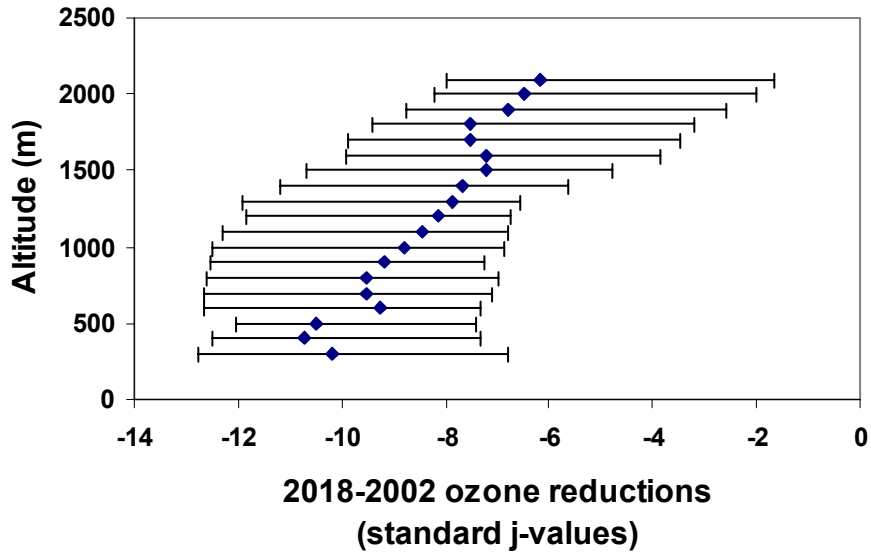
I also examined how the emissions reductions scenario, expected for 2018, would be impacted by incorporating aerosols into CMAQ. Figures 15 a and b show the CMAQ O₃ reductions (CMAQ 2018 – CMAQ 2002) for profiles made during the July 15-18 episode (at locations where the aircraft made spirals) for the standard CMAQ runs (Figure 15 a) and the revised CMAQ runs (Figure 15 b). The revised CMAQ reductions and standard CMAQ reductions are similar, with the largest

reductions (10 ppb) near the surface and smaller reductions (7 ppb) at 2000 m. Figure 15 c shows the difference between:

$$[(2018 \text{ revised} - 2002 \text{ revised}) - (2018 \text{ standard} - 2002 \text{ standard})] \quad (10)$$

The differences between O₃ reductions using revised CMAQ and standard CMAQ (Equation 10) are small (Figure 15 c) for the locations where the UMD research aircraft made spirals. However, the revised reductions are smaller than the standard reductions, and this means the standard CMAQ run slightly overestimates reductions at the surface (by 0.6ppb). Above 1000 m the standard CMAQ run underestimates reductions. The column contents in Table 3 suggest that the reductions using the revised CMAQ runs are 3% larger than the reductions using the standard CMAQ runs.

a



b

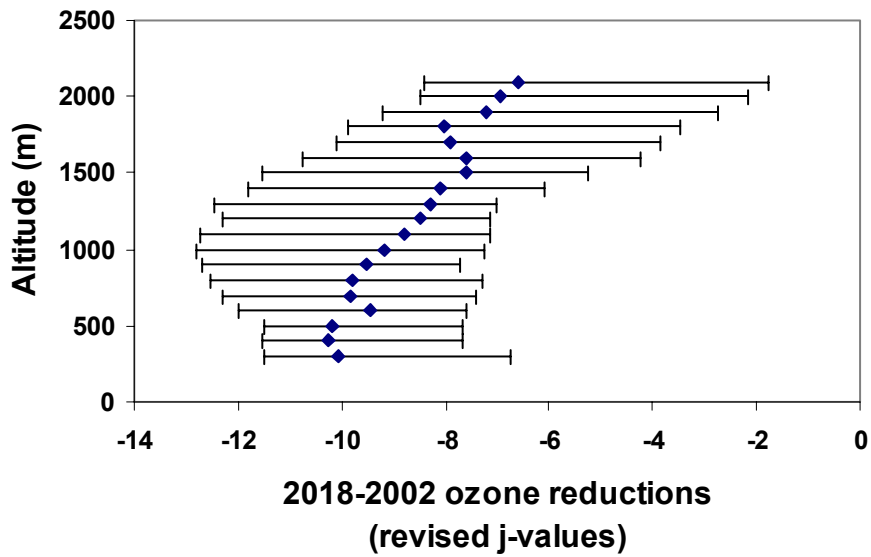


Figure 15 a b. Median CMAQ ozone reductions (CMAQ 2018 – CMAQ 2002) using a) standard j-values and b) revised j-values. Error bars represent the 25th and 75th percentiles. The largest reductions occur near the surface.

c

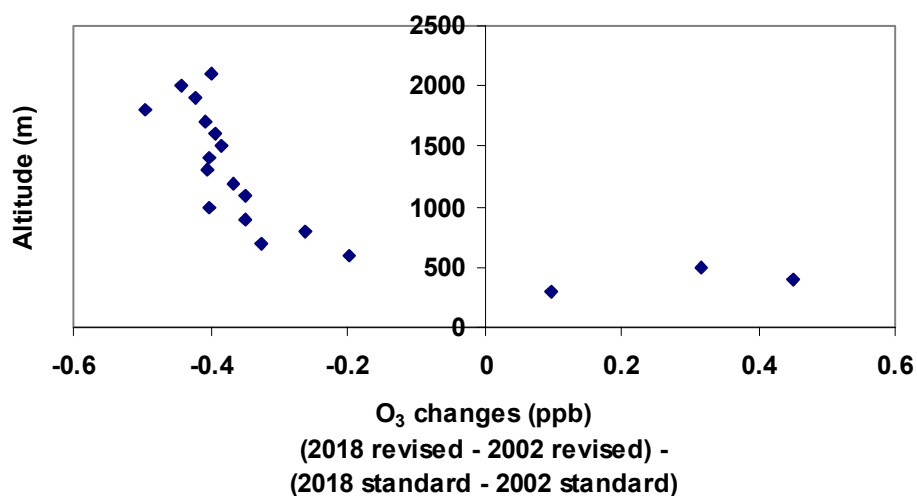


Figure 15 c. Changes in O₃ reductions of revised CMAQ– standard CMAQ. Near the surface standard CMAQ overestimates the reductions and above 500 m the standard CMAQ underestimates the reductions.

Figure 16 shows the results of Equation 10 (differences in O₃ reductions for revised and standard CMAQ runs) for the Eastern US. These differences are plotted at three levels (approximately the surface, 500 m and 3400 m) at 14 UT and 18 UT. The positive changes show that the standard model over-predicts O₃ reductions (because the revised CMAQ reductions are smaller than the standard CMAQ reductions) by up to 2 ppb near the surface. Above 500 m the standard model under-predicts O₃ reductions by up to 2 ppb.

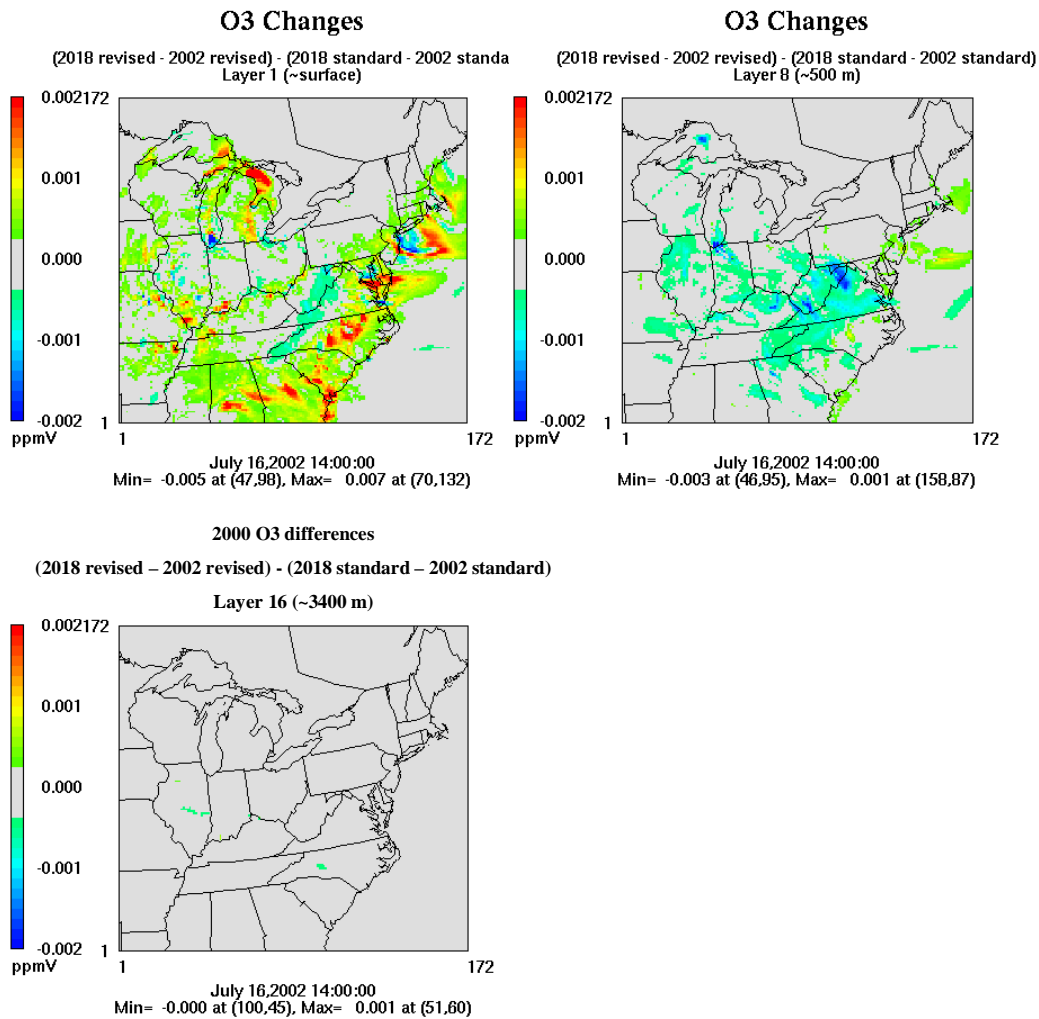


Figure 16a. O₃ differences of [(2018, revised – 2002, revised) – (2018, standard – 2002, standard)] for the 1st, 8th, and 16th layers at 14 UT. The standard CMAQ runs over-predict O₃ reductions near the surface (warm colors). Above 500 m the standard model under-predicts O₃ reductions.

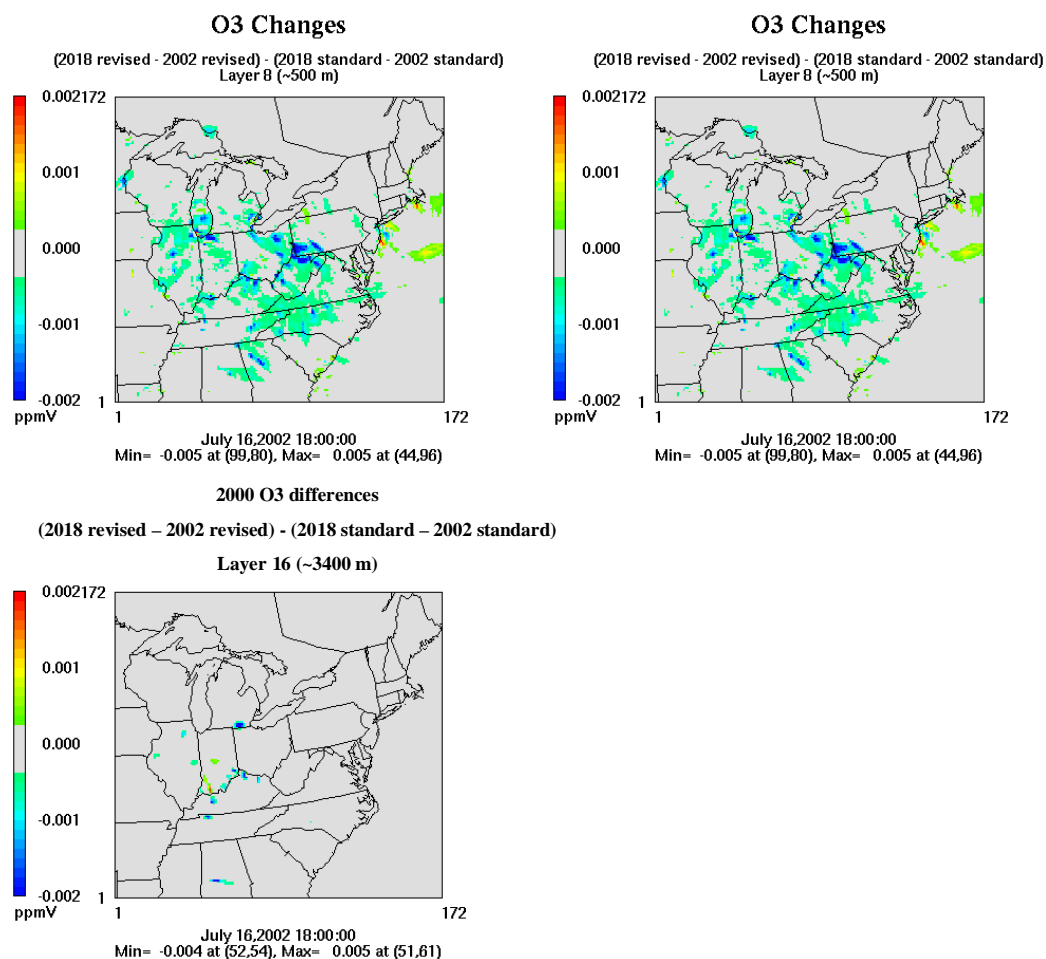


Figure 16b. O₃ differences of [(2018, revised – 2002, revised) – (2018, standard – 2002, standard)]. For the 1st, 8th, and 16th layers at 18 UT. The standard CMAQ runs over-predict O₃ reductions near the surface (warm colors). Above 500 m the standard model under-predicts O₃ reductions.

This study has important policy implications. The National Ambient Air Quality Standards (NAAQS) regulate surface O₃ and the EPA requires states to use the CMAQ model to determine future compliance, for surface sites. Above I have shown that accounting for aerosols in the photolysis rates of NO₂ decreases O₃ production near the surface. State agencies that are not in compliance with NAAQS O₃ standards can use this model bias to their advantage when developing the State

Implementation Plans. The reductions in O₃ (incurred by reductions point and mobile NO_x emissions) generated with the standard CMAQ model are overestimated at the surface. This must be accounted for when state agencies develop plans to reduce O₃.

5.2.3 SO₂ Comparisons

Modeled SO₂ from CMAQ and GOCART was compared to aircraft profiles. Figure 17 shows the median of 118 CMAQ and aircraft SO₂ profiles (ppb) for 2002 (June – August), with error bars representing the 25th and 75th percentiles. These profiles were made in the area contained by 37.18 to 44.53° latitude and -79.44 to -68.36° longitude. CMAQ over-predicts SO₂ by a factor of 1.2 at 200 m and by a factor of 4.6 at 2300 m (Figure 18). CMAQ over-predicts the column content by 55% (Table 4).

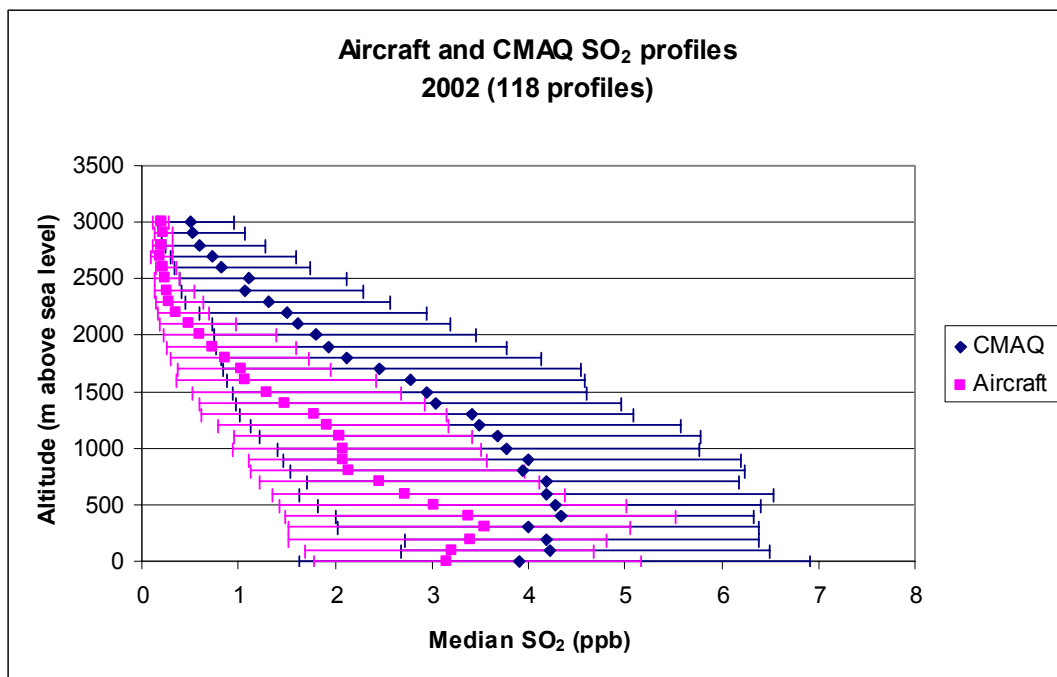


Figure 17. Median CMAQ and aircraft profiles of SO₂ from 2002 (June –August). The median was obtained from 118 profiles. The error bars represent the 25th and 75th percentiles. Though the error bars overlap, CMAQ over-predicts SO₂ throughout the profile.

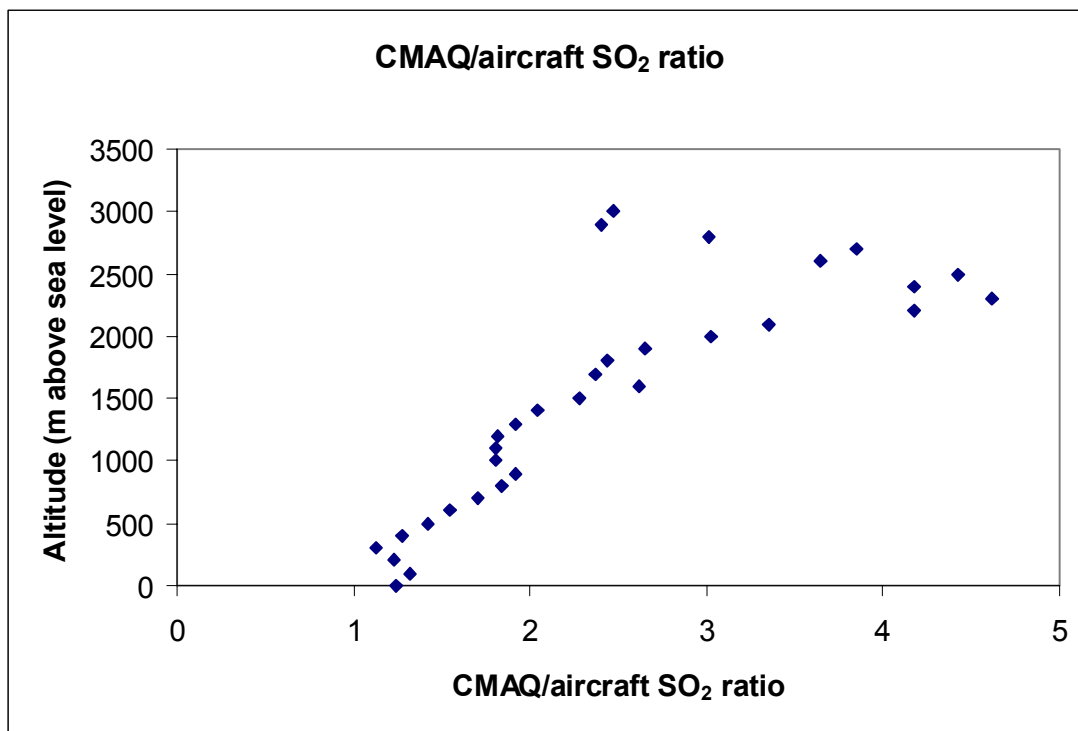


Figure 18. The ratio of median CMAQ SO₂ mixing ratios divided by median aircraft SO₂ mixing ratios. CMAQ over-predicts SO₂ by a factor of 1.2 at 200 m and a factor of 4.6 at 2300 m.

Column content (g m ⁻²)	Aircraft	CMAQ
average	0.009	0.014

Table 4. The average aircraft and CMAQ SO₂ column content (g m⁻²) for 118 profiles. The average CMAQ column content is 55% larger than the average aircraft column content.

Figure 19 shows median SO₂ profiles (µg/m³) from 223 GOCART and aircraft averaged profiles for 2000 to 2003 (April – August) with error bars representing the 25th and 75th percentiles. These profiles were made in the area contained by 34 to 44°

latitude and -82.5 to -67.5° longitude. Figure 20 shows the ratio of GOCART/aircraft SO₂ at each of the seven altitudes examined. GOCART over-predicts SO₂ by a factor of 1.4 at 100 m and by a factor of 2 at 1250 m. The GOCART column content is 50% larger than the aircraft column content (Table 5). Although CMAQ and GOCART are representative of different times and locations and are not strictly comparable with each other, they show a consistent high bias relative to observations.

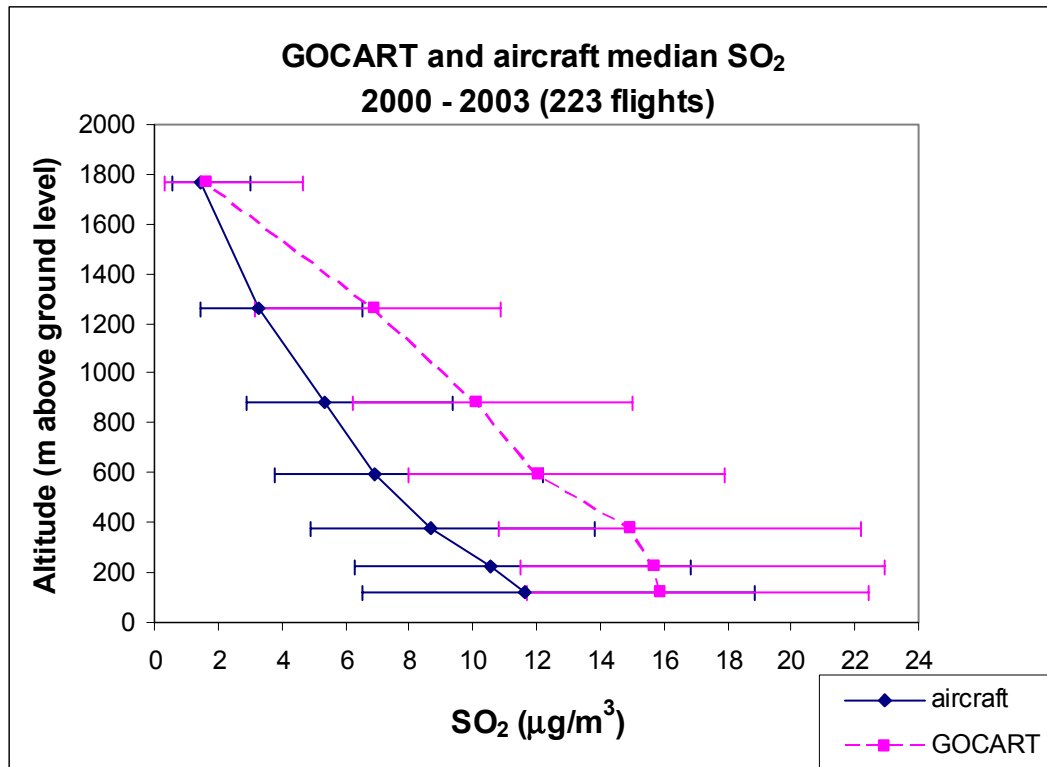


Figure 19. Median GOCART and aircraft profiles of SO₂ from 2000-2002 (April –August). The median was obtained from 223 profiles. The error bars represent the 25th and 75th percentiles. Though the error bars overlap, GOCART over-predicts SO₂ up to 1800 m.

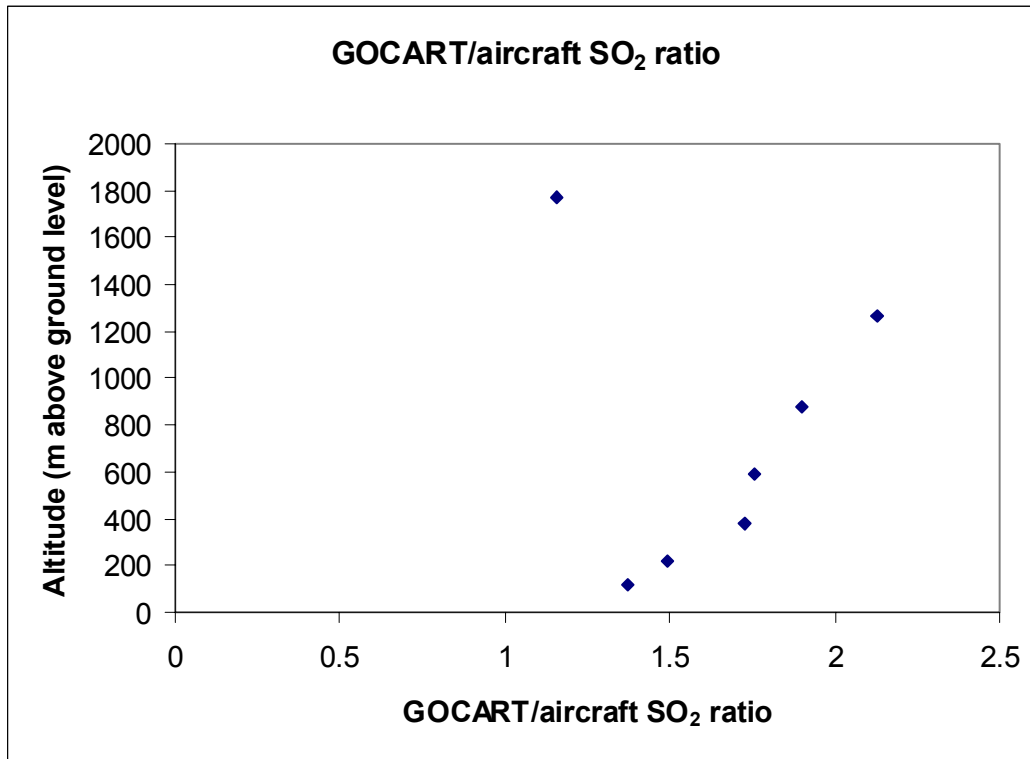


Figure 20. The ratio of median GOCART SO₂ mixing ratios divided by median aircraft SO₂ mixing ratios. GOCART over-predicts SO₂ by a factor of 1.4 at 100 m and a factor of 2 at 1250 m.

Column content		
(g m ⁻²)	Aircraft	GOCART
average	0.012	0.018

Table 5. The average aircraft and GOCART SO₂ column content (g m⁻²) for 223 profiles. The average GOCART column content is 50% larger than the average aircraft column content.

Differences between CMAQ and measured SO₂ were calculated and sorted as those for O₃. The profile differences are smallest for SO₂ with small mixing ratios (around 2 ppb at the surface). Figures 21-23 show CMAQ and aircraft profiles with the 5th percentile smallest differences, median differences and 95th percentile largest

differences. Back trajectories (from HYSPLIT) are also shown. Profiles associated with the median differences show that the model over-predicts SO₂ above 1500 m. The profile over Easton, MD on June 25, 2002 shows that the model does under-predict SO₂ sometimes. Profiles associated with the 95th percentile largest differences show that the model over-predicts SO₂ by a factor of two to five throughout the profile. There does not appear to be a relationship among wind speeds and direction and SO₂ profiles.

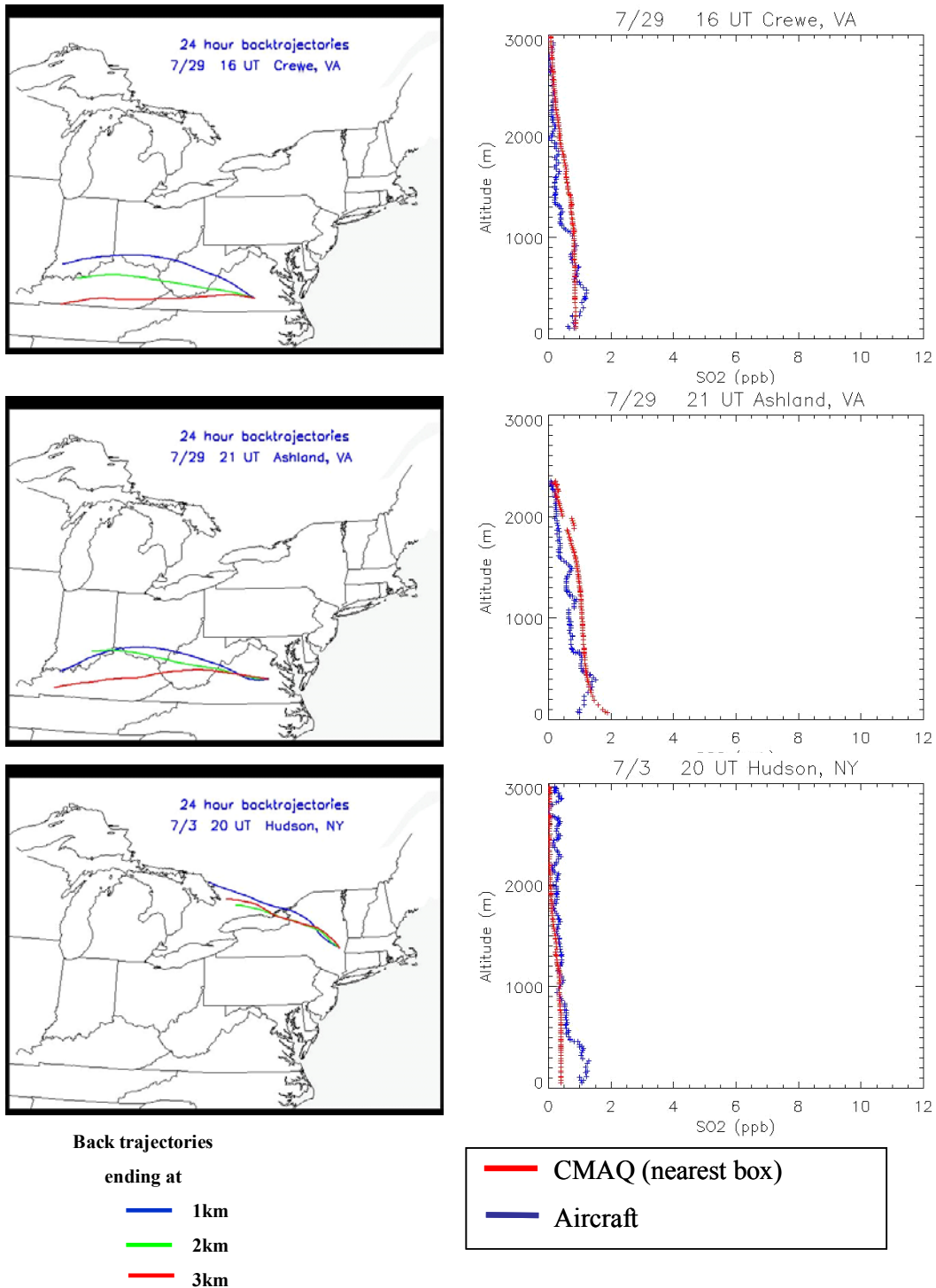


Figure 21. CMAQ and aircraft SO₂ profiles associated with the 5th percentile smallest differences (best agreement). The red profiles represent CMAQ SO₂ from the closest (center) grid cell. In general CMAQ over-predicts SO₂. Back trajectories at 3 altitudes are also shown.

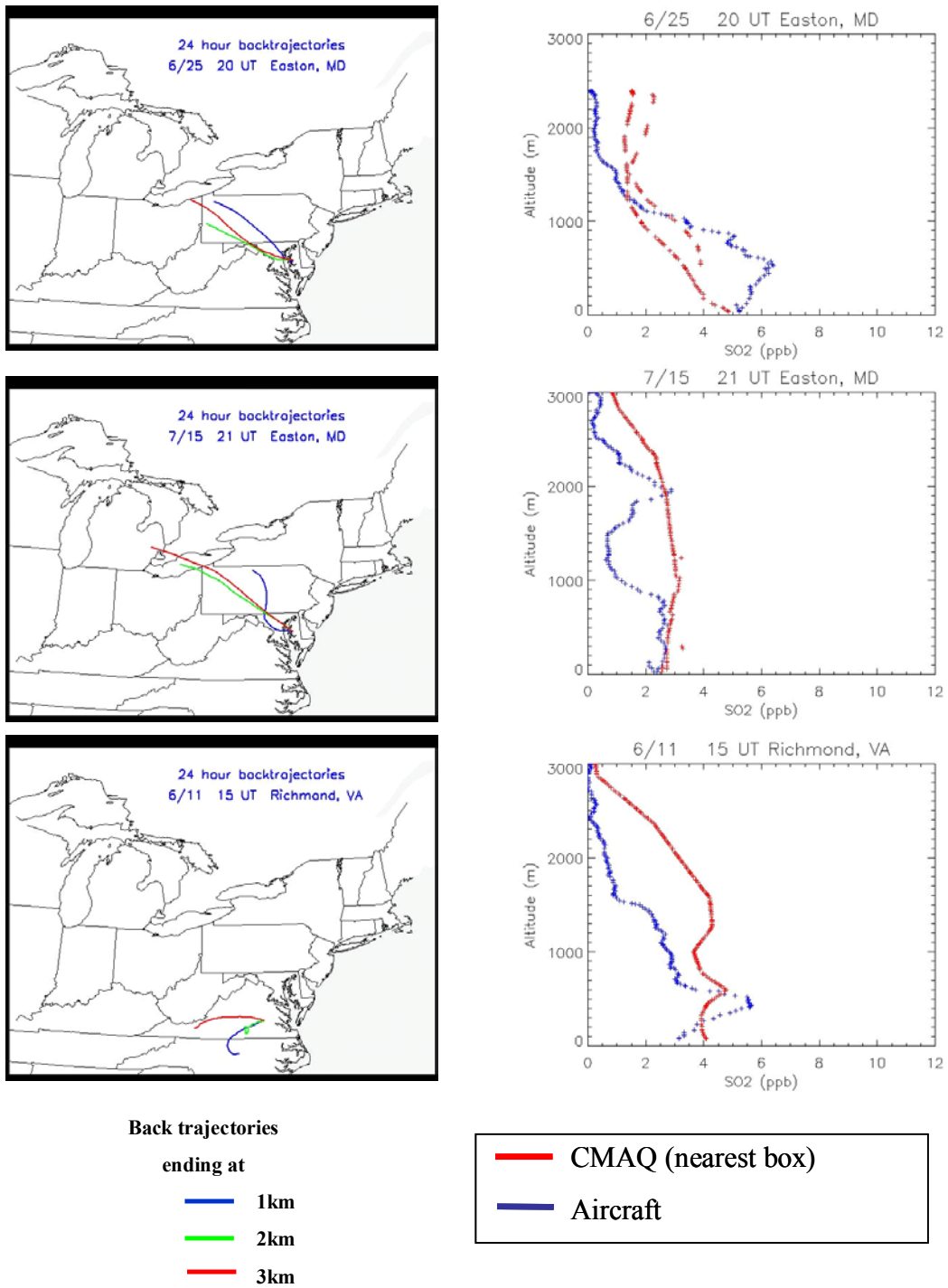


Figure 22. CMAQ and aircraft SO₂ profiles associated with the median differences. The red profiles represent CMAQ SO₂ from the closest (center) grid cell.

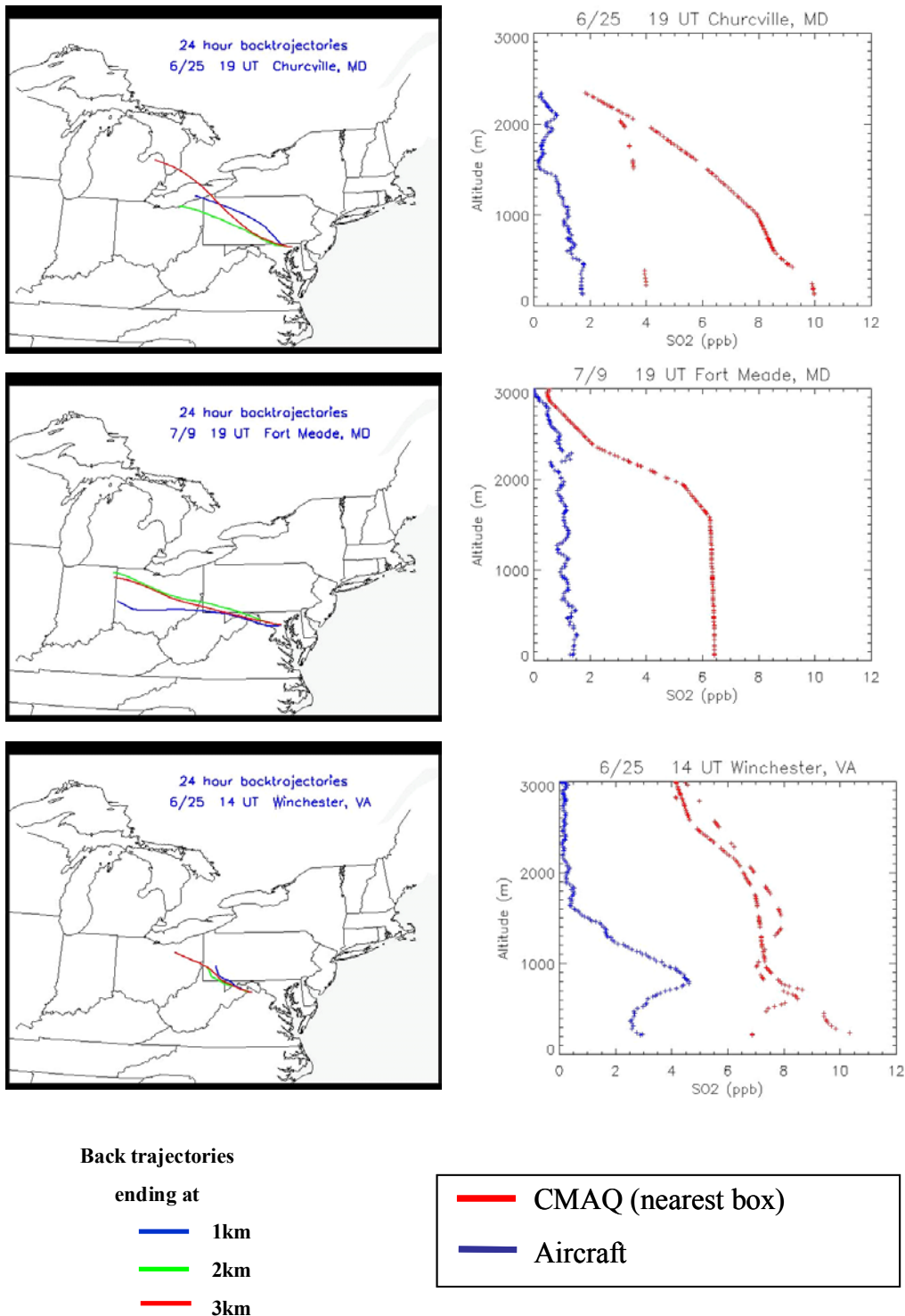


Figure 23. CMAQ and aircraft SO₂ profiles associated with the 95th percentile largest differences (worst agreement). The red profiles represent CMAQ SO₂ from the closest (center) grid cell.

Differences between GOCART simulations and aircraft observations of SO₂ were calculated in a manner similar to the differences between CMAQ and aircraft. GOCART has coarse vertical resolution and there were only seven altitude layers to compare with the aircraft profiles. For this reason only one altitude bin with the seven layers (k=1 from Equation 1 in chapter 4) was analyzed for differences. Figures 24-26 show profiles associated with the 5th percentile smallest differences, median differences, and 95th percentile largest differences. Profiles associated with the median differences show that the model tends to over-predict SO₂, however profiles associated with the 95th percentile largest differences show the model sometimes over-predicts and sometimes under-predicts SO₂.

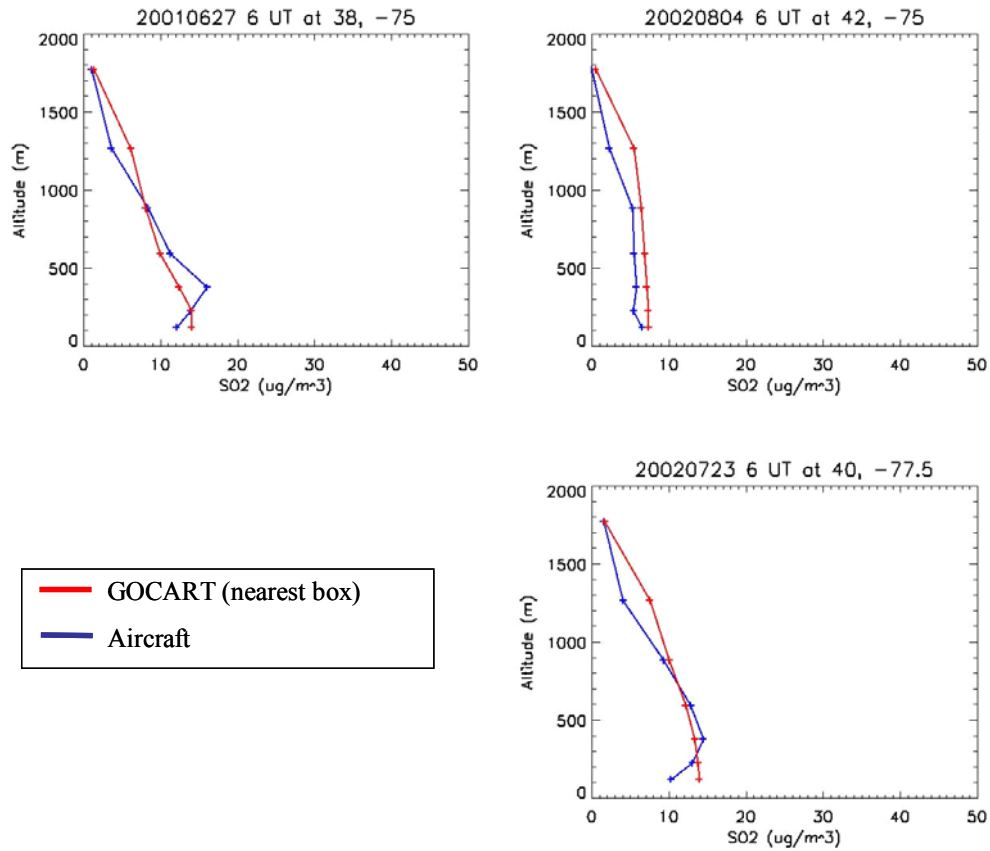


Figure 24. GOCART and aircraft SO_2 profiles associated with the 5th percentile smallest differences (best agreement). The red profiles represent GOCART SO_2 from the closest (center) grid cell.

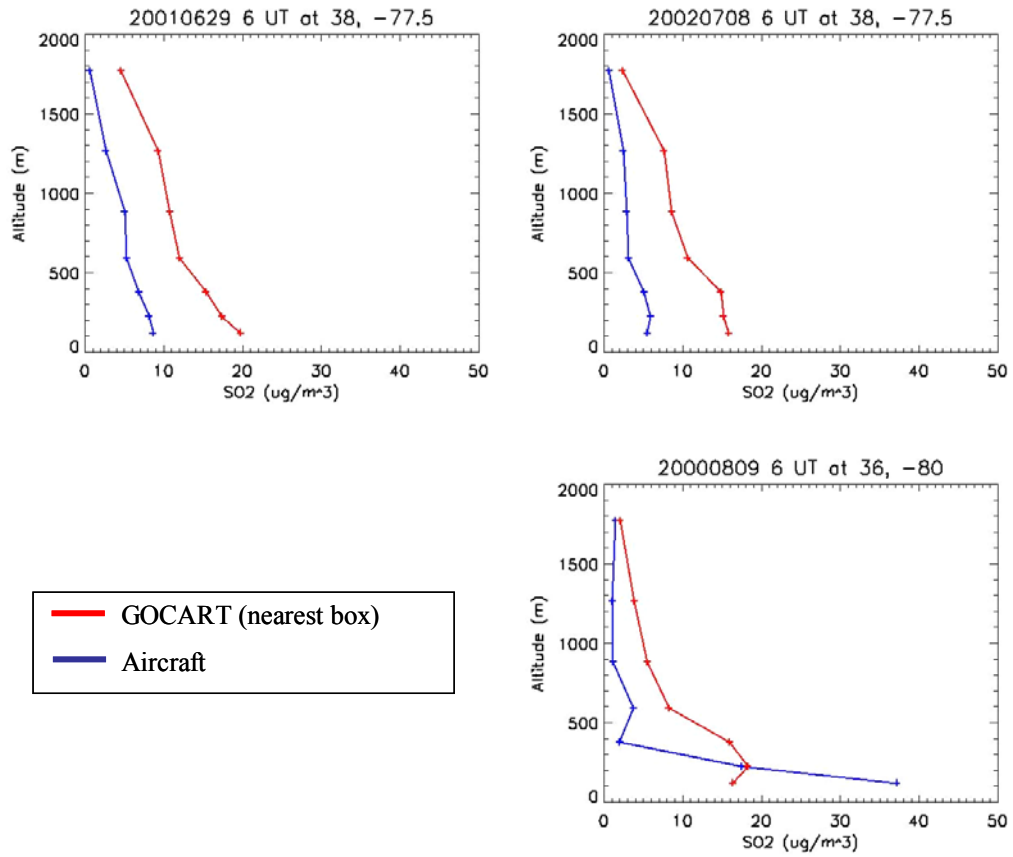


Figure 25. GOCART and aircraft SO₂ profiles associated with the median differences. The red profiles represent GOCART SO₂ from the closest (center) grid cell. GOCART gets the right shape, but the magnitude is too large.

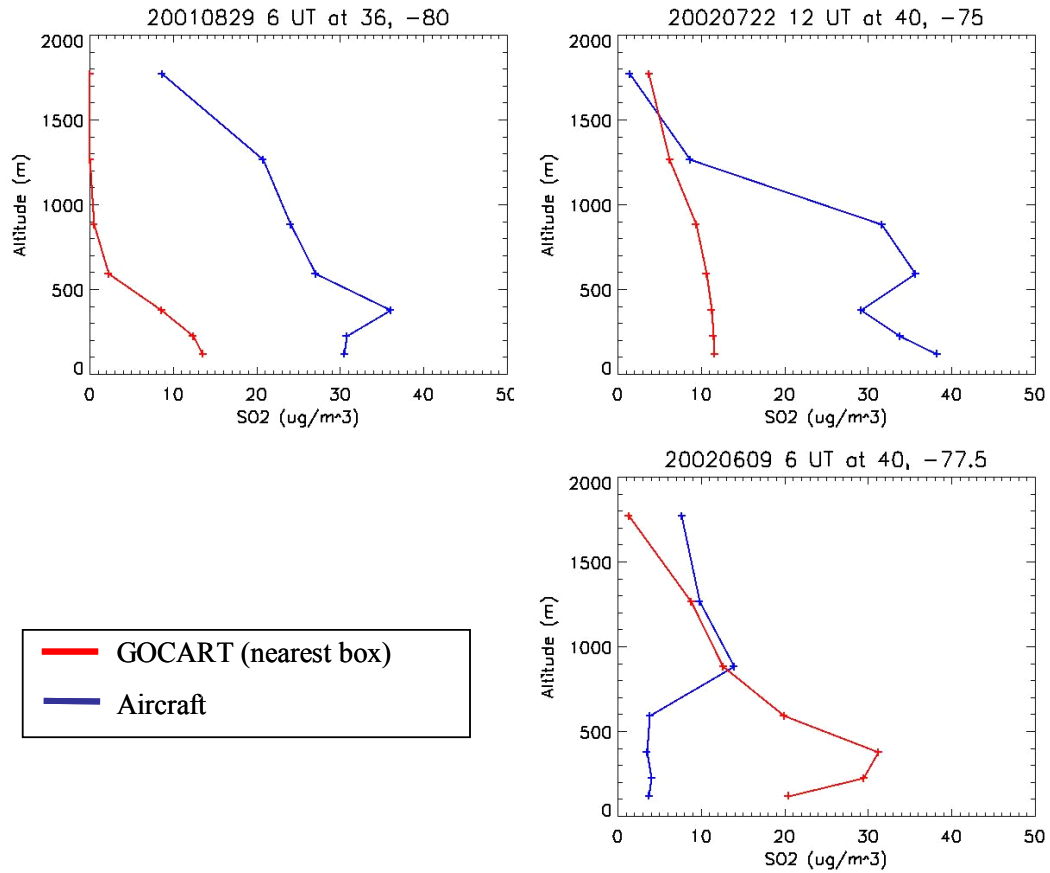


Figure 26. GOCART and aircraft SO₂ profiles associated with the 95th percentile largest differences (worst agreement). The red profiles represent GOCART SO₂ from the closest (center) grid cell. GOCART gets the right shape, but the magnitude is too large.

The model over-prediction could be a result from:

1. Emissions that are too large, with losses modeled correctly.
2. Correct emissions, but the loss in the model is too slow.

To test possibility 1 (that the emissions are too large), I calculated the flux of SO₂ using national inventories of point and area SO₂ sources (area sources are composed of mobile emissions) as well as accounting for a small contribution from biogenic sources. I compared these SO₂ fluxes with those used in GOCART. For my SO₂ flux

calculation I used the EPA's AirData (<http://epa.gov/air/data/geosel.html>) database for the United States point and area SO₂ sources (emissions are in g/hr).

I used the National Pollutant Release Inventory (NPRI) database for Canadian point source emissions. The NPRI database does not report area emissions and therefore I estimated them from the EPA's AirData database. I calculated the slope between the US state populations – x-axis, (ESRI data and maps 2000) and US state area SO₂ emissions- y-axis, by forcing the line through zero (Figure 27). This slope of area emissions/population was used to approximate area emissions from Canadian municipalities using Canadian populations (ESRI data and maps 2000). I also estimated the small contribution of SO₂ from biogenic sources using sulfur fluxes presented in Wayne (2000); the biogenic contribution of SO₂ is 0.7% of the contribution from anthropogenic emissions. I calculated the total flux of SO₂ for half of the United states and some Canadian municipalities by adding the point and area source emissions for each state (or municipality) to the biogenic contribution and dividing this by the total area of the state (or municipality). Figure 28 shows a comparison of the SO₂ fluxes I calculated from the national databases and the SO₂ flux used in the GOCART model. The average flux from the national inventories (Figure 28 a) is $2.8 \times 10^{-4} \text{ g m}^{-2} \text{ hr}^{-1}$ and the average flux from GOCART (Figure 28 b) is $2.5 \times 10^{-4} \text{ g m}^{-2} \text{ hr}^{-1}$, only 16% smaller than the average flux from the national inventories. The SO₂ emissions used in CMAQ were generated with SMOKE which converts the resolution of the national inventories into a resolution that can be used in CMAQ. Because the SO₂ fluxes from the models (CMAQ and GOCART) are similar to those I calculated using the national inventories, it is unlikely that model emissions

are too large by a substantial amount. The likely explanation for why the model SO₂ is larger than measured is that the model removal of SO₂ is too slow.

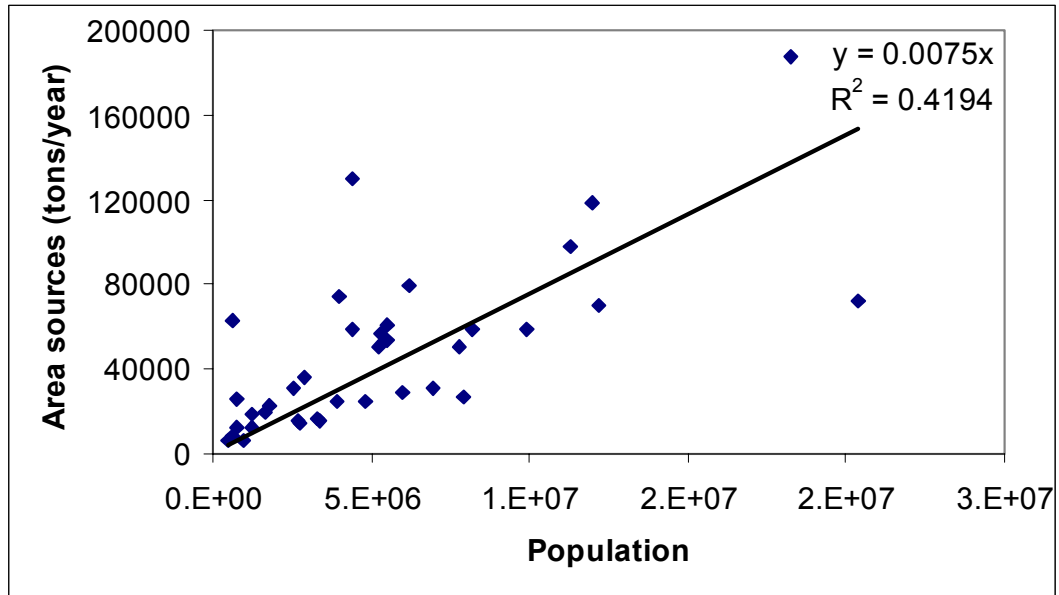


Figure 27. US state population and area sources of SO₂.

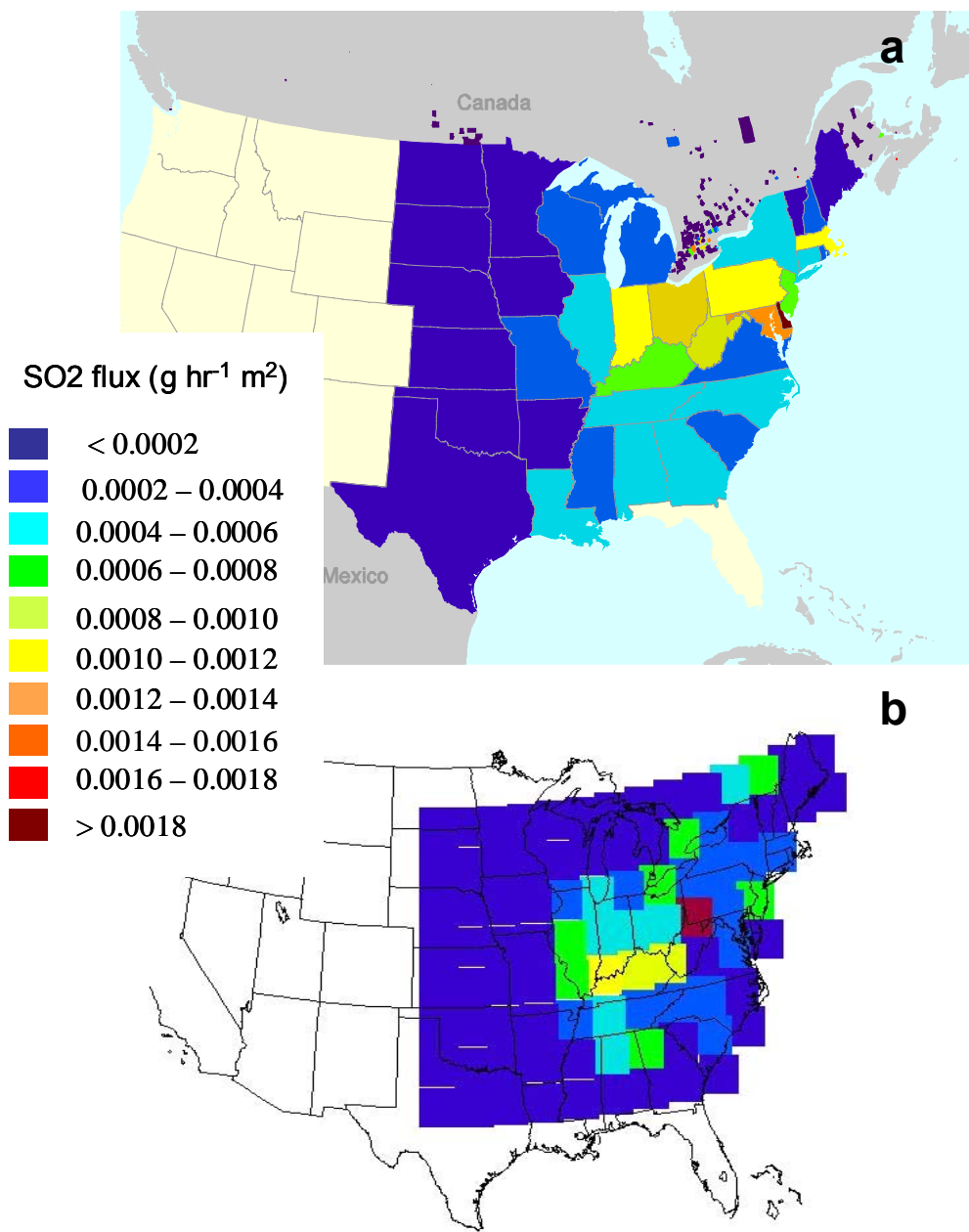


Figure 28. a) The SO₂ flux (g hr⁻¹ m⁻²) calculated using national emission inventories and b) the SO₂ (g hr⁻¹ m⁻²) flux used by GOCART.

The model may underestimate reactions that oxidize SO₂ to sulfate properly and this could explain a model loss of SO₂ that is too slow (possibility 2). SO₂ oxidation to sulfate via H₂O₂ in clouds is well understood and in the Mid-Atlantic region with an acidic environment this is the most probable reaction pathway for

sulfate formation (Seinfeld and Pandis, 1998). Figure 29 shows the mixing ratio of H_2O_2 over the average CMAQ domain and at a specific rural location (Big Meadows, VA) for July 1, 2002. H_2O_2 is 2-4 times greater than SO_2 , from 1000 – 2000 m, (Figure 17) and large enough to oxidize completely the SO_2 to sulfate. It is therefore likely that the model generates enough H_2O_2 to react with SO_2 . Heterogeneous oxidation on mineral aerosols is not as well understood (Detener et al., 1996; Zhang et al., 2006), and may be more difficult to account for in the models. The models may also not fully account for wet and dry deposition in the Mid-Atlantic region, thus increasing the lifetime of SO_2 . The models may also under-represent clouds (as described by Mueller et. al., 2006), where SO_2 is oxidized to sulfate with H_2O_2 and therefore produce an SO_2 lifetime that is too long. There are no NAAQS exceedences of SO_2 in the Mid-Atlantic region, but there are exceedences of $\text{PM}_{2.5}$ for which sulfate (with an SO_2 precursor) is a major component, accounting for 30% of $\text{PM}_{2.5}$ mass (Rees et al., 2004; Schwab et al., 2004; Frank et al., 2006; Ondov et al., 2006).

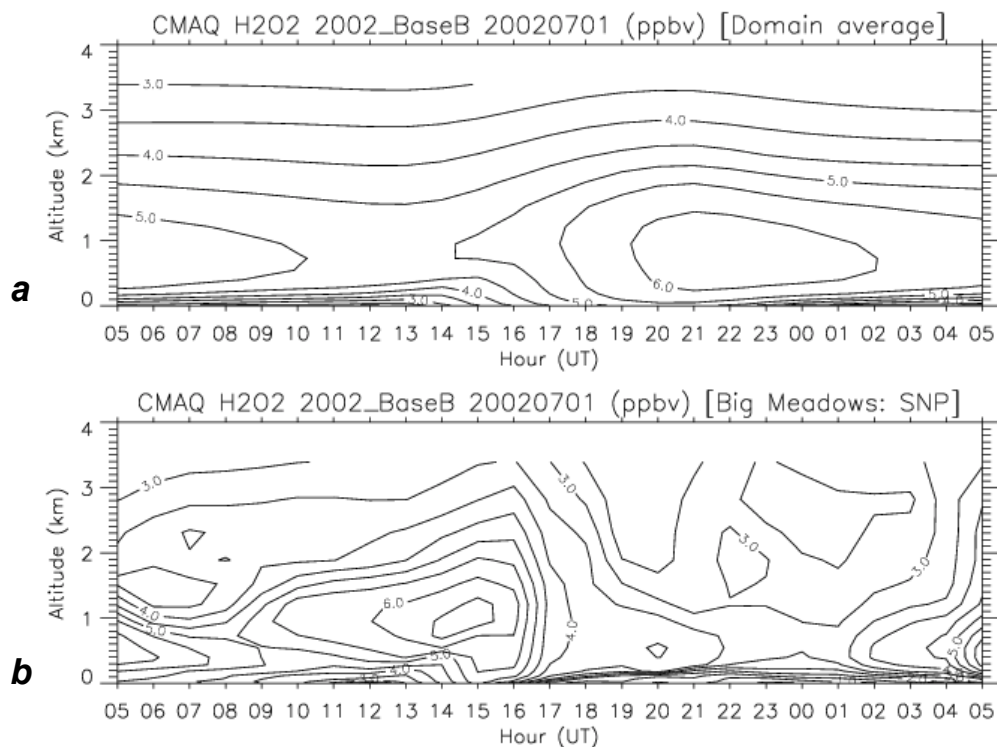


Figure 29. The CMAQ domain average H_2O_2 (ppbv) for a day in July 2002 (a) and the CMAQ H_2O_2 for a rural site (Big Meadows at Shenandoah National park) for the same day. The H_2O_2 is 2-4 times greater than CMAQ SO_2 (from Figure 17) at 1000-2000 m. The altitudes presented are above ground level.

5.2.4 Lifetime Calculation

The CMAQ and GOCART overestimation of SO_2 in the atmosphere suggests that the models do not properly simulate the lifetime of SO_2 ; specifically the models usually overestimate the lifetime. I have calculated the SO_2 lifetime for the conditions when aircraft observations were made (in the daytime for June through August in the Mid-Atlantic region see Figure 1 in Chapter 2 for map of locations). The mean profile of SO_2 shows a rapid decrease in mixing ratio with increasing altitude. This shows that SO_2 is destroyed on time scales fast relative to mixing in the planetary boundary layer. If SO_2 is on average destroyed before it is advected away

from the source region, the Eastern US, then we can assume that the rate of emissions into the atmosphere is equal to the rate of loss in the atmosphere (i.e., production equals loss). For an air column the production is the flux, F , in $\text{g m}^{-2} \text{s}^{-1}$. Because the steady state approximation can be applied to the system the rate of loss ($L \text{ g m}^{-2} \text{s}^{-1}$) of SO_2 in an air column is

$$L = \int_0^{\infty} k'[\text{SO}_2]dz \quad (11)$$

Where k' is the effective first order rate constant, s^{-1} , $[\text{SO}_2]$ is the concentration of SO_2 in g m^{-3} as a function of altitude, z . The product of k' and $[\text{SO}_2]$ must be integrated to an altitude where the concentration of SO_2 is much less than at the surface. At steady state the flux is equal to the loss and can be written as:

$$F = \int_0^{\infty} k'[\text{SO}_2]dz \quad (12)$$

The effective first order rate constant is the sum of all losses, including dry deposition, attack by OH, and oxidation by H_2O_2 in cloud droplets. Equation 12 can be rearranged to separate the integral of the effective first order rate constant k' that is the inverse of the mean lifetime, τ (s).

$$\tau = \frac{1}{k'} = \frac{1}{F} \int_0^{\infty} [\text{SO}_2]dz \quad (13)$$

5.2.5 Verification of Lifetime Equation and Results

If Equation 13 is valid then we can use it to calculate the lifetime from measurements of SO_2 made aboard the UMD research aircraft. I developed a method to test Equation 13 using the Gaussian plume equation multiplied by a lifetime factor ($\exp^{-t/\tau}$, where τ is a user-defined lifetime) to generate SO_2 profiles from a known

source. I calculated the average lifetime by averaging the integrated profiles and dividing them by the source flux. If the lifetime I calculated using Equation 13 was the same as the user-defined lifetime then Equation 13 is valid. The Gaussian plume equation is:

$$C(x, y, z) = \frac{q}{2\pi\mu\sigma_y\sigma_z} \exp\left(-\frac{y^2}{2\sigma_y^2}\right) \left[\exp\left(-\frac{(z-h)^2}{2\sigma_z^2}\right) + \exp\left(-\frac{(z+h)^2}{2\sigma_z^2}\right) \right] \quad (14)$$

Here C is the concentration at an altitude z , a distance x downwind of a source and a distance y that is perpendicular to the x -axis. The emission rate is given by q , μ represents the wind speed and was assumed to be 6 m s^{-1} (the average wind speed for all 48 hr back trajectories ending at 1 km, associated with flights the UMD research aircraft made in 2002), h represents the effective stack height, assumed to be 200 m, and σ_y and σ_z are functions of x and represent the standard deviation of the plume distribution in the horizontal and vertical directions respectively. To determine the σ_y and σ_z values I assumed that the stability class was D, which is a neutral stability class and associated with winds greater than 6 m s^{-1} and moderate incoming solar radiation during the day (Schnelle and Dey, 2000). The equations for σ_y and σ_z are given below:

$$\sigma_y = ax^b \quad (15)$$

$$\sigma_z = cx^d \quad (16)$$

Where $a = 44$ and $b = 0.51$ for stability class D (Schnelle and Dey, 2000) and $c = 68$ and $d = 0.89$ for stability class D (Seinfeld and Pandis, 1998). The effective stack height, h from Equation 14, is the sum of the actual height of the stack, H plus the plume rise Δh . The plume rise can be calculated using the Holland plume rise

formula (Schnelle and Dey, 2000), however, for simplicity, I assumed that all stack heights were 200 m.

To test the method for determining SO₂ lifetime (using Equation 13) I generated SO₂ profiles from a single source of 4.5×10^7 g/day, in 14400 grid cells of 0.01° latitude by 0.01° longitude at 24 altitude levels from 0 – 30 km. To account for the lifetime (due to chemical or physical removal of SO₂) I multiplied the Gaussian plume dispersion Equation 13 by $\exp^{-t/\tau}$, where t is the time it takes to get to the sampling point from the source and τ is a user-defined input lifetime. Figure 30 shows the SO₂ column contents in this box generated from this one source. The flux of SO₂ from the one source was 1.35×10^4 g m⁻²day⁻¹ for the chosen domain. US EPA (2003) states that 86% of SO₂ is generated from fuel combustion and the rest (14%) is generated from transportation and industrial sources. To account for these transportation and industrial sources I added 509 g day⁻¹ to each grid cell. This added a 2.2×10^{-5} g day⁻¹ m⁻² to the flux and 2.5×10^{-5} gm⁻² was added to the column content in each grid cell.

Figure 30 shows the SO₂ column contents generated by one SO₂ source. In order to calculate the lifetime, the column contents are divided by the flux (the emission rate/ area of the box). Sampling any single point will probably not return the lifetime that is input into the model. However, an average of lifetimes from all sampling points in the box must equal the lifetime put into the model.

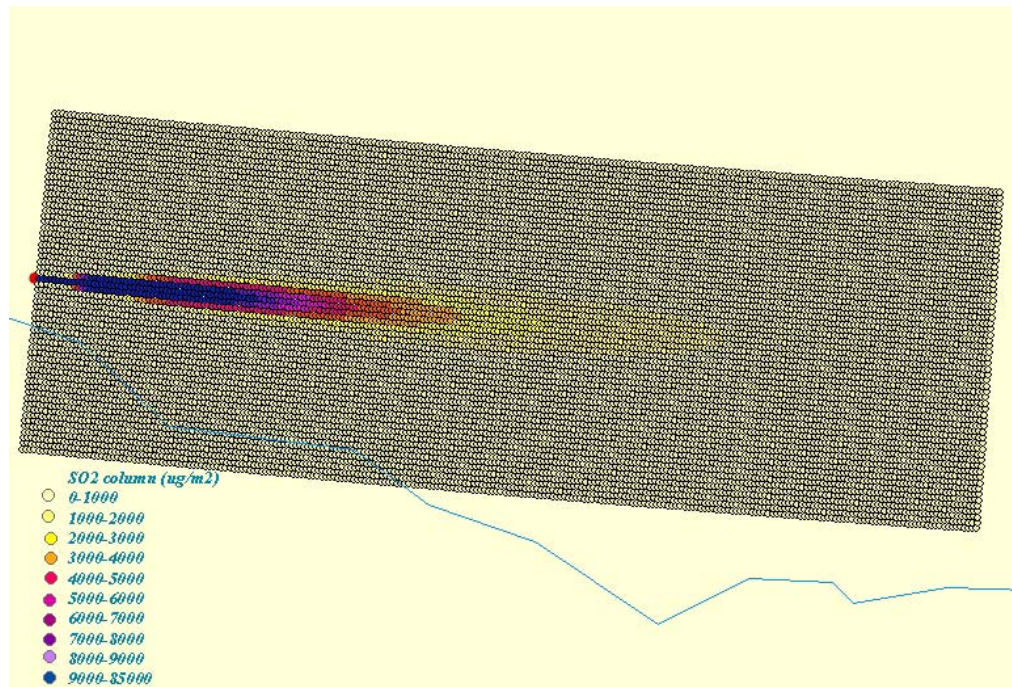


Figure 30. SO₂ column contents generated using a Gaussian plume dispersion model with one source.

To calculate the lifetime of SO₂ from UMD aircraft profiles I am limited to the locations over which the aircraft flew; the number of locations is a small fraction of the 14400 grid of 0.01° latitude by 0.01° longitude described above. I performed a test to determine if the locations and number of spirals made by the UMD research aircraft were sufficient to calculate the average lifetime using Equation 13. In 2002 the UMD airplane flew at 17 different locations and made a total of 90 different spirals sampling SO₂. Even though there were only 17 locations, the SO₂ profiles were independent because the winds changed between sampling days. To represent these locations in the model the 17 locations were shifted by 0.1 degree latitude or longitude, North, South, East, and West for a total of 85 sampling points. To test the effects of nudging the points on lifetime, the 85 points were shifted 0.15 degrees latitude or longitude, North, South, East, and West. This resulted in 5 sets of 85

samples that should have similar average lifetimes. Figure 31 shows the locations of these 425 sampling points (5 x 85) with sources of SO₂ in green. The sampling locations are represented by pink circles.

I also adjusted the area of the box used to calculate the flux in order to determine how that affected the resulting lifetime. Lifetimes of 8, 16, 24 and 32 hours were tested using three different sized boxes to calculate the flux of SO₂. Figure 32 shows the boxes used in this study and Table 6 gives the locations of the boxes and the distances and times between the westernmost sampling point and the western edge of the box.

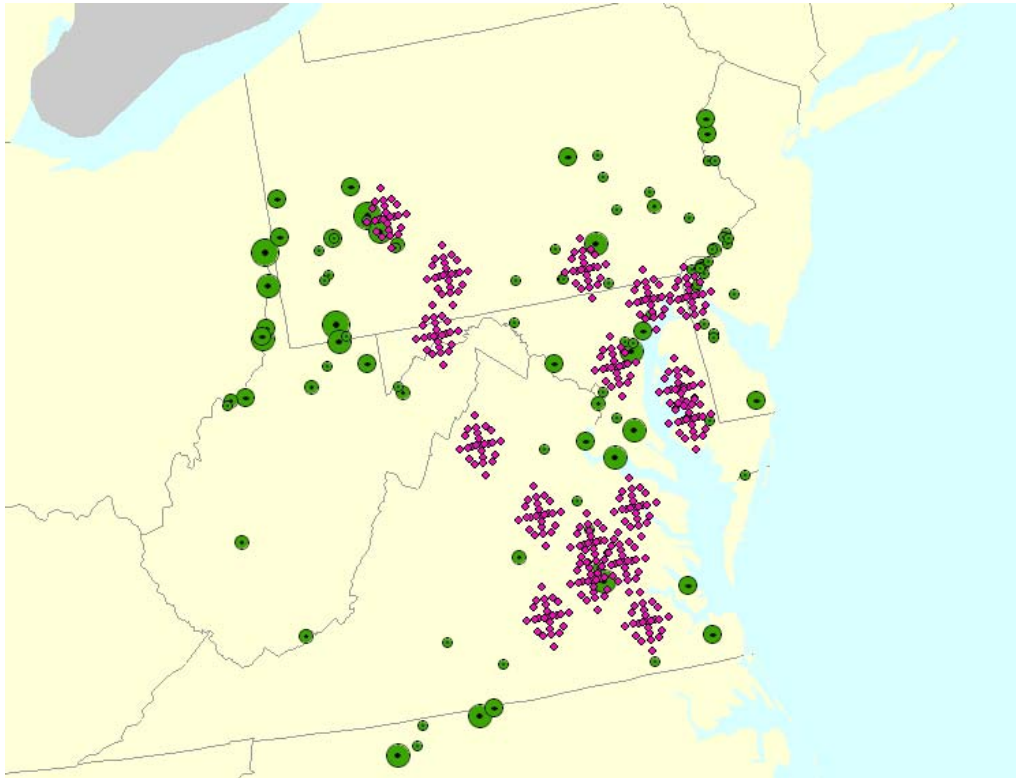


Figure 31. The locations of the 425 sampling points to be used in the simplified Gaussian plume dispersion model are shown in pink. The green circles represent power plants emitting SO₂ and the size of the circle represents the relative size of SO₂ emissions.

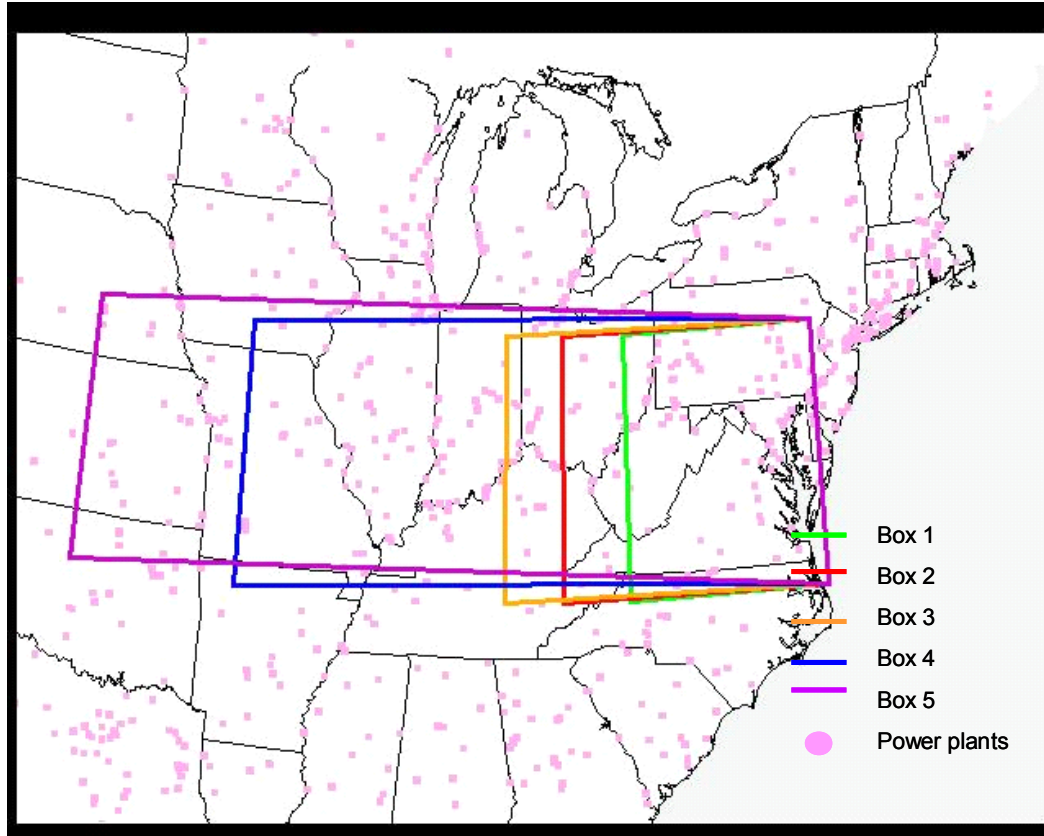


Figure 32. Boxes used to determine SO₂ flux from point sources.

	Box 1	Box 2	Box 3	Box 4	Box 5
Initial latitude	36.1	36.1	36.1	36.1	36.1
Final latitude	41.2	41.2	41.2	41.2	41.2
Initial longitude	-83.5	-85.3	-88.5	-93.5	-98.5
Final longitude	-75.5	-75.5	-75.5	-75.5	-75.5
Distance from western most sample point (m) to western edge of box	3.6E+05	5.3E+05	8.0E+05	1.2E+06	1.7E+06
Time (hours) from western most sample point to western edge of box	16.7	24.7	36.8	6.9	77.0

Table 6. Location of box edges (from Figure 32) in degrees latitude and longitude. Also shown is the time needed for sources from the western most

points of the box to arrive at the western most sampling point.

Table 7a shows the lifetimes generated using an input lifetime of 8 hours and using 3 different fluxes (from Box 1, Box 2 and Box 3) and 5 different sets of 85 sampling locations for a total of 15 groups of 85 measurements of lifetimes. The lifetimes and SO₂ column contents appear to be lognormally distributed (Figure 33). The mean μ_x and variance σ_x^2 for a lognormal distribution are given by the following (Wilks, 1995)

$$\mu_x = \exp[\mu_y + 0.5*\sigma_y^2/2] \quad (17)$$

$$\sigma_x^2 = (\exp[\sigma_y^2] - 1) * \exp[2\mu_y + \sigma_y^2] \quad (18)$$

Where μ_y and σ_y^2 are the mean and variance of the transformed variable $y = \ln(x)$. The lognormal statistics for each of the sets of lifetimes calculated with different fluxes (from Box 1, Box 2 and Box 3) are shown in Table 7b. Table 7c shows the average lifetime of all 15 groups with the standard deviation and the standard error (the standard deviation / $\sqrt{15}$). Statistics for lifetimes calculated using inputs of 16, 24 and 32 hours are shown in Tables 8-10. I calculated the 2- σ uncertainty associated with the lifetimes generated using the method, by accounting for the accuracy (the difference between the median and the 95th percentile of the 15 average lifetimes) and the precision (the standard error). I added these in quadrature and determined there was a 30% uncertainty associated with the method assuming a normal distribution, the uncertainty associated with the method assuming a lognormal distribution was 20%.

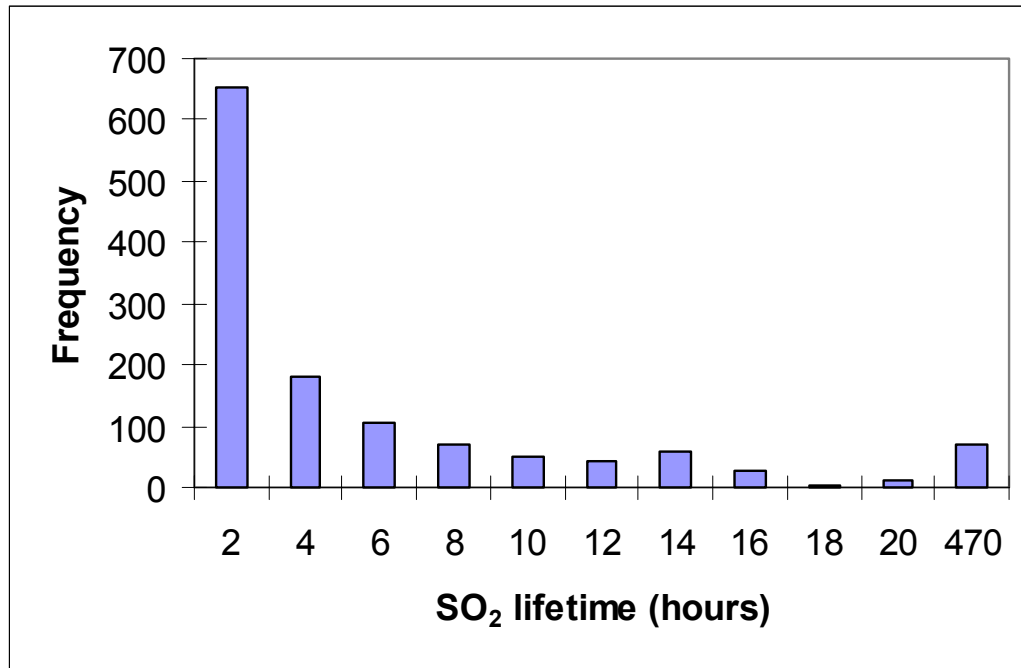


Figure 33. Histogram of SO₂ lifetimes calculated using Gaussian plume dispersion model and an input lifetime of 8 hours.

A						C		
Box 1	Center	North	South	West	East		Normal Distribution	Log-normal Distribution
Mean	9.43	6.65	7.09	5.35	5.87	Mean	7.32	6.25
Standard Error	5.12	2.70	3.59	0.93	1.52	Standard Error	0.44	0.29
Standard Deviation	47.22	24.86	33.14	8.53	14.05	Standard Deviation	1.70	1.11
Box 2	Center	North	South	West	East			
Mean	10.74	7.76	8.28	6.34	7.08			
Standard Error	5.37	2.82	3.77	0.97	1.60			
Standard Deviation	49.48	26.03	34.74	8.97	14.77			
Box 3	Center	North	South	West	East			
Mean	11.31	8.22	8.75	6.74	7.55			
Standard Error	5.53	2.91	3.88	1.00	1.65			
Standard Deviation	50.99	26.82	35.79	9.22	15.22			
B								
Box 1	Center	North	South	West	East			
Mean	5.87	5.33	4.69	6.98	5.49			
Standard Error	3.19	2.60	2.12	4.06	2.96			
Standard Deviation	29.41	23.95	19.58	37.46	27.26			
Box 2	Center	North	South	West	East			
Mean	7.70	6.87	6.42	8.13	7.53			
Standard Error	3.15	2.56	2.35	3.20	3.06			
Standard Deviation	29.07	23.57	21.65	29.49	28.17			
Box 3	Center	North	South	West	East			
Mean	7.99	7.19	6.74	8.05	7.79			
Standard Error	2.78	2.32	2.18	2.59	2.64			
Standard Deviation	25.60	21.37	20.06	23.87	24.36			

Table 7. a) Statistics of SO₂ lifetimes (hours) from profiles generated using a Gaussian plume model assuming a lifetime of 8 hours for boxes 1, 2 and 3 for a) an assumed normal distribution b) an assumed lognormal distribution. c) The average lifetime for all sets (Center, North, South, West and East) for boxes 1, 2 and 3 as well as the standard deviation and standard error (standard deviation / $\sqrt{15}$).

A						C		
Box 3	Center	North	South	West	East		Normal Distribution	Log-normal Distribution
Mean	16.88	13.78	14.49	12.25	13.04	Mean	15.30	14.76
Standard Error	5.90	3.33	4.18	1.45	2.05	Standard Error	0.74	0.42
Standard Deviation	54.43	30.67	38.52	13.38	18.93	Standard Deviation	2.87	1.63
Box 4	Center	North	South	West	East			
Mean	18.54	15.30	16.09	13.72	14.62			
Standard Error	6.08	3.42	4.30	1.50	2.11			
Standard Deviation	56.05	31.53	39.62	13.82	19.44			
Box 5	Center	North	South	West	East			
Mean	22.71	18.80	19.76	16.89	17.99			
Standard Error	7.35	4.13	5.19	1.82	2.55			
Standard Deviation	67.72	38.11	47.88	16.73	23.50			
B								
Box 3	Center	North	South	West	East			
Mean	15.14	14.16	15.51	14.55	14.75			
Standard Error	3.86	3.40	4.52	3.45	3.71			
Standard Deviation	35.58	31.34	41.71	31.79	34.18			
Box 4	Center	North	South	West	East			
Mean	15.39	14.41	16.57	14.85	15.02			
Standard Error	2.65	2.34	3.58	2.47	2.52			
Standard Deviation	24.46	21.56	32.99	22.74	23.24			
Box 5	Center	North	South	West	East			
Mean	18.63	17.50	18.45	18.03	18.10			
Standard Error	3.00	2.67	3.23	2.82	2.80			
Standard Deviation	27.67	24.62	29.75	25.96	25.82			

Table 8 a) Statistics of SO₂ lifetimes (hours) from profiles generated using a Gaussian plume model assuming a lifetime of 16 hours for boxes 3, 4 and 5 for a) an assumed normal distribution b) an assumed lognormal distribution. c) The average lifetime for all sets (Center, North, South, West and East) for boxes 3, 4 and 5 as well as the standard deviation and standard error (standard deviation / $\sqrt{15}$).

A						C		
Box 3	Center	North	South	West	East	Normal Distribution	Log-normal Distribution	
Mean	20.56	17.51	18.34	15.84	16.65	Mean	20.23	20.71
Standard Error	6.06	3.52	4.31	1.70	2.28	Standard Error	1.04	0.73
Standard Deviation	55.86	32.43	39.71	15.69	20.98	Standard Deviation	4.01	2.82
Box 4	Center	North	South	West	East			
Mean	23.73	20.52	21.49	18.77	19.76			
Standard Error	6.22	3.60	4.41	1.76	2.33			
Standard Deviation	57.37	33.19	40.64	16.22	21.46			
Box 5	Center	North	South	West	East			
Mean	29.58	25.68	26.86	23.59	24.81			
Standard Error	7.52	4.36	5.33	2.14	2.82			
Standard Deviation	69.35	40.15	49.15	19.72	26.01			
B								
Box 3	Center	North	South	West	East			
Mean	19.72	18.66	21.70	18.71	19.19			
Standard Error	4.52	4.03	6.21	3.99	4.37			
Standard Deviation	41.68	37.20	57.22	36.77	40.25			
Box 4	Center	North	South	West	East			
Mean	21.15	20.01	24.64	20.08	20.66			
Standard Error	3.00	2.65	4.95	2.74	2.87			
Standard Deviation	27.69	24.46	45.62	25.22	26.45			
Box 5	Center	North	South	West	East			
Mean	25.94	24.68	26.33	24.81	25.14			
Standard Error	3.31	2.97	3.72	3.08	3.06			
Standard Deviation	30.52	27.42	34.26	28.39	28.23			

Table 9. a) Statistics of SO₂ lifetimes (hours) from profiles generated using a Gaussian plume model assuming a lifetime of 24 hours for boxes 3, 4 and 5 for a) an assumed normal distribution b) an assumed lognormal distribution. c) The average lifetime for all sets (Center, North, South, West and East) for boxes 3, 4 and 5 as well as the standard deviation and standard error (standard deviation / $\sqrt{15}$).

A						C		
Box 4	Center	North	South	West	East		Normal Distribution	Log-normal Distribution
Mean	27.58	24.40	25.48	22.50	23.56	Mean	29.17	28.67
Standard Error	6.30	3.71	4.47	1.93	2.48	Standard Error	1.48	1.26
Standard Deviation	58.10	34.18	41.21	17.83	22.83	Standard Deviation	5.75	4.88
Box 5	Center	North	South	West	East			
Mean	34.86	30.99	32.30	28.72	30.04			
Standard Error	7.62	4.49	5.41	2.36	3.01			
Standard Deviation	70.28	41.41	49.88	21.76	27.75			
Box 6	Center	North	South	West	East			
Mean	41.35	36.80	38.34	34.16	35.70			
Standard Error	8.95	5.28	6.36	2.79	3.54			
Standard Deviation	82.52	48.65	58.60	25.68	32.67			
B								
Box 4	Center	North	South	West	East			
Mean	25.44	24.19	30.80	23.95	24.84			
Standard Error	3.30	2.91	6.03	2.96	3.16			
Standard Deviation	30.43	26.87	55.63	27.29	29.16			
Box 5	Center	North	South	West	East			
Mean	31.54	30.21	32.28	30.01	30.50			
Standard Error	3.58	3.23	4.07	3.32	3.29			
Standard Deviation	33.03	29.80	37.56	30.57	30.36			
Box 6	Center	North	South	West	East			
Mean	37.46	35.89	38.16	35.65	36.23			
Standard Error	4.22	3.81	4.73	3.89	3.88			
Standard Deviation	38.91	35.14	43.64	35.89	35.75			

Table 10. a) Statistics of SO₂ lifetimes (hours) from profiles generated using a Gaussian plume model assuming a lifetime of 32 hours for boxes 3, 4 and 5 for a) an assumed normal distribution b) an assumed lognormal distribution. c) The average lifetime for all sets (Center, North, South, West and East) for boxes 3, 4 and 5 as well as the standard deviation and standard error (standard deviation / $\sqrt{15}$).

The above study was used to determine the uncertainty associated with the method. I calculated the actual lifetime of SO₂ for 180 daytime profiles made in June, July and August from 2000-2003 in the Mid-Atlantic region using equation 13. I integrated all aircraft profiles of SO₂ from the lowest altitude where measurements were made (usually 3 m above ground) to 5000 m. The aircraft generally measured SO₂ up to 3000 m. I assumed SO₂ was 0.07 ppb between 5000 m and the highest altitude the aircraft sampled (Thornton et al. 1987; Andronache et al. 1997). Extrapolating the SO₂ to 5000 m added 9% on average to the column measured by the aircraft. I calculated the flux using national inventories and an estimate of the biogenic contribution as described in section 5.2.3. Back trajectories of 12, 24, 32, 40 and 48 hours (with one hour interval outputs) were used to determine which states to include in the flux calculation. The flux associated with each state (or municipality) was weighted by the number of back trajectory points in the state divided by the total number of back trajectory points. The weighted fluxes were then summed. Figure 34 shows 24 hr back trajectories for all 180 profiles.

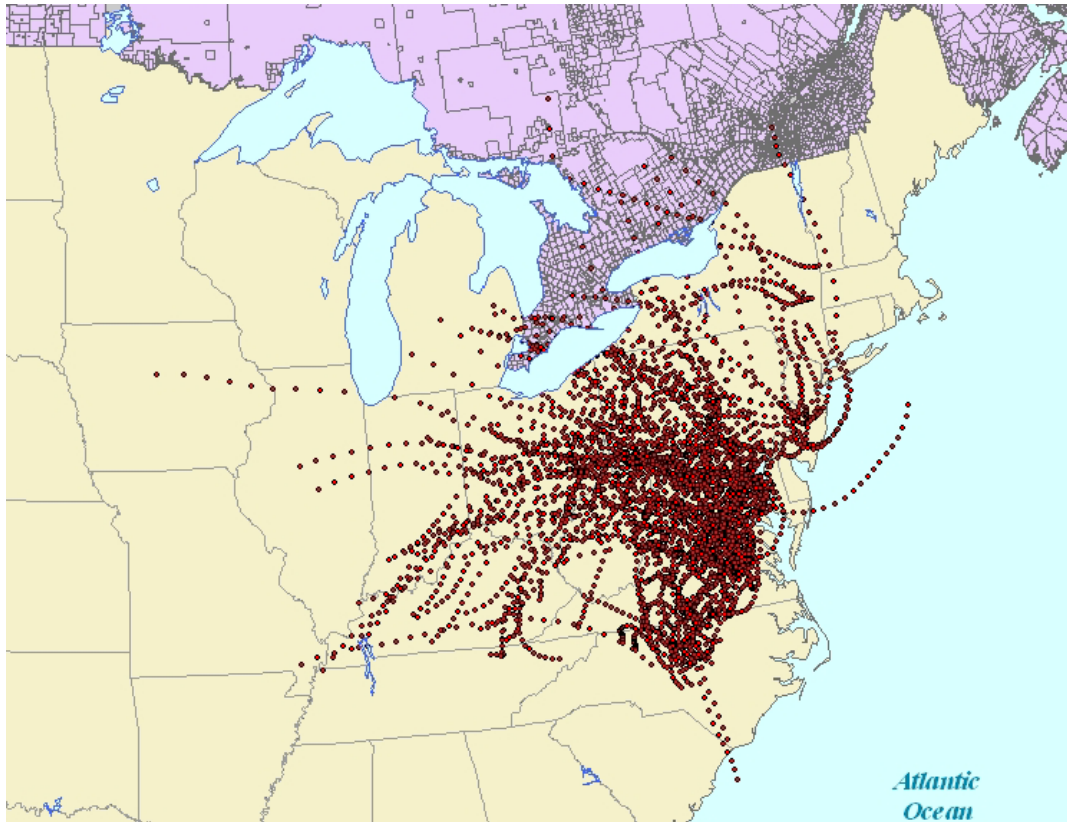


Figure 34. Back trajectories of 24 hr (with one hr intervals) associated with the 180 SO₂ profiles used to calculate the SO₂ lifetime.

Statistics for lifetimes are shown in Table 11 and a histogram of the lifetimes is shown in Figure 35. The fluxes used to calculate the lifetime were determined using 24 hour back trajectories. I calculated the uncertainty associated with the lifetime by accounting for four factors:

1. The uncertainty associated with the method (Equation 13), determined from the simplified Gaussian plume model to be 30% assuming a normalized distribution (the uncertainty associated with the method was 20% assuming a lognormal distribution).

2. The standard error (Table 11), calculated from the standard deviation of all 180 lifetimes and divided by the square root of the number of independent days flights made (in this case 60 days).
3. Uncertainties associated with area and point source emissions (area source emission uncertainties were estimated to be 50% and point source emission uncertainties were estimated to be 16% using the Luke et al. (1997) reported uncertainty).
4. Uncertainties associated with SO₂ measured aboard the University of Maryland research aircraft (assumed to be 16% from Luke et al. (1997)).

To determine the uncertainty associated with area sources I recalculated the lifetime assuming a 50% uncertainty associated with area source emissions and this resulted in a 6% uncertainty associated with the lifetime. I also recalculated the lifetime assuming a 16% uncertainty associated with the point source emissions and this resulted in a 14% uncertainty associated with the lifetime. Therefore the total uncertainty associated with emissions was 20% (14% + 6%). I then added the four factors listed above in quadrature to get the 2- σ uncertainty of 7 hours. The average lifetime is 19 ± 7 hours (at the 95 percent confidence level). The lognormal average lifetime is 20 ± 6 hours. These lifetimes are within the range of model results (for the global average SO₂ lifetime) of 0.6 to 2.6 days (Pham *et al.*, 1995; Chin *et al.*, 1996; Rested *et al.*, 1998; Koch *et al.*, 1999; Roelofs *et al.*, 1998; Berglen *et al.*, 2004) and are on the shorter side of the lifetime estimates.

	Lifetime statistics (hours)
Mean	19
Standard Error	1.7
Median	17
Standard Deviation	13
Minimum	1.5
Maximum	63
Count	180

lognormal distribution	Lifetime statistics (hours)
Mean	20
Standard Deviation	17
Standard Error	2.2

Table 11. Statistics for SO₂ lifetime. The standard error is the standard deviation divided by the square root of 60 (the number of days sampled).

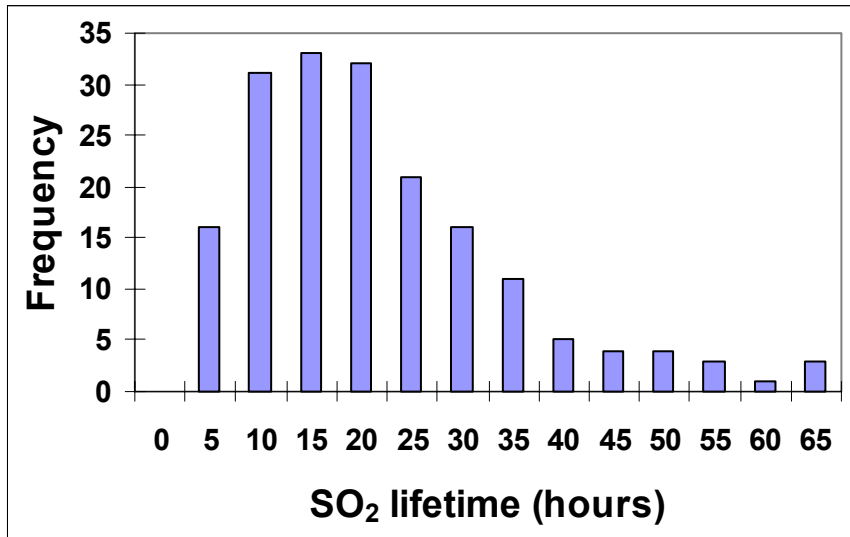


Figure 35. Histogram of SO₂ lifetimes calculated using 24 hour back trajectories to weight the flux. These lifetimes were calculated from 180 profiles measured in the daytime in the summer from 2000-2003.

As discussed above, GOCART uses similar emissions to that presented in national inventories and CMAQ emissions are derived from these national inventories. Therefore it is unlikely that the models over-estimate SO₂ because the emissions of SO₂ are too large. The model over-prediction is likely explained by inadequate oxidation of SO₂ to sulfate in clouds. Mueller et al. (2006) found the CMAQ has difficulty generating typical cloud cover, and reduced cloud cover results in less oxidation of SO₂ by H₂O₂. UMD CMAQ runs may also underestimate cloud cover. Future work should include a verification of CMAQ and GOCART cloud cover.

To investigate the effects of OH on the lifetime of SO₂, the EPA's Community Multi-scale Air Quality (CMAQ) was used to generate OH. CMAQ version 4.5.1 was used with CBIV chemistry, 2002 base year emissions supplied by a regional planning organization, and MM5 version 3 meteorology that was nudged back to observations using data assimilation (Zhang and Anthes, 1982; Grell et al., 1995; Zhang and Zheng, 2004). We have examined OH profiles (from the surface to 645 mbar) from CMAQ for days in 2002 when the University of Maryland Research aircraft made spirals. The CMAQ OH profiles along 24-hr Hysplit back trajectories (ending at 1 km and the location of the UMD aircraft spiral) were averaged to get the 24 hour average OH profile. All of the 24 hour average OH profiles associated with aircraft profiles (made in June through August 2002) were then averaged. This average OH profile represents the daily average OH likely encountered by the SO₂ plumes measured aboard the University of Maryland Research aircraft in 2002. The effective second order rate constant, for the SO₂ + OH reaction, changes by only 2%

between the surface and 645 mbar and so it can be approximated with the high pressure rate constant of 9.5×10^{-13} molecules $\text{cm}^{-3} \text{s}^{-1}$ (JPL, 2006). The approximate lifetime of SO_2 (with respect to OH oxidation), τ_{OH} (seconds), can be calculated as shown below:

$$\tau_{OH} = (k_{OH} \times [OH])^{-1} \quad (5)$$

Here k_{OH} is the high pressure rate constant (molecules $\text{cm}^{-3} \text{s}^{-1}$) and $[OH]$ is the concentration of OH (molecules cm^{-3}). The approximate average SO_2 lifetime, with respect to OH oxidation, for days and locations where the University of Maryland research aircraft made flights is shown as a function of altitude in Figure 36. The average SO_2 lifetime (with respect to OH oxidation) between the surface and 950 mbar, is seven days, and this suggests that OH accounts for only 11% of SO_2 removal.

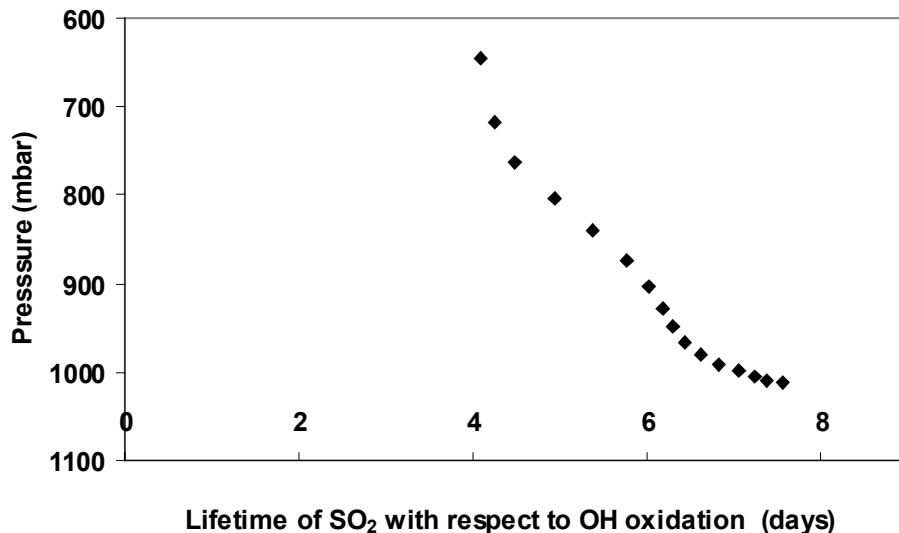


Figure 36.

The lifetime of SO₂ with respect to OH oxidation, where OH was generated from CMAQ. Between the surface and 950 mbar the average lifetime of SO₂ (with respect to OH oxidation) is seven days.

5.3 Conclusions

Aircraft measurements of O₃ were compared with CMAQ. CMAQ over-predicts O₃ from the surface to 600 m, and under-predicts O₃ by 10% between 600 and 2600 m. The CMAQ column content is 3% smaller than the aircraft column content. Possible explanations for the modeled and measured differences include misrepresentation of clouds and aerosols, especially in how they affect photochemistry. I made adjustments in the photochemistry of CMAQ by accounting for aerosol properties measured during a four day event in July 2002. The aerosol properties affected the photolysis of NO₂ and this affected the O₃ production. In general the revised CMAQ model runs over-predicted O₃ above 500 m (~1 ppb) and under-

predicted O₃ below 500 m (1-4 ppb). O₃ reductions are expected for 2018 because stricter regulations on power plant emissions will be implemented and motor vehicles should have cleaner emissions. I tested how the expected decreases in O₃ would be affected if CMAQ accounted for aerosol properties in the NO₂ photochemistry. At the surface, I found that the standard CMAQ runs over-predict O₃ reductions up to 2 ppb and above 500 m the standard CMAQ runs under-predict O₃ reductions up to 2 ppb.

SO₂ from CMAQ and GOCART were also compared with aircraft profiles. The models tend to over-predict the SO₂ column content by 50-55% (GOCART and CMAQ respectively). This over-prediction may result from an over-prediction of the lifetime by either including too large emission sources of SO₂ or not accounting for destruction processes properly. I calculated the summertime lifetime of SO₂ in the Mid-Atlantic region to be 19 ± 7 hours from *in-situ* measurements of SO₂. This is on the short side of typical global model estimates of the SO₂ lifetime. The emissions used in CMAQ and GOCART do not appear to be overestimated and thus it is likely that these models underestimate the rate of removal of SO₂. I examined the CMAQ profiles of OH to determine the lifetime of SO₂ with respect to oxidation by OH. Oxidation by OH roughly accounts for 25% of the SO₂ lifetime. This suggests that CMAQ underestimates oxidation of SO₂ in clouds.

Chapter 6: A Side by Side Comparison of Filter-based PM_{2.5} Measurements at a Suburban Site: A Closure Study

6.1 Introduction

6.1.1 Background

As shown in Chapter 1, numerous counties in the Mid-Atlantic region violated the NAAQS PM_{2.5} standards. Models can be effective tools to determine sources and methods for reducing PM_{2.5}, but this requires accurate measurements of PM_{2.5}. In this Chapter I will give results from ambient measurements an uncertainty analysis of PM_{2.5} samplers used in the Speciation Trends Network. There are no NAAQS standards for speciated mass; however, understanding the PM_{2.5} composition can aid states in determining sources of PM_{2.5}. This is one reason why data is collected from monitors in the Speciation Trends Network. Accurate and precise measurements of the speciated mass are necessary to determine sources and develop strategies to reduce PM_{2.5}. Some work presented in this chapter is from Hains et al. (2007b).

A part of the Maryland Aerosol Research and Characterization study (MARCH- Atlantic) was conducted in Maryland in the Baltimore-Washington corridor. Experiments were carried out during 2002 at a suburban site in Maryland, United States, where two samplers from the U.S. Environmental Protection Agency (USEPA) Speciation Trends Network: Met One Speciation Air Sampling System – STN_S and Thermo Scientific Reference Ambient Air Sampler – STN_R, two Desert Research Institute Sequential Filter Samplers – DRI_F, and a continuous TEOM monitor (Thermo Scientific Tapered Element Oscillating Microbalance, 1400a), all run in parallel. These monitors differ not only in sampling configuration but also in

protocol-specific sample analysis procedures. I will present statistics for PM_{2.5} mass and speciated mass as well as an uncertainty analysis for the different samplers. This Chapter addresses PM_{2.5} concentration and composition as a function of time for summer and winter and the uncertainty associated with PM_{2.5} measurements.

6.1.2 Experiment

STN_{RS} and DRI_F differ in filter types used to collect aerosol as well as flow rates required by the specific cyclone to maintain a stable cut-point at 2.5 μm. Figure 1 illustrates all the sampler configurations and Table 1 summarizes the specifications of the samplers along with analytical methods for determining all species reported. STN_R samplers are considered FRM equivalent (Solomon et al., 2003) and have been compared with other samplers (Peters et al., 2001b, 2001c; Solomon et al., 2003), while DRI_F has been successfully deployed in many air quality studies since 1988 (Chow et al., 1992, 1996; Chen et al., 2002; Watson and Chow, 2002).

	DRI analysis *	RTI analysis **
PM_{2.5}	mass gravimetry	mass gravimetry
Trace elements	x-ray fluorescence	x-ray fluorescence
Sulfate	ion chromatography	ion chromatography
Nitrate	ion chromatography	ion chromatography
Ammonium	automated colorimetry	ion chromatography
Chloride	ion chromatography	chlorine is measured with XRF
Sodium ion	atomic absorption	ion chromatography
Potassium ion	atomic absorption	ion chromatography
EC	thermal optical reflectance (IMPROVE)	thermal optical transmittance (NIOSH***)
OC	thermal optical reflectance (IMPROVE)	thermal optical transmittance (NIOSH***)

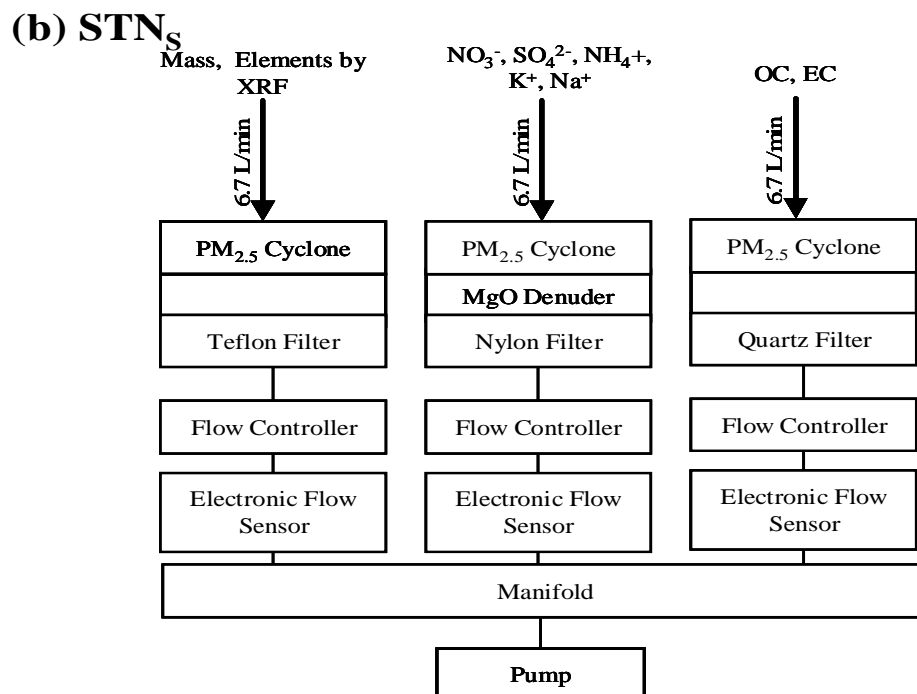
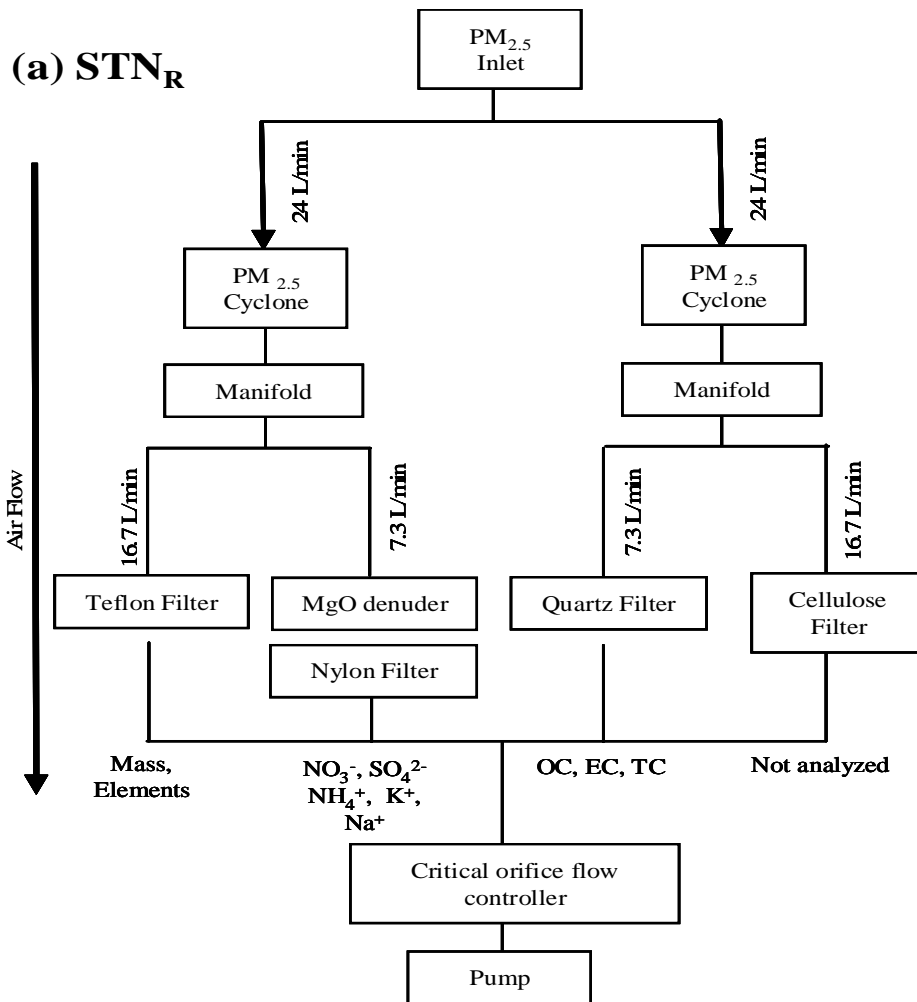
Instrument specifications			
	DRI_F	STN_R	STN_S
Flow (L min⁻¹)	20 ± 0.8	16.7 ± 0.3 (mass and elements)	6.7 ± 0.1
Cyclone	Bendex 240	7.3 ± 0.1 (ions and carbon)	SC 2.141
Nitric acid denuder coating	Aluminum oxide	Magnesium oxide	Magnesium oxide
Sample inlet height (m)	10	15	15
Filter diameter (mm)	47	47	47

Table 1. Analytical methods for species collected by DRI_F (analyzed by DRI) and STN_{RS} (analyzed by RTI) and instrument specifications. Flow rate uncertainties are ± 1-σ.

* DRI operating procedure, 1990; Chow et al., 1993c; Chow et al., 2001.

** US EPA, 2001; Thermo Anderson, 2001.

*** National Institute for Occupational Safety and Health.



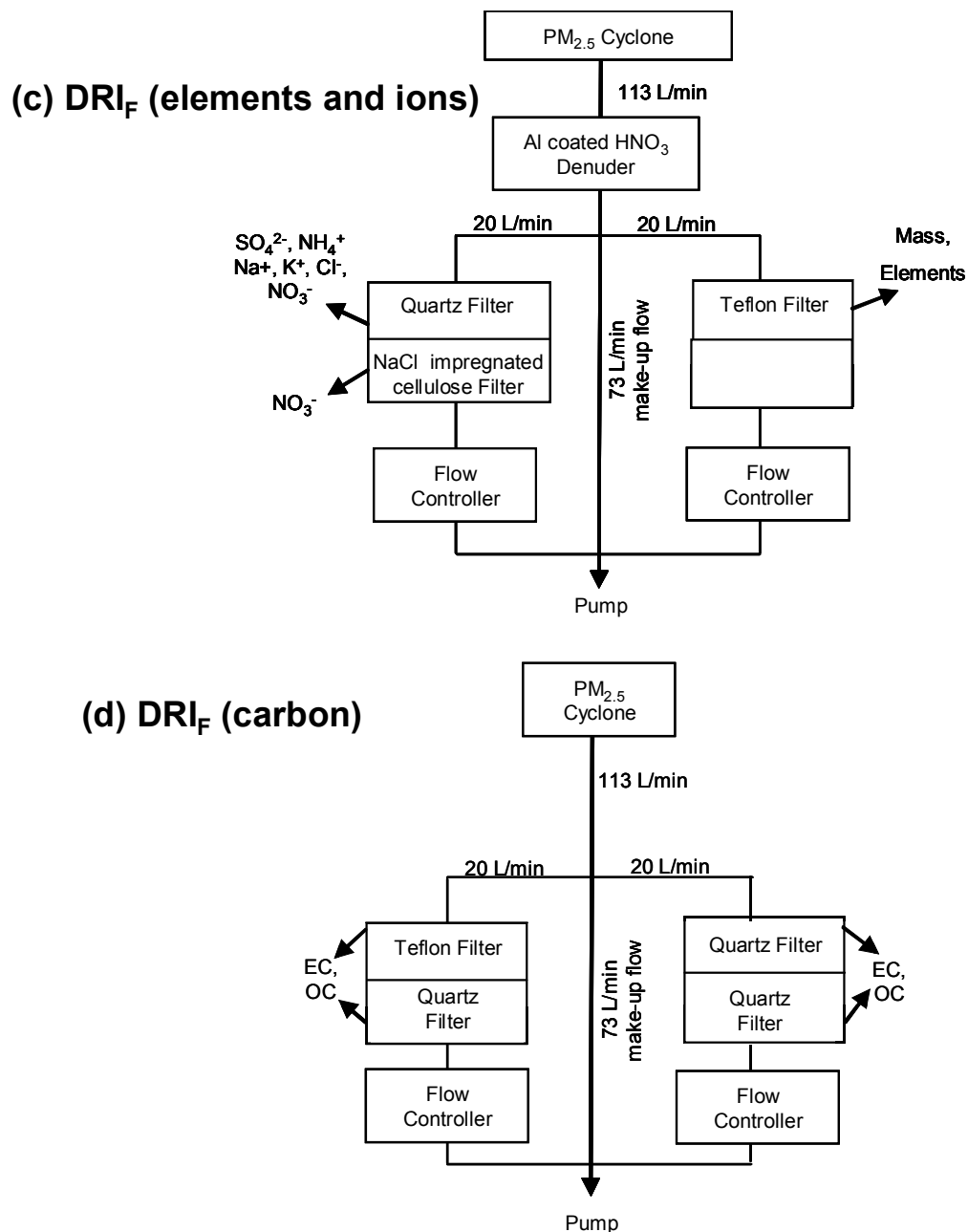


Figure 1. Sampler configuration for a) STN_R (Anderson RAAS) b) STN_S (Met-One SASS) c) DRI_F for elements and ions d) DRI_F for carbonaceous material.

STN_{RS} use a critical orifice to set the flow rate and monitors it with a mass flow sensor. STN_{RS} record ambient temperature and pressure and this is used to convert the mass flow to volumetric flow. The average volumetric flow rate and total volume sampled are recorded for every 24-hr sampling period (Thermo Anderson,

2001; US EPA, 2001). The STN_R flow was calibrated with a flow audit device (BGI deltaCal) and the STN_S flow was calibrated with a bubble meter (Sensidyne/Gilian Gilibrator 2). The DRI_F also uses a critical orifice to maintain constant flow, but the flow was measured and adjusted only once every third day using a rotameter (calibrated against a NIST-traceable Roots meter). The flow rate is recorded before and after each three-day sampling period for the DRI_F , and it can drop by 4% due to buildup of water and particles on the filter. DRI uses the average flow rate (from the initial and final flow) to calculate the total volume sampled and the resultant mass concentration. STN_{RS} record the total volume sampled, which is calculated from the mass flow sensor, temperature and pressure readings.

The sample flow rates for $PM_{2.5}$ mass were 20, 16.7, and 6.7 $L\ min^{-1}$ in DRI_F , STN_R , and STN_S , respectively. Since all the samplers used 47-mm filters, DRI_F imposed an approximately 17% larger face velocity than the STN_R and an 82% larger face velocity than the STN_S around the filter. The STN_R sample flow rate was 7.3 L/min for ions and carbon (similar to the STN_S) and the DRI_F imposed a 64% larger face velocity than the STN_R .

Cyclones used by STN_R and STN_S (Table 1) exhibit different size-selection curves at their specified flow, but Peters et al. (2001c) found that only sites dominated by crustal material had significantly different $PM_{2.5}$ mass collected by the two samplers. Chen et al. (2002) showed a minor crustal material contribution at FME, ~3% of $PM_{2.5}$ mass on average, and therefore strong biases resulting from imperfect size cut are not expected in this study. There may also be diffusion losses of ultrafine particles between the sampler inlet and filter which vary with the different flow rates

used by DRI_F, STN_R and STN_S. Ultrafine particles (< 0.1 μm in diameter) typically contribute little to PM_{2.5} mass in this environment (e.g., Tolocka et al., 2005; Ondov et al., 2006) and strong biases resulting from diffusion losses are unlikely.

The DRI_F used a front quartz-fiber filter with a sodium-chloride-impregnated cellulose backup filter to collect nitrate. The backup filter captured nitrate volatilized from the front filter (Zhang and McMurry, 1992). These filters were located behind a bundle of aluminum-oxide-coated denuders to remove gaseous nitric acid.

Specifications of the denuders are described in Chow et al. (1993a). The STN_R and STN_S collected nitrate particles behind a magnesium-oxide denuder on a single nylon filter (Figure 1). Specifications of the denuders are described in Research Triangle Institute (2000). Frank (2006) found that denuded nylon filters captured more nitrate than undenuded Teflon filters. The different denuders and filter types used by the STN_{RS} and DRI_F in this study likely affect the nitrate collection efficiency as suggested by Solomon et al. (2003) and Frank (2006).

Quartz-fiber filters were used in all the samplers to collect carbonaceous material, and DRI_F used backup filters to account for known sampling artifacts from volatile organic compounds (McDow and Huntzicker, 1990; Turpin et al., 1994; Chow et al., 1996; Chow et al., 2001). For carbon analysis, RTI adopted the Speciation Trends Network-Thermal Optical Transmission (STN-TOT) method (Peterson and Richards, 2002; OC/EC Laboratory, 2003), while DRI used the Interagency Monitoring of Protected Visual Environments-Thermal Optical Reflectance (IMPROVE-TOR) method (Chow et al., 1993b). The IMPROVE-TOR and STN-TOT differ in temperature steps used to extract OC and EC and in optical

charring corrections. They usually yield equivalent total carbon (TC) but different OC and EC concentrations (Chow et al., 2001; Schmid et al., 2001; Chow et al., 2004; Subramanian et al., 2004; Chow et al., 2005a). The IMPROVE-TOR method generally assigns less OC and more EC to a filter sample than the STN-TOT method.

DRI quantified water-soluble potassium (K^+) and sodium (Na^+) with atomic absorption spectroscopy (AAS) and RTI quantified the species with ion chromatography (IC). AAS has a lower detection limit (Chow et al., 1993c; Technology Transfer Network Air Quality System, 2006). There were also differences in blank collection. A field blank was collected every third day for the DRI_F sampler and once every two weeks for the STN_S sampler. Only one field blank was collected for the STN_R sampler. DRI corrected for field blanks as part of their analysis (Watson et al., 1989a; 1989b), but RTI did not. To correct STN_{RS} samples for field blanks, we averaged all STN_{RS} blank values, converted them from mass/filter to $mass/m^3$ using the volume sampled by the instrument, and then subtracted the blanks from the mass measurement.

Sample recovery was scheduled for different time periods. The DRI_F filters were collected from the site every three days, so that used filters remained in the sampler for up to 2.5 days (an average of 1.5 days). The STN_R filters were collected every day, immediately after the sampling finished, so that used filters remained in the sampler for less than 30 minutes. The STN_S filters were collected every other day, so that used filters remained in the sampler for about 12 hours. Chen (2002) performed an audit experiment in summer 2001 at FME with the DRI_F samplers, to determine how filters left in the sampler may be affected by volatile losses and/or

passive collection. He found that OC and TC mass (measured on the front quartz-fiber filters) decreased (by 38% and 29%, respectively) during a 2.5-day period after sampling. Total PM_{2.5} mass and sulfate mass varied less than their respective uncertainties.

A TEOM measures near real-time continuous PM_{2.5} mass. The TEOM at FME drew ambient air in at 3 L/min through a PM_{2.5} cyclone inlet. A constant volumetric flow was achieved using a mass flow controller corrected for ambient temperature and pressure. The air stream was heated to 50°C to maintain a low, relatively constant relative humidity. This heating likely increased volatilization of nitrate and semi-volatile organic compounds. The TEOM measurements were adjusted with scaling factors of $1.03 \times \text{TEOM mass} + 3.0$ to account for loss of semi-volatile material and to be compatible with FRM measurements as recommended by Patashnick and Rupprecht (1991). The mean mass concentration was recorded every 30 minutes, every hour, and every eight hours. All one-hour measurements made in a day were averaged to compare with the DRI_F and STN_S data.

6.2 Results and Discussion

6.2.1 Uncertainty Analysis

Uncertainties associated with flow control and sample analysis need to be accounted for to determine the uncertainty in total PM_{2.5} and each reported species concentration. For STN_{RS}, the species concentration (with units of mass m⁻³ at ambient temperature and pressure) is calculated using the equation below:

$$\text{Species concentration} = m \times (t \times \text{mass flow} \times \text{MM}^{-1} \times R \times T \times P^{-1})^{-1} \quad (1)$$

Here m is the mass of a given species on the filter, t is the time over which sampling occurred, mass flow has units of mass time⁻¹, MM is the molar mass of the air sampled, R is the gas constant (0.08314 L atm K⁻¹ mol⁻¹), T is ambient temperature and P is the ambient pressure. Uncertainties in the calculated concentration reflect uncertainties in the laboratory analysis, the mass flow sensor reading, the temperature reading and the pressure reading. Uncertainties associated with the integration time appear to be less than 1% and are therefore not included in the error analysis. US EPA (2001) states that STN_{RS} temperature readings must be within ± 4 K of the actual temperature and pressure readings must be within ± 0.013 atm of the actual pressure. These ranges represent part of the uncertainty associated with the measurements. The precision associated with a commercial mass flow sensor for the maximum allowable mass flow, i.e., $\pm 2\%$ at the 1- σ level, is used as an estimate of the mass flow sensor uncertainty (Table 1). Flanagan et al. (2006) report the percentage difference in laboratory replicates of $\text{PM}_{2.5}$ and speciated masses. I adopted their values of laboratory uncertainty to calculate the total uncertainty. The resultant ± 2 - σ uncertainty, u , (i.e., the 95% confidence level) associated with $\text{PM}_{2.5}$ mass, sulfate, ammonium, OC or elemental concentration is given by:

$$u = \text{mass concentration} \times [(\delta A/A)^2 + (\delta \text{mf}/\text{mf})^2 + (\delta T/T)^2 + (\delta P/P)^2]^{1/2} \quad (2)$$

Here $\delta A/A$ represents fractional uncertainty associated with the laboratory determination of the mass of a species (uncertainties from Flanagan et al., 2006 were used), $\delta \text{mf}/\text{mf}$ represents the fractional uncertainty associated with the mass flow meter measurements, and $\delta T/T$ and $\delta P/P$ represent the fractional uncertainty

associated with temperature and pressure measurements, respectively. RTI did not report uncertainties for samples analyzed in 2002, however they did report uncertainties for samples measured in the U.S. in 2005 to the EPA's Air Quality System database (AQS, Technology Transfer Network Air Quality System, 2006). The uncertainties reported by RTI include laboratory analysis ($\pm 1\text{-}\sigma$ uncertainty) and a 5% uncertainty associated with flow control and shipment of the samples (RTI, 2004). Using their uncertainties associated with concentrations that were similar to (within $\pm 1\%$ of) the FME samples, and multiplying them by two to obtain the $\pm 2\text{-}\sigma$ uncertainties, I found the resultant uncertainties are on average 2.5 times larger than those calculated from Equation (2) for most species except $\text{PM}_{2.5}$ mass (Table 2). For this Chapter I adopt the RTI reported $\pm 2\text{-}\sigma$ uncertainties. Kim et al., (2005) report fractional uncertainty associated with measurements made in New York, New Jersey and Vermont. Uncertainties they reported for sulfate, ammonium and calcium agreed within 20% of the uncertainties used in this paper.

	Calculated 2σ uncertainty (%)	RTI reported 2σ uncertainty (%)
$\text{PM}_{2.5}$	10	10
OC	12	27
Sulfate	9	16
Ammonium	4	14
Iron	6	16

Table 2. Comparison of $2\text{-}\sigma$ uncertainty in concentration calculated using Equation 2 and RTI reported $2\text{-}\sigma$ uncertainty (from 2005 AQS database).

The DRI_F measures the flow rate using a pressure drop across a critical orifice. Ambient temperature and pressure can alter this flow rate. DRI calculates the uncertainty for each measurement by accounting for the variability between the initial

and final flow tests through 24-hr sampling (typically $\pm 4\%$), as well as precision in laboratory analyses (Chow et al., 1993c). The monthly average concentration of species and the average uncertainty (i.e., the average of all $2\text{-}\sigma$ uncertainty values for the month) for STN_{RS} versus DRI_{F} are shown in Table 3 along with the signal-to-MDL (minimum detection limit) ratio, where the MDL was obtained from Chow et al. 1993c) for the DRI samplers and the median of all 2005 MDL values reported by RTI (to the EPA's AQS database) for the STN samplers. The signal-to-noise ratio for each species can be calculated from Table 3 by dividing the species average by the $2\text{-}\sigma$ uncertainty.

	Deming Slope	Deming Intercept	Correlation (r)	Average Difference (STN _r -DRI _f)	RMS Difference	STN _r species average ($\pm 2\sigma$ uncertainty)	STNR Signal-to-MDL	DRI _f Signal-to-MDL	DRI _f species average ($\pm 2\sigma$ uncertainty)
PM_{2.5}	0.76	0.62	0.98	1.47	1.66	8.77 \pm 0.94	11.9	8.58	7.30 \pm 0.98
Sulfate	0.89	-0.01	0.94	0.28	0.35	2.32 \pm 0.40	193	240	2.04 \pm 0.27
Ammonium	0.98	-0.03	0.92	0.05	0.14	1.02 \pm 0.14	60.2	115	0.98 \pm 0.12
Nitrate (with backup*)	0.80	-0.22	0.97	0.52	0.57	1.49 \pm 0.29	171	115	0.97 \pm 0.11
Nitrate (no backup)	0.89	-0.71	0.93	0.88	0.93	1.49 \pm 0.29	171	72	0.61 \pm 0.04
OC	0.68	0.72	0.80	-0.12	0.73	1.88 \pm 0.63	7.82	58.7	2.00 \pm 0.53
EC	2.72	-0.20	0.65	-0.40	0.49	0.35 \pm 0.45	1.45	22.2	0.75 \pm 0.18
TC	0.91	0.60	0.80	-0.52	0.97	2.23 \pm 0.78	9.28	80.7	2.74 \pm 0.61
Bromine	0.66	1.62	0.88	-0.61	1.10	2.95 \pm 1.52	5.46	21.0	3.56 \pm 1.66
Calcium	0.75	1.25	0.85	3.20	4.72	17.8 \pm 4.79	2.40	19.2	14.6 \pm 9.40
Potassium	0.92	5.46	0.97	-1.59	5.06	47.4 \pm 7.94	6.59	64.5	49.0 \pm 10.5
Iron	0.82	3.45	0.95	4.78	9.51	46.4 \pm 6.68	22.12	245.1	41.7 \pm 5.63
Silicon	2.06	-25.01	0.50	-6.72	16.71	29.9 \pm 12.7	2.98	24.4	36.6 \pm 10.7
Titanium	0.71	-0.25	0.48	1.08	1.95	2.84 \pm 2.72	0.57	3.5	1.76 \pm 52.2

Table 3a. January average concentrations and uncertainties for PM_{2.5}, sulfate, ammonium, nitrate, OC, EC, TC, bromine, calcium, potassium, iron, silicon and titanium measured with the STN_{RS} and DRIF. The $\pm 2\text{-}\sigma$ uncertainty is just the average of all uncertainties for the month. Deming slope, intercept, correlation coefficient, monthly average difference and RMS difference for species measured with STN_R and DRIF in January and STN_S and DRIF in July are presented. Slopes and intercepts were calculated with the y-axis = DRIF and the x-axis = STN_{RS}. Bromine, calcium, potassium, iron, silicon and titanium are reported in units of ng/m³ and shaded in grey. All other species are reported in units of $\mu\text{g}/\text{m}^3$.

*Only DRIF collected nitrate with a front and backup filter.

	Deming Slope	Deming Intercept	Deming Correlation (r)	Average Difference (STN _s -DRI _f)	RMS Difference	STN _s species average ($\pm 2\sigma$ uncertainty)	STN _s Signal-to-MDL	DRI _f species average ($\pm 2\sigma$ uncertainty)
PM_{2.5}	0.88	-0.50	0.96	3.75	5.59	27.8 \pm 2.82	37.62	24.4 \pm 1.29
Sulfate	0.89	-0.20	0.97	1.29	2.28	9.72 \pm 1.43	810.10	8.44 \pm 0.43
Ammonium	1.08	0.10	0.95	-0.32	0.73	2.61 \pm 0.36	153.51	2.93 \pm 0.24
Nitrate (with backup*)	0.62	0.17	0.54	0.06	0.25	0.60 \pm 0.17	68.89	0.54 \pm 0.05
Nitrate (no backup)	0.01	0.03	0.13	0.57	0.63	0.60 \pm 0.17	68.89	0.03 \pm 0.04
OC	0.93	-0.14	0.99	0.64	1.14	6.97 \pm 1.35	29.05	6.33 \pm 0.63
EC	2.02	0.03	0.58	-0.51	0.62	0.47 \pm 0.48	1.98	0.98 \pm 0.33
TC	0.97	0.12	0.98	0.13	1.03	7.45 \pm 1.45	31.03	7.32 \pm 0.72
Bromine	0.82	1.06	0.88	-0.42	1.15	3.58 \pm 1.45	6.63	4.00 \pm 0.52
Calcium	0.79	-2.92	0.89	14.95	26.73	56.1 \pm 8.39	7.57	41.1 \pm 3.79
Potassium	0.92	3.00	0.94	7.51	54.82	135 \pm 12.3	18.87	128 \pm 7.64
Iron	0.98	-6.39	0.88	7.85	44.62	91.0 \pm 15.7	43.35	83.2 \pm 5.85
Silicon	0.84	9.51	0.88	19.61	148.55	175 \pm 26.7	17.65	157 \pm 17.0
Titanium	0.45	1.47	0.58	2.73	8.68	7.68 \pm 3.21	1.54	4.95 \pm 18.6

Table 3 b

Same as Table 3 a, but for July.

6.2.2 Gravimetric Mass Comparisons

Comparisons of daily STN_R and STN_S $PM_{2.5}$ with DRI_F $PM_{2.5}$ are shown in Figure 2 and their error bars (representing the $\pm 2\text{-}\sigma$ uncertainty) overlap only part of the time. Table 3 shows the Deming slope and intercept, which reduces variance in both independent (x) and dependant (y) variables (Cornbleet and Gochman, 1979), as well as the correlation coefficient, monthly average difference and monthly RMS difference between the two pairs of measurements. Good correlations ($r \sim 0.95$) are found between STN_R and DRI_F and between STN_S and DRI_F with respect to $PM_{2.5}$ mass, though both the STN_R and STN_S measurements are generally larger than the DRI_F measurements. The percentage differences ($[(STN_{RS}-DRI_F) / (STN_{RS} + DRI_F)]/2 \times 100$) ranged from 8 to 31% between daily $PM_{2.5}$ from STN_R and DRI_F and from -38 to 67% between STN_S and DRI_F . To determine whether the daily differences were statistically significant I calculated the z-test values for each day using the standard formula (Wilks, 1995):

$$z = \{(xbar_1 - xbar_2) - E[xbar_1 - xbar_2]\} / (s_1^2/n_1 + s_2^2/n_2)^{1/2} \quad (3)$$

Here $xbar_1$ and $xbar_2$ are the individual measurement of $PM_{2.5}$ from STN_{RS} and DRI_F , respectively. The $s_{1(2)}$ represents the STN_{RS} (DRI_F) $\pm 1\text{-}\sigma$ uncertainty value for the specified day. It is assumed that $n = 1$ and the expected value of the difference between $xbar_1$ and $xbar_2$, i.e., $E[xbar_1 - xbar_2]$, is zero. A z-value less than 1.96 indicates the two measurements are significantly different at the 95% confidence level. Table 4 shows the percentage of days when the paired measurements were significantly different under this test. In January 62% of the daily measurements of

PM_{2.5} were significantly different, and in July this percentage was lowered slightly to 50%.

	Percentage of significantly different values January	Percentage of significantly different values July
PM _{2.5}	62%	50%
Nitrate	100%	0%
Sulfate	15%	33%
Ammonium	15%	38%
OC	36%	8%
EC	NA	NA
TC	69%	8%
Bromine	0%	5%
Calcium	NA	65%
Potassium	0%	26%
Iron	15%	29%
Silicon	29%	30%
Titanium	NA	NA

Table 4. Percentage of days when the species measured with STN_{RS} and DRI_F were significantly different at the 95% confidence level. Only species with concentrations greater than three times the MDL were compared. Comparisons could not be made for EC, calcium (January), nitrate (July) or titanium because over half of the measurements were too small.

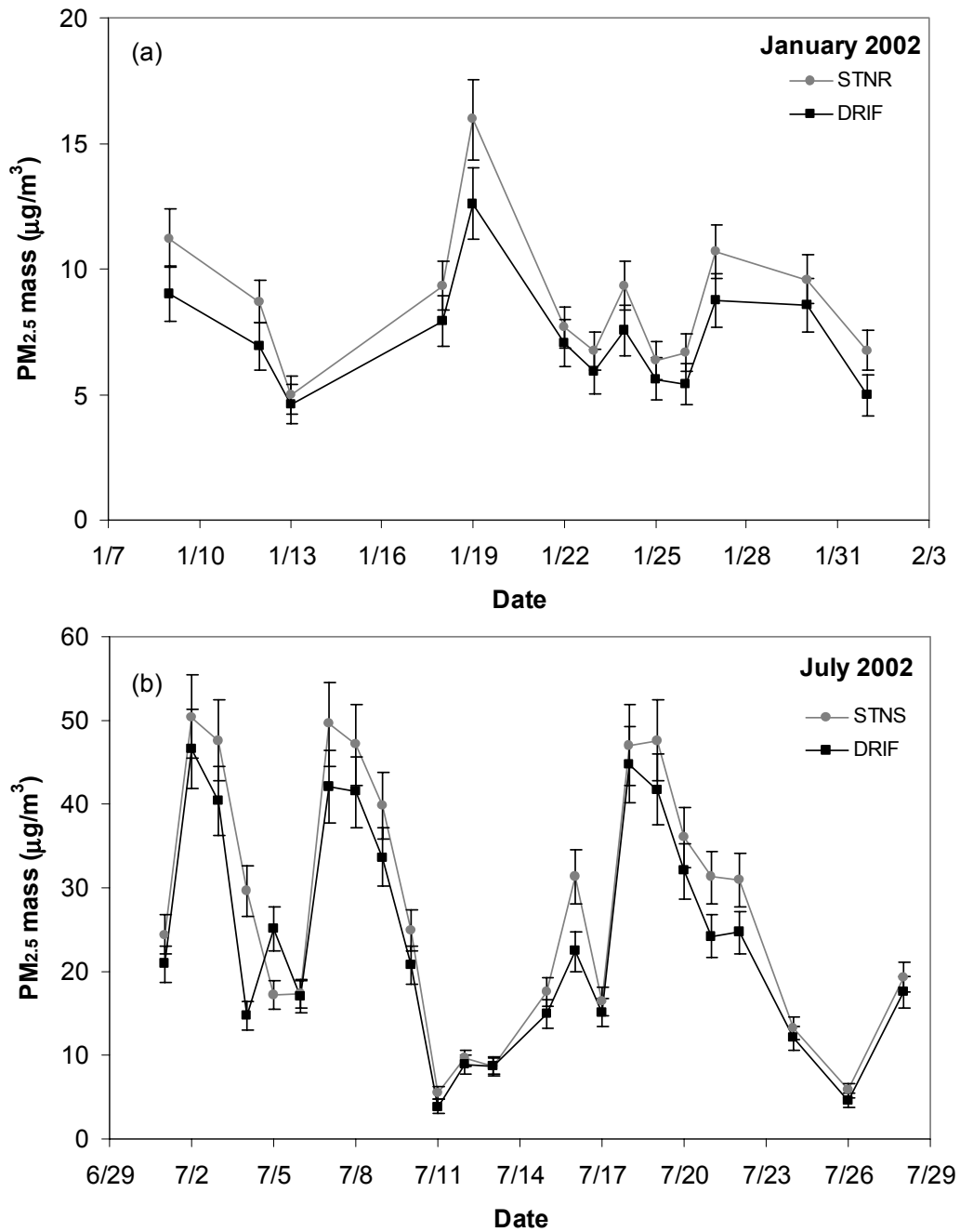


Figure 2. Time series of PM_{2.5} concentrations measured with STN_{RS} and DRIF for January (a) and July (b). Error bars represent ±2-σ uncertainty.

Watson and Chow (2002) compared mass concentrations obtained with the STN_R and DRIF (both analyses were performed at DRI) and found similar results.

They attribute the discrepancies between the DRI_F and the STN_R to different instrument inlet designs, flow controls, and resulting cyclone cutoff efficiencies. As discussed in the experimental section above, large particle intrusion is not expected to be a major issue at FME despite the uncertainty in the flow and size cut. Other reasons for the inter-sampler discrepancies include differences in face velocity which may result in losses of volatile material. For submicrometer particles, the overall filter collection efficiency decreases with increasing face velocity (Liu et al. 1983; Lippmann 1995; McDow and Hutzicker, 1990). The overall efficiency of membrane filters, however, is close to 100% for particles larger than the pore size (Lippmann 1995), which is $\sim 0.2 \mu\text{m}$ in this study.

The TEOM data are available for half of July 2002, and comparisons were made between it and the DRI_F and STN_S . The DRI_F and STN_S versus TEOM have r -values of 0.95 and slopes within 11% of unity (Table 5). These results agree with prior studies (Chen et al., 2003; Rees et al., 2004; Lee et al., 2005a; Lee et al., 2005b). The RMS difference is greater for STN_S -TEOM than DRI_F -TEOM. The STN_S - TEOM average difference is positive and about half of the RMS difference, while the DRI_F -TEOM average difference is slightly negative and about 1/8 of the RMS difference (Table 5). The magnitude of these differences indicates a systematic bias (in addition to random noise) between the STN_S and TEOM measurements. In contrast, deviations between the DRI_F and TEOM appear to be random in nature (Figure 3a) and generally fall within 10% of the Deming regression line. Chen (2002) and Chen et al. (2003) found similar results when comparing the DRI_F to the TEOM in summer months from 1999-2001. The addition of the $3.0 \mu\text{g}/\text{m}^3$ offset added to

TEOM measurements may not fully compensate for volatile losses from the heated inlet.

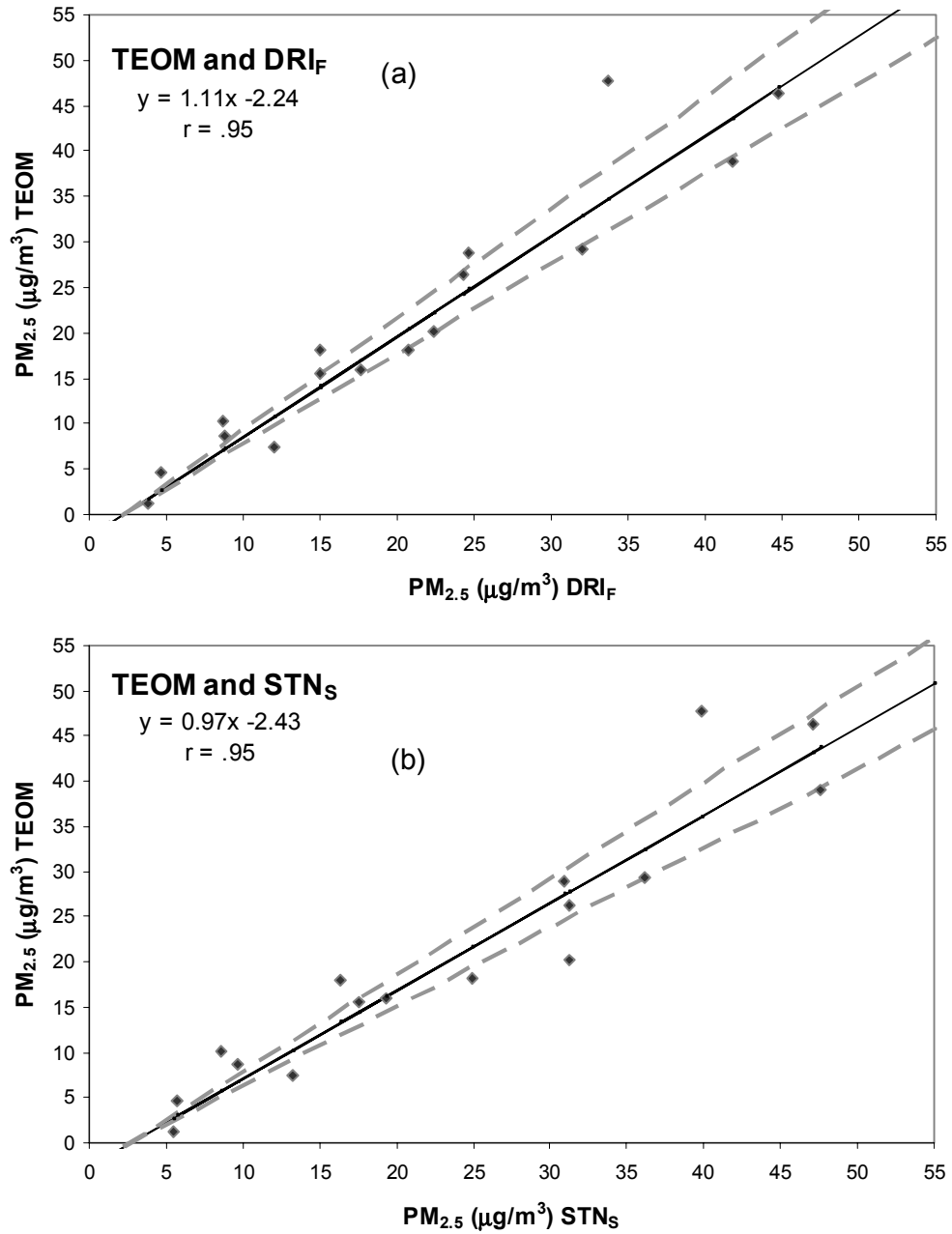


Figure 3. Comparisons of PM_{2.5} total mass between TEOM and (a) DRI_F and (b) STN_S. Deming regression line shown in black, $\pm 10\%$ (of the regression line) shown in broken grey. The TEOM and DRI_F generally agree within experimental error.

x	y	Slope	Intercept	Correlation (r)	N	Average Difference (x-y)	RMS Difference	Monthly Average x	Monthly Average y
STN _s	TEOM	0.97	-2.64	0.95	16	2.96	5.35	24.06	21.10
DRI _F	TEOM	1.11	-2.24	0.95	16	-0.48	4.28	20.62	21.10

Table 5. Deming slope, intercept, correlation, and average and RMS difference ($\mu\text{g}/\text{m}^3$) for the STN_s versus TEOM, and the DRI_F versus TEOM as well as N, number of days comparisons were made. The averages ($\mu\text{g}/\text{m}^3$) for each sampler for the 2nd half of July are also given.

6.2.3 Chemical Compositions

Besides gravimetric mass, Tables 3 and 4 include the statistics and comparisons of major contributing species to PM_{2.5} including sulfate, ammonium,

nitrate, OC, EC, TC, bromine and potassium as well as crustal mass made of calcium, iron, silicon and titanium. In January, 15% of the paired sulfate measurements were found to be significantly different, but in July this fraction increased to 33%.

Although sulfate measurements from the different instruments are well correlated with r -values greater than 0.94, the STN_{RS} consistently report higher values than the DRI_F . Since the average deviation is 14 to 17% for both $PM_{2.5}$ and sulfate (Table 3), there appears to be a bias in the flow control, allowing more or less sample volume than specified. It should be noted that sulfate concentration is not sensitive to a small difference in the size cut. Chen (2002) show that sulfate mass from DRI_F increases by 4% when filters are exposed for 72 hours after sampling while total mass may either increase (by 1%) or decrease (by 3%). This suggests that the different filter exposure times may have minimal effects on the differences between DRI_F and STN_{RS} for sulfate and mass.

DRI_F and STN_{RS} measure nitrate on different filter substrates behind different denuder configurations (Figure 1). Comparisons between the front only DRI_F filters and front plus backup DRI_F filters with STN_{RS} have both been made. The nitrate concentrations are well correlated in the winter (without or with backup filter concentrations added), although DRI_F measures only 3 to 65% of the average STN_R nitrate (without or with backup filter concentration added; see Table 3). All differences were found statistically significant (Table 4). The nylon filters used by STN_R appear to retain much more nitrate than single quartz-fiber filters. Moreover, the DRI_F filters remained in the field for up to 2.5 days longer, and this led to more nitrate loss through volatilization. The DRI_F July average nitrate (on the front filter)

is below its 2- σ uncertainty and most of the nitrate (above the 2- σ uncertainty) was found on the backup filter. The July measurements of nitrate do not correlate well ($r = 0.13$ front filter only, $r = 0.54$ front and backup filter), and the DRI_F nitrate accounts for 6 to 90% of the STN_S (without or with backup filters added). When the DRI_F front and backup nitrate are compared with STN_S , there are no significant differences (Table 4).

Ammonium shows good inter-sampler correlation with r -values greater than 0.92, and significant differences in 15 to 38% of the daily measurements in January and July. In January the average difference as well as the RMS difference between the DRI_F and the STN_R measured ammonium is negligible. In July the DRI_F monthly average is slightly greater than the STN_S average, but within 11% (Table 3). Like nitrate, ammonium can also be volatilized readily (Appel and Tokiwa, 1981; Appel et al., 1984; Chow et al., 2005b; Pathak et al., 2004). Pathak et al., 2004 found that there were substantially less losses of ammonium than nitrate on filter samplers possibly resulting from chemical reactions on the filter.

For total carbon (TC) that is independent of thermal/optical method, the STN_S concentration is similar to that of the DRI_F . The STN_R concentration is less than DRI_F , but within 20%. Inter-sampler differences of TC were significant 8% of the time in July and 69% in January (Table 4). Correlation between the DRI_F and STN_S is good in July with an r -value of 0.98, much better than the r -value of 0.80 between the DRI_F and STN_R in January. Since the TC concentration was low in January ($<1/3$ of that in July) and close to the MDL, more scatter could be expected. The OC/EC ratio was 5.4 in -January, compared with 14.8 in July (based on STN_{RS}). This reflects

larger secondary organic aerosol contributions in the summer (Polidori et al., 2006). OC correlation was similar to that of TC with an r-value of 0.99 in July and an r-value of 0.80 in January. OC is the dominant fraction of TC in both seasons and this explains the similar relationship. EC correlation is poor between the paired measurements both in winter and summer and the STN_{RS} EC are generally only ~50% of the DRI_F EC, likely because of the different ways $STN-TOT$ and $IMPROVE-TOR$ define EC (Chow et al., 1993b; Peterson and Richards, 2002; OC/EC Laboratory, 2003). STN_{RS} EC concentrations were generally less than 3 times the MDL and for this reason the z-test comparison was not performed.

McDow and Hutzicker (1990) demonstrate that increases in face velocity increase volatilization of organic species. The DRI_F and STN_{RS} all use 47-mm filters. Assuming that the filter holder has negligible effects on the area of the filter impacted by the flow, the face velocity can be approximated by the flow rates such that the DRI_F has the largest face velocity (with a flow rate of 20 L min^{-1}) for OC collection, followed by STN_R and STN_S (with flow rates of $\sim 7 \text{ L min}^{-1}$). In July the average DRI_F OC and TC are smaller than the STN_S , and these differences may be partly attributed to the effects of face velocity. The higher temperatures in July might facilitate OC volatilization, especially from the DRI_F filters that were left in the field for a longer time period. However, in January the DRI_F TC is larger than the STN_R . This is explained neither by flow control differences nor by face velocity. A problem specific to the TC and OC measurement is the blank correction and the only field blank collected for the STN_R sampler showed relatively high OC. The STN_R field blank OC was on average 50% of the non-blank corrected OC, while the STN_S and

DRI_F field blank OC was on average 20% of the non-blank corrected OC. The winter STN_R TC and OC might have been overcorrected. The quantification of OC mass might also be affected by different thermal analysis protocols that define the OC and EC split differently.

Inter-sampler comparisons of crustal species, including silicon (in July), calcium and iron, as well as trace elemental species that are > 3 times the MDL (bromine and potassium) all have r-values greater than 0.85. STN_S generally reports larger crustal species concentrations than DRI_F does, consistent with the situation for PM_{2.5} mass and sulfate. The smaller DRI_F concentration could be reflected by either a small DRI_F/STN_S slope (< 1) or a negative intercept (Table 3). STN_{RS} and DRI_F differences for silicon, calcium, iron and potassium concentrations were significant 0 to 30% of the time in January and 25 to 65% of the time in July. Calcium (in January), and Titanium, were below three times the MDL and thus the z-test was not performed for these species.

6.2.4 Mass Closure

Reconstructed mass from the sum of individual species determines the degree to which the gravimetrically measured total mass is explained by the measured species (Chow et al., 1996; Andrews et al., 2000; Malm et al., 2005; Frank et al., 2006). To reconstruct the PM_{2.5} mass, the crustal mass, organic mass and mass of all other species are added together. The crustal mass is the sum of silicon, calcium, iron and titanium multiplied by factors to account for oxygen associated with them (Frank, 2006) as shown below:

$$\text{Crustal mass} = 3.73 \times \text{silicon} + 1.63 \times \text{calcium} + 2.42 \times \text{iron} + 1.94 \times \text{titanium} \quad (4)$$

There is much debate over what factor should be used to determine the oxygen, nitrogen and hydrogen associated with organic carbon, and this factor can range from 1.2 to 2.5 (Turpin and Lim 2001; Rees et al., 2004; El-Zanan et al., 2005). We multiply the organic carbon by a factor of 1.8, similar to Rees et al. (2004), because the area is highly influenced by regional sources. Front and backup filter nitrate are included in the DRI_F reconstructed mass.

The reconstructed mass from the DRI_F samplers is well correlated with the measured gravimetric mass in both January and July ($r = 0.94 - 0.99$, see Table 6), and a good correlation is also found for STN_S . The July DRI_F reconstructed $\text{PM}_{2.5}$ mass overestimates the gravimetric mass by 6% while the STN_S reconstructed mass underestimates the gravimetric mass by just 3%. For STN_R in January, the average measured and reconstructed mass differ by less 2%, although their correlation is not as good ($r = 0.80$). Histograms of the difference between the gravimetric and reconstructed masses (i.e., the residuals) are shown in Figure 4. In January, the DRI_F residuals are shifted negatively from the normal distribution, with a mode at $-1 \mu\text{g m}^{-3}$. The STN_R residuals have a mode at zero and an apparent outlier, which explains the poorer correlation. There is better overlap between the DRI_F and STN_S residuals in July, but the DRI_F residuals are still less than STN_S residuals.

	Average gravimetric mass	Average reconstructed mass	RMS difference	Average difference (gravimetric - reconstructed)	Slope	Intercept	Correlation (r)
January							
DRI _F	7.3	8.8	1.7	-1.5	1.2	0.38	0.94
STN _R	8.8	8.9	1.7	-0.12	0.93	0.73	0.80
July							
DRI _F	24.1	25.5	2.1	-1.4	0.99	1.5	0.99
STN _S	27.8	27.3	3.2	0.57	0.99	-0.37	0.98

Table 6. Average reconstructed mass for STN_{RS} and DRI_F for January and July (units are in $\mu\text{g}/\text{m}^3$). Also shown is the Deming slope, intercept, and correlation for the gravimetric (x-axis) and reconstructed mass (y-axis). The DRI reconstructed mass is generally larger than the gravimetric mass and the STN reconstructed mass is generally smaller than the gravimetric mass.

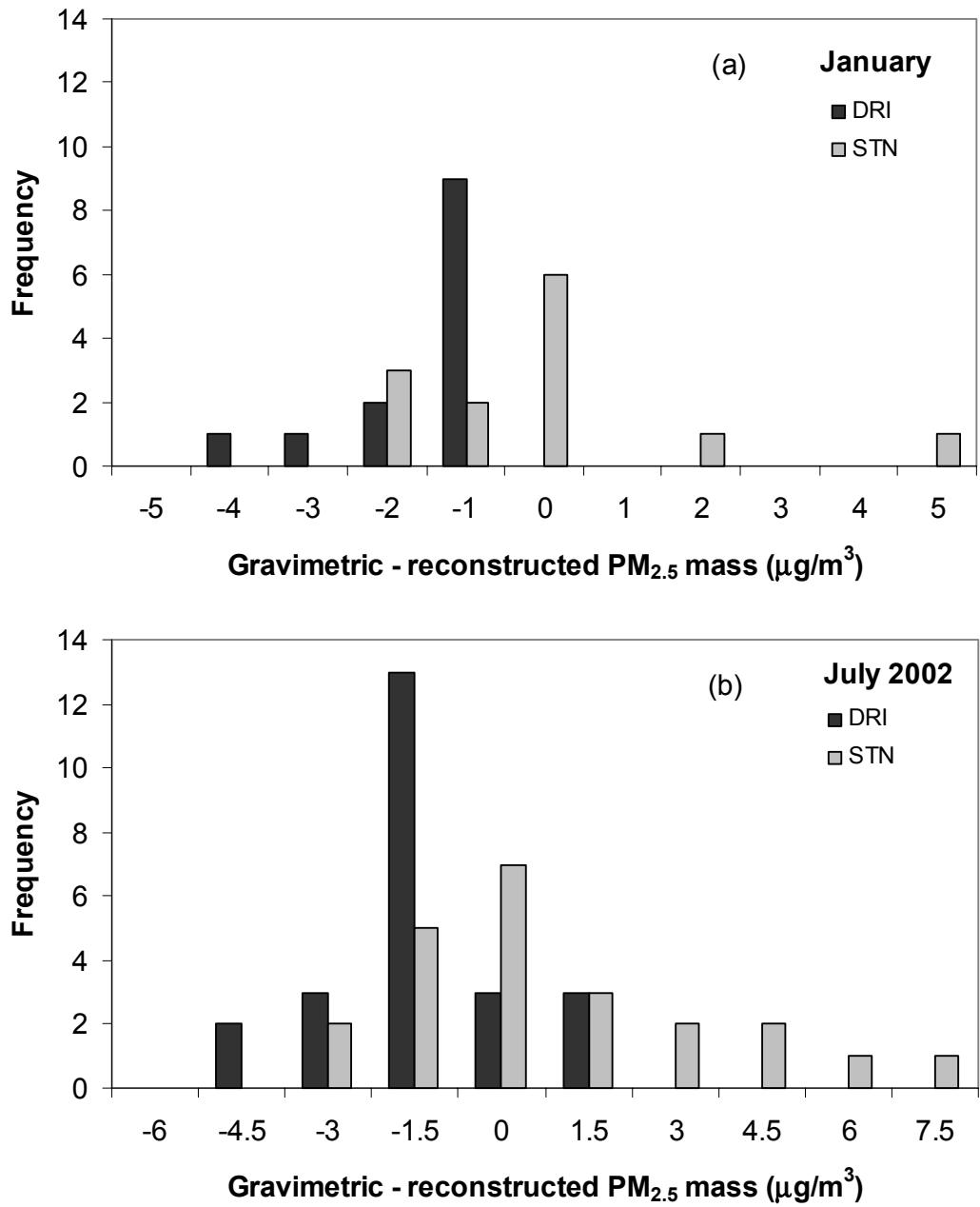


Figure 4. Frequency distribution of gravimetric – reconstructed differences (residuals), for January DRI_F and STN_R and July DRI_F and STN_S.

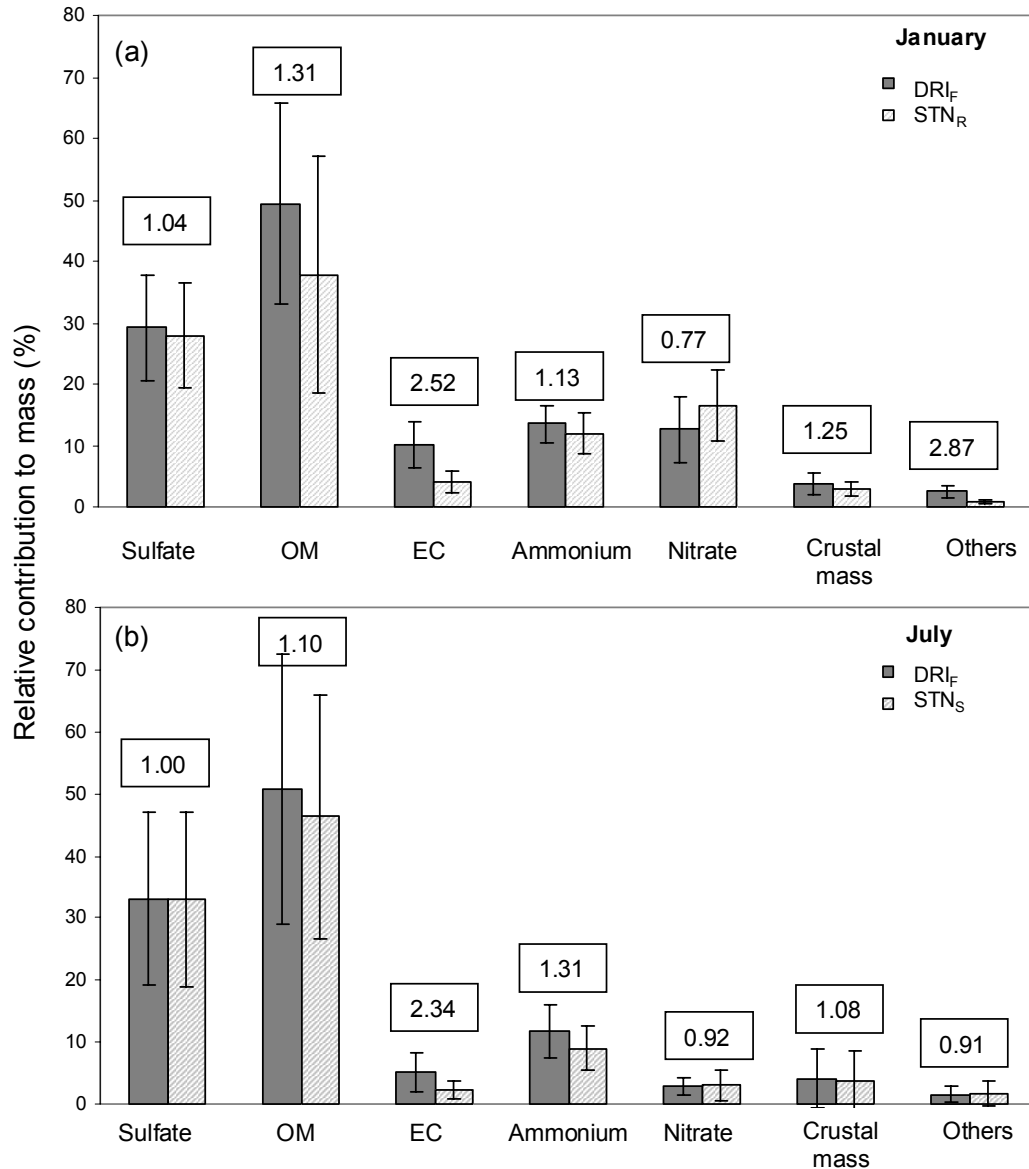


Figure 5. Contributions of individual species to PM_{2.5} mass (relative contribution) for (a) January and (b) July. Numbers in boxes are the DRI_F relative contribution divided by STN_{RS} relative contribution. Error bars represent the standard deviation of the relative contributions.

Figure 5 shows the contributions of sulfate, organic matter (OM = OC × 1.8), EC, ammonium, nitrate, crustal mass and the sum of all other species, to total mass (the relative contribution) as well as the ratios of DRI_F/STN_{RS} relative contribution.

Here nitrate from the front and backup filter of DRI_F was used. In January and July STN_{RS} report larger sulfate concentrations, but the relative contribution of sulfate to total mass is similar for STN_{RS} and DRI_F (shown by the ratios of relative contribution [DRI_F/STN_{RS}] being close to unity in Figure 5). A systematic bias could explain why the difference between the sulfate concentrations does not show up in the relative contributions. This bias can result from differences in how the two instruments record volume as described in the experimental section. In January DRI_F reports more OM concentration than STN_R and the relative contribution of OM to total mass from DRI_F is greater than that from STN_R. In July DRI_F reports less OM concentration than STN_S and the relative contribution of OM to total mass from DRI_F is greater than that from STN_S. This should not negate the above argument that there is a systematic bias between the two instruments. The relative contribution of OM to total mass is affected by artifacts in both mass and OC measurements. The differences in OM relative contribution are not the same as the differences in sulfate relative contribution because of issues related to organic sampling artifacts, blank correction and analysis protocols. The mass closure of DRI_F usually exceeds 100%, consistent with an uncorrected positive organic sampling artifact. For STN_R, however, the problem associated with organic sampling artifacts has been offset by a relatively high blank subtraction in this study. The organic sampling artifact is a major issue regarding PM_{2.5} mass closure, particularly for low PM-loaded samples.

6.3 Conclusions

Measurements from the DRI and RTI analyzed samplers (DRI_F versus STN_R and DRI_F versus STN_S) at Fort Meade, MD were generally well correlated.

- $PM_{2.5}$, sulfate, OC, TC and ammonium all had r-values in excess of 0.8.
- The STN method reported larger $PM_{2.5}$ mass than the DRI method by 14 – 17% and generally showed larger concentrations than the DRI_F .
- Possible causes for the bias between STN_{RS} and DRI_F include different flow monitoring strategies, DRI_F losses of volatile species because used filters remained in the field for a longer time and/or because face velocities were larger than those for the STN_{RS} .
- With the current state of ambient monitoring it is reasonable to expect uncertainties of at least 20% (at the 95% confidence level) for $PM_{2.5}$, sulfate, ammonium, and organic matter.

Even though the $PM_{2.5}$ mass measurements were well correlated, differences between the measurements were statistically significant more than 50% of the time under the current uncertainty estimates. The uncertainty associated with $PM_{2.5}$ mass must be raised from 10% to 20% for January measurements, and from 10% to 28% for July measurements, to make the differences statistically significant only 5% of the time (using a z-test and assuming only random errors). Even though the measurements of speciated mass were well correlated, the differences between the samplers are statistically significant at the 95% confidence level from 5 to 100% of the time. Particularly, measurements of EC did not compare well. Two different analysis methods, IMPROVE-TOR and STN-TOT, were used, and these two methods are known to define EC differently. Nitrate correlated well between the two samplers in January, however the DRI_F measurements were substantially smaller than those

from the STN_R and all the measurements were significantly different using a z-test. In July the nitrate correlation was weaker, possibly because of the increased volatility and lower concentration of the nitrate aerosol. It is likely that the STN_{RS} nylon filters retained more nitrate than the DRI_F quartz filters (e.g. Frank 2006). At FME this problem was mitigated somewhat because DRI_F used backup filters. Residuals of gravimetric – reconstructed mass were generally small and negative for both DRI_F and STN_{RS}. The differences possibly result from the organic sampling artifact and/or conversion factor between the mass of organic carbon and organic matter.

Overall, the error estimates used in the current STN network (i.e., from AQS) may be too low to account for the actual uncertainty in the measurements, and to some extent this may impact the conclusions of trend analyses and receptor modeling based on the STN data. With the current state of ambient monitoring it is reasonable to expect uncertainties of at least 20% (at the 95% confidence level) for PM_{2.5}, sulfate, ammonium, and organic matter and larger uncertainties for EC and nitrate. Further evaluation for these sampling systems is recommended through side-by-side measurements at multiple locations for longer periods of time.

Chapter 7: Conclusions

7.1 Summary

In Chapters 3-6 I presented work from clustering back trajectories and profiles of trace gases and aerosols, comparisons of model and measured profiles of trace gases and surface comparisons of aerosols to explain sources, sinks and distributions of aerosols and trace gases in the Mid-Atlantic region. From 1995 - 2002, airborne measurements of O₃, CO, SO₂, and aerosol properties were made during summertime air pollution episodes over the Mid-Atlantic U.S. (34.7° to 44.6°N, 68.4° to 81.6°W) as part of the Regional Atmospheric Measurement, Modeling, and Prediction Program (RAMMPP). In Chapter 3, I presented statistics for all profiles made. Little diurnal variation was identified in the CO, SO₂, and Ångström exponent profiles, although the Ångström exponent profiles decreased with altitude. Boundary layer O₃ was greater in the afternoon, while lower free tropospheric O₃ was invariant at ~55 ppbv. The single scattering albedo increased from morning to afternoon (0.93 ± 0.01 - 0.94 ± 0.01); however, both profiles decreased with altitude. A cluster analysis of back trajectories in conjunction with the vertical profile data was used to identify source regions and characteristic transport patterns during summertime pollution episodes. When the greatest trajectory density lay over the northern Ohio River Valley, the result was large O₃ values, large SO₂/CO ratios, highly scattering particles, and large aerosol optical depths. Maximum trajectory density over the southern Ohio River Valley resulted in little pollution. The greatest afternoon O₃ values occurred during periods of stagnation. North-northwesterly and northerly flow brought the least pollution overall. The contribution of regional transport to

afternoon boundary layer O₃ was quantified. When the greatest cluster trajectory density lay over the Ohio River Valley (~59% of the profiles), transport accounted for 69-82% of the afternoon boundary layer O₃. Under stagnant conditions (~27% of the profiles), transport only accounted for 58% of the afternoon boundary layer O₃. On average transported O₃ accounts for 64% of the O₃ measured in the aircraft profiles (this is a weighted average shown in Table 1). This transported O₃ may be an underestimate because we were unable to account for O₃ precursors produced by upwind sources. The results from this study provide a description of regional chemical and transport processes that will be valuable to investigators from the Baltimore, New York, and Pittsburgh EPA Supersites.

Cluster	% of flights made for this cluster	% O ₃ transported	weighted % O ₃ transported
1	26	67	18
2	19	67	13
3	27	54	14
4	10	82	8
5	6	62	4
6	4	73	3
7	6	56	3
8	3	55	2
weighted average			64

Table 1. The percent of O₃ transported for each back trajectory cluster and the weighted average of O₃ transported from upwind sources for all clusters.

Upwind emission sources of NO_x and SO₂ play a crucial role in the amount of O₃ and aerosols in the lower troposphere in the Mid-Atlantic region. In Chapter 4 a hierarchical clustering method was used to separate distinct chemical and meteorological events from over 150 aircraft vertical profiles in the lower troposphere

measuring O₃, SO₂, CO, and particle absorption and scattering in the Mid-Atlantic US. Forty-eight-hour back trajectories were run for each profile and the integrated NO_x and SO₂ point source emissions encountered by each trajectory were calculated using data from the EPA Clean Air Market Division's database. Greater integrated point source NO_x emissions along the back trajectories were correlated with greater O₃ mixing ratios measured during the flights, indicating that O₃ mixing ratios are strongly influenced by and can be predicted with point source emissions. The amount of CO observed depended on where the profiles were made, and larger CO values were found in areas with larger mobile source emissions. Profiles with greater particle absorption were associated with greater CO values.

There is a pervasive "background" SO₂ profile over the eastern US with mixing ratios decreasing smoothly from about 3.5 ppb near the surface to 0.2 ppb at 2400 m. Most SO₂ measured fit this clean profile, but there were exceptions and the clustering method was able to separate these profiles with larger SO₂ values. Profiles with larger, more scattering particles, were correlated with greater integrated SO₂ emissions. The clustering technique also separated profiles made during the 2002 Canadian forest fires.

The UMD aircraft measurements of O₃ have also been compared with EPA's Community Multiscale Air Quality (CMAQ) model. CMAQ under-predicts O₃ by 10% above 500 m altitude. I performed a sensitivity test of the model to determine how including aerosols with NO₂ photolysis rate coefficients affected O₃ production using a revised CMAQ run. These adjustments of the chemistry had modest impacts on CMAQ calculated profiles. In general the revised CMAQ run generated more O₃

above 500 m (~1 ppb), and generated less O₃ (1-4 ppb) below 500 m and brought them into closer agreement with observations. Improvements in the model's ability to describe clouds might increase the oxidation of SO₂ to sulfate and thereby bring the modeled O₃ in closer agreement with measurements.

The UMD aircraft SO₂ measurements were also compared with CMAQ and GOCART. Both models over-predicted SO₂ aloft by ~50%. Possible reasons for this include problems with the emissions inputs and the difficulty the models have resolving clouds. Because the models over-predict SO₂, they likely over-predict the lifetime of SO₂. This has far-reaching policy implications on the ability of the models to describe the oxidation product of SO₂ (sulfate) and the ability of the models to describe PM_{2.5} accurately. Some locations in the Mid-Atlantic are not in compliance with PM_{2.5} standards, and improvement of the models ability to replicate the oxidation of sulfate will aid in the development of state implementation plans for the reduction of PM_{2.5}.

Assessing the effects of air quality on public health and the environment requires reliable measurement of PM_{2.5} mass and the individual chemical components of fine aerosols. In Chapter 6 PM_{2.5} measurements that are part of a newly-established national network were compared with more conventional sampling systems. Experiments were carried out during 2002 at a suburban site in Maryland, United States, where two samplers from the U.S. Environmental Protection Agency Speciation Trends Network: Met One Speciation Air Sampling System – STN_S and Thermo Scientific Reference Ambient Air Sampler – STN_R, two Desert Research Institute Sequential Filter Samplers – DRI_F, and a continuous TEOM monitor

(Thermo Scientific Tapered Element Oscillating Microbalance, 1400a) were sampling air in parallel. These monitors differ not only in sampling configuration but also in protocol-specific sample analysis procedures. Measurements of PM_{2.5} mass and major contributing species were well correlated among the different methods with r-values > 0.8. Despite the good correlations, daily concentrations of PM_{2.5} mass and major contributing species were significantly different at the 95% confidence level from 5 to 100% of the time. Larger values of PM_{2.5} mass and individual species were generally reported from STN_R and STN_S. The January STN_R average PM_{2.5} mass (8.8 µg m⁻³) was 1.5 µg m⁻³ larger than the DRI_F average mass. The July STN_S average PM_{2.5} mass (27.8 µg m⁻³) was 3.8 µg m⁻³ larger than the DRI_F average mass. These differences can only be partially accounted for by known random errors. Variations in flow control, face velocity, and sampling artifacts possibly influence the measurement of PM_{2.5} speciation and mass closure. Statistical tests indicate that the current uncertainty estimates used in the STN network may underestimate the actual uncertainty.

7.2 Recommendations for Future Work

The chemical climatology has been used to evaluate modeled O₃ and SO₂. In Chapter 5, I showed that CMAQ modeled O₃ responds to radiative changes due to aerosols and so CMAQ would likely also respond to changes in clouds. A rigorous analysis of how well MM5 and CMAQ represent cloud cover should be performed. Model improvements would be useful. A determination of how changes in cloud cover affect O₃ and aerosol production would be enlightening. A detailed comparison

of measured aerosols with those generated by CMAQ would also be useful for improving forecasting of PM_{2.5} events.

Appendix A presents comparisons between aircraft and surface measurements of trace gases made for morning and afternoon flights carried out over Ft. Meade, Maryland (1999-2002). Morning aircraft measurements were averaged from 100 – 500 m and afternoon measurements were averaged from 100 – 2000 m. O₃ measurements compared better in the afternoon, likely because O₃ is better mixed in the atmosphere later in the day. CO and SO₂ measurements compared better in the morning. They both have peaks below 500m which is consistent with the expectation of CO coming from ground level combustions and SO₂ emissions from point sources. Extension of this work to all EPA surface sites near aircraft profiles may prove interesting.

Satellites can be powerful tools to monitor the movement of atmospheric pollutants and may have future uses in the prediction of pollution events. Appendix B shows results from comparisons of the Global Ozone Monitoring Experiment (GOME) satellite with UMD aircraft profiles of SO₂. Because of the coarse resolution of GOME and high level of noise, the comparison was poor. This provides an understanding of the limitations of satellite measurements of SO₂. The chemical climatology presented here can be used for validation and improvement of other satellite measurements.

Appendix A

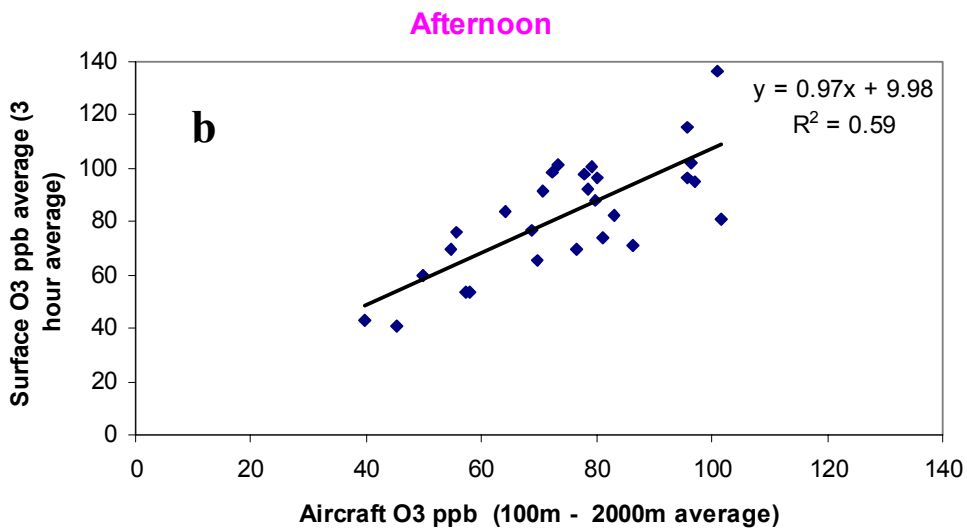
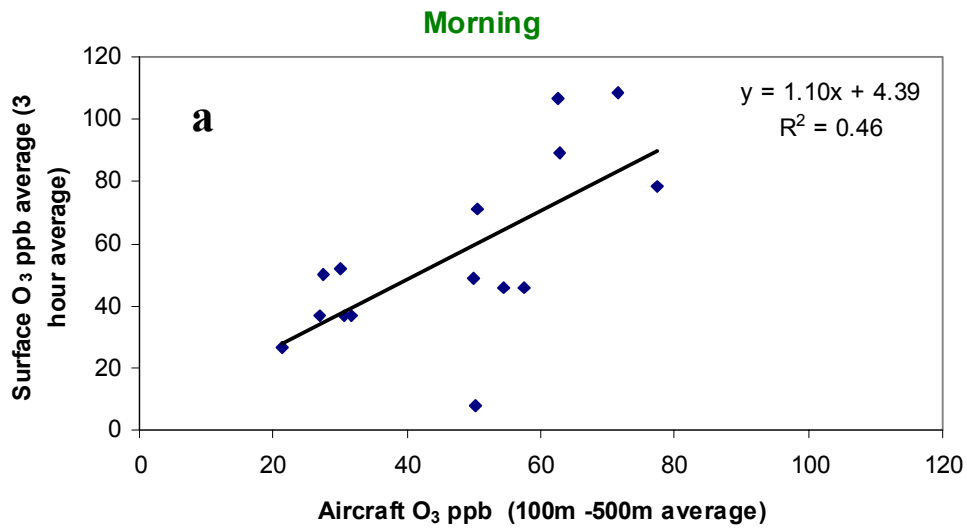
Surface and Aircraft Measurements

Understanding sources of pollution can aid in prevention of pollution events. The transport of pollutants can often be seen in vertical profiles (made with aircraft) as described in Chapter 3. Vertical profiles are expensive and are limited in space and time. Surface networks measuring trace gases and aerosols on a continuous or near-continuous basis have been set up by the EPA throughout the US to monitor pollution levels.

I compared surface measurements of O₃, SO₂, and CO with average columns measured aboard the UMD research aircraft to assess how well surface measurements represent the mixed layer and how they might be influenced by transported pollutants. During the 1999 –2002 intensive sampling period at Fort Meade, the University of Maryland research aircraft made flights over Fort Meade measuring O₃, SO₂, and CO. The shapes of O₃ profiles are affected by the breakdown of the nocturnal boundary layer and to account for this I divided the flights into morning and afternoon. Morning flights were flown between 6:00 and 12:00 EST, with an average time of 9:30 EST. Afternoon flights were flown between 12:00 and 19:00 EST, with an average time of 14:30 EST. In order to compare the aircraft measurements with surface measurements I assumed the afternoon boundary layer extended from 100 m to 2000 m and I calculated a boundary layer average for all of the trace gases in this layer. For morning flights I assumed that the residual nocturnal boundary layer was

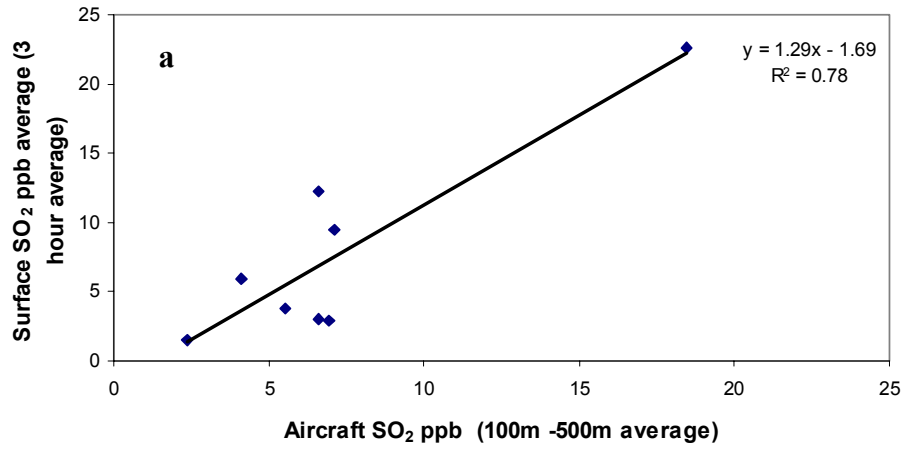
between 500 m and 2000 m, and I calculated an average below that, from 100 - 500 m, to compare with surface measurements. I used a three-hour average of the surface measurements around the time of the flight to compare with aircraft measurements.

Comparisons between surface and aircraft measurements of O₃, SO₂, and CO, for morning and afternoon flights, are shown in A.1-A.3. O₃ measurements compare better in the afternoon ($r^2 = 0.6$) than in the morning ($r^2 = 0.5$). The average difference (surface – aircraft) is smaller in the afternoon (8 ppb) than in the morning (9 ppb) and the RMS difference is also smaller in the afternoon than in the morning (A4). In the afternoon the profile is generally well mixed and this explains the better correlation and smaller differences between surface and aircraft measurements in the afternoon. SO₂ measurements compared better in the morning, when the comparison was made between the surface and the aircraft 100 – 500 m average, than in the afternoon when the comparison was made between the surface and the aircraft 100 - 2000 m average. Morning SO₂ comparisons had an r^2 of 0.8 and this dropped to 0.5 in the afternoon. The average difference (surface – aircraft) increased from 0.4 to 1.6 ppb between morning and afternoon, though the RMS difference was similar (3 ppb). The SO₂ generally peaks below 500 m (at elevations where it is emitted) and concentrations drop off substantially above this level, so the average SO₂ from 100 m to 2000 m is smaller than the average SO₂ from 100 to 500 m. Afternoon surface SO₂ was compared with aircraft average SO₂ from 100 – 500 m (A.2.c) and the r^2 of 0.7 was better than that from A.2.b which had an r^2 of 0.5.

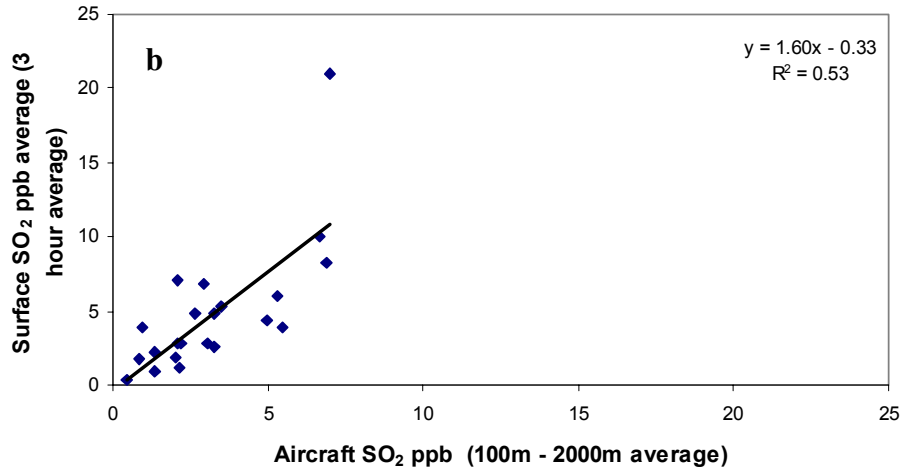


A.1. Comparison of aircraft and surface measurements of O₃ for a) morning and b) afternoon flights. The afternoon shows better correlation between surface and measurements aloft, likely due to improved mixing in the afternoon.

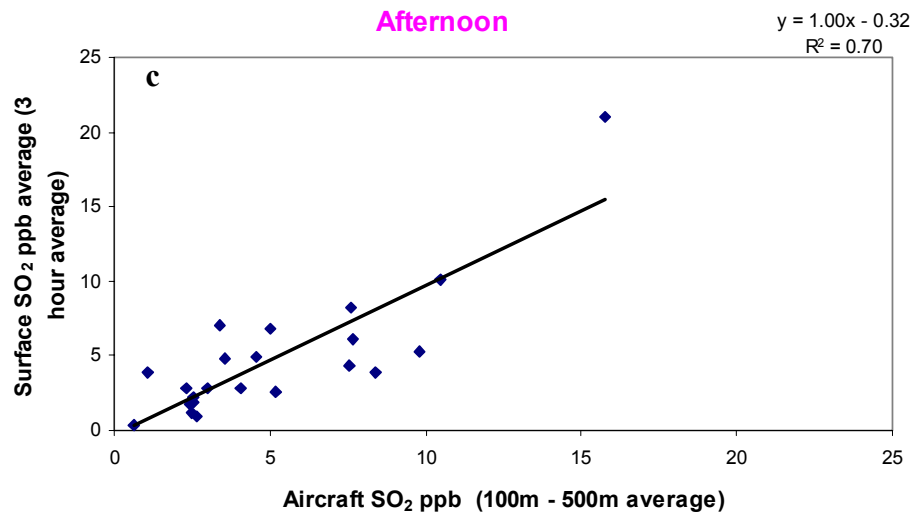
Morning



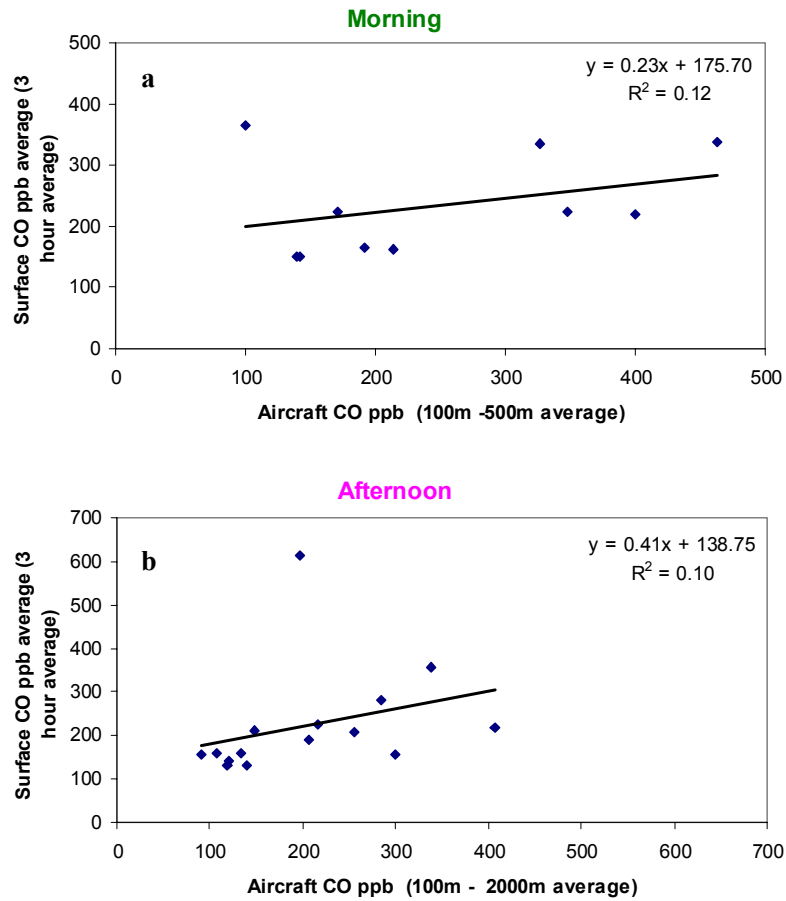
Afternoon



Afternoon



A.2. Comparison of aircraft and surface measurements of SO₂ for a) morning and b) afternoon flights (with aircraft averages from 100 -2000 m) and b) afternoon flights (with aircraft averages from 100 – 500 m). Surface measurements compare well with aircraft averages in the lower boundary layer (100 -500 m).



A.3. Comparison of aircraft and surface measurements of CO for a) morning and b) afternoon flights. Both morning and afternoon show poor correlation and this could be because of spikes in surface CO data.

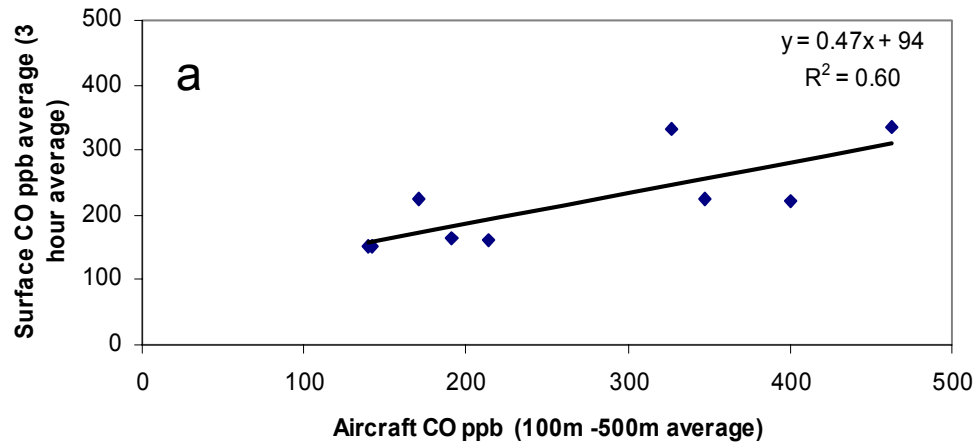
	Aircraft column average (ppb)	Aircraft standard deviation (ppb)	Surface 3-hr average (ppb)	Surface standard deviation (ppb)	RMS difference (ppb)	Average difference (surface- aircraft) (ppb)
O₃ am	47.0	17.8	56.1	29.0	22.6	9.1
O₃ pm	74.6	17.0	82.5	21.6	15.8	8.0
SO₂ am	7.2	4.8	7.7	7.0	3.4	0.4
SO₂ pm	3.2	2.0	4.8	4.4	3.5	1.6
CO am	250	125	233	83	118	-16.2
CO pm	204	95	222	124	127	17.7

A.4. Comparisons of O₃, SO₂, and CO aircraft column averages with surface measurements. Morning aircraft measurements were averaged between 100-500 m and afternoon aircraft measurements were averaged between 100-2000 m. The RMS difference, average difference (surface – aircraft), and standard deviation is also shown. All data have units of ppb.

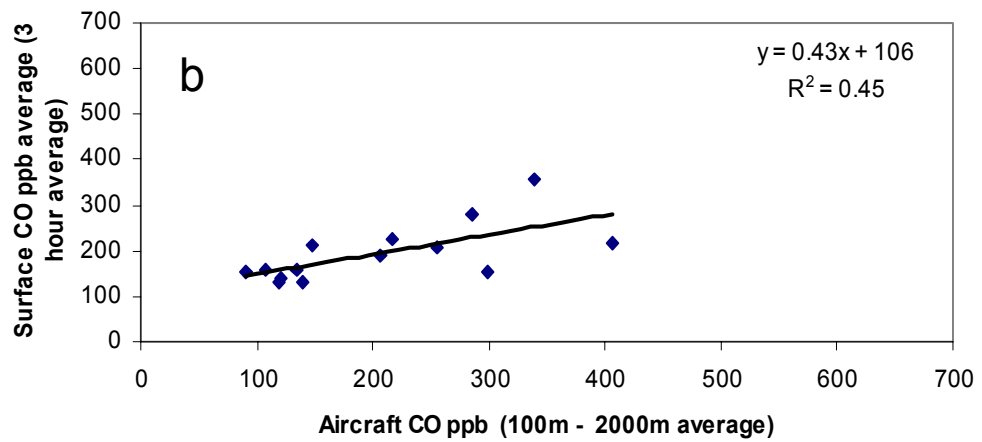
CO morning and afternoon aircraft measurements do not compare well with surface measurements (A.3). This is likely because of some peaks at the surface not seen aloft. When one outlier (June 24, 1999) is removed from the morning data, the correlation between morning surface and aircraft measurements improves from an r^2 of 0.1 to an r^2 of 0.6 (A.5a). The June 24, 1999 spiral was made at 6:00 EST, and shows CO around 100 ppb, from the surface to 3km. The small CO values are seen at nearby locations of Gaithersburg, MD and Manassas, VA. O₃ is also extremely low below 150 m (around 30 ppb for all three locations). The CO surface measurement shows 300-400 ppb from 5:00 to 7:00 EST, with a standard deviation of 64 ppb (for this specific day, this differs somewhat from the standard deviation for all days in the analysis shown in A.4). No peaks like this are seen in the aircraft profile, even below 100 m, suggesting that this is a very local plume (perhaps a vehicle was idling near

the instrument). The RH is about 90% at the surface and drops off to 50% at 300 m, suggesting that the lower level aircraft measurements were made in the inversion layer. When an outlier is removed from the afternoon measurements (A.5.b) the correlation improves from an r^2 of 0.1 to an r^2 of 0.5. This outlier occurred on June 24, 2002. The aircraft made a spiral at 15:00 pm EST, and shows 400 ppb of CO at 200 m, which decreases quickly aloft. The surface measurements show a three-hour average CO of 611 ppb, with a standard deviation of 66 ppb. Since this was an afternoon profile, I calculated the average from 100 m to 2000 m, and the peak near the surface was washed out. Though the correlation did improve when the outliers were removed, the correlation was still not as good as that for O₃ and SO₂. Thus, surface CO measurements may not be representative of the mixed layer measurements.

Morning



Afternoon



A.5. Comparison of aircraft and surface measurements of CO for a) morning and b) afternoon flights with outliers removed. The correlation improves when the outliers are removed, however the correlation is not as good as that for O₃ and SO₂.

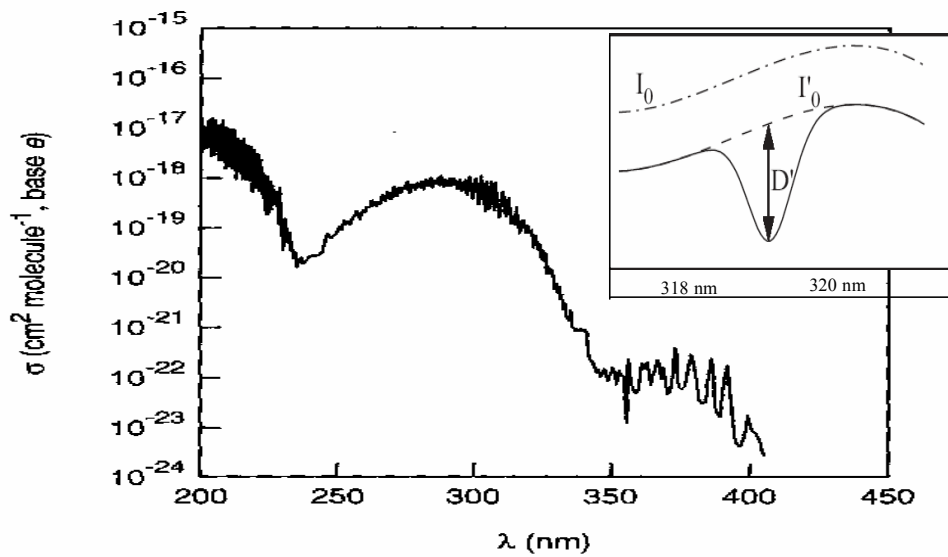
Appendix B

Satellite Measurements

Surface measurements can be made continuously to show the diurnal and seasonal variability of SO₂. A network of surface stations like those in the Sulfate Regional Experiment and the Atmospheric Integrated Research Monitoring Network provide information about regional SO₂ distributions (EPRI, 1981; Hicks, 2001) but this can be expensive and difficult to implement everywhere. Aircraft measurements provide altitude profiles and some spatial information including possible transport of pollutants. However, aircraft observations are also expensive and very limited in space and time. Satellites show SO₂ distributions around the world year round. These measurements are usually taken once daily and thus do not offer information on the diurnal variability of SO₂; nor do they provide information about the vertical distribution of SO₂. Because of their spatial coverage, satellites are great tools to monitor mesoscale and synoptic scale atmospheric events. A combination of surface, aircraft, and satellite measurements can be a powerful tool for describing the SO₂ distribution. Satellites could also be used in conjunction with models to predict and characterize pollution events. Understanding the uncertainty in satellite measurements is a key step in the advancement of satellites into the tropospheric air quality monitoring ensemble. In this Appendix I will present comparisons of SO₂ from the UMD research aircraft with those retrieved from The Global Ozone Monitoring Experiment (GOME) instrument aboard the European Research Satellite (ERS-2).

GOME Instrumentation

GOME measures scattered and reflected light from the Earth and the atmosphere. Data collected in the wavelength range of 315.5-327 nm are used to determine SO₂ column content with Differential Optical Absorption Spectroscopy (DOAS) (Eisinger et al. 1998). Beer's law enables the quantification of the concentration of a species from the absorption spectrum using measurements of attenuated and unattenuated light. It is difficult to measure the true unattenuated light, I_0 , coming from the Earth because of Mie and Rayleigh scattering, as well as absorption by atmospheric species that attenuate light. B.1 shows the absorption cross section of SO₂ in the wavelength region from 317 to 325. There is more structure in the spectrum in the smaller wavelength region of 318 to 320. DOAS fits a curve to the absorption spectrum in the larger wavelength region (317 to 325 nm) to describe the "unattenuated" beam I_0' . This "unattenuated" beam is only unattenuated by SO₂ and accounts for the difficult to measure attenuation from scattering and other atmospheric species (Platt, 1994). The differential absorption, D' is just $I_0' - I$.



B.1. SO₂ absorption cross section. In the smaller box I_0 is the true unattenuated beam of light that cannot be measured because of atmospheric scattering and absorption. I'_0 is fit over the larger wavelength region (317-325) and is only attenuated by the species of interest. The differential absorption (D') is then just $I'_0 - I$ (Finlayson-Pitts and Pitts, 2000; Platt, 2003).

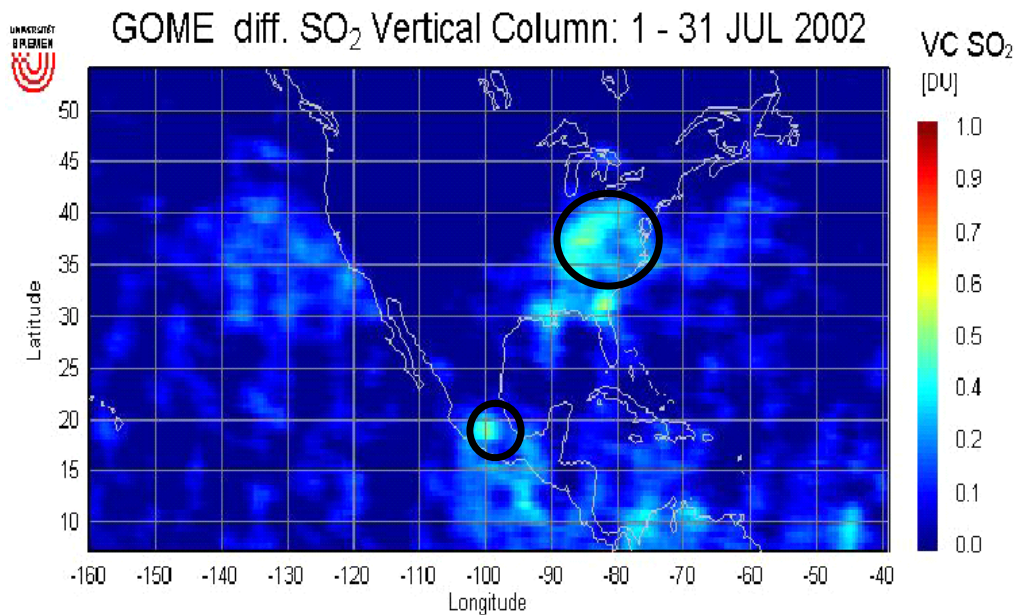
GOME measures trace gasses with a nadir scanning double monochromator.

The resolution of the monochromator is 0.17-0.33 nm. The incoming light is split into 4 channels and is recorded with a 1024 reticon photodiode array. SO₂ absorbs at 317 to 325, and the monochromator channel corresponding to this region detects the gas. The SO₂ integrated column content is then calculated using a differential optical absorption spectrometry algorithm (Eisinger et. al. 1998).

There is an overlap in the absorption signal between SO₂ and O₃ from the Huggins bands in the 300-360 nm region (Finlayson-Pitts and Pitts, 2000). This O₃ interference can be removed from the GOME data by subtracting the SO₂ signal in areas with little SO₂ (like areas over the ocean) from the SO₂ signal in an area of interest.

Comparisons between In-situ and Satellite Measurements: Implications for Revisions to the Air Mass Factor.

I have compared the aircraft column contents of SO₂ with those measured with GOME to test the sensitivity of GOME SO₂ measurements. B.2 shows a map of GOME SO₂ retrievals over North America. Plumes of SO₂ are visible over Mexico City as well as the Eastern and Midwestern US. Plumes in these areas are most likely located in the troposphere.



B.2. Map of GOME SO₂. The SO₂ plume over the Eastern US and Mexico City can clearly be seen with a column content of about 0.4 DU.

B.3 shows comparisons I made between the default GOME retrievals and aircraft column contents. The correlation between GOME and aircraft measurements is poor and GOME retrieves much less SO₂ than the aircraft measures. To improve the GOME retrievals I used *in-situ* data to modify the Air Mass Factor (AMF) used in

the GOME retrieval algorithm. The AMF is used to convert the measured slant columns of trace gases into vertical columns and can be written as:

$$\text{AMF} = \tau_{\text{slant}} / \tau_{\text{vert}} \quad (1)$$

Where τ_{slant} is the optical density along the slant path (this is what is measured by GOME) and τ_{vert} is the optical density along the vertical path. To determine the AMF, a radiative transfer model is run with and without the absorbing species to calculate respective intensities $I(\lambda)^w$ and $I(\lambda)^{w/o}$ along the slant path s_s .

$$\ln (I(\lambda)^{w/o} / I(\lambda)^w) = \int_0^{TOA} \sigma_x(s_s, \lambda) C_x(s_s) ds_s \quad (2)$$

Here x is some absorbing species, s_s is the slant path length, σ_x is the extinction cross section, and C_x is the concentration of the species of interest. The left side of Equation 2 is the slant optical density. The vertical optical density, τ_{vert} , can be calculated as:

$$\tau_{\text{vert}} = \int_0^{TOA} \sigma_x(s_v, \lambda) C_x(s_v) ds_v \quad (3)$$

Here s_v is the vertical path length. The air mass factor can be written as:

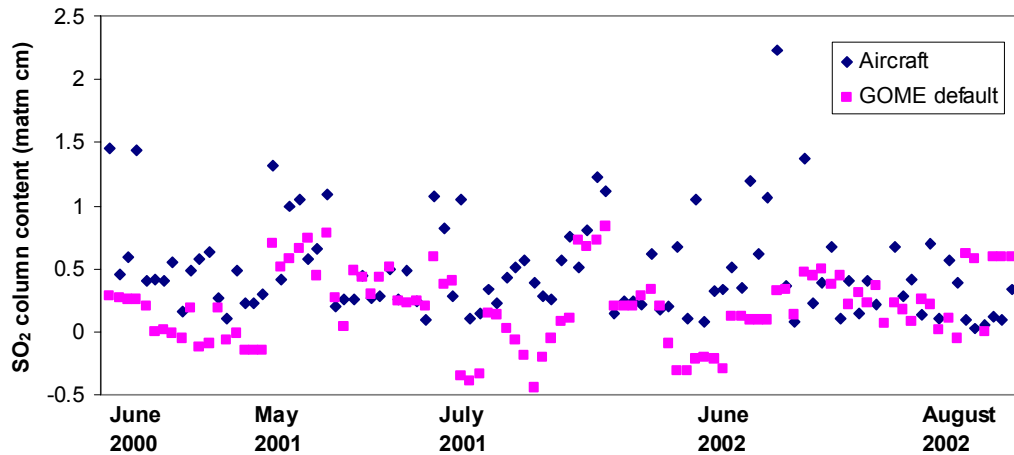
$$\text{AMF} = \ln (I(\lambda)^{w/o} / I(\lambda)^w) / \int_0^{TOA} \sigma_x(s_v, \lambda) C_x(s_v) ds_v \quad (4)$$

(Perliski et al., 1993). The extinction cross section can be measured in the lab or determined from literature. The radiative transfer model SCIATRAN solves the following equation to determine $I(\lambda)^w$ and $I(\lambda)^{w/o}$.

$$\mu \frac{dI(z, \mu, \varphi)}{dz} = -c(z)I(z, \mu, \varphi) + \frac{b(z)}{4\Pi} \int_0^{2\pi} \int_{-1}^1 p(z, \mu, \mu', \varphi, \varphi') I(z, \mu', \varphi') d\mu' d\varphi' \quad (5)$$

Here μ and μ' denote the cosine of the zenith angle, z represents altitude, φ and φ' represent the azimuthal angles in relation to the line-of-site projection on the earth's

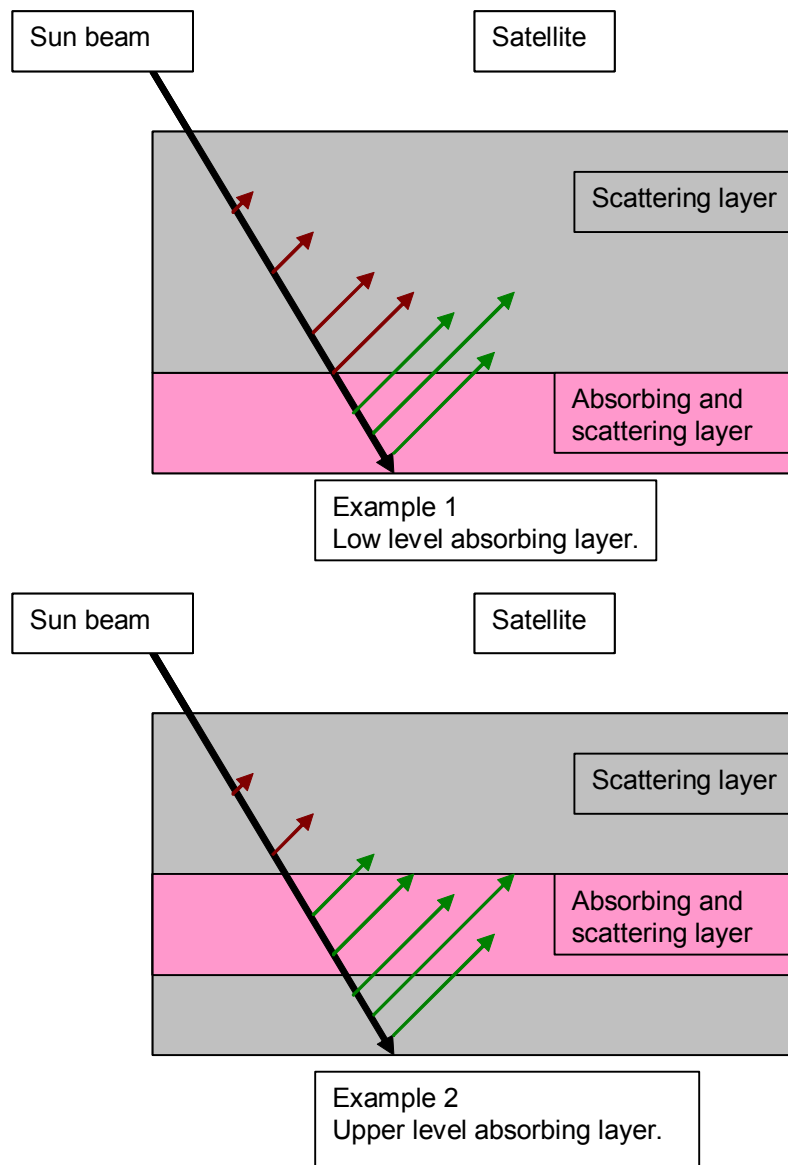
surface, c is the total extinction coefficient, b is the total scattering coefficient (the sum of the trace gas and particle scattering coefficients), and p is the total scattering phase function (Rozonov et al., 1997).



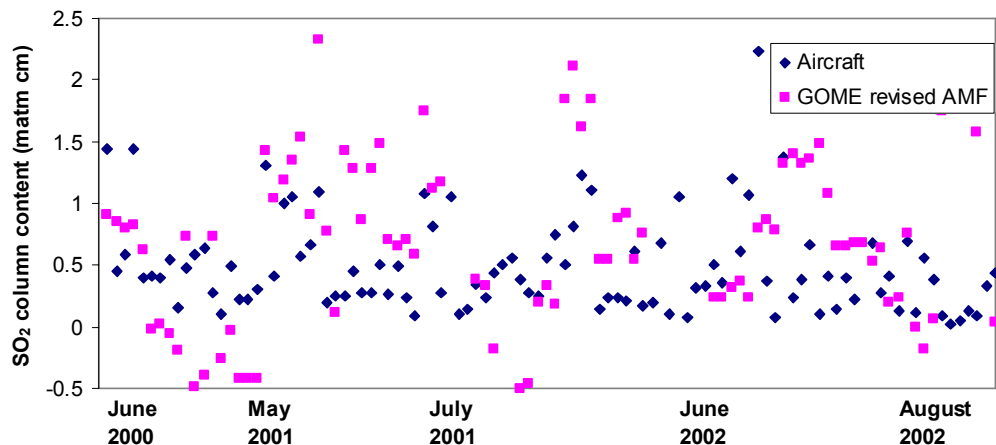
B.3. Comparison between default GOME SO₂ and UMD aircraft SO₂ (matm cm). GOME SO₂ is smaller than that measured aboard the aircraft and the correlation between the measurements is poor ($r^2 = 0.20$).

The AMF depends on the altitude of the absorbing species of interest and where the most absorption and scattering occur in a vertical column. B.4 shows how light is scattered when the absorbing and scattering layers are near the surface (Example 1) and when the absorbing and scattering layers are at higher altitudes (Example 2). Light at 320 nm is mostly attenuated by the time it reaches the surface. The path length is smaller in example 1 than in example 2 and thus the intensity reaching the satellite in example 1 will be greater than in example 2. Because the intensity is greater, the AMF for example 1 will be smaller than that for example 2. The default AMF calculation assumes the column concentration of SO₂ has a peak

above the boundary layer. I have recalculated the AMF using SO₂ profiles measured aboard the UMD research aircraft. B.5 shows results of the comparison between aircraft SO₂ columns and GOME SO₂ when a revised AMF was used. These adjustments to the AMF made the GOME retrieved SO₂ larger but did not improve the correlation between the aircraft and GOME.



B.4. Light is scattered differently when an absorbing and scattering layer is near the surface (example 1) than when the layer is above the planetary boundary layer (example 2). Red arrows denote light that is not scattered through the absorbing layer and green arrows denote light that is scattered through the absorbing layer. The length and space between the arrows represent the generalized degree of scattering (as altitude increases there are less scattering species). There is more scattering when the layer is above the planetary boundary layer (example 2) than when the layer is near the surface. This is because the light scatters on its way to the surface and then again on its way to the satellite for example 2.



B.5. Comparison between GOME SO₂, using a revised AMF, and UMD aircraft SO₂ (matm cm). The revised AMF made the retrieved GOME SO₂ larger than the default retrieval but the correlation between the measurements is poor ($r^2 = 0.16$).

GOME Interference Corrections

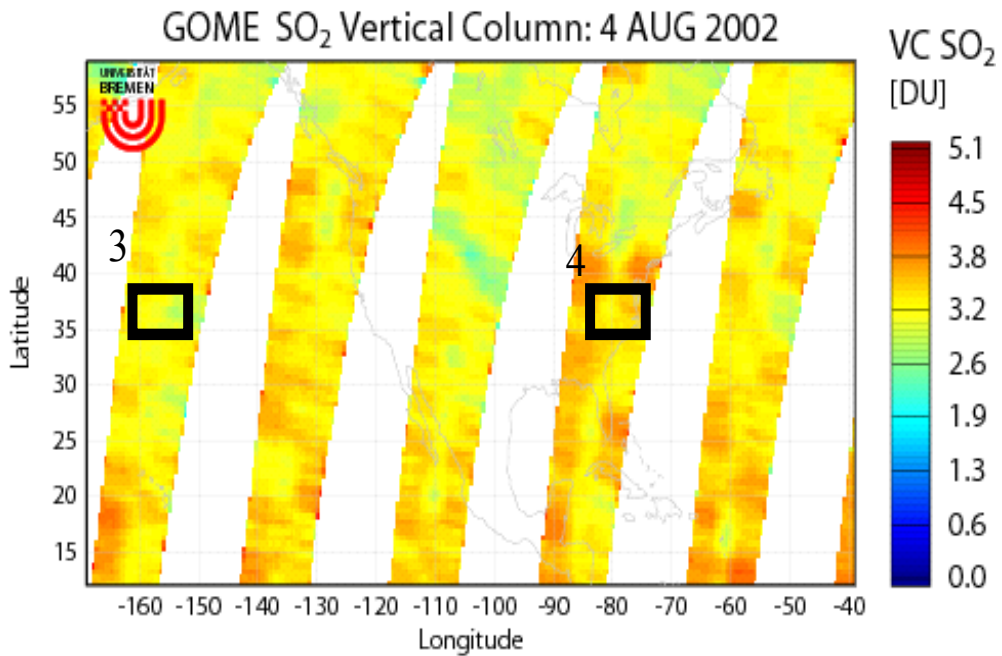
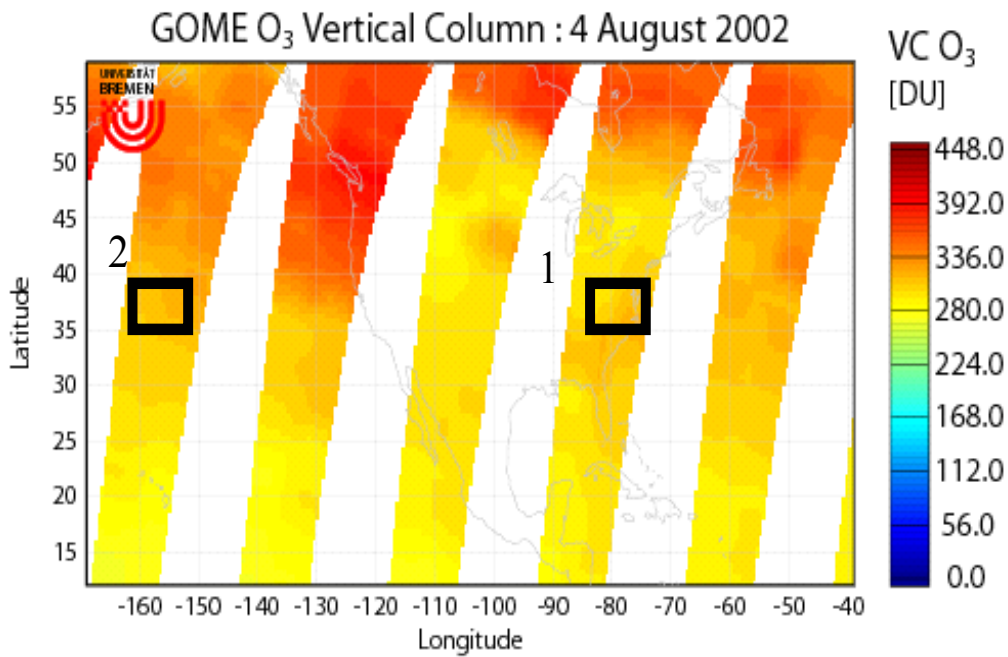
Because the SO₂ and O₃ absorption band overlap in the UV, GOME SO₂ retrievals must be corrected for O₃ interference (this process will be referred to as an O₃ correction). The default O₃ correction subtracts SO₂ retrieved columns over the Pacific Ocean (where SO₂ should be small) from the SO₂ column at the point of interest. To account for the latitudinal gradient of O₃, only the ocean SO₂ at latitudes matching that of the point of interest are used in the correction. For annual averages this correction works well but for daily GOME retrievals this correction sometimes gives negative SO₂. I have developed a method to improve the O₃ correction and this is described below.

The method to improve the O₃ correction involves finding regions over the ocean with O₃ column contents similar to those over the area of interest and is

diagrammed in B.6. For this method I first generated a map of O₃. Because O₃ has a shape different from SO₂ I had to use a different AMF. For O₃ a good approximation of the AMF can be made with the solar zenith angle (*SZA*):

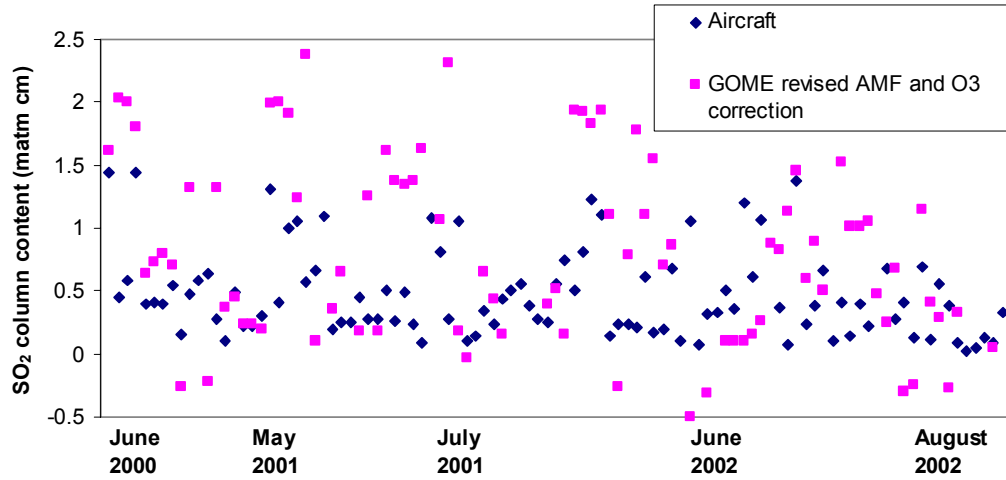
$$\text{AMF} = 1 + 1/\cos(\text{SZA}) \quad (6)$$

I made a grid of 1° latitude by 1° longitude and averaged the O₃ in each grid box. I then searched for an O₃ box over the ocean that was within 5% of the O₃ box over the area of interest (Steps 1 and 2 in B.6). The latitude and longitude of this box over the ocean was saved. Next I made a map of SO₂ using the revised AMF, described in the previous section, and found the SO₂ at the area of interest and the SO₂ at the same location as the ocean box (Steps 3 and 5). To correct for the O₃ interference at an area of interest I subtracted the SO₂ at the ocean box (that had O₃ that matched O₃ over the area of interest) from the SO₂ over the area of interest. B.7 shows a comparison of SO₂ from the aircraft with GOME retrieved SO₂ (using the revised AMF and O₃ correction). The revised O₃ correction did decrease the number of negative values, but the correlation between aircraft and GOME SO₂ is still poor. In Chapter 5 I calculated the average lifetime of SO₂ in the summer in the daytime in the Mid-Atlantic to be short, ~ 19 hours (Chapter 5, Table 11). GOME has coarse spatial resolution, and only makes measurements once a day. The short lifetime and the coarse resolution partly explain why the correlation between aircraft and GOME SO₂ was poor. The SO₂ in the Mid-Atlantic may also be below the GOME detection limit. This analysis provides an understanding of the limitations of the GOME SO₂ retrievals.



B.6. Diagram of the steps used to calculate the revised O₃ correction.

- 1.) Find O₃ over area of interest. 2.) Find matching O₃ over ocean (where SO₂ is minimal). 3.) Find SO₂ in same location as in 2. 4.) Find SO₂ column (over spiral location with no O₃ correction. 5.) Subtract SO₂ in step 4 from SO₂ in step 3.



B.7. Comparison between UMD aircraft SO₂ (matm cm) GOME SO₂, using a revised AMF and revised O₃ corrections. The revised O₃ corrections decreased the number of negative GOME retrievals but the correlation between the measurements is still poor ($r^2 = 0.15$).

Bibliography

- Andronache, C., W.L. Chameides, D.D. Davis, B.E. Anderson, R.F. Pueschel, A.R. Bandy, D.C. Thornton, R.W. Talbot, P. Kasibhatla, and C.S. Kiang, Gas-to-particle conversion of tropospheric sulfur as estimated from observations in the western North Pacific during PEM-West B. *J. Geo. Phys. Res.*, 102, 28511-28538, 1997.
- Appel, B.R. and Y. Tokiwa, Atmospheric particulate nitrate sampling errors due to reactions with particulate and gaseous strong acids. *Atmos. Environ.*, 15, 1087-1089, 1981.
- Appel, B.R., Y. Tokiwa, M. Haik, and E.L. Kothny, Artifact particulate sulfate and nitrate formation on filter media. *Atmos. Environ.*, 18, 409-416, 1984.
- Anderson, T.L., and J.A. Ogren, Determining aerosol radiative properties using the TSI 3563 Integrating Nephelometer, *Aerosol Sci. Technol.*, 29, 57-69, 1998
- Andrews, E., P. Saxena, S. Musarra, L.M. Hildemann, P. Koutrakis, P.H. McMurry, I. Olmes, and W.H. White, Concentration and composition of atmospheric aerosols from the 1995 SEAVS experiment and a review of the closure between chemical and gravimetric measurements. *J. Air & Waste Manage. Assoc.*, 50, 648-664, 2000.
- Ames R.B. and W.C. Malm, Comparison of sulfate and nitrate particle mass concentrations measured by IMPROVE and the CDN. *Atmos. Environ.*, 35, 905-916, 2001.
- Ashbaugh, L.L., A statistical trajectory technique for determining air pollution source regions, *J. Air Pollut. Control Ass.*, 33, 1096-1098, 1983.
- Berglen, T.F., T.K. Berntsen, S.A. Isaksen, and J.K. Sundet, A global model of the coupled sulfur/oxidant chemistry in the troposphere: The sulfur cycle, *J. Geophys. Res.*, 109, D19310, doi:10.1029/2003JD003948, 2004.
- Berto, A., A. Buzzi, and D. Zardi, Back-tracking water vapour contributing to a precipitation event over Trentino: a case study, *Meteorol. Z.*, 13(3), 189-200, 2004.
- Bond, T.C., T.L. Anderson, and D. Campbell, Calibration and intercomparison of filter-based measurements of visible light absorption by aerosols, *Aerosol Sci. Technol.*, 30, 582-600, 1999.
- Bodhaine, B.A., Aerosol absorption measurements at Barrow, Mauna Loa and the south pole, *J. Geophys. Res.*, 100, 8967-8975, 1995.
- Brankov, E., S.T. Rao, and P.S. Porter, A trajectory-clustering-correlation methodology for examining the long-range transport of air pollutants, *Atmos. Environ.*, 32(9), 1525-1534, 1998.

Buchdahl R, C.D. Willems, M, Vander, and A. Babiker Associations between ambient ozone, hydrocarbons, and childhood wheezy episodes: a prospective observational study in south east London. *Occup. Environ. Med.*, 57, 86–93, 2000.

Burton, G.A., G.E. Batley, P.M. Chapman, V.E. Forbes, E.P. Smith, T. Reynoldson, C.E. Schlegel, P.J. den Besten, A.J. Bailer, A.S. Green, and R.L. Dwyer, A weight-of-evidence framework for assessing sediment (or other) contamination: Improving certainty in the decision-making process. *Human Eco. Risk Assess.*, 8, 1675-1696, 2002.

Cape, J.N., J. Methven, and L.E. Hudson, The use of trajectory cluster analysis to interpret trace gas measurements at Mace Head, Ireland, *Atmos. Environ.*, 34, 3561-3663, 2000

Chen, L.-W. A., B.G. Doddridge, R. R. Dickerson, P. K. Mueller, J. C. Chow, and W.A. Butler, Seasonal variations in elemental carbon aerosol, carbon monoxide, and sulfur dioxide: Implications for sources. *Geophys. Res. Lett.*, 28, 1711-1714, 2001.

Chen, L.-W.A., Urban fine particulate matter: Chemical composition and possible origins. Doctoral dissertation, Chemical Physics, University of Maryland, College Park, 2002.

Chen, L.-W.A., B.G. Doddridge, R.R. Dickerson, J.C. Chow, and R.C. Henry, Origins of fine aerosol mass in the Baltimore-Washington corridor: implications from observation, factor analysis, and ensemble air parcel back trajectories. *Atmos. Environ.*, 36, 4541-4554, 2002.

Chen, L.-W. A., J.C. Chow, B. G. Doddridge, R. R. Dickerson, W. F. Ryan, and P.K. Mueller, Analysis of a summertime PM_{2.5} and Haze Episode in the Mid-Atlantic Region. *J. Air & Waste Manage. Assoc.*, 53, 946-956, 2003.

Chin, M., D. J. Jacob, G. M. Gardner, M. S. Foreman-Fowler, P. A. Spiro, and D. L. Savoie, A global three-dimensional model of tropospheric sulfate, *J. Geophys. Res.*, 101, 18,667–18,690, 1996.

Chin, M., R.B. Rood, S.J. Lin, J.F. Muller, and A.M. Thomson, Atmospheric sulfur cycle simulated in the global model GOCART: Model description and global properties, *J. Geophys. Res.*, 105(D20), 24671-24687, 2000a.

Chin, M., D.L., Savoie, B.J. Huebert, A.R. Bandy, D.C. Thornton, T.S. Bates, P.K. Quinn, E.S. Saltzman, and W.J. DeBruyn, Atmospheric sulfur cycle simulated in the global model GOCART: Comparison with field observations and regional budgets. *J. Geophys. Res.*, 105, 24689-24712, 2000b.

Chow, J.C., J.G. Watson, D.H. Lowenthal, P.A. Solomon, K.L. Magliano S.D. Ziman, and L.W. Richards, PM10 Source Apportionment in California San-Joaquin Valley. *Atmos. Environ.*, 26, 3335-3354, 1992.

Chow, J.C., J.G. Watson, J.L. Bowen, C.A. Frazier, A.W. Gertler, K.F. Kochy, D. Landis, and L. Ashbaugh, A sampling system for reactive species in the Western United States. In Sampling and analysis of airborne pollutants, Winegar, E.D., Keith, L.H. eds, 212-214, 1993a.

Chow, J.C., Watson, J.G., Pritchett, L.C., Pierson, W.R., Frazier, C.A., Purcell, R.G., The DRI thermal/optical reflectance carbon analysis system: Description, evaluation, and applications in U.S. air quality studies. *Atmos. Environ.*, 27, 1185-1201, 1993b.

Chow, J.C., J.G. Watson, D.H. Lowenthal, P.A. Solomon, K.L. Magliano, S.D. Ziman, and L.W. Richards, PM10 and PM2.5 Compositions in California's San Joaquin Valley. *Aerosol Sci. and Tech.*, 18, 105-128, 1993c.

Chow, J.C., J.G. Watson, Z.Q. Lu, D.H. Lowenthal, C.A. Frazier, P.A. Solomon, R.H. Thullier, and K. Magliano, Descriptive Analysis of PM2.5 and Pm10 at Regionally Representative Locations during SJVAC/AUSPEX. *Atmos. Environ.*, 30, 2079-2112, 1996.

Chow, J.C., J.G. Watson, D. Crow, D.H. Lowenthal, and T. Merrifield, Comparison of IMPROVE and NIOSH carbon measurements. *Aerosol Sci. and Tech.*, 34, 23-34, 2001.

Chow, J.C., J.G. Watson, L.-W.A. Chen, W.P. Arnott, and H. Moosmuller, Equivalence of elemental carbon by thermal/optical reflectance and transmittance with different temperature protocols. *Enviro. Sci. and Tech.*, 38, 4414-4422, 2004

Chow, J.C., J.G. Watson, L.-W.A. Chen, G. Paredes-Miranda, M.C.O. Chang, D. Trimble, K.K. Fung, H. Zhang, and J.Z. Yu, Refining temperature measures in thermal/optical carbon analysis. *Atmos. Chem. Phys.* 5, 4477-4505, 2005a.

Chow, J.C., J.G. Watson, D.H. Lowenthal, and K.L Magliano, Loss of PM_{2.5} nitrate from filter samples in central California. *J. Air & Waste Manage. Assoc.*, 55, 1158-1168, 2005b.

Chow, J.C., L.-W.A. Chen, J.G. Watson, D.H. Lowenthal, K.A. Magliano, K. Turkiewicz, and D.E. Lehrman, PM2.5 chemical composition and spatiotemporal variability during the California Regional PM10/PM2.5 Air Quality Study (CRPAQS). *J. Geophys. Res. Let.* 111, D10S04, 2006.

Code of Federal Regulations (CFR), National Primary and Secondary Ambient Air Quality Standards, Final Rules, Title 40, Parts 50-53 and 58, 18 July 1997.

- Colarco, P.R., M.R. Schoeberl, B.G. Doddridge, L.T. Marufu, O. Torres, and E.J. Welton, Transport of smoke from Canadian forest fires to the surface near Washington, D.C.: Injection height, entrainment, and optical properties, *J. Geophys. Res.*, 109, D06203, 2004.
- Colette, A., G. Ancellet, and F. Borchi, Impact of vertical transport processes on the tropospheric ozone layering above Europe. Part I: Study of air mass origin using multivariate analysis, clustering and trajectories, *Atmos. Environ.*, 39, 5409-5422, 2005a.
- Colette, A., and G. Ancellet, Impact of vertical transport processes on the tropospheric ozone layering above Europe. Part II: Climatological analysis of the past 30 years, *Atmos. Environ.*, 39, 5423-5435, 2005b.
- Cornbleet, P., and N. Gochman, Incorrect least-squares regression coefficients in method-comparison analysis. *Clin. Chem.*, 25, 432-438, 1979.
- Dentener, F. J., G.R. Carmichael, Y. Zhang, J. Lelieveld, and P.J. Crutzen, Role of mineral aerosol as a reactive surface in the global troposphere, *J. Geophys. Res.*, 101 (D17), 22869-22889, 1996.
- Diab, R.D., A. Raghunandan, A.M. Thompson, and V. Thouret, Classification of tropospheric ozone profiles over Johannesburg based on mosaic aircraft data, *Atmos. Chem. Phys.*, 3, 713-723, 2003.
- Diab, R.D., A.M., Thompson, K. Mari, L. Ramsay, and G.J.R. Coetzee, Tropospheric ozone climatology over Irene, South Africa, from 1990 to 1994 and 1998 to 2002, *J. Geophys. Res.*, 109, D20301, 2004.
- Dickerson, R.R., and A.C. Delany, Modification of a commercial gas filter correlation CO detector for increased sensitivity, *J. Atmos. Oceanic Technol.*, 5(3), 424-431, 1988.
- Dickerson, R.R., B.G. Doddridge, P.K. Kelley, and K.P. Rhoads, Large-scale pollution of the atmosphere over the North Atlantic Ocean: Evidence from Bermuda, *J. Geophys. Res.*, 100(5), 8945-8952, 1995.
- Dickerson, R.R., S. Kondragunta, G. Stenchikov, K.L. Civerolo, B.G. Doddridge, and B.N. Holben, The impact of aerosols on solar ultraviolet radiation and photochemical smog. *Science* 278, 827- 830, 1997.
- Doddridge, B.G., R.M. Morales, K.P. Rhoads, J.T. Merrill, P.C. Novelli, R.R. Dickerson, V.S. Connors, and H.G. Reichle, Jr, Ground-based and airborne observations of carbon monoxide during NASA/MAPS missions SRL-1 and SRL-2, *J. Geophys. Res.*, 103, 19305-19316, 1998.

- Dorling, S.R., T.D. Davies, and C.E. Pierce, Cluster Analysis: A technique for estimating the synoptic meteorological controls on air and precipitation chemistry – method and applications, *Atmos. Environ.*, 26A(14), 2575-2582, 1992a.
- Dorling, S.R., T.D. Davies, and C.E. Pierce, Cluster Analysis: A technique for estimating the synoptic meteorological controls on air and precipitation chemistry – results from Eskdalemuir, S. Scotland, *Atmos. Environ.*, 26A(14), 2583-2602, 1992b.
- Dorling, S.R., and T.D. Davies, Extending cluster analysis – synoptic meteorology links to characterise chemical climates at six northwest European monitoring stations, *Atmos. Environ.*, 29(2), 145-167, 1995.
- Draxler, R.R., and G.D. Rolph, HYSPLIT (HYbrid Single-Particle Lagrangian Integrated Trajectory) Model access via NOAA ARL READY website (<http://www.arl.noaa.gov/ready/hysplit4.html>), NOAA Air Resources Laboratory, Silver Spring, MD, 2003.
- DRI Operating Procedure, Sequential Filter Sampler: Operation, Maintenance, and Field Calibration. Desert Research Institute, 1990.
- Edgerton, E.S., B.E. Hartsell, R.D. Saylor, J.J. Jansen, D.A. Hansen, and G.M. Hidy, The Southeastern Aerosol Research and Characterization study, part 3: Continuous measurements of fine particulate matter mass and composition, *J. Air & Waste Manage. Assoc.*, 56, 1325-1341, 2006.
- Eisinger, M. and J. P. Burrows, Tropospheric sulfur dioxide observed by the ERS-2 GOME instrument, *Geophys. Res. Lett.*, 25, 4177-4180, 1998.
- El-Zanan, H.S., D.H. Lowenthal, B. Zielinska, J.C. Chow, and N. Kumar, Determination of the organic aerosol mass to organic carbon ratio in IMPROVE samples. *Chemosphere* 60, 485-496, 2005.
- Eneroth, K., E. Kjellstrom, and K. Holmen, A trajectory climatology for Svalbard; investigating how atmospheric flow patterns influence observed tracer concentrations, *Phys. Chem. Earth*, 28, 1191-1203, 2003.
- EPRI, Aircraft Measurements of Pollutants and Meteorological Parameters During the Sulfate Regional Experiment (SURE) Program: Research Triangle Institute, Inc., 1981.
- ESRI Data and Maps, Arcview 8.0, 2000.
- Finlayson-Pitts, B., and J. Pitts, Chemistry of the Upper and Lower Atmosphere, Academic Press, San Diego, 2000.

- Galloway, J. N. and D. M. Whelpdale, An Atmospheric Sulfur Budget for Eastern North-America, *Atmos. Environ.*, **14**(4): 409-417, 1980.
- Flanagan, J., R. Jayanty, E. Rickman, and M. Peterson, PM_{2.5} Speciation Trends Network: Evaluation of whole-system uncertainties using data from sites with collocated samplers. *J. Air & Waste Manage. Assoc.*, **56**, 492-499, 2006.
- Frank, N. H., Retained nitrate, hydrated sulfates, and carbonaceous mass in Federal Reference Method fine particulate matter for six Eastern U.S. cities. *J. Air & Waste Manage. Assoc.*, **56**, 500-511, 2006.
- Frischer T, M. Studnicka, C. Gartner, E. Tauber, F. Horak, A. Veiter, J. Spengler, J. Kuhr, and R. Urbanek, Lung function growth and ambient ozone: a 3-year population study in schoolchildren. *Am. J. Respir. Crit. Care Med.*, **160**, 390–396, 1999.
- Gauderman W.J., G.F. Gilliland, H. Vora, E. Avol, D. Stram, R. McConnell, D. Thomas, F. Lurmann, H.G. Margolis, E.B. Rappaport, K. Berhane, and J.M., Peters, Association between air pollution and lung function growth in southern California schoolchildren: results from a second cohort. *Am. J. Respir. Crit. Care Med.*, **166**, 76–84, 2002.
- Grell, G. A., J. Dudhia, and D. R. Stauffer, A description of the fifth-generation Penn State/NCAR Mesoscale Model (MM5). NCAR Tech. Note NCAR/TN-398 STR, 1995.
- Hains, J.C., B.F. Taubman, A.M. Thompson, L.T. Marufu, B.G. Doddridge, J.W. Stehr, D. Allen, and R.R. Dickerson, Origins of chemical pollution derived from Mid-Atlantic aircraft profiles using a clustering technique, *J. Geophys. Res.*, submitted 2007a.
- Hains, J.C., L.W.A. Chen, B.F. Taubman, B.G. Doddridge, and R.R. Dickerson, A side by side comparison of filter-based PM_{2.5} measurements at a suburban site: A closure study, *Atmos. Environ.*, in press 2007b.
- Harris, J.M., and S.J. Oltmans, Variations in tropospheric ozone related to transport at American Samoa, *J. Geophys. Res.*, **102**(D7), 8781-8791, 1997.
- Harrison, D., S.S. Park, J. Ondov, T. Buckley, S.R. Kim, and R.K.M. Jayanty, Highly time resolved fine particle nitrate measurements at the Baltimore Supersite. *Atmos. Environ.*, **38**, 5321-5332, 2004.
- Hicks, B. B., T. P. Meyers, R.P. Hosker, R.S. Artz, Climatological features of regional surface air quality from the Atmospheric Integrated Research Monitoring Network (AIRMoN) in the USA, *Atmos. Environ.*, **35**(6): 1053-1068, 2001.

- Hodzic, A., R. Vautard, B. Bessagnet, M. Lattuaati, F. Moreto, Long-term urban aerosol simulation versus routine particulate matter observations, *Atmos. Environ.*, 39, 5851-5864, 2005.
- Hogrefe, C., J. Biswas, B.Lynn, K. Civerelo, J.Y. Ku, J. Rosenthal, C. Rosenzweig, R. Goldberg, and P.L. Kinney, Simulating regional-scale ozone climatology over the eastern United States: model evaluation results, *Atmos. Environ.*, 38, 2627-2638, 2004.
- Hopke, P.K., Receptor models in air-pollution. *Trac-Trends in Analytical Chemistry* 3, R6-R7, 1984.
- IPCC Climate Change 2001: The scientific Basis, 2001.
- Jorba, O., C. Perez, F. Rocadenbosch, and J.M. Baldasano, Cluster analysis of 4-day back trajectories arriving in the Barcelona area, Spain, from 1997 to 2002, *J. Appl. Meteor.*, 43(6), 887-901, 2004
- JPL Publication, Chemical kinetics and photochemical data for use in atmospheric studies. Evaluation Number 15, JPL Publication 06-2, 2006.
- Kalkstein, L.S., G. Tan, and J.A. Skindlov, An evaluation of three clustering procedures for use in synoptic climatological classification, *J. Appl. Meteor.*, 26, 717-730, 1987.
- Kelley, P., R.R. Dickerson, W.T. Luke, and G.L. Kok, Rate of NO₂ photolysis from the surface to 7.6-km altitude in clear-sky and clouds, *Geophys. Res. Lett.*, 22, 2621-2624, 1995.
- Kim, E., and P.K. Hopke, Identification of fine particle sources in mid-Atlantic US area. *Water Air and Soil Poll.* 168, 391-421, 2005.
- Kim, E., P.K. Hopke, and Y. Qin, Estimation of organic carbon blank values and error structures of the speciation trends network data for source apportionment. *Journal J. Air & Waste Manage. Assoc.*, 55, 1190-1199, 2005.
- Koch, D., D. J. Jacob, I. Tegen, D. Rind, and M. Chin, Tropospheric sulfur simulation and sulfate direct radiative forcing in the Goddard Institute for Space Studies general circulation model, *J. Geophys. Res.*, 104, 23,799– 23,822, 1999.
- Laden, F., L.M. Neas, D.W. Dockery, and J. Schwartz, Association of fine particulate matter from different sources with daily mortality in six US cities. *Enviro. Health Perspect.* 108, 941-947, 2000.

- Lake D.A., M.P. Tolocka, M.V., Johnston, and A.S. Wexler, Mass spectrometry of individual particles between 50 and 750 nm in diameter at the Baltimore supersite. *Enviro. Sci. & Tech.* 37, 3268-3274, 2003.
- Lee, G., J.T. Merrill, and B.J. Huebert, Variation of free tropospheric total nitrate at Mauna Loa Observatory, Hawaii, *J. Geophys. Res.*, 99(D6), 12821-12831, 1994.
- Lee, J.H., P.K. Hopke, T.M. Holsen, A.V. Polissar, D.W. Lee, E.S. Edgerton, J.M. Ondov, and G. Allen, Measurement of fine particle mass concentrations using continuous and integrated monitors in eastern US cities. *Aerosol Sci. and Tech.*, 39, 261-275, 2005a.
- Lee, J.H., P.K. Hopke, T.M. Holsen, and A.V. Polissar, Evaluation of Continuous and filter-based methods for measuring PM_{2.5} mass concentration. *Aerosol Sci. and Tech.*, 39, 290-303, 2005b.
- Levy, R.C., Second generation retrieval of tropospheric aerosol properties over land from inversion of visible and near-infrared spectral reflectance: Application over Maryland, Doctoral Dissertation, Atmospheric and Oceanic Science, University of Maryland, 2007.
- Lippmann M., Filters and filter holders. In: Cohen BS, Hering SV, eds. Air sampling instruments for evaluation of atmospheric contaminants, 8th ed. Cincinnati, OH: American Conference of Governmental Industrial Hygienists, Inc., pp. 247-279. 1/15/98 110 NIOSH Manual of Analytical Methods, 1995.
- Liu B.Y.H., D.Y.H. Pui, and K.L. Rubow, Characteristics of air sampling filter media. In: Marple VA, Liu BYH, eds. Aerosols in the mining and industrial work environments, vol. 3, instrumentation. Ann Arbor, MI: Ann Arbor Science, pp. 989-1038, 1983.
- Logan, J.A., Tropospheric ozone: Seasonal behavior trends and anthropogenic influence, *J. Geophys. Res.*, 90, 10,463-10,482, 1985.
- Luke, W.T., Evaluation of a commercial pulsed fluorescence detector for the measurement of low-level SO₂ concentrations during the Gas-Phase Sulfur Intercomparison Experiment, *J. Geophys. Res.*, 102(D13), 16255-16265, 1997.
- Malm, W.C., J.F. Sisler, D. Huffman, R.A. Eldred, and T.A. Cahill, Spatial and seasonal trends in particle concentration and optical extinction in the United States. *J. Geophys. Res.*, 99, 1347-1370, 1994.
- Malm, W.C., B.A. Schichtel, R.B. Ames, and K.A. Gebhart, A 10-year spatial and temporal trend of sulfate across the United States. *J. Geophys. Res.*, 107, 4627, 2002.

- Malm, W.C., B.A. Schichtel, M.L. Pitchford, L.L. Ashbaugh, and R.A. Eldred, Spatial and monthly trends in speciated fine particle concentration in the United States. *J. Geophys. Res.*, 109, D03306, 2004.
- Malm, W.C., D.E. Day, C. Carrico, S.M. Kreidenweis, J.L. Collett, G. McMeeking, T. Lee, J. Carrillo, and B. Schichtel, Intercomparison and closure calculations using measurements of aerosol species and optical properties during the Yosemite Aerosol Characterization Study. *J. Geophys. Res.*, 110, D14302, 2005.
- Marufu, L.T., B.F. Taubman, B. Bloomer, C.A. Piety, B.G. Doddridge, and R.R. Dickerson, The 2003 North American electrical blackout: An accidental experiment in atmospheric chemistry, *Geophys. Res. Lett.*, 31, L13106, doi:10.1029/2004GL019771, 2004
- McDow, S.R., and J.J. Huntzicker, Vapor adsorption artifact in the sampling of organic aerosol : Face velocity effects. *Atmos. Environ.*, 24, 2563-2571, 1990.
- Mebust, M., B. Eder, F. Binhowski, and S. Roselle, Models-3 Community Multiscale Air Quality (CMAQ) model aerosol component 2. Model evaluation, *J. Geophys. Res.*, 108(D6), 4184, doi:10.1029/2001JD001410, 2003.
- Moody, J.L., and J.N. Galloway, Quantifying the relationship between atmospheric transport and the chemical composition of precipitation on Bermuda, *Tellus 40B*, 463-479, 1988.
- Moody, J.L., J.W. Munger, A.H. Goldstein, D.J. Jacob, and S.C. Wofsy, Harvard Forest regional-scale air mass composition by Patterns in Atmospheric Transport History (PATH), *J. Geophys. Res.*, 103(D11), 13181-13194, 1998
- Moody, J.L., S.J. Oltmans, H. Levy II, and J.T. Merrill, Transport climatology of tropospheric ozone: Bermuda, 1988-1991, *J. Geophys. Res.*, 100(D4), 7179-7194, 1995
- Moy, L.A., R.R. Dickerson, and W. F. Ryan, Relationship between back trajectories and tropospheric trace gas concentrations in rural Virginia, *Atmos. Environ.*, 28(17), 2789-2800, 1994.
- Mueller, S.F., E.M. Bailey, T.M. Cook, and Q. Mao, Treatment of clouds and the associated response of atmospheric sulfur in the Community Multiscale Air Quality (CMAQ) modeling system, *Atmos. Environ.*, 40, 6804-6820, 2006.
- Nicolet, M. R.R. Meier, and D.E. Anderson, Radiation field in the troposphere and stratosphere-II. Numerical Analysis. *Planet. Space. Sci.*, 30, 935-983, 1982.

Novakov, T., D.A. Hegg, and P.V. Hobbs, Airborne measurements of carbonaceous aerosols on the East Coast of the United States, *J. Geophys. Res.*, 102, 30,023–30,030, 1997.

OC/EC Laboratory Environmental and Industrial Sciences Division, Research Triangle Institute, Standard Operating Procedure for the Determination of Organic, Elemental, and Total Carbon in Particulate Matter Using a Thermal/Optical Transmittance Carbon Analyzer, 2003.

Ogulei, D., P.K. Hopke, L.M. Zhou, P. Paatero, S.S. Park, and J. Ondov, Receptor modeling for multiple time resolved species: The Baltimore supersite. *Atmos. Environ.*, 39, 3751-3762, 2005.

Ondov, J.M., T.J. Buckley, P.K. Hopke, D. Ogulei, M.B. Parlange, W.F. Rogge, K.S. Squibb, M.V. Johnston, and A.S. Wexler, Baltimore Supersite Highly time- and size-resolved concentrations of urban PM_{2.5} and its constituents for resolution of sources and immune responses. *Atmos. Environ.*, 40, S224-A237, 2006.

Park, R., The interaction of regional- and global-scale atmospheric chemistry, transport, and climate processes. Doctoral dissertation, Meteorology, University of Maryland, College Park, 2001.

Park S.S., D. Harrison, J.P. Pancras, and J.M. Ondov. Highly time-resolved organic and elemental carbon measurements at the Baltimore Supersite in 2002. *J. Geophys. Res.*, 110, D07S06, 2005a.

Park S.S., J.M. Ondov, D. Harrison, and N.P. Nair, Seasonal and shorter-term variations in particulate atmospheric nitrate in Baltimore. *Atmos. Environ.*, 39, 2011-2020, 2005b.

Patashnick, H. and E.G. Rupprecht, Continuous PM₁₀ measurement using the Tapered Element Oscillating Microbalance. *J. Air & Waste Manage. Assoc.*, 41, 1079-1083, 1991.

Pathak, R.K., X. Yao, and C.K. Chan, Sampling artifacts of acidity and ionic species in PM_{2.5}. *Enviro. Sci. & Tech.*, 38, 254-259, 2004.

Perliski, L. and S. Solomon, On the Evaluation of Air Mass Factors for Atmospheric Near-Ultraviolet and Visible Absorption Spectroscopy. *J. Geophys. Res.*, 98 (D6) 10363-10374, 1993.

Peterson, M.R., and M.H. Richards, Thermal-Optical-Transmittance Analysis for Organic, Elemental, Carbonate, Total Carbon, and OCX₂ in PM_{2.5} by the EPA/NIOSH Method. RTI Conference proceedings, 2002.

Peters, A., D.W. Dockery, J.E. Muller, and M.A. Mittleman,. Increased particulate air pollution and the triggering of myocardial infarction. *Circulation* 103, 2810-2815, 2001a.

Peters, T.M., G.A. Norris, R.W. Vanderpool, D.B.Gemmill, R.W.Wiener, R.W. Murdoch, F.F. McElroy, and M. Pitchford, Field performance of PM2.5 Federal Reference Method samplers. *Aerosol Sci. and Tech.*, 34, 433-443, 2001b.

Peters, T.M., R.A. Gussman, L.C. Kenny, and R.W. Vanderpool,. Evaluation of PM2.5 size selectors used in speciation samplers. *Aerosol Sci. and Tech.*, 34, 422-429, 2001c.

Pham, M., J.F. Muller, G. Brasseur, C. Granier, and G. Megie, A three-dimensional study of the tropospheric sulfur cycle, *J. Geophys. Res.*, 100, 26061-26092, 1995.

Platt, U., Differential Optical Absorption Spectroscopy (DOAS) in *Air Monitoring by Spectroscopic Techniques* (M.W. Sigrist. Ed.), *Chemical Analysis Series*, Vol 127, pp.27-84, Wiley, New York, 1994.

Platt, U., Recent Developments in DOAS: an Overview. Poster presentation, Second International DOAS Workshop 2003.

Polidori, A., B.J. Turpin, H-J. Lim, J.C. Cabada, R. Subramanian, S.N. Pandis, and A.L. Robinson, Local and regional secondary organic aerosol: Insights from a year of semi-continuous carbon measurements at Pittsburgh. *Aerosol Sci. and Tech.*, 40, 861-872, 2006.

Rees, S.L., A.L. Robinson, A. Khlystov, C.O. Stanier, and S.N. Pandis, Mass balance closure and the Federal Reference Method for PM2.5 in Pittsburgh, Pennsylvania. *Atmos. Environ.*, 38, 3305-3318, 2004.

Remer, L.A., S.Gasso, D.A. Heff, Y.J. Kaufmann, and B.N. Holben, Urban/industrial aerosol: Ground based Sun/sky radiometer and airborne in-situ measurements, *J. Geophys. Res.*, 102, 16849-46859, 1997.

Research Triangle Institute, Final data summary report for year 1 of the chemical speciation of PM2.5 filter samples project, 2000.

Restad, K., I. S. A. Isaksen, and T. K. Berntsen, Global distribution of sulfate in the troposphere: A three-dimensional model study, *Atmos. Environ.*, 32, 3593-3609, 1998.

Roelofs, G.-J., J. Lelieveld, and L. Ganzeveld, Simulation of global sulfate distribution and the influence on effective cloud drop radii with a coupled photochemistry-sulfur cycle model, *Tellus, Ser. B*, 50, 224- 242, 1998

Rozanov, V.V., D. Diebel, R.J.D. Spurr, and J.P. Burrows, GOMETRAN: A radiative transfer model for the satellite project GOME, the plane parallel version, *J. Geophys. Res.*, 102(D14):16683-16695, 1997.

Ruidavets J.B., M.Cournot, S. Cassadou, M.Giroux, M. Meybeck, and J.Ferrieres, Ozone air pollution is associated with acute myocardial infarction. *Circulation*, 111, 563–569, 2005.

Russell, A., G.R. McGregor, and G.J. Marshall, An examination of the precipitation delivery mechanisms for Dolleman Island, eastern Antarctic Peninsula, *Tellus 56A*, 501-513, 2004

RTI, Quality Assurance Projects Plan Chemical Speciation of PM2.5 Filter Samples. Research Triangle Park, NC, 2004.
<http://www.epa.gov/ttn/amtic/files/ambient/pm25/spec/rtiqap.pdf>

Ryan, W.F., B.G. Doddridge, R.R. Dickerson, R.M. Morales, K.A. Hallock, P.T. Roberts, D.L. Blumenthal, J.A. Anderson, and K.L. Civerolo, Pollutant transport during a regional O₃ episode in the Mid-Atlantic states, *J. Air & Waste Manage. Assoc.*, 48, 786-797, 1998.

Schmid, H., L. Laskus, H.J. Abraham, U. Baltensperger, V. Labanchy, M. Bizjak, P. Burba, H. Cachier, D. Crow, J. Chow, T. Gnauk, A. Even, H.M. Brink, K.P. Giesen, R. Hitzenberger, E. Hueglin, W. Maenhaut, C. Pio, A. Carvalho, J.P. Putaud, D.Toom-Sauntry, and H. Puxbaum,. Results of the "carbon conference" international aerosol carbon round robin test stage I. *Atmos. Environ.*, 35, 2111-2121, 2001.

Schnelle, K.B., and Dey, P.R., Atmospheric dispersion modeling compliance guide, New York: McGraw-Hill, 2000.

Schubert, S.D., R.B. Rood, and J. Pfaendtner, An assimilated data set for earth science applications, *Bul. Am. Met. Soc.* 74, 2331-2342, 1993.

Schwab, J., H. Felton, and K. Demerjian, Aerosol chemical composition in New York state from integrated filter samples: Urban/rural and seasonal contrasts *J. Geophys. Res.*, 109,(D16) D16S05, 2004.

Schwartz, J. and L.M. Neas, Fine particles are more strongly associated than coarse particles with acute respiratory health effects in schoolchildren. *Epidemiology*, 11, 6-10, 2000.

Seigneur, C., Current Status of air quality models for particulate matter, *J. Air & Waste Manage. Assoc.*, 51, 1508-1521, 2001.

Seinfeld, J.H. and S.N. Pandis, Atmospheric chemistry and physics: From air pollution to climate change, John Wiley and Sons, Inc. New York, 1998.

- Solomon, P., K. Baumantt, E. Edgerton, R. Tanner, D. Eatough, W. Modey, H. Maring, D. Savoie, S. Natarajan, M.B. Meyer, and G. Norris, Comparison of integrated samplers for mass and composition during the 1999 Atlanta Supersites project. *J. Geophys. Res.* 108, 8423, 2003.
- Stohl, A., G. Wotawa, P. Seibert, and H. Kromp-Kolb, Interpolation errors in wind fields as a function of spatial and temporal resolution and their impact on different types of kinematic trajectories, *J. Appl. Meteor.*, 34, 2149-2165, 1995.
- Stohl, A., Computation, accuracy and applications of trajectories – a review and bibliography, *Atmos. Environ.*, 32(6), 947-966, 1998.
- Stunder, B.J.B, An assessment of the quality of forecast trajectorye., *J. Appl. Meteor.*, 35, 1319-1331, 1996.
- Subramanian, R., A.Y. Khlystov, J.C. Cabada, and A.L. Robinson, Evaluation of measurement methods: Positive and negative artifacts in particulate organic carbon measurements with denuded and undenuded sampler configurations. *Aerosol Sci. and Tech.*, 38, 27-48, 2004.
- Taubman, B.F., L.T. Marufu, C.A. Piety, B.G. Doddridge, J.W. Stehr, and R.R. Dickerson, Airborne characterization of the chemical, optical, and meteorological properties, and origins of a combined ozone/haze episode over the eastern U.S., *J. Atmos. Sci.*, 61(14), 1781-1793, 2004a.
- Taubman, B.F., L.T. Marufu, B.L. Vant-Hull, C.A. Piety, B.G. Doddridge, R.R. Dickerson, and Z. Li, Smoke over haze: Aircraft observations of chemical and optical properties and the effects on heating rates and stability, *J. Geophys. Res.*, 109, D02206, doi:10.1029/2003JD003898, 2004b.
- Taubman, B.F., J.C. Hains, A.M. Thompson, L.T. Marufu, B.G. Doddridge, J.W. Stehr, C.A. Piety, and R.R. Dickerson, Aircraft vertical profiles of trace gas and aerosol pollution over the mid-Atlantic United States: Statistics and meteorological cluster analysis, *J. Geophys. Res.*, 111, D10S07, 2006
- Technology Transfer Network Air Quality System, 2006.
<http://www.epa.gov/ttn/airs/airsaqs/detaildata/downloadaqsddata.htm>
- Tesche, T.W., R. Morris, G. Tonnesen, D. McNally, J. Boylan, and P. Brewer, CMAQ/CAMx annual 2002 performance evaluation over the eastern US, *Atmos. Environ.*, 40, 4906-4919, 2006.
- Thermo Anderson, RAAS Operator's Manual. Chemical speciation monitor, 2001.

Thermo Scientific, Model 43C Pulsed fluorescence SO₂ analyzer instruction manual, 2004a.

Thermo Scientific, Model 48C UV gas filter correlation CO analyzer instruction manual, 2004b.

Thermo Scientific, Model 49C UV photometric O₃ analyzer instruction manual, 2004c.

Thornton, D.C., A.R. Bandy, A.R. Drieger, Sulfur dioxide over the western Atlantic ocean. *Global Biogeochem. Cycles*, 1, 317-328, 1987.

Tolocka, M.P., D.A. Lake, V. Johnston, and A.S. Wexler, Size-resolved fine and ultrafine particle composition in Baltimore, Maryland. *J. Geophys. Res.*, 110, D07S04, 2005.

TSI, Model 3550/3560 Series Integrating nephelometer, Instruction manual, 1997.

Turpin, B.J., J.J. Huntzicker, and S.V. Hering, Investigation of organic aerosol sampling artifacts in the Los Angeles Basin. *Atmos. Environ.*, 28, 3061-3071, 1994.

Turpin, B. J. and H. Lim, Species contributions to PM_{2.5} mass concentrations: Revisiting common assumptions for estimating organic mass. *Aerosol Sci. and Tech.*, 35, 602-610, 2001.

US EPA Emissions Monitoring and Analysis Division Monitoring & Quality Assurance Group, Strategic plan. Development of the Particulate Matter (PM_{2.5}) quality system for the chemical speciation monitoring trends sites, 1999.

US EPA Office of Air Quality and Planning Standards, National Air Pollution Emission Trends, 2000.

US EPA, Model SASS & SuperSASS PM_{2.5} Ambient Chemical Speciation Samplers Field Operation Manual, 2001.

US EPA, National air quality and emissions trends report. 2003 Special Studies Edition, 2003.

Vukovich, F.M., Boundary-layer ozone variations in the eastern United-States and their association with meteorological variations – long-term variations, *J. Geophys. Res.*, 99, 16839-16850, 1994.

Vukovich, F.M., R. Wayland, and J. Sherwell, Characteristics of ozone in the Baltimore-Washington area as established from one-hour average concentrations, *J. Air & Waste Manage. Assoc.*, 49, 794-803, 1999.

- Watson, J. G., J.A. Cooper, and J.J. Huntzicker, The Effective Variance Weighting for Least-Squares Calculations Applied to the Mass Balance Receptor Model. *Atmos. Environ.*, 18, 1347-1355, 1984.
- Watson, J.G., J.L. Bowen, J.C. Chow, C.F. Rogers, M.G. Ruby, M.J. Rood, and R.T. Egami, High volume measurements of size classified suspended particulate matter, in: *Methods of Air Sampling and Analysis 3rd edition* (J.P. Lodge), Lewis Publishers, Inc., Chelsea, MI, 1989a.
- Watson, J.G., P.J. Lioy, and P.K. Mueller, The measurements process: Precision, accuracy, and validity in: *Air sampling instruments for evaluation of atmospheric contaminants 7th edition*, (S.V. Hering), American Conference of Governmental Industrial Hygienists, Cincinnati, OH, pp. 51-57, 1989b.
- Watson, J.G. and J.C. Chow, Comparison and evaluation of in situ and filter carbon measurements at the Fresno Supersite. *J. Geophys. Res.* 107, 8341, 2002.
- Wayne, R.P., *Chemistry of Atmospheres Third Edition*, Oxford University Press, New York, 2000.
- Weed, D.L., Weight of evidence: A review of concept and methods. *Risk Analysis* 25, 1545-1557. 2005.
- White, M.C., R.A. Etzel, W.D. Wilcox, and C. Lloyd, Exacerbations of childhood asthma and Ozone pollution in Atlanta. *Environ Res.*, 65, 56-68, 1994
- Wilks, Daniel, *Statistical Methods in the Atmospheric Sciences*. Academic Press, San Diego, 1995.
- Wong G.W., F.W. Ko, T.S.Lau, S.T. Li, D. Hui, S.W. Pang, R.Leung, T.F. Fok, and C.K.W. Lai, Temporal relationship between air pollution and hospital admissions for asthmatic children in Hong Kong. *Clin Exp. Allergy*, 31, 565-569, 2001.
- Zhang, D. and R.A. Anthes, A high-resolution model of the planetary boundary layer - Sensitivity tests and comparisons with SESAME-79 data. *J.App. Meteo.*, 21, 1594-1609, 1982.
- Zhang, X. Q., and P.H. McMurry, Evaporative Losses of Fine Particulate Nitrates During Sampling. *Atmos. Environ.*, 26, 3305-3312, 1992.
- Zhang, Y., B. Pun, S. Wu, K. Vijayaraghavan, and C. Seigneur, Application and evaluation of two air quality models for particulate matter for a Southeastern U.S. episode. *J. Air & Waste Manage. Assoc.*, 54, 1478-1493, 2004.

Zhang, D.-L. and W.-Z. Zheng, Diurnal cycles of surface winds and temperatures as simulated by five boundary-layer parameterizations, *J.App. Meteo.*, 43, 157-169, 2004.

Zhang, X., G. Zhuang, J. Chen, Y. Wang, X. Wang, Z. An, and P. Zhang, Heterogeneous reactions of sulfur dioxide on typical mineral particles, *J. Phys. Chem. B*, 110, 12588-12596, 2006.